Study of the local order around magnetic impurities in semiconductors for spintronics

Mauro Rovezzi

UNIVERSITE JOSEPH FOURIER
SCIENCES.TECHNOLOGIE.SANTÉ

THÈSE

présentée pour obtenir le grade de

DOCTEUR EN SCIENCES DE L'UNIVERSITÉ JOSEPH FOURIER - GRENOBLE I

Spécialité Physique de la Matière Condensée et du Rayonnement

par

Mauro ROVEZZI

Étude de l'ordre locale autour d'impuretés magnétiques dans les semiconducteurs pour l'électronique de spin

Directeur de thèse : Francesco d'Acapito

soutenue publiquement le 6 Octobre 2009 devant le jury composé de

Henri Mariette	*Président*
Pierre Lagarde	*Rapporteur*
Roberto Gunnella	*Rapporteur*
Krystyna Ławniczak-Jabłońska	*Examinateur*
Francesco d'Acapito	*Examinateur*

Thèse préparée au sein du laboratoire GILDA CRG

European Synchrotron Radiation Facility - Grenoble

Study of the local order around magnetic impurities in semiconductors for spintronics

Mauro Rovezzi

PhD thesis

Version 1.0c

October 6, 2009

Publication: Grenoble, October 2009.
Realized with LaTeX 2_ε.
Printed at ESRF.

Remerciements

Ce travail de thèse a été effectué au laboratoire Italien GILDA CRG installé dans le synchrotron ESRF de Grenoble et a été possible grace à la direction de Francesco d'Acapito à qui s'addressent mes premiers remerciements pour m'avoir appris l'art de la spectroscopie XAFS, accompagné dans la vie scientifique de ces quatre années de thèse, et pour avoir patiemment supporté mes problemes quotidiennes.

Je tiens aussi à remercier Settimio Mobilio, directeur du laboratoire GILDA CRG, le *Consiglio Nazionale delle Ricerche* qui a financé ce travail et l'ESRF pour le rayonnement de synchrotron et le cadre de vie scientifique hautement stimulant dans le quel cette thèse s'est deroulée.

Je voudrais exprimer ma gratitude envers les membres du jury : le président Prof. Henri Mariette, Dr. Pierre Lagarde et Prof. Roberto Gunnella qui ont accepté d'etre rapporteurs de ce manuscrit et Prof. Krystyna Ławniczak-Jabłońska.

En plus, je n'aurais pas pu aboutir cette étape sans le support quotidien de ma famille, mes amis et ma compagne. Celles et ceux qui je remercie à la fin de ce texte mais qui occupent la partie la plus importante de ma vie.

Collaborateurs

Ce travail a premièrement été possible grace à mes collaborateurs qui ont produit les échantillons ; il s'est enrichi ensuite grace aux caracterisations complementaires et les calculs *ab initio* dont j'ai pu participer et, en plus, avec les échanges directes et indirectes entre ce riche monde fait d'etre humains, j'ai pu mettre ensemble les pieces du puzzle. Sans oublier celles et ceux avec qui j'ai travaillé indirectemnt, je tiens à remercier explicitement celles et ceux que j'ai eu la possibilité de connaitre directement (en ordre d'apparition dans ce manuscrit et sans détailler la place de chacune et chacun) :

- pour le GaMnAs : Jacek K. Furdyna et Xinyu Liu à Notre Dame ;
- pour GaFeN : Alberta Bonanni, Andrea Navarro-Quezada, Tian Li, Bogdan Faina à Linz, Tomasz Dietl, Piotr Bogusławski et Paweł Jakubas à Varsovie, Aldo Amore Bonapasta et Francesco Filippone à Rome ;
- pour GeMn : Matthieu Jamet, Thibaut Devillers, André Barski, Clément Porret, Ing-Song Yu, Vincent Favre-Nicolin, Samuel Tardif, Emmanuel Arras, Pascal Pochet à Grenoble ;
- pour les nano-fils : Federico Boscherini à Bologne, Faustino Martelli, Fauzia Jabeen et Silvia Rubini à Trieste ;
- le groupe GILDA : Chiara Maurizio, Fabrizio Bardelli, Hernan Gabriel Pais, Fabrizio Lamanna et Fabio D'Anca à Grenoble, Vinicio Tullio et Vittorio Sciarra à Frascati.
- pour la ReflEXAFS : Federico Benzi et Ivan Davoli à Rome.

M.R.

Contents

Introduction

La spintronique avec les semiconducteurs vise à introduire un grade de liberté additionnel, le spin, dans le contexte actuel des dispositifs pour l'électronique. Historiquement, les deux domaines du stockage et du traitement de l'information ont été traités séparément, en se limitant, quand au premier, à des matériaux magnétiques, où l'information est stockée dans les spins des éléments magnétiques tandis que le deuxième aux semiconducteurs, où seuls les courants des porteurs sont utilisés dans les canaux des transistors. Aujourd'hui, la nécessité d'une plus grande densité de l'information et la réduction de la consommation d'énergie pousse cette technologie à converger vers des dispositifs capables de stocker et de traiter l'information sans la nécessité du passage de courant électrique. Suite à l'approche bottom-up, la fonctionnalisation des matériaux semiconducteurs par l'intermédiaire du dopage avec des éléments magnétiques est une aventure passionnante et, pour certains aspects, un domaine de recherche controversé que a vu une large communauté scientifique le traiter au cours des trente dernières années. À commencer avec les matériaux semimagnétiques jusqu'aux semi-conducteurs magnétiques dilués (Diluted Magnetic Semiconductors, DMS) et aux nano-objets ferromagnétiques dans les semiconducteurs, d'importantes découvertes ont été réalisées dans la compréhension des mécanismes physiques impliqués dans le ferromagnétisme de ces matériaux, mais le problème est toujours ouvert. L'une des approches prometteuses consiste à unifier les aspects fondamentaux de la croissance, la théorie et de la caractérisation, en les laissent interagir les uns les autres dans un cycle d'auto-cohérence. Cette thèse est un travail inséré à l'échelle de la caractérisation structurale et est destiné à être une partie de ce cycle.

L'approche expérimentale choisi dans cette étude est par le point de vue de la structure locale fourni par la spectroscopie d'absorption des rayons X (X-ray Absorption Fine Structure, XAFS). Cette technique est aussi un outil puissant qui, en exploitant la haute brillance de la troisième génération de synchrotrons, permet une enquête détaillée de la structure atomique autour des impuretés magnétiques intégrés dans une série de semiconducteurs hôtes, où les échantillons sont produites par certains des groupes les plus actifs dans ce domaine. En fait, malgré la XAFS est un outil de caractérisation structurale établie dans la science des matériaux, n'a pas été l'outil privilégié dans l'étude des semiconducteurs ferromagnétiques, car, en raison de la forte dilution des éléments magnetiques, elle nécessite la collecte et l'analyse des données avec une attention particulière. Ce problème est abordé, d'une part, directement par le travail expérimental sur une station XAFS (la ligne de lumière "GILDA"), afin de faire face à l'exigence de la croissante fonctionnalisation, et, d'autre part, en complétant avec d'autres outils avancées de caractérisation comme la diffraction des rayons X au synchrotron, la micro-

scopie électronique à transmission et par les calculs effectués dans le cadre de la théorie du fonctionnel densité (Density Functional Theory, DFT).

La nécessité d'une caractérisation structurale à l'échelle nanométrique est nécessaire pour comprendre le magnétisme des couches minces de DMS, car les méthodes de caractérisation standard ne montrent généralement pas de contraste chimique et la sensibilité à l'environnement local, donc les revendications de la réalisation de DMS à haute température de transition ferromagnétique sont soumises à l'incertitude concernant la contamination, la décomposition spinodale et la séparation de phase à l'échelle nanométrique.

Cette thèse est divisée en trois parties comme suit :

I. Le contexte scientifique est mis en place dans le *Chapitre 1* où un aperçu des aspects fondamentaux de la spintronique avec les semiconducteurs est fournie avec une attention particulière au ferromagnétisme dans les matériaux DMS et à l'évolution récente vers les systèmes DMS non uniformes. Le *Chapitre 2* passe en revue les bases de la spectroscopie XAFS dans un approche de type tutoriel axée sur l'application des méthodes d'analyse de DMS, la réalisation expérimentale conduisant à la collecte de données sont également signalés. En outre, un aperçu des techniques des dépôts et monitorage *in situ* et la complémentarité avec les outils de caractérisation magnétique et structurale sont donnés dans le *Chapitre 3* ; les calculs DFT utilisés dans ce travail y sont également illustrés.

II. Les applications systématiques des méthodes précédents à des cas spécifiques sont détaillées dans les *Chapitres 4–7*. Le point de départ est représenté par le système DMS le plus étudié et bien compris, le GaAs dopé avec du Mn, (*Chap. 4*), où les défauts de Mn interstitiel impliqué dans des phénomènes de surface à cause de leur haute mobilité sont étudiés en vue de mieux comprendre l'efficacité des traitements après croissance utilisés aujourd'hui afin d'augmenter la température de transition ferromagnétique. Un pas en avant est fait par l'étude du GaN dopé Fe (*Chap. 5*), un nouveau composé DMS prometteur constituant un bon plan de travail pour tester de nouveaux résultats théoriques et de la possible fonctionnalisation, car ses propriétés magnétiques et structurelles peuvent être réglées par le dopage autour de son limite de solubilité et le co-dopage avec d'impuretés accepteur/donneur. Un fascinant système supplémentaire est représenté par le Mn dans Ge (*Chap. 6*) qui subit une décomposition spinodale en nano-colonnes ferromagnétiques auto-organisés riches en Mn, donc la résolution de la structure locale de cette nouvelle phase constitue un point crucial. En outre, afin d'aller vers des structures DMS à une seule dimension, le Mn dans des nano-fils III-V à été enquêté (*Chap. 7*). Enfin, les conclusions générales et les perspectives de la présente étude sont résumés (*Chap. 8*).

III. La dernière partie est consacrée à des travaux complémentaires. En particulier, dans l'*Annexe A* est présenté un dispositif expérimental mis au point sur la ligne de lumière GILDA afin d'effectuer des mesures XAFS optimisés pour des couches minces, tandis que dans l'*Annexe B* est montré la mise en œuvre d'un nouvel algorithme XAFS pour l'analyse des données recueillies dans le mode de réflexion totale.

Introduction

The semiconductor spintronics research field aims to introduce an additional degree of freedom, the spin, in the current electronics devices. Historically, the two fields of information storage and processing have been treated separately, confining the first to magnetic materials where the information is stored in the spins of the magnetic elements while the second to semiconductors where only charges currents are used in the transistors channels. Nowdays, the need for higher information densities and reduction in energy consumption is leading this technology to converge in single devices capable to store and process information without the need for a continuous charge. Following the bottom-up approach, the functionalisation of semiconductor materials through the doping with magnetic elements is an exciting and for some aspects controversial research field that has seen an active and wide scientific community dealing with in the last thirty years. From the semimagnetic materials to the diluted magnetic semiconductors (DMS) and the ferromagnetic nano-objects into semiconductors, important discoveries have been done in understanding the underlying physical mechanisms involved in the ferromagnetism of these materials but the whole problem is still open. One of the promising approaches through the solution consists in unifying the fundamental aspects of the growth, theory and characterization, letting them to interact each other in a self-consistent cycle. The present thesis is a work inserted at the structural characterization step and is intended to be a part of this cycle.

The experimental approach chosen in this study is the local structure point of view of the x-ray absorption fine structure spectroscopy (XAFS). This technique is as a powerful tool that, exploiting the high brilliance of third generation synchrotron radiation sources, permits the detailed investigation of the atomic structure around magnetic impurities incorporated in a series of semiconductors hosts, where state-of-the-art samples are produced by some of the most active groups in this field. In fact, despite XAFS is a well established structural characterization tool in material science, has not been the privileged tool in the study of ferromagnetic semiconductors since, due to the high dilution level of the probed atomic species, it requires advanced data collection and analysis. This stimulating problem is tackled, on one side, by the direct experimental work on a XAFS facility (the "GILDA" beamline), in order to deal with the demanding functionalisation and, on the other side, by complementing with other advanced characterization tools like synchrotron x-ray diffraction, transmission electron microscopy and by modelling through first principle calculations performed in the framework of the density functional theory.

The need for a detailed structural characterization at the nanoscale is due to understand the magnetic response of thin DMS films since standard characterization methods do not show usually chemical contrast and sensitivity to the local environment, so claims about high-

temperature ferromagnetism in DMS are persistently subject of uncertainty concerning contamination, spinodal decomposition or nanoscale phase separation.

This thesis is divided in three parts detailed as follows:

I. The scientific context is introduced in *Chapter 1* where an overview of the basics aspects of the semiconductor spintronics is given with particular attention to the ferromagnetism in DMS materials and the recent developments through the non-uniform DMS systems. *Chapter 2* reviews the basics of the XAFS spectroscopy in a tutorial approach focusing on the application of the analysis methods to DMS; the experimental set-ups leading to the collected data are also reported. In addition, an overview on the employed deposition and *in situ* monitoring techniques with the complementary structural and magnetic characterization tools are given in *Chapter 3*; first principle calculations used in this work are also illustrated there.

II. The systematic application to specific case studies of the previous methods are detailed in *Chapters 4–7*. The starting point is represented by the most studied and well understood DMS system, Mn-doped GaAs, (*Chap. 4*) where the surface phenomena involving Mn interstitial defects mobility are investigated in order to better understand the effective post-growth treatments used nowdays to increase ferromagnetic transition temperature. A step forward is done by the study of Fe in GaN (*Chap. 5*), a new promising DMS consisting in a workbench for testing new theoretical findings and possible functionalisation, since its magnetic and structural properties can be tuned by doping around its solubility limit and co-doping with shallow impurities. A fascinating additional system is represented by Mn in Ge (*Chap. 6*) that undergoes spinodal decomposition into Mn-rich self-organized ferromagnetic nanocolumns, thus resolving the structure of this new phase is a crucial point. In addition, in order to move forward one-dimensional DMS, Mn in III-V nanowires is investigated (*Chap. 7*). Finally, the general conclusions and outlooks of the present study are summarized (*Chap. 8*).

III. The last part is dedicated to additional work conducted as a complementary part of the present study. In particular, in *Appendix A* is presented an experimental apparatus developed at the GILDA beamline in order to perform optimized XAFS measurements on epilayers, while in *Appendix B* is shown the implementation of a new algorithm to analyze XAFS data collected in total reflection mode.

Part I

Materials and methods

Spintronique avec les semiconducteurs

Résumé du Chapitre 1

Le chapitre traite le contexte scientifique dans le quel est encadré ce travail de thèse, la spintronique (ou électronique de spin) réalisée avec les matériaux semiconducteurs [1]. Il s'agit d'une branche du champ de recherche multidisciplinaire et en rapide évolution de la spintronique [2] qui vise à exploiter non seulement la charge mais aussi le spin des porteurs (électrons et trous). Ceci permettant d'utiliser le même dispositif pour le traitement et le stockage des informations avec conséquent augmentation des fréquences de calcul et une réduction de la consommation d'énergie. Aujourd'hui la spintronique a vu son application à des dispositifs qui utilisent matériaux magnétorésistifs mais pas les semiconducteurs où on cherche à réaliser un transistor à effet de spin [3], c'est à dire un dispositif où il y a une injection de spin efficace entre un materiel ferromagnétique et un autre non magnétique, une diffusion de spin longue, une manipulation de spin efficiente et la détection finale. Entre les matériaux les plus prometteurs pour la réalisation de ces dispositifs font partie les semiconducteurs magnétiques dilués (DMS). Il s'agit de semiconducteurs où des atomes magnétiques sont introduit (metaux de transition ou terres rares) en faible quantité (quelque % atomique). Ceci permet au semiconducteurs hôte de gagner des propriétés magnétiques tout en gardant ses propriétés électriques. Les DMS ont un rôle très important dans l'injection de spin dans les semiconducteurs parce que il a été démontré que cette fonction ne peut pas être accomplie par un métal [4] mais aussi ils permettent de contrôler leur propriétés magnétiques (électriques) avec un champ électrique (magnétique) appliqué de l'extérieur [5]. Ces propos justifient une recherche très active dans ce domaine depuis trente ans pour trouver une classe de DMS avec un temperature de transition ferromagnétique (temperature de Curie, T_C) qui dépasse largement la temperature ambiante.

Pour comprendre le magnétisme dans les DMS, le premier pas est de considérer des systèmes où la distribution des ions magnétiques est aléatoire et uniforme (Sec. 1.2). Ici l'approche suivi est semi-phénoménologique, dans le sens que les Hamiltoniens qui décrivent le système sont construit sur la base d'observations expérimentales. L'insertion des atomes magnetiques dans la structure du semi-conducteur porte à une redistribution des niveaux énergétiques sous l'-effet du champ cristallin et d'autres facteurs comme l'état de charge et le relaxations de la structure. L'identification de ces niveaux reste donc le point de départ. Ensuite les interaction d'échange qui portent à l'état magnétique macroscopique sont décrits. En particulier, le modèle *p-d* de Zener [6] est mis en avant parce il explique le ferromagnétisme observé dans les arséniures dopés au Mn et historiquement ses prévisions (Fig. 1.4) ont été à la base de plusieur

investigation expérimentales.

La dernière partie du chapitre est consacré aux DMS non uniformes (Sec. 1.3), où il y a une séparation chimique en zones à haute et d'autres à faible concentration de ions magnetiques. Ce phénomène est du à la décomposition spinodale, un processus différent de la énucléation. En effet, si d'un coté on cherche à éviter la précipitation de phases cristallines qui empêcherait l'utilisation dans un dispositif, de l'autre la décomposition spinodale peut amener à la création d'objets nanométriques auto-organisés dans le semi-conducteur avec une T_C élevée qui peuvent être exploités dans l'injection de spin. Pour traiter ce cas théoriquement et apporter des prévisions pour orienter les recherches expérimentales, les méthodes *ab initio* sont préférés. Quelque exemple de résultats récents est donc apporté à ce propos.

1

Semiconductor spintronics

In this chapter is given a rapid review on the semiconductor spintronics, a branch of the multidisciplinary fast-growing spintronics (or spin-electronics) research field, that aims to combine both charge and spin control of the carriers (electrons and holes) in the information-processing devices. After an overview on the current applications and motivations, the basics of diluted magnetic semiconductors are outlined and, from this picture, a step forward is done through the self-organization of nano-magnets into semiconductors, the way this technology is proceeding nowdays. It is worth noting that in the last ten years many important reviews articles and books have been dedicated to this topic and additional details can be found there [7, 2, 1, 8, 9, 10], in particular the Magnetic Semiconductor Spintronics Web Project[1] *is an interesting source for selected publications and data in this research field.*

1.1 Motivation and applications

The first development in spin-electronic field was spintronics based on magnetoresistive (MR) elements [10], known also as magnetoelectronics [11, 12], where two ferromagnetic layers are separated by a nonmagnetic metal or insulator and a semiconductor is not essential. This approach is already successful in device applications [13] such as magnetic sensors, read heads, and magnetic random access memory (MRAM) [14, 15] exploiting giant magnetoresistance [16, 17] and tunneling magneto-resistance [18] effect of MR elements. Utilizing the same technology of MRAM, MR elements are expected to be used as a programmable magnetologics [19] in the near future. The second parallel route was spintronics based on semiconductors [8, 20] that follows the concept of spin field effect transistor (FET) [3, 21], and spin injection, transportation, and detection in semiconductors using ferromagnet/semiconductor heterostructures [4, 22, 23] and/or doping semiconductors with magnetic ions, the case of diluted magnetic semiconductors (DMS) [24, 25, 26] are the major challenges on this route. In addition, a third new approach is getting interest nowdays, the molecular spintronics [27].

A successful spintronics application requires three basic functions: 1) an efficient spin injection from a ferromagnetic to a non-magnetic material; 2) reasonably long spin diffusion (at least tens of nanometers) and efficient spin manipulation; 3) spin detection. Although all these functions are equally important, the starting point is the injection and it is of particular interest for the current subject; a recent detailed review is found in Ref. [28] (and a tutorial-oriented in Ref. [9]). Optical spin injection by circularly polarized light has been a standard way to inject spin-polarized carriers into semiconductors but for application in real devices is preferable the

[1] See `http://unix12.fzu.cz/ms`

electric injection. The starting point for electric spin injection was the use of ferromagnetic metals using standard junctions. Although this method present problems of interface diffusion with the possibility to create undesiderated alloys, it has been demonstrated in a purely diffusive regime that it is inefficient (less than 0.1 %) [4, 29]. This is a fundamental barrier due to the conductivity difference between the two materials. In order to overcome this problem, it is possible to use tunnel contacts at the interface [30] or substitute the ferromagnetic metal with a ferromagnetic semiconductor (e.g. DMS) as successfully done with BeMnZnSe in AlGaAs/GaAs [31] and with GaMnAs in GaAs [32]. This justify the search for DMS with ferromagnetic transition temperatures well above room temperature. In addition, the interest in DMS is not only limited to the spin injection but also to the possibility to control their electric properties using a magnetic field and, *vice versa*, their magnetic properties using an electric field [5].

1.2 Diluted magnetic semiconductors

Diluted magnetic semiconductors (DMS) are semiconductor compounds ($A_{1-x}M_xB$) where a fraction x of the cations (few %) is randomly substituted by magnetic elements as transition metals (TM) or rare earths (RE) where the magnetic properties in the host semiconductor AB originate from $3d$ or $4f$ open shells. DMS were discovered 30 years ago [33] and, since then, many compounds were extensively studied: II-VI [24, 25], IV-VI [34], III-V [35, 36] (just to cite a few reviews). Focusing on TM (Mn in particular) in III-V and II-VI compounds, a brief review of the recently proposed mechanism for ferromagnetism in DMS is presented in this section.

1.2.1 Magnetic impurities in semiconductors

The starting point for the description of DMS is the electronic structure of TM impurities in semiconductors, an interesting and long standing problem [37]. In fact, when an isolated atom is introduced in a crystalline host semiconductor a variety of factors should be considered, as the atom's valence state, the lattice relaxation effects, the many electrons effects, etc. According to the Anderson model [38, 39, 40], the character of the magnetic impurity is determined by a competition of the hybridization of local and extended states (delocalizes magnetic electrons) and the on-site Coulomb interactions among the localized electrons (stabilizes the magnetic moment).

Dividing electron states in localized magnetic d shells and extended band states (s, p orbitals) – Vonsovskii model – the $3d$ shells levels of TM are indicated in Fig. 1.1 to respect the band energies of the host II-VI and III-V semiconductors. The "donors" levels denote the ionization energy of the magnetic electrons ($TM^{2+} \rightarrow TM^{3+}$ or d^N/d^{N-1}) whereas the "acceptors" correspond to their affinity energy ($TM^{2+} \rightarrow TM^{1+}$ or d^N/d^{N+1}). The difference between the two is the Coulomb (Hubbard) repulsion energy U in the semiconductor matrix [42].

It is probably safe to state that the treated DMS can be classified as magnetic insulators, in a sense that the states derived from the open $3d$ shells do not contribute to the Fermi volume but give rise to localized magnetic moments [43]. Recently, detailed reviews are given for magnetic impurities (with particular attention to Mn) in wide band-gap III-V semiconductors [44, 45] and for Fe in III-V and II-VI [46]. In the case of Mn in II-VI DMS, it acts as an isoelectronic impurity and do not introduce bound states. The two $4s$ electrons participate to the covalent bonding, while the d shell remains relatively inert. Hence, in zero magnetic field, II-VI DMS look like the non-magnetic alloy where the energy gap depend on the Mn concentration and

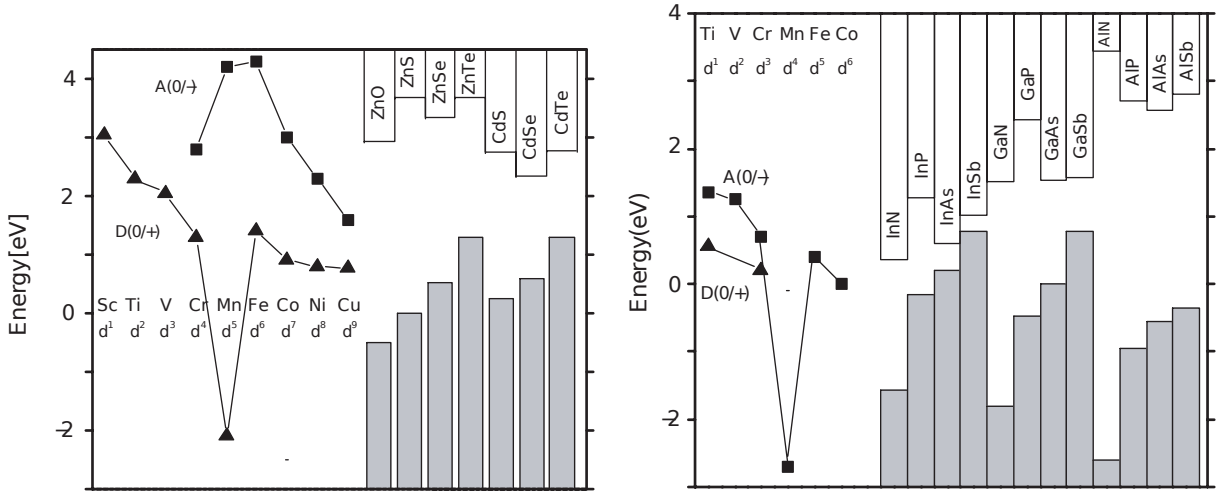

Figure 1.1: Approximate positions of TMs levels relative to the conduction and valence band edges of II-VI (left) and III-V (right) compounds. The $d^{\mathrm{N}}/d^{\mathrm{N}-1}$ donor (triangles) and $d^{\mathrm{N}}/d^{\mathrm{N}+1}$ acceptor (squares) states are denoted. Reproduced Fig. 6 from [41]

the crystal lattice follow the Vegard law. In III-V DMS, Mn atoms introduce energy levels in the gap and for arsenides and antimonides it behaves as a shallow acceptor. It keeps its d^5 configuration and is surrounded by a weakly bound hole [47].

1.2.2 Exchange interactions

In order to go further in the understanding of the origin of ferromagnetism in these materials it is important to consider which are the relevant magnetic interactions [48]. As in most magnetic materials, the magnetic dipole-dipole interaction plays a minor role since its strength is low at typical interatomic distances [49]. In addition, the relativistic effects that lead to spin-orbit interaction provide a more plausible source of phenomena that are potentially useful for spintronics [50, 51, 52] but, although these terms are critical for specific properties (e.g. magnetic anisotropy), they are not crucial for the magnetic order itself. The universal ultimate origin of ferromagnetism is the interplay between the electronic spin degree of freedom, the repulsive Coulomb interactions between electrons and the Fermi statistics. This last in particular, in the terminology of magnetism, is recognized as the ultimate origin when speaking of *exchange* interactions.

Understanding the magnetic order in a particular system is a challenging problem of solid-state physics [49, 54, 53]. The first approach, chosen here and treated in the following, is to proceed in a semi-phenomenological way by determining the exchange interactions that couple the local spins, comparing the simplified model Hamiltonians with the experimental observations. A second parallel *ab initio* approach is based on density functional theory; it is not treated at this point and details can be found in Refs. [55, 56, 57].

A picture of the relationships between five exchange interactions is given in Fig. 1.2. For itinerant electrons, Stoner's *itinerant exchange* [49] is applied but this cannot work for localized spins as in DMS. On the other hand, Heisenberg's *direct exchange* [49] is less important than the indirect exchange channels because *d*-orbitals do not overlap. It plays a role in the Kramers-Anderson's *superexchange* [58]. In fact, the latter case apply to local moments separated by non-magnetic atom, where (in a crystal) an electron can be transferred by the non-magnetic atom

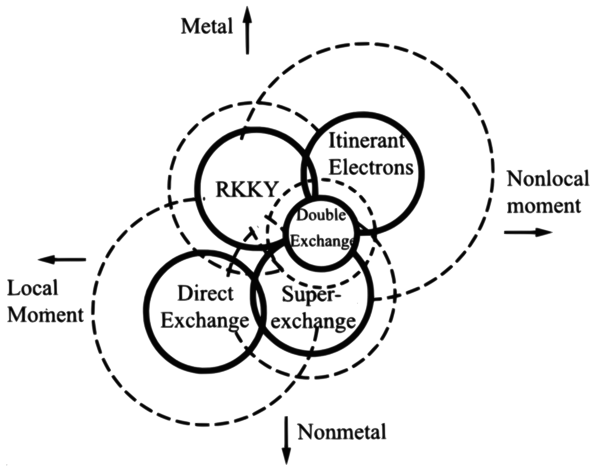

Figure 1.2: The relationship among five exchange interactions. The solid (dashed) lines represent the main (enlarged) region of application. Reproduced Fig. 17.1.2 from [53].

to an empty shell of the magnetic atom and interact, via direct exchange, with the electrons forming its local moment. In (III,Mn)V materials, superexchange gives an antiferromagnetic contribution to the interaction between Mn moments located on neighboring cation sites [48]. Also Zener's *double-exchange* mechanism [59] assumes an intermediate non-magnetic atom but combined with the on-shell Hund's rule couples magnetic moments ferromagnetically. Finally, the Zener's *kinetic-exchange* [60] or indirect-exchange interaction arises in models with local *d*- or *f*-shells moments whose coupling is mediated by $s-$ or *p*-band itinerant carriers. When the band carrier polarization is weak, the effect is described by the Rudermann-Kittel-Kasuya-Yosida (RKKY) theory [61, 62]. The basic idea behind the RKKY interaction is that the conduction band is magnetized in the vicinity of the magnetic ion, with the polarization decaying with distance from the magnetic ion in an oscillatory fashion.

These exchange interactions in DMS can also be seen from another point of view [63, 64], distinguishing in $s(p)$-d and d-d exchange interactions. The former between band states and localized TM d orbitals, the latter as indirect exchange between TM d orbitals (because in DMS they do not overlap) mediated by valence/conduction band states. The s-d exchange interaction is a direct exchange, while the p-d exchange interaction is a kinetic exchange. Belong to d-d exchange interactions: the superexchange, double exchange (and Bloembergen–Rowland) for insulators, the RKKY for metals.

A recent reviews of these interactions applied to DMSs are found in Refs. [48, 43, 57].

1.2.3 Carrier mediated ferromagnetism (p-d Zener model)

The p-d Zener model of carrier-mediated ferromagnetism was proposed by Dietl *et al.* [6], successively treated into details [65] and recently reviewed [43]. This model has been successful in explaining a number of properties observed for a selected class of DMS [66], in particular the ferromagnetic transition temperatures (T_C) in p-$Ga_{1-x}Mn_xAs$ and p-$Zn_{1-x}Mn_xTe$. In addition, its predictions on possible materials with T_C exceeding room temperature have stimulated active research in the last ten years.

This model considers a disorder-free system through the virtual-crystal (VCA) and mean-field (MFA) approximations and the holes, that mediate the ferromagnetic order in a weak coupling limit, reside in the valence band (contrary to impurity-band models). In the stable

magnetic phase the total free energy of the system is minimized, that is, the free energy density functional $\mathcal{F}[\mathbf{M}(\mathbf{r})]$ is minimized to respect the local magnetization $\mathbf{M}(\mathbf{r})$ [42, 43].

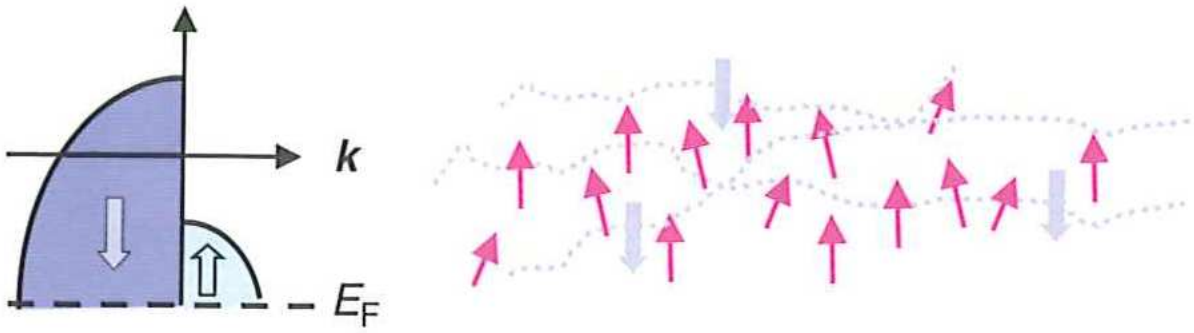

Figure 1.3: Pictorial presentation of the carrier-mediated ferromagnetism in p-type DMSs. Reproduced Fig. 9.9 from [43].

A pictorial view is given in Fig. 1.3: the Zener's kinetic exchange (p-d exchange) and the RKKY interaction lead to ferromagnetic order of the localized spins (smaller arrows) resulting in the spin splitting of the valence band. The corresponding redistribution of the carriers between spin subbands lowers energy of the holes, which at sufficiently low temperatures overcompensates an increase of the free energy associated with a decrease of Mn entropy [43].

One of the predictions of this model is that T_C for a specific semiconductor follows the formula: $T_C = Cxp^{1/3}$, where x is the mole fraction of substitutional Mn^{2+} ions, p is the free hole concentration, and C is a constant specific to the host material. In Fig. 1.4, where are reported the computed values of T_C for various p-type semiconductors containing 5 % of Mn and 3.5×10^{20} holes/cm^3 [6], is visible that, on the basis of this model, the two best candidates for exceeding room temperature are (Ga,Mn)N and (Zn,Mn)O. Unfortunately, up to now, this prediction is not confirmed by the experiments and, on the basis of recent findings, an extension of the present DMS picture is given in the following.

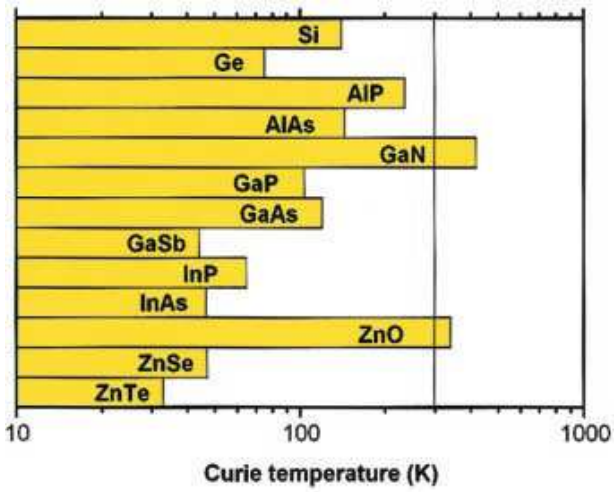

Figure 1.4: Computed values of T_C for various p-type semiconductors containing 5 % of Mn and 3.5×10^{20} holes/cm^3. Reproduced Fig. 3 from [6].

1.3 Non-uniform DMS

Until now, it is assumed that the distribution of magnetic impurities in the DMS is random but macroscopically uniform. On the other hand, contrasting results have been found experimentally for the ferromagnetism of wide-gap nitrides and oxides DMS [67, 36] and this has lead to the idea that such DMS undergo spinodal decomposition during the growth, conducted in most cases in non-equilibrium conditions. The first observations of such decomposition in TM-rich and TM-poor regions, that differs from phase precipitation, were in (Ga,Mn)N [68], (Al,Cr)N and (Ga,Cr)N [69]; since then, started a growing interest on these self-organized coherent nanostructures [70, 71] from both experimental and theoretical side. Here, after the definition of spinodal decomposition, some few theoretical results are presented.

1.3.1 Spinodal decomposition

Spinodal decomposition is a mechanism by which a solution of two or more materials can separate into distinct regions with different material concentrations. This mechanism differs from nucleation in the sense that phase separation due to spinodal decomposition occurs throughout the material, and not just at nucleation sites. The theory for spinodal decomposition was developed by Cahn and Hilliard in the '60s [72, 73, 74, 75, 76, 77] and it is not treated here but is given only a description of the free energy in a binary system.

Considering an alloy $A_{1-c}B_c$, the Gibbs free energy, $f(c)$, is a function of the concentration c. A possible behavior is shown in Fig. 1.5 where the two minima represent two stable phases and all the intermediate concentrations are instable or metastable. For c_0 in the region where $\partial^2 f/\partial c^2 < 0$ the system tend to decompose spontaneously. In fact, $xf(c_1) + (1-x)f(c_2) < f(c_0)$ that means the free energy lower by Δf moving from one phase at c_0 to two phases at c_1 and c_2. This process and the region where it happens are called spinodal decomposition/region. On the other hand, in the regions where $\partial^2 f/\partial c^2 > 0$ and inside the miscibility gap, the decomposition is not energetically favorable and, apparently, the free energy increases. Therefore, the system is "stable" with respect to small fluctuations. In other words, it is metastable with respect to infinitesimal composition fluctuations. Therefore the system requires large composition fluctuations to decrease the energy. This is obtained by the formation of a nucleation center of one stable phase that grows until the equilibrium.

Using the Cahn-Hilliard formalism is possible to calculate analytically the early stages of the decomposition to find characteristic distances and frequencies but to obtain the final state, *ab initio* methods have to be used.

1.3.2 *Ab initio* approach

In order to consider spinodal decomposition into DMS and consequently have a picture of the ferromagnetism, the *ab initio* approach has been followed. Calculations are generally based on density functional theory within the local density approximation (basics aspects with references are given in Sec. 3.3). A plethora of methods exist to implement these calculations and reviewing them is beyond the present scope. After first studies that follow the "standard" supercell approach [78, 79] the works of Katayama-Yoshida *et al.* [80] have demonstrated that the Korringa-Kohn-Rostoker coherent potential approximation (KKR-CPA) and Monte Carlo methods (details in Ref. [81]) give interesting new results that permit not only to have a picture of the magnetism in DMS but also to predict new materials and functionalizations.

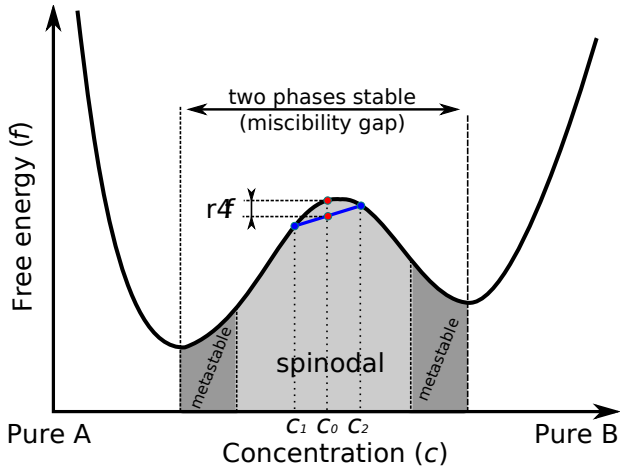

Figure 1.5: Possible free energy curve of a binary system undergoing spinodal decomposition between two stable phases and metastable zones.

Using this approach, has been found that spinodal decomposition in DMS brings to high T_C even if the magnetic exchange interaction is short ranged. In particular, applying Monte Carlo loops to the Ising model [82] leads to the spinodal three dimensional Dairiseki-phase [83] or, assuming layer by layer growth, to the one-dimensional Konbu-phase [84]. In addition, contrary to the Dairiseki-phase, the Konbu-phase is normally low T_C (explained by an isotropic Heisenberg model [85]); on the other hand, if δ-layers of magnetic impurities are introduced, the effect is to connect the one-dimensional structures and consequently obtain high T_C ferromagnetism. A pictorial view of these decomposed structures is given in Fig. 1.6.

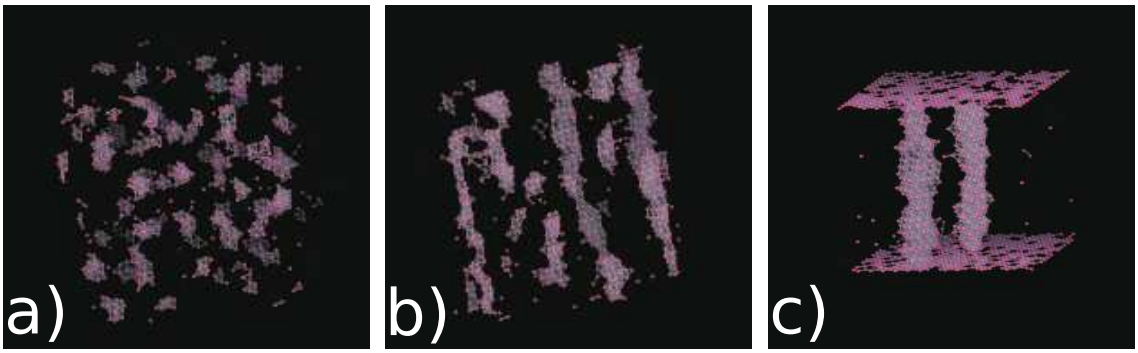

Figure 1.6: Simulated spinodal decomposition phases for (Ga,Mn)N in the bulk (three dimensional Dairiseki-phase) - a), under layer by layer growth (one-dimensional Konbu-phase) - b) and the connected fragments using δ-doping in (Zn,Cr)Te - c). Adapted Figs. 2,3 from [84].

Spectroscopie d'absorption des rayons X

Résumé du Chapitre 2

Le chapitre donne un bref aperçu sur les principes de base et les méthodes de la spectroscopie d'absorption des rayons X (XAFS) en vue d'introduire les outils théoriques et pratiques utilisées dans ce travail.

La théorie de la spectroscopie XAFS, dans la forme que on l'utilise aujourd'hui, a été développée dans les années soixantedix [86] et depuis, cette technique a été utilisé largement dans les installations de rayonnement synchrotron sur plusieurs domaines de la physique de la matière. L'objet de cette spectroscopie est l'analyse quantitative de la structure fine que on observe sur le coefficient d'absorption de rayons X autour d'une seuil d'absorption. Ces oscillations sont le résultat d'un phénomène d'interférence quantique connecté à l'effet photoélectrique. En effet, le photoélectron émis par excitation de l'atome avec les rayons X subit un processus de diffusion avec les atomes voisins avant d'être absorbé à nouveau (Fig. 2.1). En changeant l'énergie des rayons X envoyés sur l'échantillon on obtient un spectre d'absorption, $\mu(E)$. Selon l'énergie du photoélectron émis on peut distinguer le spectre XAFS en deux regions : XANES et EXAFS (Fig. 2.2). Grâce à un diffèrent libre parcours moyen, on obtient, respectivement, des informations structurales plus liés à la géométrie et le état de valence d'une part et la structure locale d'une autre part.

Les bases théoriques de la spectroscopie XAFS sont donnés dans la section 2.2. Pour calculer la formule standard EXAFS, la théorie de la diffusion multiple est normalement utilisée, où le phénomène d'absorption est traité en approche semi-classique, c'est à dire, en traitant l'atome d'un point de vue quantique et le champ électromagnétique classiquement. En partant de la règle d'or de Fermi et en appliquant des approximations successives (single électron, approximation de dipôle, potentiel de *muffin-tin*) on obtient la formule standard donnée en version de diffusion simple [87] dans l'Eq. 2.5 ou élargie à des chemins de diffusion multiple [88, 89] dans l'Eq. 2.9. Ensuite des élément de réflectivité des rayons X sont donnés pour donner les bases théoriques de la technique ReflEXAFS, qui permet à la spectroscopie XAFS d'être utilisé comme une sonde de surface.

La section 2.3 traite la collecte des données expérimentales. Le lignes de lumière utilisées sont décrite avec attention particulière à celle où a été principalement fait ce travail, c'est à dire le laboratoire "GILDA". Il se compose d'une part optique (Fig. 2.3), deux miroirs pour la soustraction des harmoniques et la collimation du faisceau, plus le monochromateur à double cristal de Si qui, permet aussi la focalisation dynamique dans le plan horizontal. Les stations

expérimentales sont séparées pour la partie EXAFS (Fig. 2.4) et la partie ReflEXAFS (Fig. 2.5). La collecte des données se fait en transmission pour les échantillons de référence et en fluorescence pour les systèmes dilués objet de ce travail.

La dernière partie du chapitre (Sec. 2.4) montre les techniques d'analyse des données employés dans cette thèse. Une vue d'ensemble est donnée dans le schéma de la Fig. 2.6 et les partie les plus importantes sont détaillés ensuite. En particulier, l'extraction du signal et l'analyse de Fourier (Fig. 2.7) suivi de la création du modèle théorique et l'évaluation de ceci sur les données expérimentales.

2

X-ray Absorption Fine Structure spectroscopy

This chapter is a short review on the basic principles and methods of the x-ray absorption fine structure (XAFS) spectroscopy in order to introduce the theoretical and practical tools used in this work. In particular, three main aspects are treated: the theoretical framework, focused on the Extended-XAFS; the experimental apparata and data collection modes, mainly at the GILDA beamline; the data analysis, focused on the application to the present case study. The interested reader can find a more general/detailed description of the theoretical, experimental and data analysis aspects in many review papers [90, 91, 92, 93, 94, 95, 89, 96, 97] and books [98, 99, 100].

2.1 Introduction

XAFS spectroscopy was developed, in the form used nowdays,[1] in the early '70s [86] and is widely used at synchrotron radiation facilities. It refers to the oscillations observed on the absorption coefficient above the absorption edge of a deep core state. Regardless of the complexity of the sample, the XAFS signal comes from all the atoms of a single element as selected by the x-ray energy. For x-ray with energy less than 10^2 KeV, the x-ray absorption from a material is mainly due to the photoelectric effect: in fact, Compton scattering is important only at higher energies while pair production is forbidden in this energy range. The fine structure is interpreted as a quantum-interference phenomenon related to the photoelectric effect. It is caused by the self-interference of the photoelectron wave function that is partially reflected by the atoms surrounding the photoabsorber. A pictorial view of this effect is shown in Fig. 2.1.

The acronym XAFS covers both the x-ray absorption near edge structure (XANES) and the extended x-ray absorption fine structure (EXAFS) spectroscopies. This typical division is shown in Fig. 2.2 where the absorption coefficient, $\mu(E)$, is reported for an oxide model compound. XANES is the region extending a few tens of eV above the absorbing edge ($\approx$ 50 eV) where the photoelectron wavelength is of the order of the interatomic distance and the photoelectron mean free path is some tens of Å; for this reason, multiple scattering effects are dominant and, although this has a more difficult theoretical interpretation, permits to determine the valence state and coordination geometry of the atoms around the absorber. The EXAFS region extends from $\approx$ 50 eV up to $\approx$ 1000 eV above the edge; in this region the photoelectron wavelength is lower than the interatomic distances and the photoelectron mean free path is shorter than

[1] XAFS first observation and early interpretation started in 1931 [101] but its explanation remained unresolved for about 40 years [102].

$\approx$ 10 Å. This characteristic can be used to determine the local atomic structure of a particular element within a sample in terms of number and kind of atoms as well as interatomic distances, thermal and structural disorder.

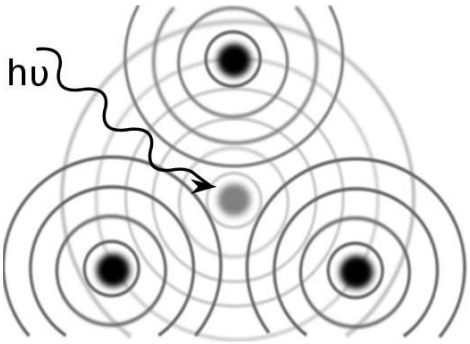

Figure 2.1: Pictorial view of the photoelectron interference effect: the central atom (gray) absorbs the photon of energy $h\nu$, the outgoing photoelectron wave is partially scattered backward by the neighboring atoms (black).

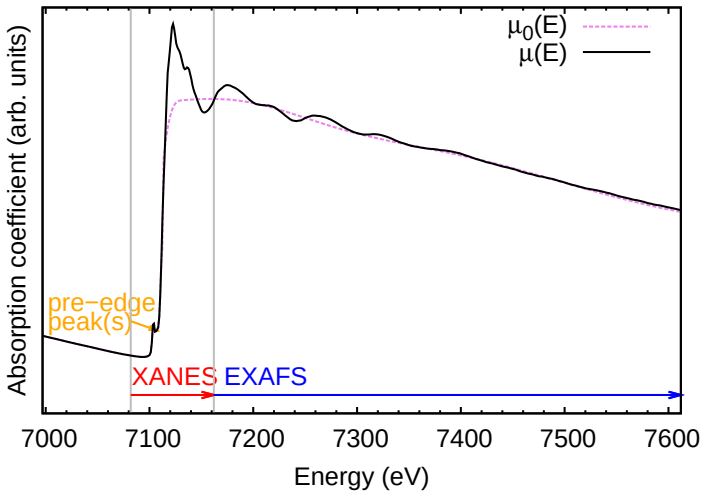

Figure 2.2: Absorption coefficient spectrum $\mu(E)$ of a Fe_2O_3 model compound (crystalline powder) near Fe K-edge (E_0 = 7112 eV). The contribution $\mu_0(E)$ to the absorption that does not account for interference effects is also shown. XANES and EXAFS regions are marked. The pre-edge peak(s) region is also highlighted.

2.2 Theoretical framework

In the following are given the theoretical basis of the present characterization work. In particular, more attention is given to the EXAFS theory keeping in mind the application to semiconductors, while the XANES scenario is simply introduced. Finally, some elements of x-ray reflectivity are presented in order to treat the ReflEXAFS tool, an application of the EXAFS spectroscopy to enhance the surface sensitivity.

2.2.1 EXAFS

The starting point is an x-ray absorption spectrum, that is the measurement of the absorption coefficient, $\mu(E)$, or of a quantity that is directly connected with it, as a function of the energy of the impinging photons ($E = h\nu = \hbar\omega$). The simplest way to think at $\mu(E)$ is to consider a sample of thickness t and a monochromatic x-ray beam passing through it. The transmitted beam intensity is $I = I_0 e^{-\mu t}$, where I_0 is the incident beam intensity and μ depends on the photon energy, the atomic density and the atomic species in the sample. The general trend of μ with energy is decreasing, interrupted by discontinuities that represent specific absorption edges corresponding to the binding energies of deep electronic levels. For example, excitation of electrons from $1s$, $2s$, $2p_{1/2}$, $2p_{3/2}$ and $3s$ states correspond to the K, L_I, L_{II}, L_{III} and M edges, and so on, according to the established x-ray nomenclature. Since the binding energies grow monotonically with the atomic number Z, an edge energy corresponds to a well defined atomic species. This behavior explain the chemical sensitivity of the technique. For a given

absorption edge, the EXAFS spectrum $\chi(E)$ is defined phenomenologically as the normalized oscillatory part:

$$\chi(E) = \frac{\mu(E) - \mu_0(E)}{\Delta\mu_0} \tag{2.1}$$

where $\mu_0(E)$ is the smoothly varying atomic-like background absorption as indicated in Fig. 2.2 and $\Delta\mu_0$ a normalization factor approximated by the magnitude of the jump in absorption at the edge energy E_0.

The physical process leading to the EXAFS standard formula in the framework of multiple scattering theory is described in a semiclassical way, treating the atom from a quantistic point of view and the electromagnetic field classically. The linear absorption coefficient μ represents the reduction in the energy density carried by the electromagnetic field, due to the interaction with the material [103]. It can be expressed as:

$$\mu(\omega) = \frac{2\hbar}{\varepsilon_0 \omega c A_0^2} n \sum_f W_{fi} \tag{2.2}$$

where ω is the incident photon frequency, n the density of the absorber atoms in the material, A_0 the amplitude of the vector potential associated to the electric field and ε_0 is the dielectric constant of vacuum. $\mu(\omega)$ depends on the probability of transition W_{fi} for the photoabsorber from the initial state $|\mathbf{\Psi}_i\rangle$ to the different possible final states $|\mathbf{\Psi}_f\rangle$, corresponding to possible different core holes or multiple excitations.

In order to calculate the probability of transition W_{fi}, the time dependent perturbation theory is exploited, which permits to expand in series the interaction potential between the atom and the electromagnetic field, and to use the only first term of the series if the interaction is weak. The transition probability is, in this way, determined using the Fermi's golden rule:

$$W_{fi} = \frac{2\pi}{\hbar} \sum_f |\langle \mathbf{\Psi}_i | \mathbf{H}_I | \mathbf{\Psi}_\mathbf{f} \rangle|^2 \delta(E_f - E_i - \hbar\omega) = \frac{2\pi}{\hbar} |\langle \mathbf{\Psi}_i | \frac{e}{m} \sum_j \mathbf{A}(\mathbf{r}_j) \cdot \mathbf{p}_j | \mathbf{\Psi}_\mathbf{f} \rangle|^2 \rho(E_f) \tag{2.3}$$

where the label f identifies all final states compatible with the energy conservation dictated by the Dirac delta function which, in the case of transition to the continuum can be replaced by the final density of states $\rho(E_f)$; $\mathbf{H}_I$ is the atom–electromagnetic field interaction Hamiltonian operator, which is the scalar product of the vector potential of the radiation field $\mathbf{A}(\mathbf{r}_j)$ in the position $\mathbf{r}_j$ and the electron momentum operator $\mathbf{p}_j$, where the sum index j labels all the electrons in the system.

In order to solve Eq. 2.3, some important approximations are established. The first one is the *one-electron approximation* that consists in considering the photoelecton energy high enough to leave the atom before the relaxation of the electron clouds, due to the change in the atomic charge, occurs. The relaxation time depends both on the atom and the chemical environment and is estimated to 10^{-15}–10^{-16} s [104] while the time needed for a 1–1000 eV photoelectron to exit from the atom is about 10^{-16}–10^{-18} s. With this assumption, the wave functions can be factorized in $\mathbf{\Psi} = \mathbf{\Phi}^{N-1} \cdot \phi_c$, where ϕ_c is the wave function of the core electron and $\mathbf{\Phi}_{N-1}$ refers to the other $N-1$ passive electrons. Within this approximation, the Hamiltonian will act only on the electron that makes the transition while the other N electrons will be approximated by a single configuration Slater determinant composed of one electron orbitals. For the ground state these orbitals will be obtained from a suitable self-consistent atomic calculation corresponding to the ground-state electronic configuration, while for the excited state the relaxation of the

electronic charge around the core hole can be accounted for by adopting a different basis set of self-consistent orbitals, optimized for the final state configuration. In addition, the possibility of either shake-up and shake-off processes for the other electrons, that lower the transition probability, is accounted by the term $S_0^2 = \langle \mathbf{\Phi}_i^{N-1} | \mathbf{\Phi}_f^{N-1} \rangle$. In general $S_0^2 \leq 1$, being 1 only when the relaxation probability of the atomic electrons is zero in the photoelectron lifetime.

The matrix element can be further simplified by assuming the *dipole approximation*, considering the photon wavelength bigger than the extension of the core electron wave function, thus neglecting the spatial variation of the vector potential ($e^{ikr} \cong 1$). However it should be noticed that this approximation is not a big limitation of the theory and, if necessary, multipole expansions for the transition operator can be inserted in the calculation.

In the framework of these approximations, the x-ray absorption cross section[2] is

$$\sigma(\hbar\omega) = 4\pi^2 \alpha \hbar\omega |\langle \phi_c | \widehat{\varepsilon} \cdot \mathbf{r} | \phi_f \rangle|^2 \rho(E_f) \tag{2.4}$$

where $\widehat{\varepsilon}$ is the polarization vector and (in SI units) $\alpha = e^2/4\pi\varepsilon_0\hbar c \cong 1/137$ is the fine structure constant. As an important consequence of the dipole approximation, the selection rules have to be taken into consideration to determine, on the basis of the symmetry, which final states are allowed for a given initial state; for a free atom they are: $\Delta l = \pm 1$ and $\Delta m = 0(\pm 1)$ for linearly (circularly) polarized radiation. Thus, for a K-edge (s symmetry, $l = 0$) the transition will be to p states.

At this point, for the estimation of the photoelectron wave function in the final state is important to have a good description of the potential generated from the neighboring atoms. The commonly used model is the *muffin-tin approximation*, consisting in spherically averaging the potential around each atom and adopting a constant interstitial potential in between. The efficacy of such simplified model lies on the photoelectron scattering dependence on the inner part of the atomic potential wells. As a result of the muffin-tin approximation the atomic scattering properties are independent of the actual atomic positions. The distance of the neighbors affects only the phase factor associated with the free propagation of the photoelectron from one atomic center to another. In this approximation, the calculation of the absorption cross-section is simplified into a multiple scattering problem of the final state wavefunction by a collection of spherically symmetric scattering centers.

Under these approximations, it is possible to derive the standard EXAFS formula. In order to better understand the role played by each term, the single scattering derivation is first presented and then extended to multiple scattering.

Single scattering

In the hypothesis of single scattering, where the photoelectron wave is reflected once by a coordination shell of atoms, averaging the polarization dependence on the whole solid angle (appropriate for isotropic samples) and considering the photoemission from the 1s state, the single scattering EXAFS formula, as a function of the photoelectron wave number $k = \sqrt{2m(E - E_0)/\hbar^2}$ is thus obtained (many equivalent derivations exists, e.g. see Ref. [87]):

$$\chi(k) = -\sum_j S_0^2(k) \frac{N_j}{kR_j^2} |f_j(k,\pi)| \sin(2kR_j + 2\delta + \varphi_j(k)) e^{-2k^2\sigma_j^2} e^{-\frac{2R_j}{\lambda_j(k)}} \tag{2.5}$$

where each term of the sum indicates the contribution from the shell j composed by N_j atoms

[2] Related to $\mu(\hbar\omega) = \sum_{i=1}^{n} \varrho_i \sigma_i(\hbar\omega)$ by the atomic concentration ϱ of the n constituent atoms.

of the same species at a distance R_j from the absorber. The term $S_0^2(k)$, as previously noticed, accounts for the inelastic losses due to multielectron processes during the photoemission. $f_j(k,\pi) = |f_j(k,\pi)|e^{i\varphi(k)}$ is the backscattering function from the atoms in the shell j; in fact the backscattering modulates both the amplitude and the phase of the photoelectron wave. δ is the phase shift induced by the central atom. $\lambda_j(k)$ is the energy-dependent photoelectron mean free path; it is determined by losses in the propagation of the photoelectron and includes excitations and inelastic scattering. $e^{-2k^2\sigma_j^2}$ is the Debye-Waller factor in the harmonic approximation [105], where σ_j is the temperature-dependent root mean square fluctuation of the bond length R_j; the characteristic period of thermal vibrations (10^{-13}–10^{-14}) is higher than the mean photoelectron lifetime (10^{-15}–10^{-16}), so the σ value accounts for both static and thermal disorder.

Multiple scattering extension

In order to have a multiple scattering description of XAFS, the Green's function formalism has been used [106]. Within this framework the x-ray absorption cross section (Eq. 2.4) is rewritten in terms of the imaginary part of the one particle Green's function [88, 89]:

$$\sigma(\hbar\omega) = 4\pi^2\alpha\hbar\omega\frac{1}{\pi}\Im\langle\phi_c|(\widehat{\varepsilon}^*\cdot\mathbf{r}')G(\mathbf{r},\mathbf{r}',E)(\widehat{\varepsilon}\cdot\mathbf{r})|\phi_c\rangle \tag{2.6}$$

Following this approach, it has been demonstrated that the polarization averaged cross-section for a transition to a final state of angular momentum l is:

$$\sigma(\hbar\omega) = \frac{\sigma_0(\hbar\omega)}{(2l+1)sin^2(\delta_l^0)}\Im\sum_m[(\mathbf{I}-\mathbf{TG})^{-1}\mathbf{T}]_{L,L}^{0,0} = \sigma_0(\hbar\omega)[1+\chi] \tag{2.7}$$

where $\sigma_0(\hbar\omega)$ is the atomic cross section; $\mathbf{I}$ is the unit matrix, $\mathbf{T}$ and $\mathbf{G}$ are the atomic scattering and propagator matrices, respectively. Each element of the matrices is identified by four indices: i, j running over the sites of the atoms surrounding the central one and L, L' (where $L = l, m$) being angular momentum indexes. $\mathbf{G}$ is an off-diagonal matrix and describes the free propagation among the sites, $\mathbf{T}$ is diagonal in the site and angular momentum indices and accounts for the energy-dependent scattering properties of the atomic potential. Thus the $\mathbf{T}$ matrix depends on the atomic composition of the sample while the $\mathbf{G}$ matrix depends on the geometrical arrangement of the atoms.

The matrix in Eq. 2.7 can be expanded $\mathbf{T}(\mathbf{I}-\mathbf{TG})^{-1} = \mathbf{T}(\mathbf{I}+\mathbf{TG}+\mathbf{TGTG}+\mathbf{TGTGTG}+\cdots)$ and at sufficiently high energies above the edge (e.g. ≈ 50 eV) it is convergent. Thus, in the EXAFS region the absorption coefficient can be expanded in a series of sums in which each one accounts for all the contributions from multiple scattering involving a definite number of atoms [94]:

$$\chi = \sum_{i\neq 0}\chi_2^{0i0} + \sum_{i\neq j;\ i,j\neq 0}\chi_3^{0ij0} + \sum_{i\neq j\neq k;\ i,k\neq 0}\chi_4^{0ijk0} + \cdots \tag{2.8}$$

The general term $\chi_\Gamma^{0ijk\ldots0}$ is the partial EXAFS signal that considers $\Gamma-1$ scatterings (Γ-legged path) with atomic sites indexed by i, j, k, ...; thus, for example, the single scattering contribution of Eq. 2.5 is $\sum_{j\neq0}\chi_2^{0i0}$. Finally, it can be demonstrated [89] that each term of Eq. 2.8 can be written in a similar form to Eq. 2.5 using "effective" parameters:

$$\chi_\Gamma(k) = S_0^2\frac{N_\Gamma}{kR_\Gamma^2}|f_\Gamma(k)|\sin(2kR_\Gamma + 2\delta + \varphi_\Gamma(k))e^{-2k^2\sigma_\Gamma^2} \tag{2.9}$$

therefore $\chi_\Gamma(k)$ represents the partial contribution of order Γ to the EXAFS signal and only the most relevant terms can be used in the data analysis to properly describe the system under investigation. In practice, the number of relevant scattering paths is limited by the rapid damping of the signal for long path lenghts (usually it is found a negligible amplitude for lenghts ≥ 10 Å) and the fact that the amplitude of multiple scattering paths quickly decreases with Γ (usually neglected for $\Gamma > 4$). As an example, in Ref. [107] are reported the main multiple scattering contributions for the diamond structure.

Polarization

In the previous statements it is assumed a polarization-averaged cross section that is valid for isotropic samples (cubic structures in the present study), but it is worth noting that, due to the polarization of the synchrotron radiation coupled with the directional dependence of the photoabsorption process, the coordination number N_s for non-isotropic structures have to be replaced by an effective multiplicity number given by [91]:

$$\tilde{N}_s = 3 \sum_{i=1}^{N_s} \cos^2 \alpha_{i,s} \tag{2.10}$$

where $\alpha_{i,s}$ is the angle between the polarization vector $\widehat{\varepsilon}$ and the vector distance $\mathbf{r}_i$ absorber–scatterer i^{th} in the s^{th} coordination shell.

2.2.2 XANES

In the XANES region, the multiple scattering series (Eq. 2.8) does not converge [88] and the inversion of the "$\mathbf{I} - \mathbf{TG}$" matrix is necessary to calculate the absorption spectrum. This regime is called full multiple scattering (FMS) because an infinite number of scattering paths contribute to the XAFS cross section. Due to the low energy of the photoelectron, XANES is also sensitive to the details of the scattering potential [108] and to the three-dimensional position of atoms contained within a radius greater than that necessary to reproduce the EXAFS [109]. As a consequence, a quantitative analysis of the XANES is not generally possible, even if some geometrical fitting of the experimental XANES spectra has been successfully reported [110, 111, 112].

Although these limitations due to time-consuming calculations, XANES is used in many different fields because it is more easily recorded than EXAFS (especially for dilute elements) and more sensitive to the three-dimensional atomic geometry. Structural qualitative information are obtained in a "finger-printing" approach that consists in comparing an experimental spectrum to a number of reference compounds of known structure or to simulated theoretical structures.

Finally, XANES can also give information on the site symmetry of the absorbing atom (e.g., tetrahedral or octahedral) and on its oxidation state. This approach consists in fitting the shape and position of the pre-edge peak(s) and has been largely employed in the field of mineralogy (for a specific example, see Ref. [113]). This is the privileged method also employed in the present work.

2.2.3 ReflEXAFS

EXAFS in total reflection mode (ReflEXAFS) is an experimental technique that provides local order information around a given atom with high surface sensitivity [114]. This is due to the

extremely small extinction length (a few 10^1 Å) of the evanescent wave appearing when the probe beam shines the sample in total reflection conditions [115]. The noticeable advantage of this technique is the possibility to use the x-ray absorption spectroscopy (a bulk probe) to investigate surface effects. In particular, the technique permits the analysis of buried interfaces; systems that are difficult to be analyzed even with more sophisticated surface investigation equipment. Applications of ReflEXAFS can be found in literature on a variety of fields, namely chemical reactions at the solid state [116, 117], surface treatments [118, 119], structural studies of thin films [120, 121]. A variety of spectrometers dedicated to this method is available on the major synchrotron radiation sources [122, 116, 123, 124, 125, 126, 127].

Collecting spectra in the conventional modes (transmission of fluorescence) permits the measurement of the absorption coefficient μ of the sample that is proportional to the imaginary part β of the complex sample refractive index $n = 1 - \delta - \iota\beta$. In detail:

$$\delta = \frac{\lambda^2}{2\pi} N r_e (f_0 + f_1) \qquad \beta = \frac{\lambda^2}{2\pi} N r_e f_2 = \frac{\lambda \mu}{4\pi} \tag{2.11}$$

Here N is the atomic density (at/cm^3), r_e is the electron classical radius ($r_e = 2.82 \times 10^{-13}$ cm), λ is the wavelength *in vacuo*, f_0 the scattering factor, f_1 the anomalous correction and f_2 is the imaginary part of the total scattering factor f.

Spectra collected in reflection mode, that is at an incidence angle ϕ smaller than the critical angle for total external reflection $\phi_c = \sqrt{2\delta}$, are less straightforward to analyze, since the measured signal - the sample reflectivity $\Re$ as a function of the photon energy E - depends in a complex way on both the real (δ) and imaginary (β) part of the refractive index. By introducing the following variables [115]:

$$Y(E) = \frac{\beta}{\delta} \qquad X(\phi, E) = \frac{\phi}{\phi_c} \tag{2.12}$$

It is possible to define a new variable h as:

$$h(\phi, E) = X^2 + \sqrt{(X^2 - 1)^2 + Y^2} \tag{2.13}$$

With h, the ideal reflectivity $\Re^{ideal}$ can be expressed:

$$\Re^{ideal}(\phi, E) = \frac{h - X\sqrt{2(h-1)}}{h + X\sqrt{2(h-1)}} \tag{2.14}$$

and the actual reflectivity $\Re$ is calculated accounting for the effect of the roughness Σ via [128]:

$$\Re(\phi, E) = exp(-q_z q_z^t \Sigma_n^2 / 2) \Re^{ideal}(\phi, E) \tag{2.15}$$

The presence of the δ contribution in $\Re(E)$ gives rise to a considerable change in the shape of the spectrum, that passes from a Θ-function-like shape below the critical angle to a cusp-like shape above it. Moreover, the phase of the oscillations shifts with the collection angle and the amplitude of the oscillations undergoes a considerable reduction, as pointed out in Refs. [129, 130, 116]. Thus, a suitable data treatment to obtain reliable quantitative structural parameters, is needed.

In the literature different methods were proposed with the aim of analyzing the ReflEXAFS spectra for concentrated samples, namely Martens and Rabe [129] and Poumellec *et al.* [131] inverted the reflectivity function $\Re$ of the sample to obtain the related β function $\beta = f(\Re)$;

Borthen and Strehblow [130] wrote the background-subtracted reflectivity $\chi_{\Re}$ as a linear combination of β and δ, Heald *et al.* [116] proposed a suitable modification of the amplitude and phase of the theoretical paths in order to match the experimental data. Recently, a new method is developed as a part of this work [132]; it is described in details in App. B.

Conversely, in the case of diluted samples, if the absorbing chemical species contribute negligibly to the refractive index of the probed layer, a conventional analysis can be safely carried out [133].

2.3 Experimental

The experimental stations and the employed collection modes for XAFS data are described in this section. Particular attention is given to the Italian beamline (GILDA) at the European Synchrotron Radiation Facility (ESRF) where this work is principally conducted. In addition, since measurements are conducted at Mn and Fe K-edges, respectively, 6539 eV and 7112 eV, the following discussion is focused around this energy range.

2.3.1 GILDA beamline

The beamline "GILDA" [134] (*General purpose Italian beamLine for Diffraction and Absorption*) was built to provide to the Italian scientific community[3] a third generation synchrotron radiation source of high brilliance and intensity. The design provides a high resolution ($\Delta E/E \approx 10^{-4}$) and high flux ($10^{11}$ ph/s) source of x-rays in the 5–50 KeV energy range for experiments of x-ray absorption and x-ray diffraction. The x-ray source is a 0.8 T bending magnet of the ESRF. The beamline is constituted of four different lead shielded hutches: the first allocates the optical elements, while the remaining are dedicated to the experimental stations. The first experimental hutch is dedicated to absorption experiments; the second allow to perform powder diffraction measurements with medium resolution (FWHM $\approx$ 0.05 deg); the third is dedicated to non standard experiments and allocates an ultra high vacuum chamber.

Optics

The schematic layout of the beamline optics is shown in Fig. 2.3. The mirrors, used for harmonic rejection, present two parallel coatings of Pd and Pt and work, respectively, at an incident angle of 3.3 and 2.7 mrad where the cut-off is approximately 18 KeV and 26 KeV. In addition, the second mirror is bent in order to vertically focus the beam on the sample. The monochromator is a double Si crystal in which the first is flat and the second can be bent; a pair of Si(111) and Si(311) are commonly used (5–30 KeV), while the Si(511) permit to reach higher energies. It is run in dynamical focusing mode [135] and this permits to obtain an horizontally focused beam on the sample. During normal operation the beam size on the sample is around 1.0×0.1 (hor $\times$ vert) mm^2 FWHM: the spot size is determined by the slope errors of the various optical elements and are by far smaller for mirrors than for the sagittally focusing crystal [136, 137]. The low vertical divergence of the beam is an important parameter for working in total reflection conditions since the critical angle for the studied species is few mrad; on the other hand the beam size can result too big and the use of slits is necessary. In addition, when working at low energies harmonics can still pass the Pd-mirror filter; in this case, the harmonic

[3] GILDA is a Collaborating Research Group (CRG) financed by the Italian Research Council (CNR) and the National Institute for Nuclear Physics (INFN); it allocates 70 % (30 %) of its beamtime to Italian (European) users.

rejection is achieved by detuning the angle between the monochromator crystals [138, 139]. In fact, because the Darwin width is narrower for higher harmonics, tilting the first crystal slightly from the Bragg angle (detuning) results in a reduction of the higher-harmonic intensity.

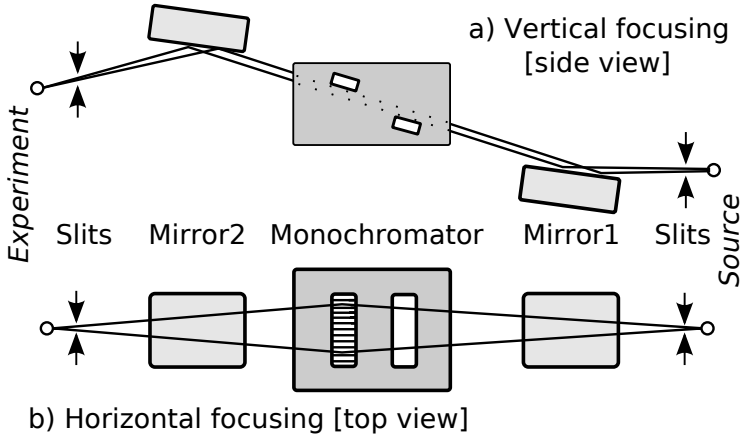

Figure 2.3: Schematic layout of the beamline optics: a) vertical focusing realized by the bending of the second mirror; b) horizontal focusing provided by the sagittal focusing.

EXAFS station

The basic collection mode to measure the absorption coefficient is the transmission one, that consists in measuring the incoming (I_{in}) and transmitted (I_{out}) beam intensity through the sample and obtain $\mu = ln(I_{in}/I_{out})$. This is possible if the sample absorbs some tens percent of the incoming radiation and it is not the case for diluted samples where the absorbing species are typically below 10 % atomic. In this case the fluorescence yield [140] or electron yield [141] detection modes are used. For this work, only the fluorescence detection is used, employing an energy-resolving high-purity Ge solid-state detector with 13 elements.

These detection schemes are implemented in the EXAFS station as shown in Fig. 2.4. Two ionization chambers, I_0 and I_1, measure the incoming and transmitted beam, respectively. Between them, two twin vacuum chambers (can reach $\approx 10^{-5}$ mbar), Ch_1 and Ch_2, allocate samples and work alternatively (e.g. Ch_1 mount the sample to measure in fluorescence mode and Ch_2 a reference foil for energy calibration). Considering Ch_1 (Fig. 2.4), the sample (s_1) is cooled down by a liquid N_2 (or He) cryostat (dark gray circle), it is mounted perpendicularly to the x-ray beam and rotated by an angle α (usually 45 deg). The detector is orthogonal to the beam, optimizing the collection of the fluorescence signal with respect to the Compton and elastic scattering. Measurements done in this geometry are referred in the following as "standard" or "vertical" geometry, in order to distinguish from measurements done with the sample parallel to the beam ("horizontal" geometry) as it is the case for the total reflection or grazing incidence measurements. In particular, for this last case an optimized apparatus is developed as part of the present work and it is discussed in App. A. Finally, it is worth noting that in the vertical geometry the polarization vector, η (Fig. 2.4) is perpendicular (parallel) to sample surface for α = 0(90) deg.

ReflEXAFS station

Measurements in total reflection (Sec. 2.2.3) are performed in the ReflEXAFS chamber [126] (Fig. 2.5). The sample is mounted in a low vacuum chamber on a translation stage coupled

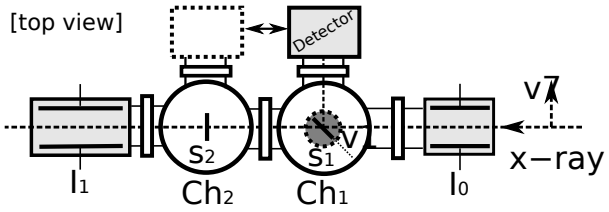

Figure 2.4: Schematic layout of the EXAFS station.

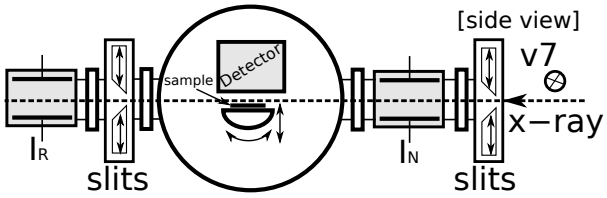

Figure 2.5: Schematic layout of the ReflEXAFS station.

to a goniometer for the rotation that move with a minimum step of 20 μm and 0.002 deg, respectively. In order to keep the beam trace on the sample also at glancing incidence, the incidence beam is sized at 70 μm with slits and monitored by the ionization chamber I_N while I_R is used during the alignment and to collect the reflectivity signal, using second slits to, respectively, block the reflected and direct beam.

2.3.2 LUCIA beamline

The beamline "LUCIA" [142, 143, 144] (*Line for Ultimate Characterization by Imaging and Absorption*) is a French–Swiss beamline at the Swiss Light Source[4]. It is operative in a "tender" (0.8–8 KeV) energy range and its design is oriented to the micro-focus, combining micro x-ray absorption spectroscopy (μXAS) with elemental mapping by x-ray micro-fluorescence (μXRF). In fact, the source is an undulator coupled with a spherical mirror for horizontal demagnification, the harmonics rejection is performed by two planar mirrors coated with nickel, the monochromator is a double crystal and the final focusing is done with a "Kirkpatrick-Baez" (KB) reflecting mirrors system.

2.4 Data analysis

In this section are reported the chosen procedures for data analysis in the study of diluted magnetic semiconductors. Most of them can be applied to other systems but the best solution remains to customize the analysis techniques to specific systems. In particular, the leading idea here is to use the methods that has been successfully applied to crystalline systems.

Overview

In order to have a graphical representation of a typical XAFS data analysis used for this work, a flowchart[5] is shown in Fig. 2.6: the two sides represent, respectively, the theoretical (left) and experimental (right) parts. Starting from the experiment, the raw data are treated in order to have a good signal-to-noise ratio; the common procedures are: deglitching (removing glitches from diffraction effects) and merging multiple spectra. Once obtained the working μ(E) spectrum, it is normalized and, eventually, calibrated to the reference spectra; it can be used for XANES simulations or, in case of the presence of pre-edge peak(s), fitted to get charge state and coordination information from the position and height, respectively. To proceed at the EXAFS quantitative analysis the fine structure, χ(k), is extracted with a background removal

[4]Now moved to the "SOLEIL" synchrotron; the description here is relative to measurements at SLS.

[5]The scheme used is: connectors ⓐ, processes or auxiliary operations [a], input/output [a], decision ◈, document [a].

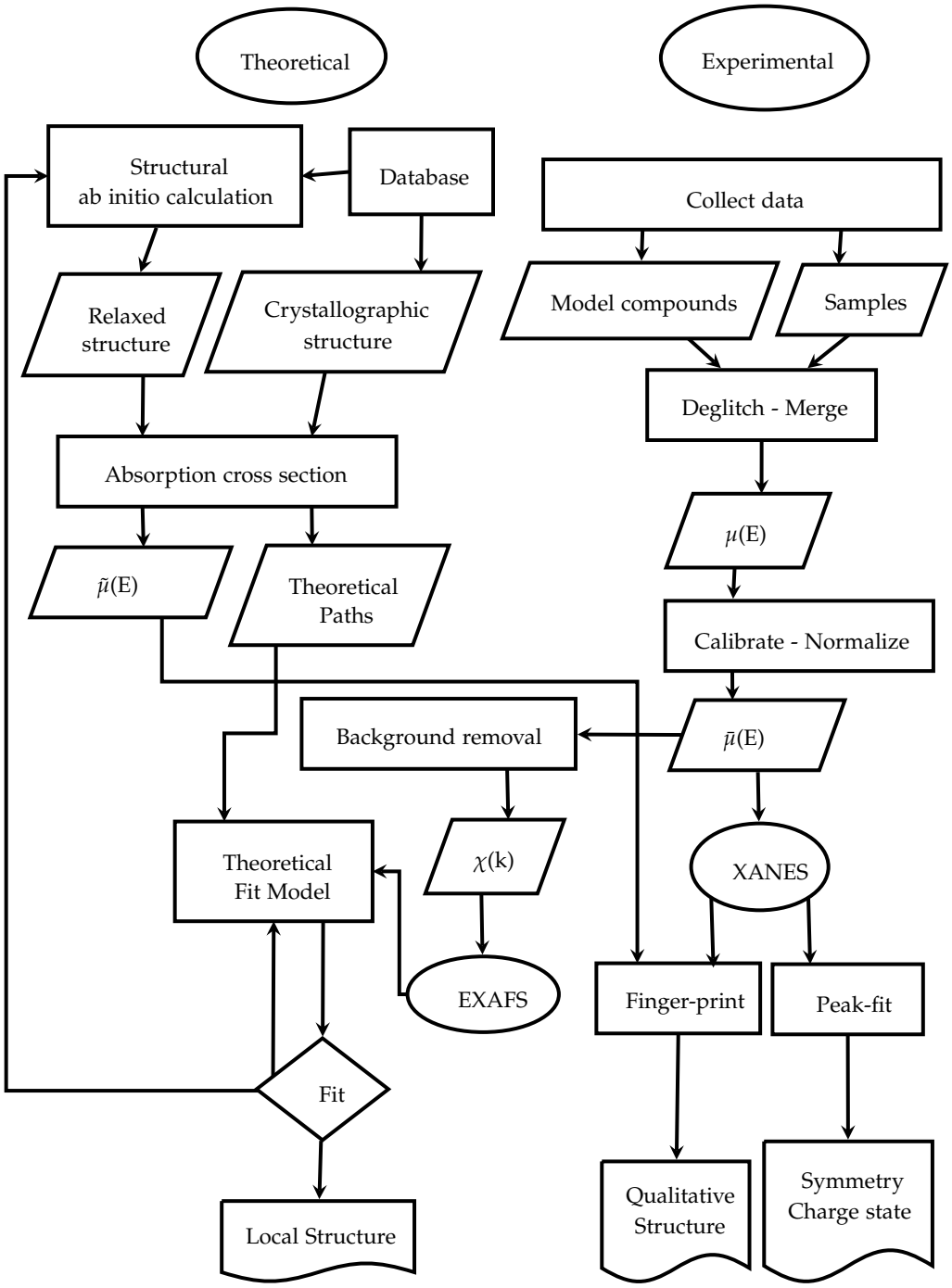

Figure 2.6: Flowchart of a typically used XAFS data analysis.

procedure. At this point the experimental data are ready and the physical model is built using scattering paths calculated from structures coming from a crystallographic database or relaxed structures using theoretical methods (DFT in this case). For a given theoretical model, the fit of the experimental data can be successful and the structural results are reported but normally a convergence loop enter this step until the best fit is found. The XANES analysis is done qualitatively producing an absorption spectrum for each guessed structure that is compared with the experimental data alone or summed in linear combination. In the following some important parts of the analysis are recalled within more details.

2.4.1 Data processing

The energy edge value (E_0) depends on the chemical environment of the absorber and, being difficult to estimate it theoretically, it is normally chosen at the inflection point of $\mu(E)$. The absolute calibration of the energy scale is done collecting simultaneously for each spectrum the absorption coefficient from a reference foil (e.g. metallic Mn, Fe). After the calibration, the pre-edge features are fitted subtracting an arctangent-like background, that is minimizing the function $f(x) = a_1 \text{atan}[(x - a_2)a_3] + a_4$, and fitting the residual with PseudoVoight functions (xGaussian + (1-x)Lorentzian); these operations are done using a Levenberg-Marquardt algorithm and the software FITYK.[6]

The EXAFS signal, $\chi(k)$, is extracted from the absorption raw data, $\mu(E)$, with the VIPER program [145] or the AUTOBK algorithm [146] implemented in the ATHENA software [147]. Both employ smoothing splines functions. An example of this operation is showed in Fig. 2.7. This is a very critical step in the analysis, since a bad background removal affects the EXAFS spectrum and thus the possibility of precisely determine the structural environment around the absorber. For this reason, two independent softwares are used and, in case, the background extraction is adjusted after a first rough fit.

Qualitative information on the local environment are also obtained via a Fourier transform (direct and inverse) using Hanning window function, which ramps up and down as $\cos^2$ in the range defined by the slope parameter (to prevent the "border effects") and choosing the window ranges to filter the interested information (Fig. 2.7). Often the transform is done on the k^n-weighted EXAFS spectrum (n between 1 and 3) to enhance the contribution of the part of the spectrum better described by the EXAFS formula and to be less sensitive to possible errors in the background removal. The Fourier transform modulus (Fig. 2.7) represent a pseudo radial distribution function of the atoms around the absorber but it is worth noting that it is not a radial distribution because the phase shifts induced by the potential of the atoms determine a shift of the peaks with respect to the actual interatomic distances. Moreover, the peaks height is dependent not only on the coordination numbers but also on the atomic species, the Debye-Waller factors and the scattering amplitudes.

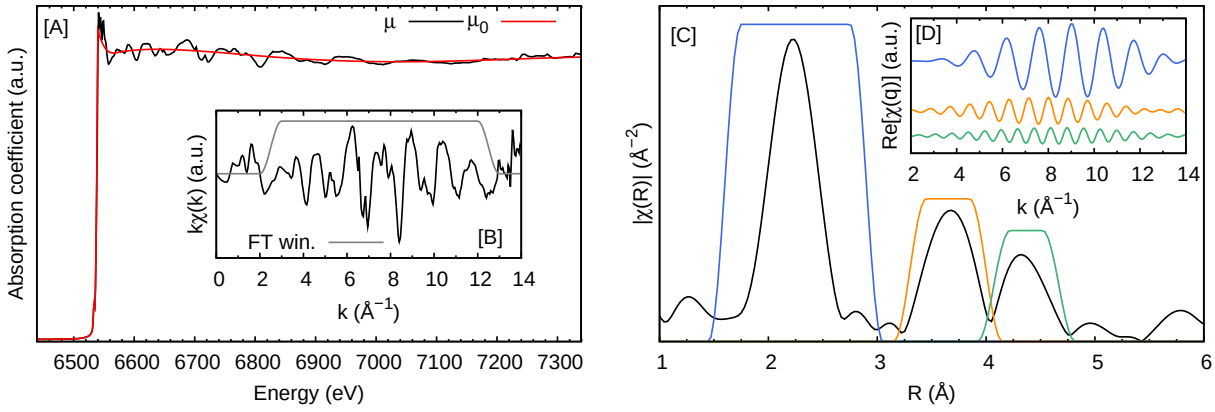

Figure 2.7: Example of data processing for $Zn_{0.9}Mn_{0.1}Se$ fluorescence spectrum at Mn K-edge: the background (μ_0) is removed [A] to obtain the EXAFS spectrum [B]. Consequently it is Fourier-filtered to obtain a pseudo radial distribution function [C] whose peaks can be back-filtered to extract their contribution in the EXAFS signal [D]. Hanning windows are used for the Fourier transforms and, for convenience, are scaled in the plot.

[6] See `http://www.unipress.waw.pl/fityk/`

2.4.2 Theoretical models

The quantitative EXAFS analysis is carried out with the IFEFFIT program [148] that provide basic analysis functions and the minimization algorithm (Levenberg-Marquardt). The physical model and the variables parametrization is done with the ARTEMIS graphical interface [147] using the scattering paths calculated from the atomic models described in the specific sections of the next chapters. The theoretical EXAFS signals used in the analysis are computed with the FEFF8.4 code [149] using muffin-tin potentials and the Hedin-Lunqvist approximation for their energy-dependent part and automated self-consistent potential calculations.[7]

The input structures for calculating theoretical paths and build the fitting models, are chosen in the crystallographic form from the Inorganic Crystal Structure Database, ICSD[8] or, alternatively, in their "relaxed" form calculated by Density Functional Theory (DFT, see Sec. 3.3). The use of simulated defects in semiconductors is particularly useful for DMS; in fact, using the first approach, only the host semiconductor structure is reported in the crystallographic databases and the magnetic impurity is introduced at crystallographic sites (usually at substitutional or interstitial positions) resulting in a structure where atomic position are not optimized for minimizing the total energy of the system. DFT overcomes this problem but can still suffer from the underlying approximations done in the calculation. Nevertheless, it is possible to proceed in a self-consistent way recalculating the input structures in the case from the fit on experimental data are obtained corrections to distances $\Delta R_i > 2$ %. In the case the fit is on a real absolute minimum, this procedure converges in two steps. On the other hand, the approach based on crystallographic structures fetched from a database remains the best solution in identifying the precipitation of secondary phases.

The common parametrization procedures are: the S_0^2 transferability, that is, the procedure of finding its value fitting the EXAFS spectrum of the corresponding reference compound (or eventually, calculate it theoretically) and use this value in the fit for the unknown species, is justified by the hypothesis that the inelastic losses are mostly dependent on the absorber atom and less on the chemical environment; a common energy shift ΔE_0 is used in order to account the misalignment of the data with respect to the theoretical calculations.

Finally, in order to discriminate between similar models, a χ^2 analysis is used; it is modified to take into account the present limitations in the analysis of EXAFS data. In particular, even state-of-the-art methods are unable to reproduce experimental data to the point of providing a χ^2 function equal to the number of degrees of freedom of the fit ν, as should be in the text-book case [150, 151]. This is due to systematic errors occurring in the data collection and to errors in the calculation of the theoretical signals. To circumvent this problem, the noise (Σ) of the experimental data is set to yield a value of the χ^2 function at minimum equal to ν for one model, taken as a reference. The model is chosen as that providing the lowest residual in the fit. The same value of Σ is then used for other models and the values of χ^2 at minimum are compared using probability tables the χ^2 function to exceed a given value, taking into account the different number of degrees of freedom. Models which give an increase of χ^2 greater than the 90 % confidence level [151] for the related ν value are discarded. This method is equivalent to others proposed in the literature (see Refs. [152, 153] and references therein).

[7] Self-consistency is expected to be more important for XANES calculations, but even for EXAFS, in order to have a more reliable determination of the Fermi level or to account for the charge transfers. This permits to do fits with single energy shift ΔE_0.

[8] See `http://icsd.ill.fr`

Techniques complémentaires

Résumé du Chapitre 3

Ce chapitre traite les techniques complémentaires et les outils théoriques utilisés dans ce travail pour assister l'étude de la structure locale par XAFS. En effet, une compréhension des techniques de croissance épitaxiale et monitorage, unis aux caractérisations structurales et magnetiques, est nécessaire afin de pouvoir bien interpréter les résultats expérimentaux et créer des bons modèles théoriques. Vu la complexité de chaque domaine, seulement les concepts de base sont rappelés car l'expertise sur ces sujets est apporté plutôt par les collaborateurs de cette recherche.

Le premier pas est donc représenté par le techniques de croissance épitaxiale et leur outils de monitorage (Sec. 3.1). L'épitaxie par jet moléculaire (MBE) est la plus utilisé dans la croissance de couches minces cristallines car la déposition se fait par voie physique dans des conditions extrêmement propres. En effet, des sources solides son évaporés sous vide poussé pour diriger un jet de vapeur atomique ou moléculaire vers un substrat chauffé à une temperature approprié. Grâce aux conditions de vide poussé, le monitorage pendant la croissance se fait par la diffraction d'électrons rapides sous incidence rasante (RHEED), qui donne des informations détaillés sur la structure et la rugosité de surface. La deuxième technique de croissance employé est l'épitaxie en phase vapeur par organométalliques (MOVPE), qui a son succes grâce à la possibilité d'utilisation dans la production industrielle. Dans ce cas la déposition se fait par voie chimique où le substrat, chauffé à une temperature donnée, est exposé à des précurseurs dans un flux de gaz porteur. Dans ce conditions, le monitorage se fait par voie optique en utilisant l'ellipsométrie, c'est à dire en mesurant le changement de polarisation du faisceau de lumière envoyé sur l'échantillon.

Successivement les techniques de caractérisation sont présentés (Sec. 3.2). La partie structurale se fait par diffraction de rayons X (XRD), soit en laboratoire que au synchrotron pour avoir une meilleure résolution aux phase cristallines éventuelles. Deux géométries standard sont utilisés : la diffraction spéculaire ou θ-2θ, qui permet d'obtenir l'information relative aux plans parallèles à la couche, ou bien la diffraction en incidence rasante, sensible aux plans perpendiculaires. En plus, des informations à plus courte distance sont obtenu par microscopie d'électron en transmission (TEM) qui peut être associé à des spectroscopies pour gagner la sensibilité chimique. Enfin, la caractérisation magnetique se fait par la magnétométrie à SQUID.

La dernière partie du chapitre (Sec. 3.3) présente l'application des méthodes de modélisation *ab initio* basés sur la théorie du fonctionnel densité (DFT). En particulier sont donnés

les paramètres choisi pour obtenir l'optimisation des structures atomiques employés dans les analyses XAFS montés dans la deuxième partie de la thèse.

3 Complementary techniques

In this chapter are described the complementary experimental and theoretical tools used by collaborators for the deposition, in situ *monitoring,* ex situ *characterization and modeling of the case studies described in the next part. The information obtained by these techniques assist the study of the local structure, and* vice versa. *Due to their complexity, these techniques are not treated into details but only some basic and relevant (for the present study) aspects are outlined.*[1]

3.1 Preparation and *in situ* monitoring

3.1.1 Molecular Beam Epitaxy

Molecular beam epitaxy (MBE) takes place in high vacuum or ultra high vacuum (10^{-10} mbar). The most important aspect of MBE is the slow deposition rate (typically less than 1000 nm per hour), which allows the films to grow epitaxially. In solid-source MBE, ultra-pure elements are heated in separate effusion cells until they begin to slowly sublimate. The gaseous elements then condense on the substrate heated at given temperature, where they may react with each other. The term "beam" means that evaporated atoms do not interact with each other or vacuum chamber gases until they reach the substrate; this condition is realized in high vacuum, due to the long mean free path of the atoms.[2]

MBE growth is the result of the interactions of the molecular beam with the substrate surface: the adsorption-desorption, the diffusion, the nucleation and the interdiffusion (the description of these phenomena can be found, for example, in Refs. [154, 155]). Depending on their strength, three different mechanism of growth can be distinguished: the layer-by-layer [156, 157] (Frank-van der Merwe); a three-dimensional nucleation and coalescence of islands [158] (Volmer-Weber); adsorption of a monolayer and subsequent nucleation on top of this layer [159] (Stranski-Krastanov).

Reflection High-Energy Electron Diffraction

During the MBE operation, Reflection High Energy Electron Diffraction (RHEED) is used for *in situ* monitoring the growth of the crystal layers. A high energy beam (5–100 KeV) is directed

[1] The references given in the following are a partial and short selection from the extended literature where review articles are preferred to respect books.

[2] In kinetic theory it is $\frac{k_B T}{\sqrt{2}\pi d^2 P}$, where k_B is the Boltzmann constant, T the temperature, P the pressure and d the diameter of the gas particles.

at the sample surface at a grazing angle (0.5°–3°). The electrons are diffracted by the crystal structure of the sample and then impinge on a phosphor screen mounted opposite to the electron gun. The grazing incidence angle ensures surface specificity despite the high energy of the incident electrons. The resulting pattern (a series of streaks) is given by the intersection of the Ewald sphere (assuming elastic scattering) with the reciprocal rods (the reciprocal lattice of the surface). The distance between the streaks gives the size of the surface lattice unit cell. The intensity of the pattern depends on the film roughness and during the growth process characteristic intensity oscillations are visible, with a single oscillation usually corresponding to the completion of a single monolayer.

3.1.2 MetalOrganic Vapor Phase Epitaxy

Metalorganic vapor phase epitaxy (MOVPE) or metalorganic chemical vapor deposition (MOCVD) is a chemical vapor deposition method of epitaxial growth of materials that has become a major technique for the production of semiconductors at industrial scale [160]. In contrast to MBE, the growth of crystals is by chemical reaction and not physical deposition. The substrate, heated at a given (high) temperature, is exposed to one or more volatile precursors (using a carrier gas, N_2 or H_2, in laminar flow conditions), which react and/or decompose on the substrate surface to produce the desired deposit. Frequently, volatile by-products are also produced, which are removed by gas flow through the reaction chamber. This takes place not in a vacuum, but at moderate pressures (100–1000 mbar). The chemical reactions leading to the material growth depend on the chosen precursors and several kinetic processes and growth mechanisms occur at the solid/vapor interface [161].

Spectroscopic Ellipsometry

Since MOVPE growth is conducted in non-vacuum conditions, it is impossible to use electron scattering based diagnostic tools (like RHEED) for *in situ* monitoring; however, optical techniques like spectroscopic ellipsometry [162] have proven to be useful tools to monitor the growth (e.g. for III-V semiconductors has been reported in Refs. [163, 164, 165]). Ellipsometry is based on the change of light polarization induced by the reflection from a sample surface, measuring the angles Ψ and Δ. The polarization state of the incident light may be decomposed into an s and a p component; the s component is oscillating perpendicular to the plane of incidence and parallel to the sample surface, and the p component is oscillating parallel to the plane of incidence. The amplitudes of these components, after reflection and normalized to their initial value, are denoted by R_s and R_p, respectively. Ellipsometry measures the ratio of R_s and R_p, which is described by the fundamental equation of ellipsometry [166]:

$$\rho = \frac{R_p}{R_s} = \tan(\Psi)e^{i\Delta} \tag{3.1}$$

Thus, $\tan\Psi$ is the amplitude ratio upon reflection and Δ is the phase shift. Since ellipsometry is measuring the ratio of two values (rather than the absolute value of either), it is very robust, accurate, and reproducible. For instance, it is relatively insensitive to scatter and fluctuations, and requires no standard sample or reference beam. In addition, wit the use of Fresnel equations, ρ can be directly translated into a complex dielectric function $\varepsilon(\hbar\omega)$ [167].

Experimentally, the measurements can be spectroscopic (optical response of the grown sample at different photon energy) and kinetic (optical response during the growth).

3.2 Characterization

3.2.1 X-Ray Diffraction

X-Ray Diffraction (XRD) is the ideal tool to investigate the periodic structure of materials, to measure the lattice parameters and to evaluate the long range chemical order in alloy compounds. This is an old technique which has seen its first patterns recorded by Friedrich *et al.* [168] in the transmission (Von Laue) geometry and by Bragg [169] in the reflection geometry (Bragg). A description of the basic principles of XRD and of the equivalence of the Von Laue and Bragg's approach can be found in solid state textbooks (see for example Ashcroft and Mermin [49]). Here, the basic equations are recalled.

The diffraction condition by a family of parallel crystallographic planes occurs when the waves scattered by the planes interfere constructively each other. It leads to a relationship among the spacing of the lattice planes d_{hkl}, the wavelength λ and the incidence angle θ: $2d_{hkl}sin\theta = n\lambda$. The subscript *hkl* are used because, for each family of planes, there are perpendicular vectors in the reciprocal space, the shortest of which has a length $2\pi/d$. The coordinates of this vector (h, k, l), referred to as "Miller indices", define the family of planes under study; in case of absence of high order harmonics ($n = 1$), this vector ($\vec{q}$) is the exchanged wave vector of the scattering process. In the case of *kinematical approximation* [170] the photon is described by a plane wave, the scattering is elastic and the photons are scattered only once. The intensity of a diffracted beam is given by

$$I(q) \propto |F(q)|^2 = |\sum_j f_j e^{-\vec{q}\cdot\vec{r}_j}|^2 = |\sum_j f_j(hkl) e^{-2\pi i(hx_j+ky_j+lz_j)}|^2 \tag{3.2}$$

where r_j is the position of an atom j in the unit cell, $\vec{q}$ is a reciprocal lattice vector given by the difference between the scattered and incident wavevectors (k and k_0, respectively) and f_j is the atomic scattering factor of j-atom. The sum is over all atoms in the unit cell. $F(q)$ is the so called *structure factor*. It describes the way in which an incident beam is scattered by the atoms of a crystal unit cell, taking into account the different scattering power of the elements through the term f_i . Since the atoms are spatially distributed in the unit cell, there will be a difference in phase when considering the scattered amplitude from two atoms. This phase shift is taken into account by the complex exponential term. The atomic form factor, or scattering power, of an element depends on the type of radiation considered.

In the following are described the specific XRD geometries/techniques used to characterize the single-crystal thin films of this study. In particular, the attention is given to XRD done using synchrotron radiation not considering the standard laboratory high-resolution XRD (HRXRD) routinely done on the growth samples in order to get information on the film quality [171].

θ-2θ geometry

The θ-2θ geometry (Fig. 3.1) is one of the most used for monocrystalline thin films. In this geometry the angle ω between the source and the detector is twice the angle between the sample surface and the source ($\omega = 2\theta$). Indicating with $\vec{k}_i$ and $\vec{k}_f$ the wavevectors of the incident and diffracted beam, respectively, the transferred moment is $\vec{Q} = \vec{k}_f - \vec{k}_i$ and it is perpendicular to the crystal surface and parallel to the planes (00l) if it is oriented (001). Thus, changing θ-ω permits to scan the direction (00l) in the reciprocal space. This is called *radial scan*. The position of the peaks depends on the lattice parameters and the uniform strain (produces peak shifts) while the broadening depends on the micro-strain, crystallites size and also on

the instrumentation. The former parameters can be found after correction for instrumental broadening using the Williamson-Hall plot [172], that is, for each peak, plotting $B_{\text{corr}} \cos\theta$ as function of $\sin\theta$ and fitting the law:

$$B_{\text{corr}} \cos\theta = \frac{K\lambda}{d} + 2\frac{\Delta s}{s} \sin\theta \tag{3.3}$$

where B_{corr} is the corrected full width at half maximum (FWHM), K ≈0.9–1 is the Scherrer constant, λ the x-ray wavelength and Δss the strain. From the intercept is possible to estimate the thickness d of the diffracting precipitate and from the slope the microstrain fraction. This technique is limited in the detection of crystal sizes (normally between 10 nm and 1 μm) and other more accurate analyzing methods exist, such as the Rietveld refinement [173].

In addition, to get information on the angular dispersion of a family of planes (mosaicity) the *angular scan* (or *rocking curve* scan) is used. It consists on fixing ω for a given peak and scanning θ; this leave the vector $\vec{Q}$ to describe a circle of radius $2\pi/d_{(00l)}$.

Finally, another interesting scanning mode is the so-called *offset scan*; it consists in a radial scan where 2θ is moving with an offset Δ (that is $2\theta \pm \Delta$). This permits to cut the substrate or bulk peaks that have a small FWHM and have information on the precipitates peaks because they are larger and the diffraction enter the offsetted detector.

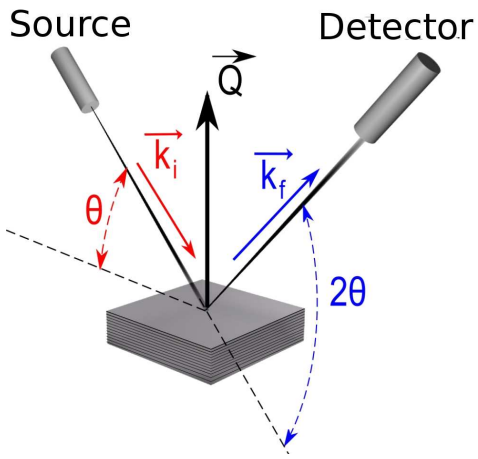

Figure 3.1: XRD in θ-2θ geometry. Adapted Fig. 2.12 from [174].

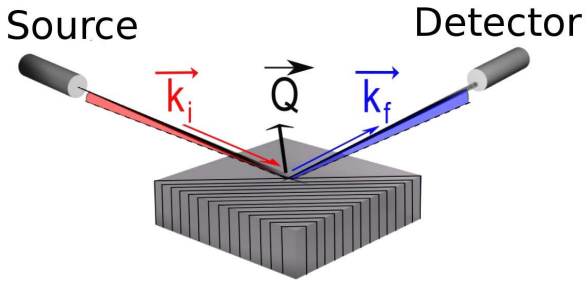

Figure 3.2: Grazing-incidence XRD geometry. Adapted Fig. 2.14 from [174].

Grazing-incidence XRD

The grazing-incidence XRD [175] consists in positioning the source and the detector at small angles (below the critical angle) to respect the sample surface, as shown in Fig. 3.2. Working in total reflection conditions assures the surface sensitivity (as discussed in Sec. 2.2.3) making this technique particularly adapted for epilayers [176]. In addition, in this geometry the diffracting planes are the ($hk0$) [177] and not the ($00l$). Thus, it is possible to have detailed direct information about the "in plane" lattice parameters and strains.

3.2.2 Transmission electron microscopy

Transmission electron microscopy (TEM) is a microscopy technique whereby a beam of electrons is transmitted through an ultra-thin sample.[3] An image is formed from the interaction of the electrons transmitted through the specimen and detected by a sensor such as a CCD camera. It is a powerful structural characterization tool widely used in the study of nanomaterials and thin films since TEM microscopes are capable of imaging at a significantly higher resolution than light microscopes, owing to the small wavelength of high energy ($>$ 100 KV) electrons.[4] On the other hand, at these wavelenghts the electrons are transmitted only through ultra-thin ($<$ 100 nm) samples, meaning that an accurate sample preparation is mandatory. This is normally done by mechanical polishing or chemical etching followed by ion milling (like focused ion beam methods). The TEM microscope, since its first design [179], has seen significant advances [180] and nowdays the main limiting factor to its resolution are aberrations due to the electronic lenses [181].

Electromagnetic lenses have an important role in the imaging methods. In fact, the unique ability to change lens strength or to deactivate a lens allows for many operating modes, passing from images (information in real space) to diffraction patterns (information in reciprocal space) [182]. In order to investigate an electron microscope image, first the electron diffraction pattern is obtained. Then by passing the transmitted beam or one of the diffracted beams through a small objective aperture (positioned in th back focal plane) and changing lenses to the imaging mode, it is possible to observe the image with enhanced contrast. When only the transmitted beam is used, the observation mode is called bright-field method, when one diffracted beam is selected, it is called dark-field method. The contrast in these images is attributed to the change of the amplitude of either the transmitted or diffracted beam due to absorption and dynamic scattering in the sample. At this low magnification it is possible to visualize dislocations in a crystalline material or measure lattice parameters when Moiré fringes appear (due to the superimposition of two different crystal lattices or orientations).

To reach higher resolution imaging, thinner samples and higher energies of incident electrons are required. Therefore the sample can be modelled as an object that does not change the amplitude of the incoming electron wavefunction but modifies the phase (pure phase object model). This mode, called high-resolution TEM (HRTEM), is obtained using a large objective aperture on the back focal plane, incorporating both the transmitted and diffracted beams. The image results from the multiple beam interference and is called phase-contrast image. However, a proper interpretation of this image can be achieved by accurate simulation [183].

In order to get chemical sensitivity, TEM is coupled with spectroscopy tools. In fact, electrons can interact with the atoms exciting atomic levels or through inelastic scattering. Considering these interactions, two techniques are used: energy dispersive x-ray spectroscopy (EDS) and electron energy loss spectroscopy (EELS). EDS measures the emitted x-ray fluorescence and this gives the chemical information. If the microscope works in scanning mode (STEM) a detailed chemical mapping at the nanoscale is obtained. EELS measures the energy losses of the transmitted beam due to inelastic scattering [184] and it is in principle capable of measuring atomic composition, chemical bonding, valence and conduction band electronic properties (a recent review is given in Ref. [185]). In fact, EELS peaks present a fine structure (EXELFS) that has the same information content of EXAFS [186] and it is analyzed like XAS [187, 188, 189].

[3] Many excellent books are written on the theory and practice of TEM. One of the first is Ref. [178].

[4] Considering relativistic effects, the *de Broglie* wavelength of electrons is $\lambda_e = h/\sqrt{2m_0eV(1+\frac{eV}{2m_0c^2})}$.

3.2.3 SQUID magnetometry

The magnetic properties of thin films are usually studied using a Superconducting Quantum Interference Device (SQUID) magnetometer [190]. In fact, this device permits to measure extremely weak (10^{-14} T) magnetic fields with the possibility to apply varying external magnetic fields (ũp to 5 T) and in a wide temperature range (2̃–400 K). The main components of a SQUID magnetometer are: a superconducting magnet; a superconducting detection coil which is coupled inductively to the sample; a SQUID connected to the detection coil; a superconducting magnetic shield (to shield the SQUID sensor from the fluctuations of the ambient magnetic field); a temperature control system (cryostat). The SQUID sensor itself consists of a superconducting ring interrupted through one (RF-based [191]) or two (DC-based [192]) Josephson-junctions [193] and it does not measure directly the magnetic field of the sample but the induced current in the coils when the sample is subjected to a vertical translation into the detection coil.

To measure the magnetization of a thin layer at a given temperature, the diamagnetic contribution of the substrate is subtracted. This is done using a sample without the doped layer (in order to take into consideration also the contribution of the buffer layer) and measuring the magnetization at an arbitrary temperature and for a known external magnetic field.

3.3 *Ab initio* calculations

Due to the complexity of the electronic structure *ab initio* calculations in the framework of the density functional theory (DFT) [194], a review of the theoretical and practical basis is beyond the scope of this manuscript; the interested reader can refers to Refs. [195, 196] and references therein for the key papers and an introduction to the technique. In this section are illustrated only the calculations methods and practical procedures used to obtain the relaxed atomic structures for the XAFS analysis (Sec. 2.4).

3.3.1 Structure optimization

DFT calculations are carried out with the QUANTUM-ESPRESSO software [197] using both the local spin density – generalized gradient approximation (LSD-GGA) [198] and the LSD-GGA+U formalism [199] as implemented with plane wave basis sets in the code [200, 201]. The last scheme is important in order to take into account the strong localization of the *d* states of the transition metals that are poorly described by LSD-GGA exchange-correlation functionals. Total energies are calculated in a supercell approach,[5] by using ultrasoft pseudopotentials [202] plane wave basis sets, the special-points Monkhorst-Pack technique for **k**-space integration [203], and the Perdew-Burke-Ernzerhof (PBE) exchange-correlation functional [198]. Geometry optimizations are performed by fully relaxing the positions of all the supercell atoms by minimizing the atomic forces (using a Verlet algorithm [204]). The spin state of the system is self-consistently determined during the wavefunction optimization. The cell parameters are calculated by minimizing the total energy of the system. Optimal values are found at the zero value of linear fits of the total stress, corresponding to the minimum of the total energy. Finally, when the relaxed atomic positions are obtained, due to the fact that they are affected by the underlying approximations, a linear scaling of the lattice parameters on the experimental values is applied in order to have more realistic atomic distances.

[5] A supercell consists in $n_1 \times n_2 \times n_3$ repetitions of the host crystal unit cell where normally are inserted impurities. This permits to avoid unwanted interactions when applying the boundary conditions.

Convergence tests of key parameters

One of the drawbacks of DFT calculations is the amount of computer calculation time needed to have accurate results. In order to avoid systematic errors due to the wrong choice of the key parameters in the simulation, it is necessary to perform a series of convergence tests, that is, studying the total energy convergence as a function of a single parameter. Normally, the investigated parameters are: the plane waves cutoffs for wavefunctions (E_{cut}^{wfc}) and charge densities (E_{cut}^{ρ}), the **k**-point Monkhorst-Pack mesh and the supercell size. Unfortunately all these parameters depend on each other but two *rules of thumb* are found and used for the calculations: 1) $E_{cut}^{\rho} = 4E_{cut}^{wfc}$; 2) For 72 atoms supercell the minimum requirement is $2\times2\times2$ mesh with $E_{cut}^{wfc} = 30$ Ryd ($3\times3\times3$ mesh with $E_{cut}^{wfc} = 35$ Ryd upper limit).

Part II

Case studies

Mn dans le GaAs

Résumé du Chapitre 4

Le (Ga,Mn)As, avec des concentrations en Mn inférieurs à 10 %, est un DMS dont le modèle de Zener explique assez bien le comportement magnétique et, pour cette raison, il est largement étudié. Pour incorporer une si haute quantité de Mn (la limite de solubilité dans le GaAs est $\approx$ 0.1 %) sans avoir des précipitations, il faut une croissance hors équilibre comme c'est le cas pour la MBE à baisse temperature (LT-MBE). En plus du Mn substitutionel dans les sites du Ga (Mn_{Ga}), cette croissance permet la création d'autre défauts, comme le Mn dans des sites interstitiel (Mn_I), qui ont un effet négatif sur les propriétés magnétiques. Pour limiter cet effet, il a été démontré l'efficacité d'un recuit après croissance à basse temperature qui permet la migration de Mn_I vers la surface (grâce à leur plus haute mobilité). Avec cette méthode il s'observe donc une augmentation de T_C qui peut dépasser 170 K pour 7 % de Mn [205].

Dans ce chapitre est présentée une étude de la structure locale autour du Mn dans une série d'échantillons de $Ga_{0.094}Mn_{0.06}As$ préparés par LT-MBE. Les mesures EXAFS ont été réalisés soit en configuration standard (incidence à 45°), soit en incidence rasante (ReflEXAFS, Fig. 4.1) pour permettre une résolution en profondeur et étudier les effets structurales des traitements après croissance comme le recuit (annealing) plus l'attaque chimique (etch-annealing). On observe que en condition standard seulement le Mn substitutionel dans les sites du Ga (Mn_{Ga}) est visible (Fig. 4.2) et que la structure est bien cristalline car est présent un bon signal sur plusieurs couches de coordination. D'autre part, les mesures en ReflEXAFS permettent d'être plus sensible à la surface et là on retrouve non seulement le signal de l'oxyde de Mn (MnO) mais aussi une contribution non négligeable de Mn dans les sites de type interstitiel tétraédrique (Mn_I, Fig. 4.3).

Une fois mis en place un modèle qui considère ces trois types de signaux, on étudie la structure locale distinguée entre surface ($\approx$ 10 nm, en modalité de réflection totale, TR) et la couche entière ($>$ 200 nm, en modalité à haute incidence, HI) ; ceci pour les parties recuites (annealed, AN) et non recuites (as deposited, AD) en fonction de l'épaisseur de la couche de revêtement de surface (capping layer, CL) pour contrôler la contribution du signal de MnO. Un exemple de l'évolution du signal EXAFS et des fits relatives pour le cas sans CL est donné dans la Fig. 4.5, alors que les résultats quantitatives générales sont donnés dans le Tab. 4.2. Pour la partie structurale on observe que il y a une dilatation locale de la distance aux premiers voisins de $\approx$ 2 % respect aux valeurs cristallographiques du GaAs et qui est constante dans la limite des erreur expérimentaux. Pour la partie contribution de chaque phase on trouve que,

en conditions HI (Fig. 4.6(b)), Mn_I est visible autour du $\approx$ 15 % et reste constante pour les parties AD et AN. Au même temps MnO est visible seulement pour les parties AN en faible quantité de $\approx$ 16 %. D'autre part, en conditions TR (Fig. 4.6(a)), Mn_I est visible seulement pour MnO $<$ 50 % (CL $>$ 4 nm) sinon ce dernier signal est dominante. En plus, dans ces cas, la différence entre AD et AN reste dans la limite des erreurs.

La dernière partie est consacrée à l'investigation des effet de etch-annealing [206], où on a fait un attaque chimique pour 30 s dans HCl à 35 % suivi d'un recuit de 20 min à 200 °C. Dans ce cas on observe que, dès le premier cycle, la contribution de Mn_I est absente en HI et reste en TR. Ceci montre directement comme cette procédure soit bien plus efficace que le simple recuit dans la neutralisation de Mn_I.

En conclusion, la présente enquête résolue en profondeur de la structure locale du Mn dans GaAs a confirmé que la technique LT-MBE permet la fabrication d'un bon système DMS avec une incorporation de type Mn_{Ga} cristalline même pour des concentrations relativement fortes (6 %). Elle a aussi permis de constater un enrichissement de Mn_I à la surface de tous les échantillons étudiés, confirmant le mode de collection en incidence rasante comme une puissante sonde locale de surface. Les effets de la croissance après-recuit sur la migration en surface de Mn_I sont aussi étudiées, mais il n'est pas possible de lier l'observation de l'efficacité de cette méthode à l'interaction avec l'oxyde de surface, car, d'un point de vue XAFS, la présence de l'oxyde ne permet pas d'être sensible au Mn_I, même avec l'utilisation d'une couche de GaAs de différentes épaisseurs. D'autre part, il est constaté que le processus d'attaque chimique plus recuit est efficace dans la suppression de Mn_I.

4

Mn in GaAs

In this chapter is presented a depth-resolved XAFS study on Mn in GaAs. Although this system is the most studied DMS, is still challenging to full reproduce experimentally the theoretical predictions about its magnetic behavior and a fine characterization at the nano-scale is mandatory. Here the surface effects and Mn defects mobility is separated from the bulk Mn local structure working in total reflection conditions (ReflEXAFS). This work is realized in collaboration with the Department of Physics of the University of Notre Dame (USA).

4.1 Introduction

The $Ga_{1-x}Mn_xAs$ ferromagnetic DMS[1] is one of the most widely studied systems exhibiting carrier mediated ferromagnetism, consistent with the Zener model, as described in Sec. 1.2.3. Recently, much attention of the research community was focused on the optimization of growth conditions and post-growth treatments in order to increase the Curie temperature (T_C) and hopefully reach room temperature. In fact, extensively studying the single-phase intrinsic ferromagnetism in this system has permitted to increase its T_C from 60 K in its first observation [207] to 180 K in recent samples [206]. Here a brief non-exhaustive review of the literature on this system is provided in order to introduce the present study. An extended recent review, with particular attention to the Fermi level engineering effects, is found in Ref. [208] (and references therein).

The equilibrium solubility of Mn in III-V semiconductors is known to be at most 10^{19} cm^{-3} ($\approx$ 0.1 % in GaAs), thus, to incorporate Mn into Ga sites (Mn_{Ga}) at high concentrations (Mn $>$ 4 %) without precipitates (e.g. MnAs), it is required a growth by low-temperature molecular beam epitaxy (LT-MBE). This also promotes creation of additional defects as Mn interstitial (Mn_I) and As antisite (As_{Ga}). This is unfortunate, as both act as double donors, making the sample less conductive and compensating the holes generated by Mn_{Ga}. Mn_I also reduce the magnetization (M), since (according to calculations) they couple in antiferromagnetic configuration with the neighboring Mn_{Ga} [209]. Mn_I have a metastable nature, since it is observed a substantial decrease in their density upon post-growth annealing [210, 211, 212]. On the other hand, As antisites are stable up to $\approx$ 450 °C [213] and cannot be removed by this treatment.

In the search for T_C increase in (Ga,Mn)As, many research groups have followed different approaches. On the basis of the Zener model predictions, it is possible to increase the total

[1] Also indicated as (Ga,Mn)As or GaMnAs in the following.

Mn concentration (x) in order to to increase the Mn_{Ga} ions concentration (x_{eff}) or to increase the holes concentration (p) by co-doping with shallow impurities. In high doping conditions ($x > 10$ %) results are still controversing, finding for T_C a decreasing [214], increasing [215] or saturating [216] character. Recently has been reported that co-doping with Be (acceptor) is useful until a limit is reached and the trend inverted [217], on the other hand, an opposite behavior is found co-doping with Si (donor) [218]. These controversies means that the underlying physics of this process is still under debate [219, 220, 48].

To avoid these problems, the best solution, up to now, seems to control Mn site occupation through fine optimization of the deposition parameters and post-growth treatments. In fact, with $x_{eff} < 7$ % T_C can reach 173 K [205] and similar results were obtained with $x \approx 9$ % by post-growth annealing [221] where the additional ≈ 2 % is represented by the removal of Mn_I. In fact, it is found that, due to their high mobility, Mn_I diffuse through the sample surface during the annealing [221, 222, 223, 224] and interact with the oxide layer. This effect is confirmed by reaching a $T_C = 180$ K with a series of etch-annealing [206]. Following this idea, it has been possible to reach $T_C = 185$ K in samples grown at $x = 12$ % [225].

In order to have detailed feedbacks on these growth optimizations and post-growth treatments, the structural characterization plays an important role. In the quest for determination of Mn location in GaMnAs, starting from the ion channeling techniques [209], many others followed, (e.g. polarized neutrons and x-ray reflectometry [223], x-ray diffraction and standing-wave fluorescence [226], muon spin relaxation [227]). XAFS investigations have also been reported, from first characterizations [228, 229] to the direct evidence of Mn_I [230, 231], the effects of high temperature annealing [232, 233], hydrogenation [234] and, recently, on the etch-annealing treatments [235].

4.2 Growth

The samples studied in this chapter are grown by LT-MBE using a Riber 32 R&D dual chamber MBE machine equipped with standard effusion cells for Ga, Mn, Be (the latter for doping) and As_2 produced by a cracker cell. The procedure followed is well established [236, 209, 237] and assures high reproducibility. After growing a GaAs buffer layer on semi-insulating GaAs(001) substrates at normal GaAs conditions (590 °C), the substrate temperature (T_S) is cooled down to 200–300 °C and a LT-GaAs buffer is deposited to a thickness between 0 and 100 nm. Epitaxial films of $Ga_{1-x}Mn_xAs$ with various Mn concentration, $0 < x < 0.10$, are then grown on the thin LT-GaAs buffer at a growth rate of ≈ 0.8 μm/h. In some cases, co-doping with Be (shallow acceptor) is also employed. In addition, in order to study the surface oxidation processes, GaAs or As LT capping layers (CL) are grown with a thickness varying from 1 to 6 nm. RHEED patterns are used to monitor the surface reconstruction during the growth, which is always carried out under As-stabilized conditions. A 1×1 surface reconstruction is observed for LT-GaAs and 1×2 for GaMnAs. After the growth, each sample is cleaved into 2 pieces and one of them annealed at 283(2) °C for 1 hour in N_2 atmosphere; this condition has been established by a systematic study [237], in agreement with literature results [238].

The magnetic properties of the grown samples are monitored by magnetization measurements using SQUID magnetometry. The value of T_C is obtained from the temperature dependence of the magnetization measured in a field of 100 Oe. Temperature dependence of the resistivity is also measured to establish the electrical properties. These measurements, in the zero-field condition, present a peak in the resistivity at a characteristic temperature that occurs slightly above T_C [239, 240, 241]. For the $Ga_{0.094}Mn_{0.06}As$ samples presented here, T_C is around

60 K and 110 K for the *as deposided* (AD) and annealed (AN) parts, respectively.

4.3 Local structure

4.3.1 Experimental

XAFS data at Mn K-edge (6539 eV) are collected at the GILDA beamline during multiple experiments with dedicated set-ups to obtain the best experimental conditions. In addition to standard settings already described in Sec. 2.3.1, the monochromator is equipped with double Si(111) crystals when working in ReflEXAFS conditions, in order to have the highest flux and with double Si(311) for standard geometry in order to reach a better energy resolution in the XANES spectra.

When working in the ReflEXAFS station (Sec. 2.3.1), the beam on the sample is sized vertically to 50 μm using a slit, preventing the projected beam spot at glancing angle to be bigger than the sample size (20 mm for GaMnAs). The intensity of the incident and reflected beam are monitored with two ion chambers whereas the fluorescence from the sample is collected with a 13 elements Hyper pure Ge diode array. Samples are mounted with the polarization vector parallel to the sample surface and the fluorescence detector on the same horizontal plane in order to reduce the elastic scattering ("grazing-exit" geometry, as discussed in App. A). Before the sample, a thin ($\delta\mu << 0.01$) Fe foil is used as a reference for the beam energy.

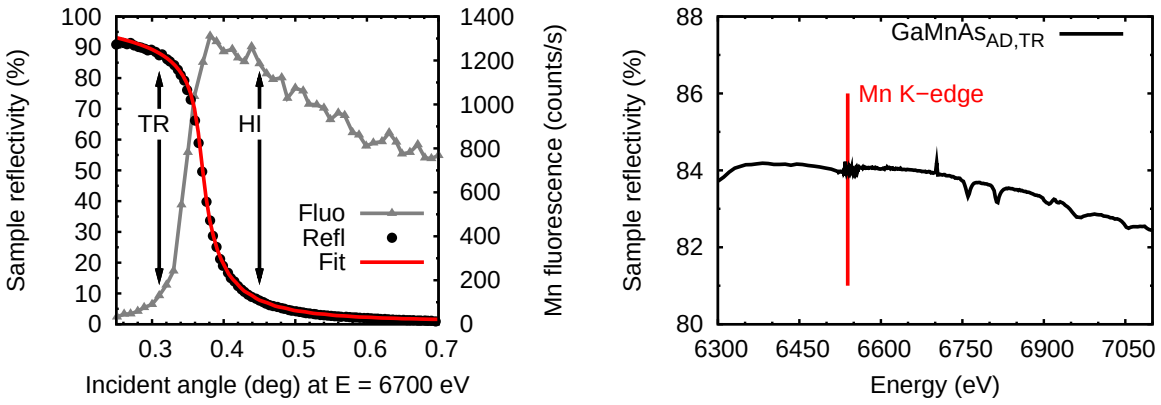

(a) Reflectivity with relative fit (ρ_{exp} = 5.157 g/cm^3) and fluorescence yield as a function of the incident angle.

(b) Reflectivity as a function of the photon energy at a fixed incident angle ϕ_w^{TR}.

Figure 4.1: Experimental conditions for collecting ReflEXAFS data on $Ga_{1-x}Mn_xAs$.

In order to obtain depth sensitivity, spectra are collected in two conditions, as shown in Fig. 4.1(a): total reflection (TR) and high incidence (HI). In TR the incidence working angle (ϕ_w^{TR}) is below the critical angle (ϕ_c), that is around 0.36 deg for GaMnAs. This condition ensures an extinction length for the probe beam of less than 10 nm so it guarantees that the information collected is really relative to the surface. Prior to each collection of XAFS data the reflectivity of the sample is collected at three fixed energy points (before, next, far the absorbing edge) and fitted with a suitable theoretical model in order to check that the experimental density of the reflecting layer is not far away from that of GaAs (5.428 g/cm^3). Then the energy scans are collected at fixed incidence angle, $\phi_w^{TR} = 0.8\phi_c$, but monitoring the reflectivity in order to be sure of maintaining the TR conditions along the whole spectrum (Fig. 4.1(a)). The

information from the whole doped layer is obtained from HI conditions, usually at an incident angle $\phi_w^{HI} = 1.2\phi_c$.

In the following, the results concerning the XAFS measurements in standard geometry (SG) are indicated as "bulk" while ReflEXAFS measurements in TR and HI are described as "surface". In fact, the HI measurements are still more sensitive to the surface than the standard geometry ones used for the bulk analysis, due to the difference in the projected extinction length on the beam path and the grazing-exit configuration of some elements of the detector. This issue is addressed quantitatively in Sec. 4.3.3.

4.3.2 Models

Mn substitutional

The main incorporation of Mn in the zinc-blende GaAs crystal (space group $Fd\bar{3}m$, n. 216, lattice parameter a = 5.6535(1) [242]) is substitutional at Ga site (Mn_{Ga}) as shown in Fig. 4.2(a). This behavior is confirmed experimentally by EXAFS, studying the local structure around Mn probing the whole doped layer in the $Ga_{0.094}Mn_{0.06}As$ LT-MBE samples of this study. In Fig. 4.2(b) is reported the EXAFS - $k\chi(k)$ - spectrum collected in standard geometry and the magnitude of its relative Fourier-transform (FT) - $|\chi(R)|$ - using standard Hanning windows (slope parameter $dk = 1$) in the ranges indicated by arrows. Qualitatively, the first three coordination shells of the zinc-blende structure are easily distinguishable in the low-distance region where single scattering (SS) events are significant.[2] At higher distances, multiple scattering (MS) signals play an increasing important role in the description of the FT spectrum. The presence of information at high distances reveals a good crystallinity around Mn atoms that helps the technique to resolve additional phases and/or defects (as described in the next experimental conditions).

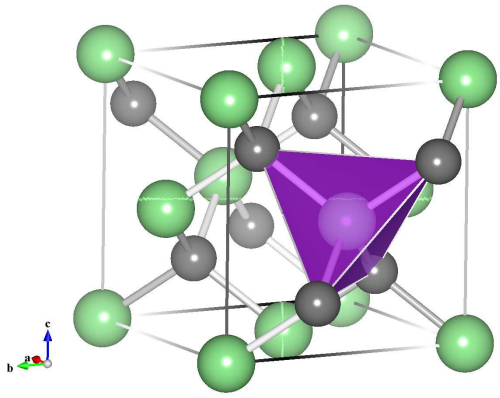

(a) Ball and stick model: Mn (violet), Ga (green), As (gray); the nearest neighbors distances are highlighted.

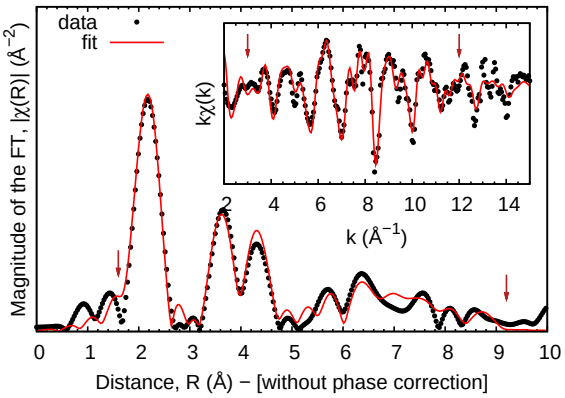

(b) EXAFS data (and relative fit) for LT-MBE $Ga_{0.094}Mn_{0.06}As$ (AN part, without CL) collected in standard geometry at 10 K.

Figure 4.2: Mn substitutional in GaAs (Mn_{Ga}).

The bulk data are analyzed also quantitatively using a multi-shell model (SS+MS) with a minimum set of common guessed variables: ΔE_0 (correction to the energy edge), S_0^2 (amplitude reduction factor), ΔR^0, ΔR^1 (expansion/contraction factors, respectively, for the first shell

[2] This is a qualitative consideration on the form of the FT, while in the quantitative analysis also multiple scattering paths (e.g. the triangular between second and third shell) are taken into accout in this region.

distance and the all others upper distances) and σ^2_{Debye} (Debye-Waller factors using a correlated Debye model [243]). A fit with this minimum variable set is visible in Fig. 4.2(b). The fit quality can be improved increasing the number of variables, in particular the number of DWFs (in the present case only the Debye temperature is fitted), but this will introduce numerical correlations that will overcome additional weak phases (as interstitials). At this point the scope is to find a reference fit model for the Mn_{Ga} phase with a minimum low-correlated variables set.

An important result for this phase is that Mn-As first shell distance is found at 2.50(1) Å, an appreciable elongation ($\Delta R^0 \approx 2$ %) with respect to the Ga-As bond in bulk GaAs (2.45 Å). Contrary to *ab initio* calculations that found a shorter distance [244], this is a value already found experimentally and commonly accepted [228, 229, 230]. It is worth noting that this is not a long range lattice distorsion since the factor used as long range parameter is $\Delta R^1 \approx 0.5$ % and justify the use of diffraction data to determine the concentration (x) in $Ga_{1-x}Mn_xAs$ [245]. In addition, these results are used in the following for fixing $S_0^2 = 0.9(1)$ and recalculating the theoretical scattering paths on the new expanded first shell distance.

Mn interstitial

In selected cases (Sec. 4.3.4), the previous fit model is proven to be statistically improved (using the methods described in Sec. 2.4) adding the Mn in GaAs tetrahedral interstitial site (Mn_I) contribution to Mn_{Ga}. The interstitial model is built using the previous zinc-blende GaAs crystallographic data and inserting the absorbing Mn at the Wyckoff position 4*b* ($\frac{1}{2}$, $\frac{1}{2}$, $\frac{1}{2}$). The local environment is shown in Fig. 4.3(a): it is similar to Mn_{Ga} except for the next-nearest coordination (violet polyhedron) of 6 Mn-Ga at 2.827 Å (crystallographic).

Mn_I is added to Mn_{Ga} model - in addition to its structural parameters (ΔR, σ) - with a common amplitude variable, Ξ, fitted after fixing $S_0^2 = 0.9$; this variable represent the average quantity (%) of Mn_I in the probed sample region since in the fits the sum of the amplitude of all included phases is constrained to 100 %. In order to reduce the noise contribution in the FT spectrum, increased at high-k by the k^2-weighting and the multiple-scattering importance, the k and R fitting ranges are reduced in this model, as visible in Fig. 4.3(b), where the resulting fit is also reported with the main additional contribution of this model, the Mn_I-Ga distance, highlighted in the FT spectrum. It is worth noting that also for the interstitial model is found an expansion of ≈ 2 % in the first coordination shell and lower, ≈ 1 %, for upper distances.

Mn oxide

Since the present study is focused on depth sensitivity and surface phenomena, a model for the thin oxide layer present in the studied samples is mandatory. The crystallographic structure for Mn oxide is chosen, between the possible cubic phases, to the NaCl-type MnO (Manganosite): space-group n. 225, $Fm\bar{3}m$, lattice parameter $a = 4.444(1)$ [246]. Other structures are also taken into consideration, like Mn_2O_3 (Bixbyite) [247] or Mn_3O_4 (Hausmannite) [248], but in order to keep the model simple, the first choice is kept for the whole analysis; the oxide contribution is modelized as a Mn–O single scattering path with coordination number 6 and distance of 2.222(1) Å [246]. As in the previous models, the theoretical paths are recalculated adjusting the distance on the experimental average value.

In selected cases (Sec. 4.3.4), this model is added to the previous ones in linear combination, using a fitted amplitude variable, Θ, in order to obtain the overall oxide content in the probed region.

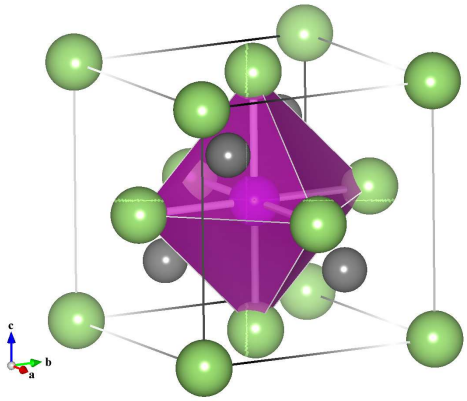

(a) Ball and stick model: Mn (violet), Ga (green), As (gray); the next nearest neighbors distances are highlighted.

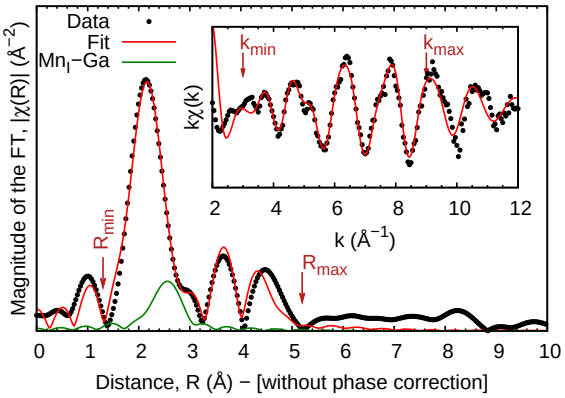

(b) Results for the Mn_{Ga} plus Mn_I model. The Mn_I-Ga contribution is highlighted; Ξ = 16(7)% for the present case. The data are from a $Ga_{0.094}Mn_{0.06}As$ (AD part with 6 nm GaAs CL) sample collected in HI conditions.

Figure 4.3: Mn interstitial in GaAs (Mn_I).

4.3.3 Standard versus grazing-incidence geometry

As previously stated, it is important to address the sensitivity issue of the technique in resolving additional signals in different experimental conditions. In Fig. 4.4 are reported the results for the standard and grazing-incidence (ReflEXAFS) geometries probing the whole doped layer of the same samples (AD and AN). The same parameters for the fits are used in both cases: while in the first (Fig. 4.4(a)) there is evidence only of Mn_{Ga}, in the second (Fig. 4.4(b)) also Mn_I and MnO are visible, with an enhanced sensitivity upon annealing. This demonstrate that, in the present experimental conditions, the surface study is crucial in understanding Mn_I mobility and interaction with the thin oxide layer present at the surface as a function of the post-growth annealing process. The quantitative results of the analysis are reported in Tab. 4.1 for the bulk and Tab. 4.2 for the surface study.

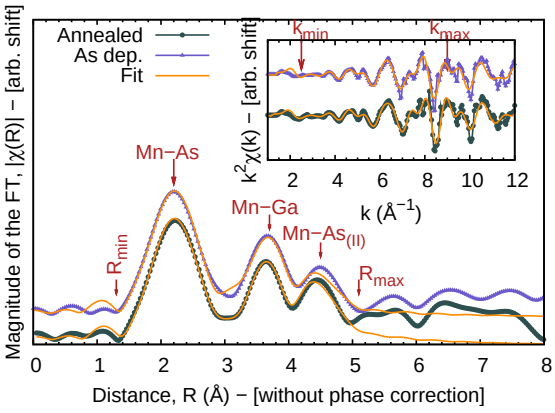

(a) Standard XAFS.

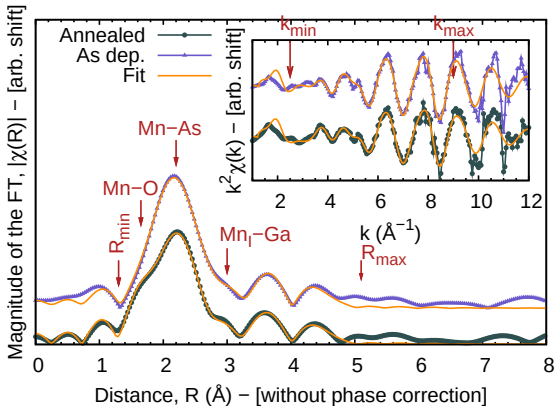

(b) ReflEXAFS at HI.

Figure 4.4: Comparison of the data collected for the bulk and surface study on the same sample ($Ga_{0.094}Mn_{0.06}As$ without CL, AD and AN parts) in the same experimental conditions and equal FTs and fit ranges. The last case, (b), evidence an enhanced sensitivity to additional signals to Mn_{Ga}.

Table 4.1: Results of the quantitative analysis for the bulk study on $Ga_{0.094}Mn_{0.06}As$ sample without CL for the AD and AN parts in the SG experimental condition. MnO and Mn_I models are not used since they are not necessary in obtaining the best fit.

Sample	CL	ϕ_w	ΔE_0 (eV) ±2	Mn_{Ga} R_{As} (Å) ±0.01	σ^2_{As} (Å^2) ±0.001	R_{Ga} (Å) ±0.05	σ^2_{Ga} (Å^2) ±0.001	R_{As2} (Å) ±0.05	σ^2_{As2} (Å^2) ±0.002
0	AD	SG	4	2.50	0.002	4.05	0.006	4.76	0.014
	AN	SG	4	2.49	0.002	4.02	0.007	4.70	0.008

4.3.4 Surface study

In this section is presented a depth-resolved systematic study of the local structure of the $Ga_{0.094}Mn_{0.06}As$ samples studied by ReflEXAFS in TR and HI positions on the as-deposited and annealed parts with different GaAs capping layers to control the oxide contribution.

In Fig. 4.5 is reported a summary of the collected spectra for the sample without a capping layer for the AD and AN parts in HI and TR positions. These spectra are representative of the whole collected spectra since they range from the heavily oxidized to the non-oxidized ones. The relative fits are also plotted in order to show the obtained quality with the previous described models. In particular, it is visible qualitatively, in the FT spectra of Fig. 4.5(a), how the MnO contribution heavily affect the low-R side of the Mn_{Ga} main peak reaching a splitting and even dominating in intensity, while Mn_I is detected as a shoulder on the high-R side. This evolution is also qualitatively visible in the peaks A–D indicated in Fig. 4.5(b), where the fine structure of these peaks representing the information at longer distances is completely damped when the oxide signal dominates. It is evident at this point that to keep the sensitivity to the additional Mn_I contribution, is mandatory to control the oxidized surface through the use of thin GaAs capping layers with different thicknesses.

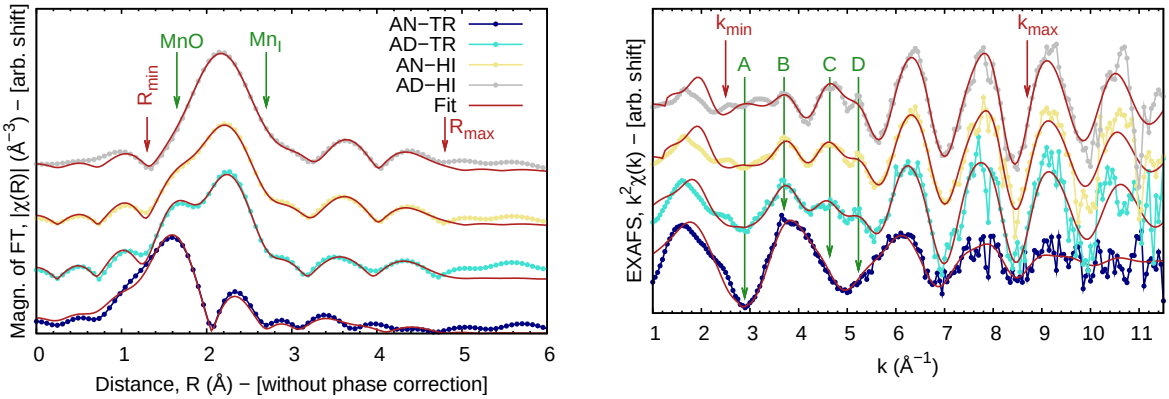

(a) Magnitude of the FT with indicated fit range (R_{min}–R_{max}) and the main additional contributions from MnO and MnI (green).

(b) k^2-weighted EXAFS spectra with indicated fit range (k_{min}–k_{max}) and the evolution of low-*k* features (peaks A–D).

Figure 4.5: Collected spectra, with relative fits, for a sample without capping layer that show how the spectra change for the AD and AN parts in the HI and TR positions.

The results of the quantitative analysis for this study are reported in Tab. 4.2. All previous described models (Mn_{Ga}, Mn_I, MnO) are used in linear combination with their respective

Table 4.2: Results of the quantitative analysis for the surface study on $Ga_{0.094}Mn_{0.06}As$ samples, as a function of the GaAs capping layer (CL) for the as-deposited (AD) and annealed (AN) parts, in the total reflection (TR) and high-incidence (HI) experimental conditions. Details on the employed variables are reported in the text. Ticks (–) mean that the relative model is not used (not necessary) in obtaining the best fit. Blank rows mean that the relative data are not collected.

Sample CL		ϕ_w	ΔE_0 (eV) ±2	MnO Θ (%) ±5	MnO R_O (Å) ±0.02	Mn_I Ξ (%) ±7	Mn_I R_{Ga} (Å) ±0.06	Mn_{Ga} R_{As} (Å) ±0.01	Mn_{Ga} σ^2_{As} (Å^2) ±0.002	Mn_{Ga} R_{Ga} (Å) ±0.05	Mn_{Ga} σ^2_{Ga} (Å^2) ±0.005	Mn_{Ga} R_{As2} (Å) ±0.05	Mn_{Ga} σ^2_{As2} (Å^2) ±0.009
0	AD	HI	6	–	–	14	2.89	2.51	0.007	4.05	0.019	4.74	0.024
		TR	5	22	2.14	–	–	2.50	0.005	4.03	0.023	4.72	0.020
	AN	HI	6	11	2.14	12	2.88	2.50	0.007	4.04	0.019	4.73	0.023
		TR	3	65	2.12	–	–	2.50	0.011	4.01	0.016	4.70	0.025
1.1	AD	HI											
		TR											
	AN	HI	7	16	2.15	21	2.82	2.49	0.004	4.12	0.018	4.83	0.060
		TR	5	62	2.13	–	–	2.50	0.006	4.10	0.012	4.92	0.030
2.2	AD	HI	6	–	–	14	2.86	2.51	0.006	4.06	0.017	4.76	0.020
		TR	5	17	2.16	11	2.86	2.49	0.006	4.04	0.014	4.74	0.015
	AN	HI	5	20	2.12	10	2.79	2.50	0.007	4.05	0.016	4.75	0.023
		TR	4	60	2.13	–	–	2.51	0.013	4.18	0.020	4.90	0.021
4.4	AD	HI											
		TR	4	–	–	19	2.94	2.49	0.005	4.00	0.012	4.69	0.022
	AN	HI											
		TR	6	–	–	15	2.93	2.52	0.004	4.00	0.016	4.69	0.018
6.0	AD	HI	7	–	–	16	2.87	2.51	0.006	4.07	0.017	4.77	0.018
		TR	7	–	–	17	2.86	2.49	0.006	4.04	0.015	4.74	0.021
	AN	HI											
		TR	6	–	–	16	2.90	2.51	0.007	4.00	0.017	4.69	0.023
Average dists.			–	–	2.14	–	2.87	2.50	–	4.05	–	4.74	–

amplitude variables (only Θ and Ξ are reported, since for Mn_{Ga} it is constrained to $100 - \Theta - \Xi$). S_0^2 and ΔE_0 are common variables and are, respectively, setted to 0.9 and guessed. The Debye-Waller factors (DWF) are defined on the Mn_{Ga} model as $\sigma_O^2 = \sigma_I^2 = \sigma_{As}^2$ for the first coordination shells of the tree models, and σ_{Ga}^2, σ_{As2}^2 for the second and third, respectively. It is worth noting that each time an additional phase is added to Mn_{Ga}, a χ^2-test is evaluated, reporting the results in the 90 % confidence limit.

The interpretation of the results in Tab. 4.2 can be divided in two parts: the structural and the composition information. From the structural point of view, the good local cristallinity is confirmed by the presence of a clear signal up to the third coordination shell and the correct scaling of DWF.[3] The distances found are mostly stable (in the limit of the error bars) and the average values are in line with those previously found experimentally (as previously discussed). On the other hand, a better insight is given analyzing the results about oxide and interstitial compositions. Plotting these results (Fig. 4.6) as a function of the capping layer and distinguishing between TR (Fig. 4.6(a)) and HI (Fig. 4.6(b)) measurements, permits to find some correlations between the oxide and interstitials surface interactions. First of all, considering the HI data, it is found that in these experimental conditions is not possible to resolve the thin oxide layer in AD samples but only in the AN ones where, for thin CL, an overall oxide fraction of $\approx$ 16 % is visible; in addition, the interstitial contribution is constant to $\approx$ 15 % for

[3] The fact that σ_{Ga}^2 and σ_{As2}^2 present big absolute values is due to the chosen modeling in the fit that aims principally to reduce correlations between variables.

Table 4.3: Results of the quantitative analysis for the etch-annealing (EAN) study for two EAN steps, in the total reflection (TR) and high-incidence (HI) conditions.

Sample	ϕ_w	ΔE_0 (eV) ±2	MnO Θ (%) ±5	MnO R_O (Å) ±0.02	Mn_I Ξ (%) ±7	Mn_I R_{Ga} (Å) ±0.06	Mn_{Ga} R_{As} (Å) ±0.01	Mn_{Ga} σ^2_{As} (Å^2) ±0.002	Mn_{Ga} R_{Ga} (Å) ±0.05	Mn_{Ga} σ^2_{Ga} (Å^2) ±0.005	Mn_{Ga} R_{As2} (Å) ±0.05	Mn_{Ga} σ^2_{As2} (Å^2) ±0.009
EAN1	HI	6	–	–	–	–	2.50	0.007	4.06	0.017	4.76	0.026
	TR	4	12	2.14	19	2.94	2.50	0.007	4.02	0.014	4.71	0.024
EAN2	HI	6	–	–	–	–	2.51	0.006	4.03	0.025	4.73	0.020
	TR	5	12	2.15	14	2.82	2.49	0.004	4.04	0.018	4.74	0.026

both AD and AN species. In the TR analysis, is found a limit for the oxide presence at ≈ 4 nm of GaAs CL, in our experimental conditions; when the oxide contribution is above 50 % (the case of AN samples with CL < 4 nm) it is not possible to resolve the presence of Mn_I since the MnO signal dominates. Finally, in the limit of the error bars, Mn_I quantity in the absence of MnO do not change for AD and AN parts.

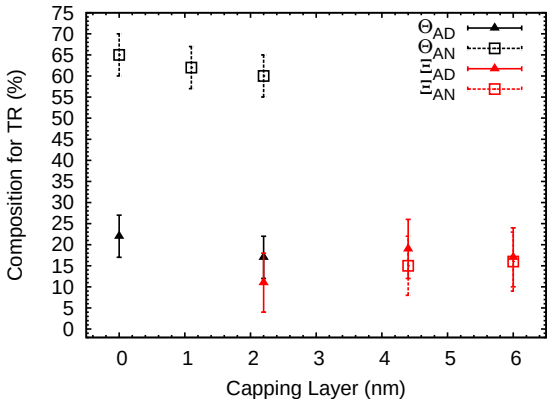

(a) Total reflection.

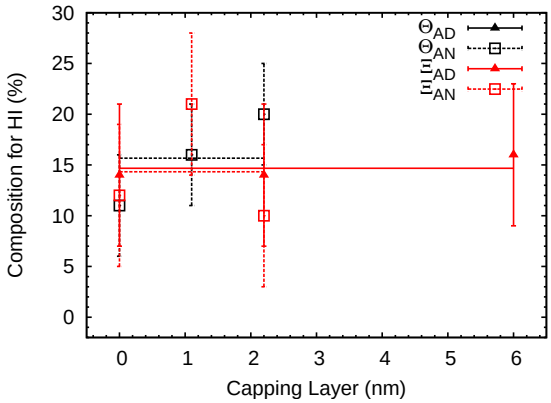

(b) High incidence. Average values are indicated by an horizontal line.

Figure 4.6: Plot of the results in Tab. 4.2 relative to Θ and Ξ variables that represent, respectively, the oxide and interstitial contribution in the probed films.

4.3.5 Post-growth etch-annealing

In order to study the structural effects of the etch-annealing (EAN) procedure described in Ref. [206], the following post-growth treatments are conducted on one $Ga_{0.094}Mn_{0.06}As$ sample without capping layer: 1) etching for 30 s in 35% HCl, rinsing in water and blow dry by N_2 gas; 2) annealing 20 min at 200 °C on hotplate under N_2 gas flow and rapid quench to room temperature under N_2 gas flow; 3) transfer to vacuum chamber and collect the XAFS data; 4) steps 1–3 are repeated.

The quantitative results of the EXAFS analysis (using the previously described models and procedures) are reported in Tab. 4.3. It is found that, already after the first treatment (EAN1), the Mn_I is not detected in the HI conditions but only in TR, where a small oxide contribution is still present.

4.4 Summary

In conclusion, the present depth-resolved investigation of the Mn local structure in GaAs has confirmed that LT-MBE permits the fabrication of a good DMS system with Mn incorporation as Mn_{Ga} in a crystalline environment even for relatively high concentration (6 %). It has also permitted to observe an enrichment of Mn_I at the surface since these additional defects are detected in grazing-incidence and not in standard geometry; this confirms the former collection mode as a powerful surface local probe. The effects of post-growth annealing on Mn_I surface migration are investigated but it is not possible to link the observed efficacy of this method to the interaction with the surface oxide since, from a XAFS point of view, the presence of the oxide phase reduces the sensitivity to Mn_I, even with the use of a GaAs capping layer of different thickness. On the other hand, it is observed that the etch-annealing process is fruitful in removing Mn_I. This is the first direct evidence of the neutralization process induced by this method.

Fe dans le GaN

Résumé du Chapitre 5

Le GaN dopé au Fe est un système qui a été peu étudié, comme semiconducteur magnétique, jusqu'à présent. Au même temps il présente des caractéristiques très intéressantes [249, 250]. Le but de ce chapitre est de donner une description détaillé de la structure locale en fonction des paramètres de croissances, notamment, la quantité de Fe, la vitesse de croissance et le co-dopage avec Si (donneur) et Mg (accepteur). En plus, l'étude XAFS a été accompagnée par des calculs DFT qui ont donné des structures relaxés en bon accord avec les résultats expérimentaux.

Les échantillons étudiés sont déposés par MOVPE en suivant une procédure bien établie [164, 250, 251, 252]. Les précurseurs employés sont Cp_2Fe, TMGa, NH_3, SiH_4, Cp_2Mg, respectivement, pour le Fe, Ga (qui règle la vitesse de croissance), N, le co-dopage avec Si et Mg. La quantité de Fe varie entre 50 et 350 sccm Cp_2Fe qui corresponds $\approx$ entre 0.1 % et 1.5 % (atomique). La vitesse de croissance va entre 5 et 12 sccm TMGa, respectivement, de 0.08 nm/s à 0.38 nm/s.

En fonction de ces paramètres, plusieurs séries sont étudiés par XAFS (Fig. 5.6). La première (Sec. 5.4.3) se propose de déterminer la limite de solubilité à une vitesse de croissance donnée (5 sccm TMGa). Qualitativement une évolution du spectre EXAFS est observée en augmentant la quantité de Fe (pics A, B et C en Fig. 5.9(a)) qui se traduit en FT (Fig. 5.9(b)) d'une situation à deux distances (R_1 et R_3) typique d'un environnement de type wurtzite à l'apparition d'une troisième distance (R_2) entre R_1 et R_3 qui augmente en intensité. Depuis l'analyse quantitative ces distances se traduisent en coordinations moyennes, respectivement, de Fe-N, Fe-Fe et Fe-Ga (valeurs reportés en Tab. 5.1(a)) qui appartiennent à un mélange de Fe substitutionel en GaN wurtzite et des précipités de ϵ-Fe_3N [253]. Il est obtenu donc un limite de solubilité de 200 sccm Cp_2Fe ($\approx$ 0.5 % dans les présents conditions de croissance). Ces résultats sont en ligne avec les mesures independantes de HRTEM (Sec. 5.3.1, résumé en Fig. 5.3) et XRD (Sec. 5.3.2, résumé en Fig. 5.5).

La deuxième série (Sec. 5.4.4) étudie l'effet de la vitesse de croissance sur l'incorporation du Fe une fois la limite de solubilité dépassée, c'est à dire, en fixant Cp_2Fe à 300 sccm. En ce cas le comportement qualitative des pics A, B et C en EXAFS (Fig. 5.10(a)) et R_1, R_2 et R_3 en FT (Fig. 5.10(b)) est inversé. Ceci se traduit quantitativement (Tab. 5.1(b)) dans la réduction de ϵ-Fe_3N pour faire place à une incorporation seulement substitutionel. Il est montré donc que la limite de solubilité du Fe dan GaN peut être augmentée considérablement en augmentant la

vitesse de croissance. Au même temps ce paramètre ne peut pas augmenter indéfinissablement car pour TMGa $>$ 15 sccm la bonne qualité de croissance est perdue.

A ce point un autre paramètre, le co-dopage, est pris en compte. La troisième série (Sec. 5.4.5) est une investigation systématique de GaFeN:Si dans le même espace des précédents paramètres (Fig. 5.6). Il est observé que il n'y a pas de changement dans les spectres EXAFS (pics A, B et C stables ; Fig. 5.11(a)), ni en FT où seulement R_1 et R_3 (Fig. 5.11(b)) sont présent. Quantitativement le Fe est toujours substitutionel en GaN et les résultats sont reporté en Tab. 5.1(c). Le co-dopage avec Mg est aussi étudié (Sec. 5.4.6) mais sur un plus petit nombre d'échantillons. Dans ce cas les effets sont inversés : la précipitation de γ-Fe [254] est favorisée. En plus, pour mieux comprendre les effets du co-dopage avec Si, l'état de charge du Fe est pris en compte avec une analyse XANES des pics pre-seuil (Sec. 5.4.7). Ceci a permis d'identifier une réduction partielle du Fe^{3+} à Fe^{2+} dans les échantillons de GaFeN:Si (résultats en Tab. 5.2).

Enfin, la dernière partie du chapitre montre comme dans ce système on peut exploiter la polarisation du faisceau (dichroïsme linéaire) et les effets des dislocations sur l'incorporation du Fe.

5 Fe in GaN

In this chapter the Fe-doped GaN system is studied. This work is the result of the scientific collaboration with the Institute of Semiconductor and Solid State Physics, *Johannes Kepler University in Linz (Austria). In the following sections an overview of the scientific context, growth and main characterizations are given with particular attention to the local structural results.*

5.1 Introduction

The use of Fe as magnetic dopant for GaN in order to realize an high temperature ferromagnetic semiconductor has become recently appealing [57]. The first application was as a semi-insulating material in AlGaN/GaN field effect transistors [255, 256] and later as ferromagnetic semiconductor [249, 257, 258]. Reports about high Curie temperature were given in literature for Fe-impanted *p*-GaN persisting up to 250 K [259] and 350 K for *p*-GaN:Mg at high Fe concentration (10%) [260]; however in both cases no comments on the possible presence of secondary phases was given. In the recent work by the Linz group the ferromagnetic features in MOVPE (Ga,Fe)N persisting up to 573 K are attributed by Fe-rich nanocrystals [250] or spinodal decomposition [261]. This means that the lack of appropriate nanoscale characterization can produce misleading reports as the high T_C of 940 K for (Ga,Mn)N [262] (for the controversy in the experimental observations see Ref. [263]).

5.2 Growth and in-situ monitoring

All samples characterized in the present study are fabricated by metalorganic vapour phase epitaxy (MOVPE) in a 200RF/4 AIXTRON MOVPE horizontal reactor (schematically shown in Fig. 5.1) according to a standard procedure [164, 250, 251, 252]. The precursors employed are trimethylgallium (TMGa), ammonia (NH_3), ferrocene (Cp_2Fe), silane (SiH_4) and bis-cyclopentadienyl-magnesium (Cp_2Mg) for respectively Ga, N, Fe, Si and Mg sources, with H_2 as carrier gas. Starting from c-plane (0001) Al_2O_3 (sapphire) substrates, upon the nitridation of the substrate in the reactor, a low-temperature 540 °C GaN nucleation layer ($\approx$ 30 nm) is deposited, then annealed under NH_3 and 1 μm thick device-quality GaN buffer layer is grown at 1020 °C and costant pressure of 200 mbar in N_2 atmosphere. Several series of 500 nm thick GaN:Fe at different substrate temperatures ranging from 750 to 1050 °C and different Cp_2Fe flow rates between 50 and 400 standard cubic centimeters per minute (sccm) are fabricated. In addition, in order to minimize long term memory effects due to the presence of residual

Fe in the reactor [255], the nominal Fe content in subsequently grown samples is alternatively switched from low to high and vice versa, and, to promote the deposition homogeneity, the samples are continuously rotated during the growth. The growth rate during the deposition is regulated by the Ga-precursor (TMGa) flow-rate and varies from 0.08 nm/s for 5 sccm to 0.38 nm/s for 12 sccm of TMGa flow. The same procedure is used also in the growth of co-doped samples with Si (donor) and Mg (acceptor). For Si an uniform doping is employed, while Mg is incorporated in the δ doping fashion, due to the fact that this enhances the p-type conduction in GaN [264, 265] and increases the Mg concentration in Fe doped GaN [249].

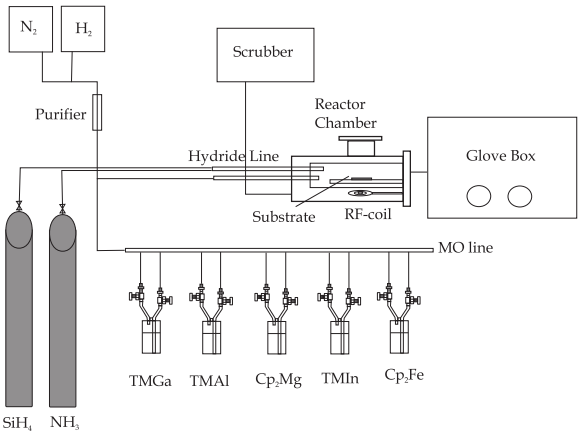

Figure 5.1: Schematic diagram of the AIX-TRON 200RF horizontal MOVPE reactor in Linz. Reproduced Fig. 2.1 from [252].

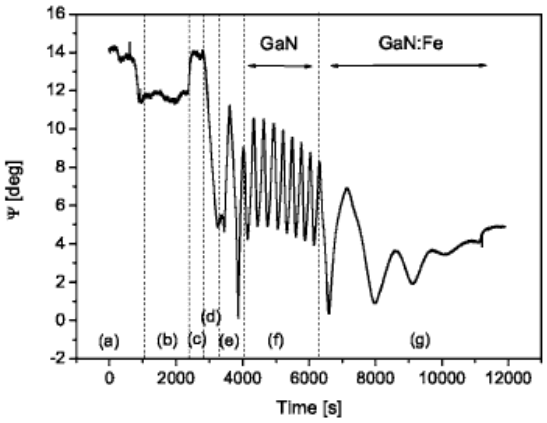

Figure 5.2: Typical kinetic ellipsometric on-line measurement. Reproduced Fig. 1 from [250].

In order to control the growth process, two main monitoring tools are employed: spectroscopic ellipsometry (SE) and *in-situ* x-ray diffraction (IXRD). Due to the fact that MOVPE is carried out in non-vacuum conditions, electron scattering based diagnostic tools like reflection high-energy electron diffraction used in ultra-high vacuum epitaxial techniques like molecular beam epitaxy are not effective. However, optical techniques like SE have proven to be useful tools to control the layer thickness and to monitor the deposition steps, providing also qualitative information on the surface roughness. The principle of ellipsometry and its use for this purpose is discussed in Sec. 3.1.2. In this case, the MOVPE reactor is equipped with a Jobin Yvon ellipsometer which allows both spectroscopic (optical response as a function of the photon energy in terms of the ellipsometric angles ϕ and Δ) and kinetic (optical response as a function of time). A typical kinetic ellipsometric on-line measurement is shown in Fig. 5.2: (a) heating of the sapphire substrate from room temperature to 1200 °C; (b) desorption under H_2 flow to stabilize the surface; (c) cooling and nitridation of the substrate; (d) deposition of the low temperature nucleation layer (NL); (e) annealing of the NL; (f) growth of the GaN buffer layer; (g) growth of the Fe-doped GaN layer. The IXRD is implemented on the MOVPE reactor through two Be windows transparent to the radiation with a PANalytical Cu x-ray tube (experimental details are described in Ref. [266]). Kinetic IXRD measurements permit to control the quality of the layers during the growth monitoring the full width at the half maximum (FWHM) of the $(11\bar{2}4)$ wz-GaN peak. Details of the analysis are reported in Ref. [250]. The *in situ* monitoring for δ-doping parameter optimization is more complex and well reported in Ref. [267].

The total Fe concentration in the samples ranges from 4×10^{19} cm^{-3} to 3×10^{20} cm^{-3} for Cp_2Fe flow-rate ranging from 50 to 350 sccm [250]. In the Si-doped (Ga,Fe)N structures the Si-content

ranges from 3×10^{18} cm^{-3} to 1×10^{19} cm^{-3} for a Si-precursor flow-rate from 5 to 30 sccm.[1]

5.3 Ex-situ characterizations

5.3.1 HRTEM

The HRTEM study is carried out on cross-sectional samples prepared by standard mechanical polishing, followed by Ar^+ ion milling at 4 KV for about one hour. The images are obtained from a 200 KV operating JEOL 2011 Fast TEM microscope with a point to point resolution of 0.19 nm. Additionally, energy dispersive x-ray spectroscopy is performed on the samples to gain information on the chemical composition of the layer.

Although Fe aggregation control is possible acting on the deposition parameters, as detailed in Sec. 5.4, three main characteristics are outlined by HRTEM as shown in Fig. 5.3: random substitutional, spinodal decomposition and second phase formation. The random substitutional regime (Fig. 5.3(a)) appears when Fe enters the GaN matrix at Ga sites without affecting the host crystal structure. This is identified by the interplanar d-spacing visible in the Fourier transformed (FT) TEM images. This regime is also identified by the absence of strain, mass or phase contrast in the images. The spinodal decomposition (Fig. 5.3(b)) is identified by mass contrast in dark and light zones in the images that represent local density fluctuations that lead to random regions with high concentration of the magnetic species [83]. The second phases, or nanocrystals, (Fig. 5.3(c)) are distinguished by Moiré fringes. Informations on the structure of these nanocrystals is obtainded by the FT analysis of the interplanar d-spacing of the images. Mainly ϵ-Fe_3N nanocrystals are identified [250] and occasionally some α-Fe crystals are found close to the surface [268].

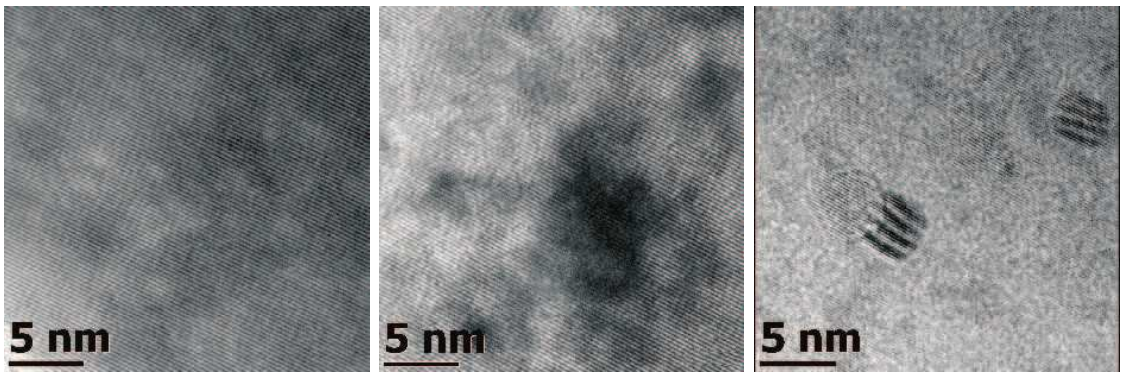

(a) Random substitutional. (b) Spinodal decomposition. (c) Second phases formation.

Figure 5.3: HRTEM images showing Fe incorporation regimes into GaN. Reproduced Fig. 5.2 from [252]

A different and still puzzling behaviour is found on an additional class of samples grown using (Al,Ga)N as buffer layer and it is reported here in order to support XAFS results of Sec. 5.4.8. As it is visible in Fig. 5.4(c), an high density of dislocations propagating from the buffer to the doped layer is present in these samples. In addition, the mass contrast analysis (Figs. 5.4(a),5.4(b)) reveals that the presence of random Fe aggregation is inversely proportional to the overall Fe quantity.

[1] Hall results interpreted with a two-layer model to discriminate between the conductivity of the buffer and the one of the (Ga,Fe)N:Si layer. Reference: M. Quast, Master Thesis, Johannes Kepler University 2008

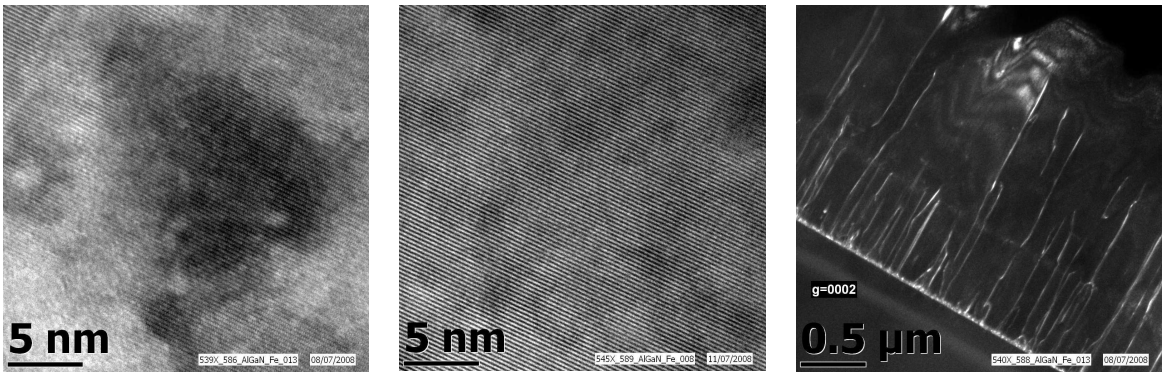

(a) Mass-contrast, 50 sccm Cp_2Fe. (b) Mass-contrast, 125 sccm Cp_2Fe. (c) Dislocations (side-view).

Figure 5.4: HRTEM images for samples grown on AlGaN buffer layer. From Tian Li [*unpublished*].

5.3.2 Synchrotron XRD

The use of synchrtron x-ray diffraction is necessary on this system in order to get informations on precipitations or long range ordering of new phases appearing in the spinodal decomposition regime due to the availability of high intensity source. Powder diffraction experiments are conducted at ID31 beam line at the ESRF and have permitted to properly identify the hexagonal ϵ-Fe_3N bainite structure of the nanocrystals as shown in Fig. 5.5. Extended results are reported in Ref. [252].

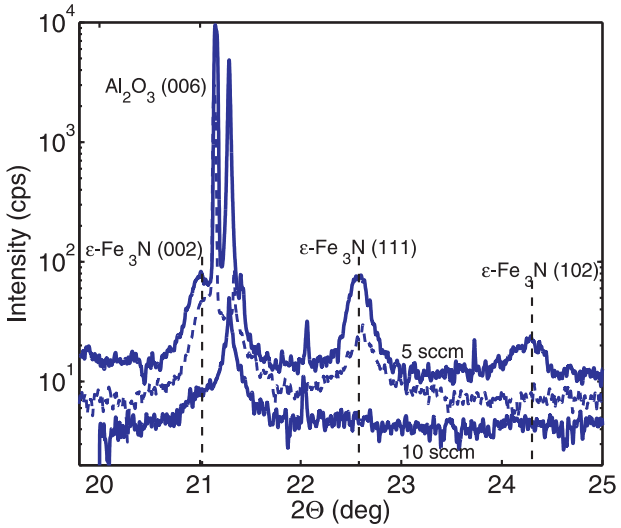

Figure 5.5: Synchrotron x-ray powder diffraction for two regimes in (Ga,Fe)N: random substitutional (TMGa 10 sccm) and nanocrystal precipitations (TMGa 5 sccm). Adapted Fig. 7.3 from [252].

5.3.3 Magnetic properties

The magnetic properties of this system are studied by SQUID [250]. Both paramagnetic and ferromagnetic behaviours are found. The paramagnetic component is dominant below the Fe solubility limit and the ferromagnetic response, that persists up to above room temperature, is enhanced above this limit where spinodal decomposition or nanocrystals are identified in the

structure. Although the ferromagnetic ordering needs a better understanding in this system, the presence of high temperature ferromagnetism can be taken as an indication of non-uniform Fe ions distribution over the GaN lattice according to TEM and XRD analysis. In fact, hexagonal ϵ-Fe_3N exibits itself a Curie temperature T_C = 575 K and a magnetic moment per Fe ion m = 2 μ_B. On the other hand, the ferromagnetic behaviour is present also when this crystalline phase is not detected so the spinodally decomposed regions could be responsible of this interesting behaviour.

In order to better understand these magnetic properties, a detailed structural model is mandatory and the XAFS technique is well suited to complement both HRTEM and XRD investigations. In fact, respect to TEM, in the case of uniform doping, it is possible to obtain detailed information on the defects and when precipitates are visible, quantify the phases on the whole doped layer; on the other hand, respect to XRD, it is possible to identify new phases and/or nano-structures without long-range ordering.

5.4 Local structure and charge state

In order to study the Fe incorporation into GaN host lattice, different samples series are studied with XAFS spectroscopy. These series are functions of deposition parameters, nominally, the Fe quantity (Cp_2Fe, sccm), the growth-rate (TMGa, sccm) and co-doping with Si and Mg. An overview of all characterized samples is given in Fig. 5.6 in a two dimensions deposition parameters space and as a function of co-doping.

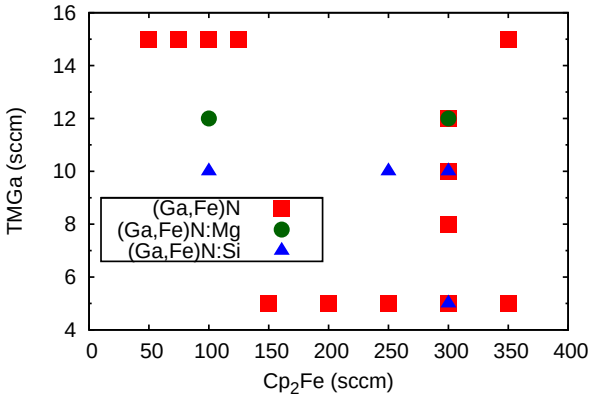

Figure 5.6: Overview of the characterized samples by XAFS.

5.4.1 Experimental

The XAFS measurements at the Fe-K edge (7112 eV) are mainly carried out at GILDA - details given in Sec. 2.3.1. The monochromator is equipped with a pair of Si(111) crystals and run in dynamical focusing mode [135]. Harmonics rejection is achieved by using a pair of Pd-coated mirrors with an estimated cutoff of 18 keV. Data are collected in the fluorescence mode using a 13-element hyper pure Ge detector and normalized by measuring the incident beam with an ion chamber filled with nitrogen gas. In order to minimize the effects of coherent scattering from the substrate, the samples are mounted on a vibrating sample holder [269] and measurements are carried out at liquid nitrogen temperature to reduce thermal disorder. For each sample the integration time for each energy point and the number of acquired spectra

are chosen in order to collect $\approx 10^6$ counts on the final averaged spectrum. In addition, before and after each measurement a metallic Fe reference foil is measured in transmission mode to check the stability of the energy scale and to provide an accurate calibration. In this way it is possible to calibrate the energy scale fixing 7112.0 eV at the first inflection point of the absorption spectrum [270].

In addition, other XAFS measurements in the same energy range are carried out at the "LUCIA" beamline at the Swiss Light Source - details given in Sec. 2.3.2. The choice of doing additional experiments on an insertion device beamline is double: it is possible to change the polarization vector at the source and obtain polarized measurements and, due to the small beam size ($< 3\ \mu m^2$), it is possible to work at grazing incidence geometry even for samples of small size ($\approx 8\ mm^2$). The grazing incidence geometry is very useful to make XAFS more sensitive to the surface and to increase the signal to noise ratio increasing the fluorescence yield respect to the elastic scattering signal (App. A).

5.4.2 Theoretical models

The physical models used in the quantitative analysis are built using the following structures.

Relaxed structures within the density functional theory

From all the native defects in wurtzite GaN [271], the more important substitutional and interstitials are choosen for Fe incorporation and, with the ϵ-Fe_3N crystal, are calculated by DFT method in order to obtain relaxed structures for the fits. The calculations for Fe defects in GaN are conducted in collaboration with the *CNR - Istituto di Struttura della Materia* (Monterotondo Stazione - Rome, Italy) through computational resources allocated at CINECA.[2] The ϵ-Fe_3N phase is calculated using the ESRF common resources.[3] These calculations are performed with the Quantum-ESPRESSO code [197], employing the basics methods described in Sec. 3.3 and the details described in the following.

Fe_{Ga} The calculation for Fe substituting Ga in wurtzite GaN (Fe_{Ga}, Fig. 5.7(a)) is done using a 72-atoms supercell (corresponding to 3x3x2 unit cells), the (1,1,1) **k**-point Monkhorst-Pack mesh, a gaussian smearing of the occupation numbers and plane waves cutoffs of 25 Ry for wavefunctions and 150 Ry for densities. The valence electrons considered in the atomic pseudopotentials are $2s$ and $2p$ for N, $3s$, $3p$, $3d$, $4s$, $4p$ for Fe, and $3d$, $4s$, $4p$ for Ga. A neutralizing background charge is imposed when dealing with charged states of Fe_{Ga}. The lattice constants of the 72-atoms supercell, as found from convergence tests, are a = 9.66 Å, c = 10.49 Å. The position of the electronic levels induced by the Fe impurity with respect to the top of the valence band is found by calculating the corresponding transition energy levels $\epsilon^{n/n+1}$, that is, the Fermi-energy values for which the charge of the defect changes from n to $n+1$. These values are found from total energies (defect formation energies) as described in Refs. [272, 273], where further details on the theoretical methods can be found. Transition energy values have to be located with respect to the GaN energy gap estimated here by the $\epsilon^{0/-}$ transition level relative to bulk GaN, thus permitting to compare defect transition levels with an energy gap calculated in a consistent way [274].

[2] See `http://www.cineca.it`

[3] Thanks to Piotr Bogusławski and Paweł Jakubas (IFPAN, Warsaw) for valuable discussions and CNR for financial support through the Short Term Mobility 2008 program (N.0002372)

Details of the atomic geometries produced by the LSD+U calculations are given in Tab. 5.1(e) for the charge states 0, +1 and -1 of Fe_{Ga}, which correspond to the Fe^{3+}_{Ga}, Fe^{4+}_{Ga} and Fe^{2+}_{Ga} forms of the impurity, respectively. Present results show that the Fe_{Ga}-N bond distances for the -1 (+1) state are slightly longer (almost the same) with respect to those of the neutral state. Moreover, no significant differences are found between the Fe_{Ga}-Ga distances estimated for the above three charge states of Fe_{Ga}.

Fe_{Td}, Fe_{Oh} Interstitial defects are calculated using the same procedures for Fe_{Ga} and changing the position of Fe in the unit cell (and consequently in the supercell) to standard positions [275]: the tetrahedral interstitial (Fe_{Td}, Fig. 5.7(b)) at Wickoff position (2/3, 1/3, u/2), and the octahedral one (Fe_{Oh}, Fig. 5.7(c)) at (0, 0, u/2) where u=0.385 [276]. These positions are given considering that Ga and N occupy, respectively, the (1/3, 2/3, 0) and (1/3, 2/3, u) positions.

The resulting distances found by the LSD+U calculations are reported in Tab. 5.1(e), where averaged values are shown in order to compare with the experimental results.

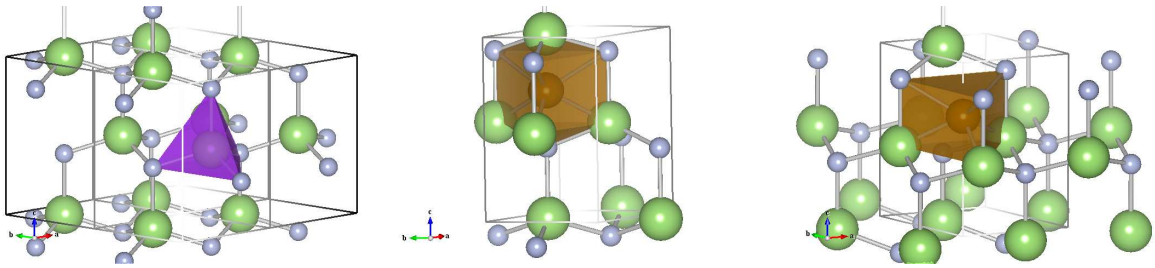

(a) Fe substitutional in Ga site, Fe_{Ga}.

(b) Fe in tetrahedral interstitial site, Fe_{Td}.

(c) Fe in octahedral interstitial site, Fe_{Oh}.

Figure 5.7: Ball-and-stick models for native defects in wurtzite GaN. Ga and N atoms are indicated, respectively, by green and light blue spheres.

ϵ-Fe_3N In the case of ϵ-Fe_3N, the starting point of the calculations is the hexagonal phase as found in literature on the nitridation process of Fe [277, 253]. The space group is $P6_322$ (No. 182) with the unit cell composed of 6 Fe atoms in the Wickoff site 6g [(x, 0, 0); (0, x, 0); (-x, -x, 0); (-x, 0, 1/2); (0, -x, 1/2); (x, x, 1/2)] where x = 0.333 and 2 N in site 2c [(1/3, 2/3, 1/4); (2/3, 1/3, 3/4)], that is, iron atoms show the motif of a slightly distorted hexagonal close packing (hcp) structure and nitrogen atoms occupy only corner-sharing octahedra (Fig. 5.8); experimental lattice parameters are: a = 4.7209(6) Å, c = 4.4188(9) Å. Satisfactorily converged results have been achieved by using the (12,12,8) **k**-point Monkhorst-Pack mesh, plane waves cutoffs of 35 Ry for wavefunctions and 140 Ry for densities.

The calculated cell parameters are: a = 4.64 Å and c = 4.34 Å, that is $\approx$ 2% contraction of the experimental values; this is a typical effect of the LSD approximation. The relaxation properly reproduces the experimental value of x that is a 0.009 contraction from the 1/3 ideal value for Fe in the hcp structure. The resulting atomic distances reported in Tab. 5.1(e) are slightly different from the crystallographic ones [253] (Tab. 5.1(d)). The above structural minimization corresponds to a magnetization of 2.2 μ_B/atom, in agreement with the experimental value found from neutron diffraction at 4.2 K [278].

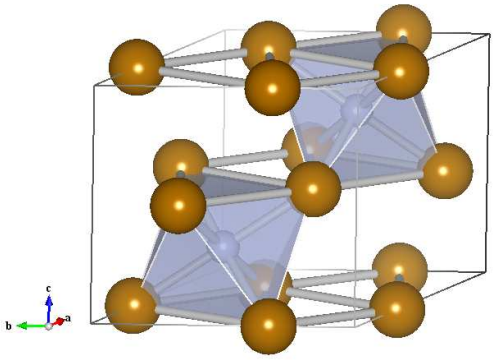

Figure 5.8: Ball-and-stick model for ϵ-Fe_3N: Fe (brown) and N (light blue).

Standard crystallographic structures

In addition to the previous relaxed structures, crystallographic structures from literature are used in the XAFS analysis in order to build possible theoretical models and test them on the experimental data. The standard Fe bcc phase (space group $Im\bar{3}m$, No. 229), α-Fe [279], the fcc (space group $Fm\bar{3}m$, No. 225) γ-Fe [254] that appears in the Fe phase diagram at high temperatures, the γ-Fe_4N [253], the fcc phase that stabilize at high N content in the Fe-N phase diagram [277] and, as minor possible phases, the tatragonal $FeGa_3$ [280] (space group $P4_2/mnm$, No. 136) and the intermetallic $Fe_{16}N_2$ [281] (space group $I4_2/mmm$, No. 139).

5.4.3 Fe solubility limit

The first series systematically studied consists of samples prepared each with different Fe content (Cp_2Fe flow rate from 150 to 350 sccm) at a fixed growth-rate (TMGa = 5 sccm) – Fig. 5.6. The recent investigation by HRTEM [268] shows on this series a solubility limit at 200 sccm at the given growth conditions. This means that after this limit precipitates appear mostly as ϵ-Fe_3N and, only at the surface of selected samples, as α-Fe. In Fig. 5.9(a) are plotted the k^2-weighted EXAFS data where qualitative differences are visible and are highlighted by the peaks A, B and C. In particular, three different spectra are visible: for 150 sccm, for 200 and 250 sccm, for 300 and 350 sccm. This difference is also found in the Fourier transformed spectra shown in Fig. 5.9(b) where, in the range R_{min}–R_{max}, from a two-peaks situation (R_1 and R_3) at 150 sccm, an intermediate third peak (R_2) appears and increases in amplitude with increasing Fe content. In the quantitative fit, the data can be reproduced with a two shell model consisting in a Fe-N and Fe-Ga average distances for R_1 and R_3, while R_2 is obtained with a Fe-Fe shell. The numerical results are shown in Table 5.1(a).

The sample with a lower Fe content exhibits two coordination shells around Fe. The observed bond length values are in agreement with those calculated via DFT for a Fe ion in a Ga-substitutional site. Thus, is possible to conclude that Fe substitutes Ga, as previously suggested by a qualitative analysis of EXAFS data [283]. The closeness of the theoretical estimates of the Fe-N distances reported in Table 5.1(e) makes it difficult to exploit the Fe_{Ga} local geometry to distinguish between its possible different charge states. However, the theoretical results support a deep acceptor character of Fe_{Ga} and locate the corresponding electronic level in the upper half of the GaN energy gap.

For samples grown with higher Fe content an additional shell appears, matching a coordination at $2.70 - 2.75$ Å. This value coincides with the experimental and calculated Fe-Fe second

Table 5.1: Results of the EXAFS quantitative analysis and comparison with theoretical models. Only average distances are reported. The values of S_0^2 and ΔE_0 are stable, in the limit of error bars, at 0.9(1) and 6(3) eV, respectively. Errors on the last significative digit are given in brackets. For XAFS results, the error bars are the diagonal elements of the covariance matrix evaluated during the fit and rescaled by the square root of the reduced χ^2. For the DFT method, they are the resulting variance of convergence tests.

(a) First (Ga,Fe)N series at TMGa = 5 sccm.

Cp_2Fe (sccm)	TMGa (sccm)	<Fe-N> R_1 (Å)	<Fe-N> σ_1 (10^{-3}Å^{-2})	<Fe-Fe> R_2 (Å)	<Fe-Fe> σ_2 (10^{-3}Å^{-2})	<Fe-Ga> R_3 (Å)	<Fe-Ga> σ_3 (10^{-3}Å^{-2})	X (%)
150	5	2.02(1)	6(2)	—	—	3.18(1)	6(2)	100(10)
200	5	1.98(1)	7(1)	2.71(3)	19(5)	3.19(1)	7(1)	70(10)
250	5	1.98(1)	7(1)	2.70(3)	22(5)	3.19(1)	7(1)	70(10)
300	5	2.01(2)	8(1)	2.74(3)	21(2)	3.21(2)	8(1)	50(10)
350	5	2.02(3)	7(2)	2.75(4)	21(2)	3.22(2)	7(2)	40(10)

(b) Second (Ga,Fe)N series at Cp_2Fe = 300 sccm.

Cp_2Fe (sccm)	TMGa (sccm)	<Fe-N> R_1 (Å)	<Fe-N> σ_1 (10^{-3}Å^{-2})	<Fe-Fe> R_2 (Å)	<Fe-Fe> σ_2 (10^{-3}Å^{-2})	<Fe-Ga> R_3 (Å)	<Fe-Ga> σ_3 (10^{-3}Å^{-2})	X (%)
300	5	2.01(1)	9(1)	2.75(2)	28(2)	3.23(1)	9(1)	50(10)
300	8	1.98(2)	12(4)	—	—	3.19(1)	9(1)	100(10)
300	10	1.97(1)	8(3)	—	—	3.19(1)	7(1)	100(10)
300	12	1.97(1)	13(5)	—	—	3.19(1)	8(1)	100(10)

(c) (Ga,Fe)N:Si series as a function of both TMGa and Cp_2Fe.

Cp_2Fe (sccm)	TMGa (sccm)	<Fe-N> R_1 (Å)	<Fe-N> σ_1 (10^{-3}Å^{-2})	<Fe-Fe> R_2 (Å)	<Fe-Fe> σ_2 (10^{-3}Å^{-2})	<Fe-Ga> R_3 (Å)	<Fe-Ga> σ_3 (10^{-3}Å^{-2})	X (%)
300	5	1.99(2)	13(3)	—	—	3.19(1)	9(1)	100(10)
300	10	1.98(2)	9(2)	—	—	3.18(1)	7(1)	100(10)
250	10	1.99(2)	14(3)	—	—	3.18(1)	8(1)	100(10)
100	10	2.01(3)	11(4)	—	—	3.19(1)	9(1)	100(10)

(d) Averaged crystallographic distances are reported from literature. For GaN [282] the Ga–N and Ga–Ga distances are, respectively, 1.95 Å and 3.18 Å.

Structure	<Fe-N> (Å)	<Fe-Fe> (Å)	<Fe-Ga> (Å)
ϵ-Fe_3N [253]	1.927(1)	2.703(2)	—
α-Fe [279]	—	2.499/2.886	—
γ-Fe [254]	—	2.579	—

(e) Calculated LSD+U atomic distances.

Structure	<Fe-N> (Å)	<Fe-Fe> (Å)	<Fe-Ga> (Å)
ϵ-Fe_3N	1.89(1)	2.67(1)	—
Fe_{Ga}^{+1}	1.97(1)	—	3.23(1)
Fe_{Ga}^{0}	1.99(1)	—	3.22(1)
Fe_{Ga}^{-1}	2.05(1)	—	3.21(1)
Fe_{Td}	2.13(1)	—	2.21(1)
Fe_{Oh}	2.00(1)	—	2.42(1)

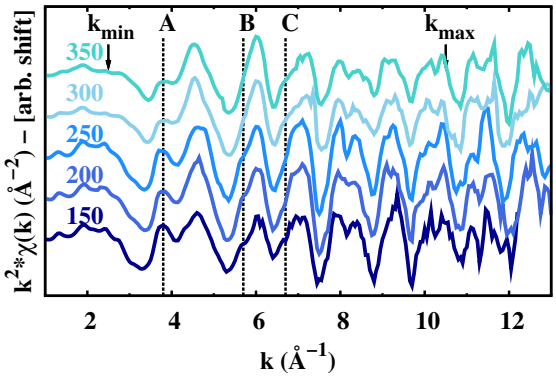

(a) k^2-weighted EXAFS signals (sccm, labels on spectra); vertical dashed lines highlight some parts of the spectra as described in the text; k_{min} and k_{max} delimit the Fourier-transformed part of the spectrum used in the fit.

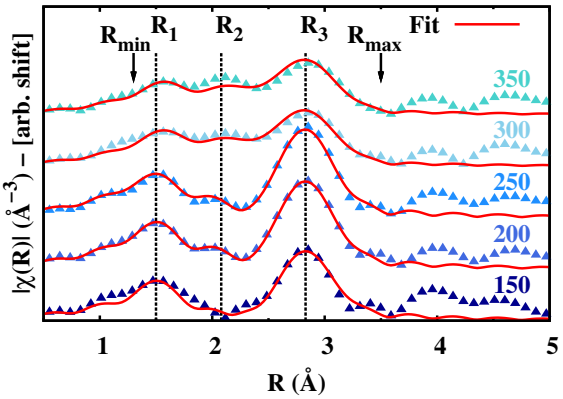

(b) Amplitude of the FT with relative fits. R_{min} and R_{max} delimit the fit region; R_1, R_2 and R_3 (with relative dashed vertical lines) indicate the main average distances found in the fit. The R scale has no phase correction, so that all the peaks appear shifted by ≈ 0.4 Å.

Figure 5.9: (Ga,Fe)N samples at TMGa = 5 sccm as a function of Cp_2Fe content.

shell distance in ϵ-Fe_3N. This suggests that Fe participates in the form of ϵ-Fe_3N. It is worth noting that in this compound the first shell corresponds to the Fe-N bonds exhibiting the same structural parameters as those specific to Fe_{Ga}. These results provide an independent confirmation of the previous results [250, 268], according to which Fe-rich nanocrystals were evidenced by neither HRTEM nor XRD and a paramagnetic response was observed by SQUID in samples with a low-Fe content, whereas samples with a high Fe content showed the presence of Fe-rich nanocrystals and a ferromagnetic behavior.

From a reduction in the amplitude of the dominating Fe-Ga signal relative to the pure substitutional specimen it is possible to estimate the relative content of Fe in the two phases (GaN and ϵ-Fe_3N), as shown in Table 5.1. From these data it is possible to infer that the flow-rate of 200 sccm Cp_2Fe corresponds to the onset of ϵ-Fe_3N precipitation, though the spinodal decomposition may begin at lower Fe contents.

It is worth to underline that no evidence is found for the α-Fe phase that should be witnessed by a double Fe-Fe shell at 2.499 and 2.886 Å [279]. Actually, this phase was shown to be present only at the surface of samples grown under particular conditions [268] and the overall Fe fraction in this phase presumably lies below the detection limit of EXAFS (about 15% in the present case).

In addition, the present data do not point to the presence of Fe in interstitial sites (comparing the distances reported in Tab. 5.1), at least in samples containing no secondary phases, for which the EXAFS signal is completely reproduced by a simple substitutional model. In the case of samples with precipitates, their contribution could *a priori* mask a signal coming from interstitials.

5.4.4 Growth rate

The second series studied permits to investigate how the Fe incorporation changes with the growth rate. In fact, by fixing the Fe content at 300 sccm (i.e., well above the previously established solubility limit), the TMGa flow-rate is increased from 5 to 12 sccm (Fig. 5.6). The

EXAFS spectra for this series are shown in Fig. 5.10(a) and their respective FTs in Fig. 5.10(b). From a qualitative point of view it is noted that for high growth rate values (TMGa $\geq$ 8 sccm) the EXAFS signal consists in two main frequencies (relative to the distances R_1 and R_3 in the FT) whereas in samples grown below that limit a further phase is detected and revealed by the peak R_2. Also in this case the quantitative analysis is conducted by reproducing data either with a substitutional model or with a combination of substitutional plus ϵ-Fe_3N phase. The results are reported in Table 5.1(b).

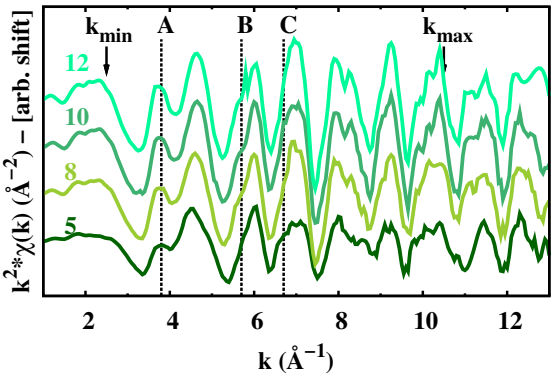

(a) k^2-weighted EXAFS signals (sccm, labels on spectra); k_{min} and k_{max} delimit the Fourier-tranformed part of the spectrum used in the fit.

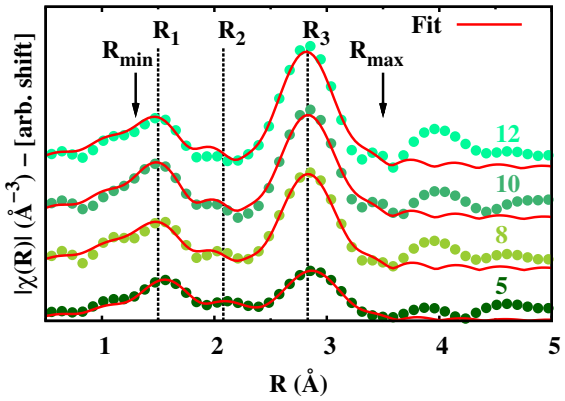

(b) Amplitude of the FT with relative fits. R_{min} and R_{max} delimit the fit region; R_1, R_2 and R_3 (with relative dashed vertical lines) indicate the main average distances found from the fit. The R scale has no phase correction, so that all the peaks appear shifted by $\approx$ 0.4 Å.

Figure 5.10: (Ga,Fe)N samples at Cp_2Fe = 300 sccm as a function of TMGa flow-rate.

The presence of ϵ-Fe_3N nanocrystals is found in the film grown at the lowest rate (TMGa = 5 sccm) while for faster growth rates the EXAFS spectra correspond exclusively to Fe_{Ga}, emphasizing the effectiveness of the fast growth in suppressing the formation of segregated phases. This observation is in qualitative agreement with the previous study [251], where HRTEM carried out for samples grown at low and high rates (although at a noticeably higher Fe content) revealed the formation of ϵ-Fe_3N only for slowly grown specimens. On the other hand, it is observed a limit of 15 sccm TMGa in the growth rate in order to keep high crystalline quality of the grown samples. Consequently this limit also the increasing of Fe solubility limit at 350 sccm Cp_2Fe.

5.4.5 Si co-doping

The effect of co-doping with Si is investigated in the samples series with variable TMGa and Cp_2Fe (Fig. 5.6). The EXAFS spectra as a function of both TMGa and Cp_2Fe are reported in Fig. 5.11(a) with their relative FTs in Fig. 5.11(b). By considering the same part of the spectra highlighted in the previous two series, it is visible in this case that no differences emerge between spectra[4] and all present a typical Fe_{Ga} signal. The Fe full inclusion in substitutional sites is confirmed by the quantitative analysis reported in Table 5.1(c).

[4]The spectrum (5,300) presents a peak at k = 11 $Å^{-1}$ that is unphysical. It is due to a distorsion by diffraction effects (as discussed in the experimental section) and a consequent problematic background removal.

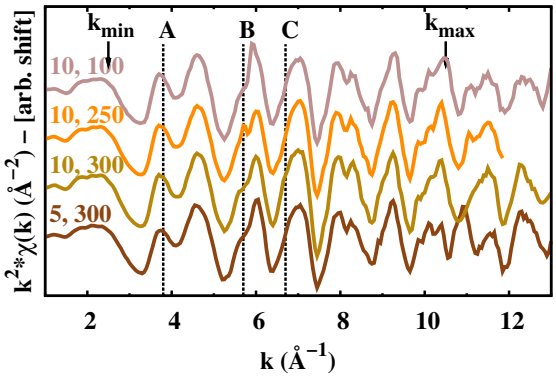

(a) k^2-weighted EXAFS signals (sccm, labels on spectra); k_{min} and k_{max} delimit the Fourier-tranformed part of the spectrum used in the fit.

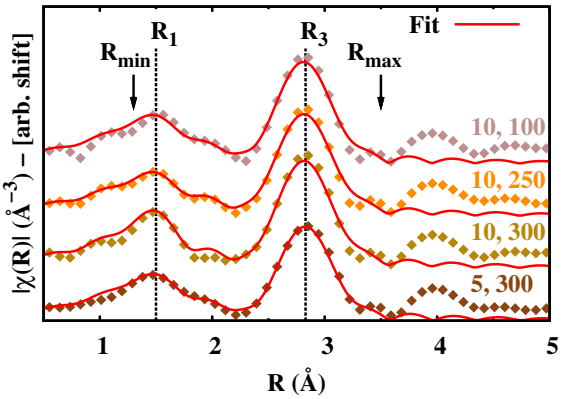

(b) Amplitude of the FT with relative fits. R_{min} and R_{max} delimit the fit region; R_1 and R_3 (with relative dashed vertical lines) indicate the main average distances. The R scale has no phase correction, so that all the peaks appear shifted by ≈ 0.4 Å.

Figure 5.11: (Ga,Fe)N:Si samples as a function of TMGa and Cp_2Fe.

5.4.6 Mg co-doping

Co-doping with Mg is also investigated. Good data for the quantitative analysis are collected only on two samples (Fig. 5.6). For the sample grown at low Cp_2Fe flow-rate (100 sccm) the substitutional character is observed, qualitatively and quantitatively in line with previous results from other samples series (Fig. 5.12(a)). On the other hand, for the sample grown at 300 sccm Cp_2Fe flow-rate an additional distance correspondig to Fe-Fe coordination is found at 2.57(1) Å (Fig. 5.12(b)). Comparing crystallographic distances from literature reported in Tab. 5.1(d), this distance is closer to fcc γ-Fe [254] than the common bcc α-Fe [279]. In addition, in order to better resolve this additional distance and discriminate the precipitated phase, the fit is expanded to upper coordination shells in order to include the multiple scattering paths and next neighbours coordinations. The result of this expansion is the significantly improvement in the fit quality with the inclusion of the multiple-scattering paths from the fcc structure. These results are in line with the XRD study [252] but both are preliminar and need further investigations.

5.4.7 Charge state

In order to get information on the charge state of Fe in the studied samples, the XANES region is analyzed. The amplitude and position of the peaks due to the partially forbidden $1s \rightarrow 3d$ transitions appearing in the pre-edge region of the absorption coefficient were widely investigated in literature as a function of the local symmetry (tetrahedral or octahedral) and valence state (Fe^{3+} or Fe^{2+}) in Fe compounds [284, 285]. The general finding is that tetrahedrally coordinated compounds exhibit a single pre-edge peak with an amplitude above 10 % of the total edge jump and a position changing with the valence state from ≈ 7112 eV in the case of Fe^{2+} to ≈ 7114 eV in the case of Fe^{3+} [284].

Here is presented a systematic investigation on the previously described sample series. Quantitative results are reported in Tab. 5.2 and two representative fits are plotted in Fig. 5.13; undoped samples exhibit only a single peak of average amplitude 13 ± 1 % and positon

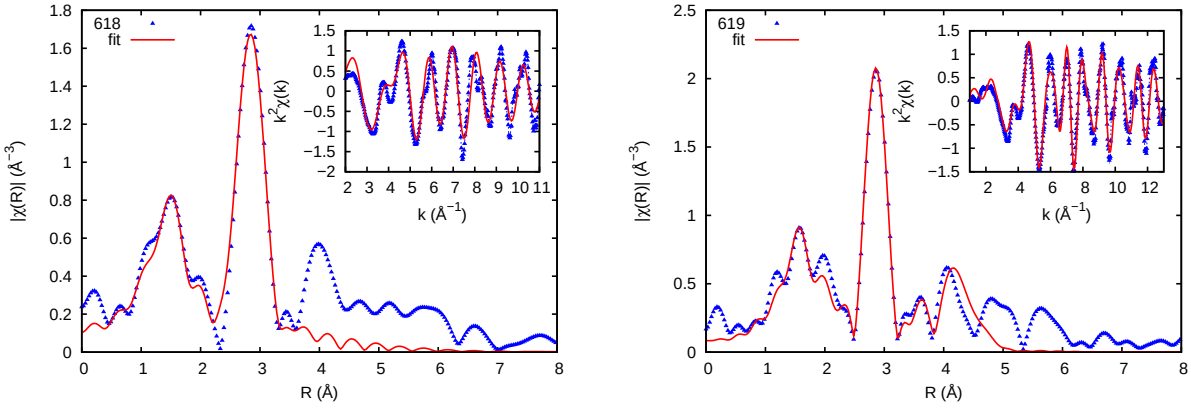

(a) Sample grown at Cp_2Fe = 100 sccm.

(b) Sample grown at Cp_2Fe = 300 sccm.

Figure 5.12: Results of the EXAFS analysis for (Ga,Fe)N:Mg samples grown at TMGa = 12 sccm. The main plot shows FTs (without phase correction) of the data and relative fit; the inset report k^2-weighted $\chi(k)$ EXAFS oscillations with relative fit.

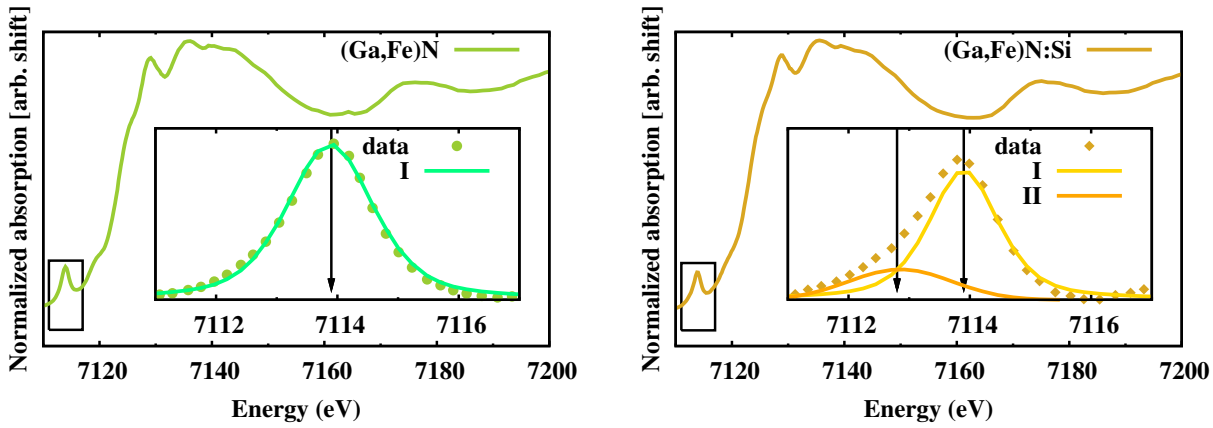

(a) (Ga,Fe)N

(b) (Ga,Fe)N:Si

Figure 5.13: Normalized XANES spectra with the pre-peak reported in the inset after baseline subtraction and the fitted functions with centroids indicated by arrows.

7113.9 ± 0.1 eV whereas the Si-doped samples present the same peak at 7113.9 ± 0.1 eV with a slightly lower average amplitude of 10 ± 1 % and a further peak at 7112.8 ± 0.1 eV of amplitude 3 ± 1 %. These data are explained by the presence of Fe^{3+} ions in the first series and a co-existence of Fe^{3+} and Fe^{2+} ions in the second case. The appearance of double peaks in the pre-edge region in case of co-existence of chemical species at different valence states was already pointed out in literature [286, 285] and in the present case evidences the partial reduction of the metal ions ($Fe^{3+} \rightarrow Fe^{2+}$) upon Si addition. This result corroborates the conclusions derived from previous electron paramagnetic resonance studies [250, 46] and from the present DFT calculation for (Ga,Fe)N. Co-doping with Si results in the appearance of an additional peak in the pre-edge region at about 7112.8 eV, which is attributed to Fe^{2+} ions in a tetrahedral environment. The fraction of the total Fe content in this particular valence state is below 20 %, the majority of Fe impurities still remaining in the Fe^{3+} configuration. This explains why it is not observed in the EXAFS data (and, in particular, in the values of the Fe-N bond length) any significant deviation when comparing the samples containing no Si impurities with the Si-

Table 5.2: Quantitative results of the XANES analysis.

Cp_2Fe (sccm)	TMGa (sccm)	peak I center (eV)	peak I height (%)	peak II center (eV)	peak II height (%)
(Ga,Fe)N					
300	5	7113.8(1)	8(1)	—	—
300	8	7113.9(1)	12(1)	—	—
300	10	7113.9(1)	14(1)	—	—
300	12	7113.9(1)	17(1)	—	—
(Ga,Fe)N:Si					
300	5	7113.9(1)	10(1)	7112.9(1)	2(1)
300	10	7113.9(1)	11(1)	7112.9(1)	3(1)
250	10	7113.9(1)	11(1)	7112.7(1)	3(1)
100	10	7113.8(1)	9(1)	7112.5(1)	4(1)

doped ones. However, the co-deposition of Si hampers the aggregation of Fe and, thus, shifts the solubility limit to higher Fe concentrations. It is worth noting that the partial reduction ($\approx$ 10 %) of Fe^{3+} to Fe^{2+} confirms the concentrations results for Si being $\approx$ 10 % of the Fe content.

The above interpretation of the XANES findings is consistent with the *ab initio* results, implying that the Fe^{2+}/Fe^{3+} state, i.e. the $\epsilon^{0/-1}$ level, resides in the GaN gap 2.25 eV above the top of the valence band. Thus, this state should be occupied by electrons provided by shallow donors, such as Si. This conclusion is further supported by the computed formation energy that results to be for the Fe^{3+} configuration by 1.35 eV higher than for the Fe^{2+} case.

5.4.8 Linear dichroism and dislocations

Measurements with the polarization vector perpendicular (90°) and parallel (0°) to the sample surface are conducted on samples series grown at the highest growth rate (15 sccm TMGa) and with different buffer layers (the standard GaN and also AlGaN). In these configurations, changing the polarization vector respect to the wurtzite *c*-axis permits to exploit the polarization dependence of XAFS (Sec. 2.2.1). The difference between 90° and 0° spectra gives the linear dichroic signal, that is, the information on the simmetry of the probed atomic site in the case of non cubic incorporation. As is visible from the insets of Fig. 5.14 in both samples types (boundary of the studied conditions: high Fe content on GaN and low Fe content on AlGaN) the linear dichroic signal is enhanced, confirming the hexagonal inclusion, and no differences are visible between them. On the other hand, if the full EXAFS spectrum is analyzed, considerable differences appear in the Fourier transformed spectra (main plot in Fig. 5.14). The twofold importance of this observation is treated separately in the next paragraphs.

The fact that the linear dichroic signal is the same in both cases means that this kind of measurement is sensitive only to the simmetry and in the case of coexistence of multi-phases it will not discriminate between them. This means that in order to avoid misleading interpretations on the structure of these systems is crucial to take into consideration not only the dichroism but also the structural information contained in single spectra.

The structural analysis for sample shown in Fig. 5.14(a) result in a Fe_{Ga} inclusion even for high Fe content (350 sccm Cp_2Fe); this is in line with results presented in the previous sections as the crucial role given by the high growth rate. On the other hand, samples grown on

AlGaN buffer present, in addition to the Fe_{Ga} phase, an intermediate distance as shown in the FT spectrum of Fig. 5.14(b). From the fit, this results in a Fe-Ga coordination at a distance of 2.48(1) Å that, comparing with the calculated average distances reported in Tab. 5.1(e), is possible to identify as the promotion of Fe_{Oh} defects by buffer dislocations.

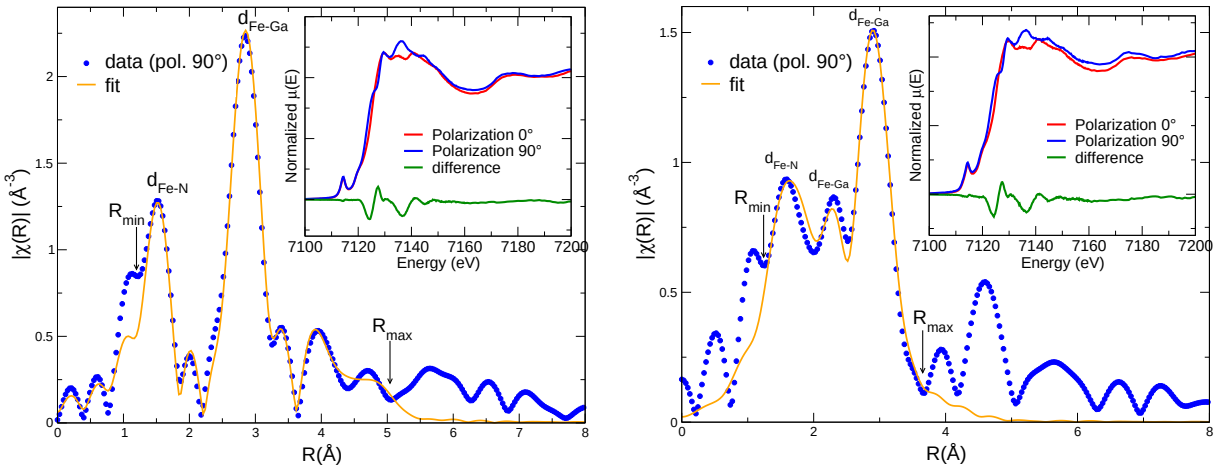

(a) (Ga,Fe)N on GaN buffer at 350 sccm Cp_2Fe and 15 sccm TMGa.

(b) (Ga,Fe)N on (Ga,Al)N buffer at 50 sccm Cp_2Fe and 15 sccm TMGa.

Figure 5.14: Fourier transform (without phase correction) of data/fits collected in double polarization cofiguration (90°, 0°) with relative normalized XANES spectra (inset) and the linear dichroic signal (difference).

5.5 Summary

The present XAFS results, together with previous HRTEM and synchrotron XRD, show how the Fe incorporation can be efficiently controlled by Fe flow, growth rate, and co-doping with Si. In particular, the aggregation of Fe cations can be minimized by increasing the growth rate and by co-doping with Si, shifting the solubility limit towards higher Fe content at given growth conditions. In addition, is shown that XAFS can give detailed informations about charge state and on the description of the local structure in case of dislocations. This means that the complementarity of XAFS with TEM and XRD is an important subject in the characterization of this system at the nano-scale.

Mn dans le Ge

Résumé du Chapitre 6

Dans ce chapitre il est détaillée une étude sur le Ge:Mn, un matériau qui, pour sa compatibilité directe avec la technologie existante du Si, a reçu beaucoup d'attention depuis les travaux de Park *et al.* [287] où il a été montré la faisabilité d'un système DMS. Au même temps, la dilution du Mn dans le Ge reste questionnable à cause d'une limite de solubilité extrêmement faible (estimé à 10^{15} cm^{-3} [288], c'est à dire une pourcentage de Mn $\approx 2\times10^{-6}$ %). Et pour cette raison, en utilisant des caractérisations structurales détaillés, on observe que le Mn a la tendance à précipiter sous forme de clusters de Ge_3Mn_5 (la phase plus stable) [289] ou bien s'accumuler sous forme de décomposition spinodale en conservant la structure cristalline du Ge. Ceci est le cas des échantillons étudiés dans ce chapitre, où la décomposition est sous forme de nano-colonnes riches en Mn qui, en certains cas, présentent un ferromagnétisme à haute temperature [290, 291] dont l'origine structurelle n'est pas encore bien saisie. L'étude XAFS permet donc de compléter les informations obtenues par HRTEM et XRD (Sec. 6.3) d'un point de vue de la structure locale.

Les échantillons étudiés sont produit par LT-MBE sur Ge(001) suivant une procédure bien établie qui assure une bonne reproductibilité [174]. Les principaux paramètres d'investigation sont la concentration en Mn, x, et la temperature de croissance, T_g. La concentration standard est x = 6 % et la gamme de temperatures où les nano-colonnes sont observées est autour de 130 °C avec l'apparition de clusters de Ge_3Mn_5 pour $T_g \geq 145$ °C. La structure locale de ces échantillons se présente assez desordonnée avec l'absence de signal visible pour des couches de coordination a longue distance comme, par exemple, dans GaMnAs. Pour compenser ce manque d'information il est nécessaire de comparer avec des échantillons de référence comme une couche mince de Ge_3Mn_5 monocristalline épitaxié sur Ge(111) et un échantillon à très basse concentration, x = 0.1 %. Grâce à l'analise de ces deux références donnée en Sec.6.5.1 pour Ge_3Mn_5 et Sec. 6.5.2 pour GeMn(0.1%), un modèle de fit qui permet d'analyser les donnés expérimentales relatives aux nano-colonnes est construit (Sec. 6.5.3). En effet, les spectres EXAFS de la Fig. 6.9 montrent une évolution du signal en fonction de x et T_g (pics *a*–*d*) de GeMn(0.1%) à Ge_3Mn_5.

L'analise quantitative reporté en Tab. 6.3 montre que, en aucun cas, les signaux EXAFS sont reproduit avec un modèle de Mn substitutionel en Ge (représenté par la distance/coordination d_2) mais d'autres contributions nécessitent d'être ajoutés. En particulier, pour les échantillons à basse concentration et basse T_g il est présent une contribution d_5 à $\approx$ 3.58 Å qui ressemble

à du Mn dans le site interstitiel hexagonal avec une forte contraction par rapport à un pur défaut en Ge ($\approx$ 3 %). D'autre part, pour les échantillons à plus haute concentrations et T_g les contributions caractéristiques du Ge_3Mn_5 (d_3 et d_4) sont retrouvés, mais avec des nombres de coordination bien plus faibles, qui augmentent proportionellement à T_g et représentent une évolution vers ceux du Ge_3Mn_5.

Un modèle qui explique ces résultats est donné dans la dernière partie du chapitre. Depuis l'analyse de la structure cristalline du Ge_3Mn_5 il se trouve que le Mn se situe dans deux positions cristallographiques non équivalentes, Mn_1 et Mn_2, et forme avec le Ge des tétrahèdres avec des distances caractéristiques (Fig. 6.5(a)). Donc une comparaison avec les résultats expérimentaux permet d'affirmer que seulement le tétrahèdre qui contient Mn_2 est présent dans les nano-colonnes. En plus, pour expliquer l'incorporation de cette structure dans le Ge, est reporté en Fig. 6.11 une possible solution en fonction d'un ensemble de défauts élémentaires dans le Ge (interstitiels plus substitutionel), qui a été aussi proposé par un autre groupe [292] et reste partiellement compatible avec les résultats EXAFS.

6

Mn in Ge

In this chapter are presented the results on Mn-rich (>30 at. %) nanocolumns that spontaneously self-assemble during the layer-by-layer growth of thin (Ge,Mn) films. The work is realized in collaboration with the Commissariat à l'Énergie Atomique *in Grenoble (CEA-Grenoble). Despite the high Mn concentration, nanocolumns still possess a diamond-like crystalline structure as derived from X-ray diffraction or high resolution transmission electron microscopy. They exhibit ferromagnetism up to 400 K. However they are metastable nano-objects in the sense that annealing the samples leads to Ge_3Mn_5 precipitates which is the most stable (Ge,Mn) alloy. Nanocolumns can be stabilized in the Ge matrix using low temperature molecular beam epitaxy (LT-MBE) which is an out-of-equilibrium growth technique. In particular here the issue of the local environment of Mn in the nanocolumns is studied in detail by means of XAFS spectroscopy.*

6.1 Introduction

The first study on the Ge-Mn phase equilibria was conducted by Zwicker *et al.* in the early 1949 [293]. Later on, followed extensive investigations establishing the relative phase diagram [294]. The interest in (Ge,Mn) as a promising high-T_C ferromagnetic semiconductor compatible with the mainstream silicon technology essentially started in 2002 with the publication by Park *et al.* [287] claiming the fabrication of a GeMn DMS with T_C of 116 K and the possibility to electrically control the ferromagnetic properties. Since then, many publications investigated different aspects of the GeMn system employing different fabrication techniques (extended bibliography is reported in Refs. [174, 292]).

Since the solubility limit of Mn in Ge is very low (estimated to 10^{15} cm^{-3} [288], that is a Mn atomic percent of $\approx 2\times10^{-6}$ %), orders of magnitude below the typical Mn concentrations employed in the fabrication of (Ge,Mn) magnetic semiconductors, the manganese dilution in a germanium crystal remains highly questionable and in most experiments (Ge,Mn) films contain either nanoscale Mn-rich regions or secondary phase precipitates like Ge_3Mn_5. This means that it is crucial to adopt in the study of this system accurate nano-structural characterization techniques in order to control the deposition parameters employed in the out-of-equilibrium deposition techniques. The object of the present study are the precipitates free LT-MBE (Ge,Mn) epilayers with Mn concentration of the order of several percent [290, 291, 295]. Up to now, considering only LT-MBE grown and uniform doped samples, two other research groups have reported on similar materials: from Germany [296, 297, 298, 299] and the USA [300, 301, 302, 303].

Seen that Ge_3Mn_5 metallic inclusions prevent any spintronics applications [304], the intermediate regime, leading to the formation of transition metal rich regions, seems to be one possible means to raise, at least locally, the Curie temperature. This kind of regions were already observed by other groups in other systems like (Zn,Cr)Te [71], (Ga,Mn)N [305] or (Ga,Fe)N [261] (as discussed in Chap. 5). In (Ge,Mn) these metal rich regions have the form of nanocolumns (NCs) and a possible explanation for their formation is given by Zeng *et al.* [303]: while Mn atoms deposited at 150 K on a Ge(001) surface are trapped in subsurface interstitial sites, Mn monomers deposited at room temperature diffuse at the germanium surface to nucleate Mn-rich clusters leading to nanocolumns when increasing the film thickness. In addition, in (Zn,Cr)Te and (Ga,Mn)N experimental observations can be qualitatively reproduced by numerical simulations in the spinodal decomposition framework [84] and also this possibility is taken into account for the current work.

Seen that this kind of chemical decomposition do not present long range order, the laboratory XRD see only the diamond Ge or the Ge_3Mn_5 precipitates, while synchrotron XRD gives additional information from the analysis of the diffuse scattering [299]. On the other hand, XAFS local structure information results appropriate in determining the structure of precipitate-free (Ge,Mn) alloys; in fact this technique has been successfully employed for ion implanted [306, 307] and digital layer alloys [308].

6.2 Growth

$Ge_{1-x}Mn_x$ films are grown using solid sources MBE by co-depositing Ge and Mn evaporated from standard Knudsen effusion cells on Ge(001) substrates. The growth procedure is well established and leads to good reproducibility [174]: starting from the *epi-ready* Ge substrate, it is introduced in the MBE chamber and the oxide surface layer thermally removed by heating at 400 °C; a Ge buffer layer ($\approx$ 40 nm) is then deposited and rapidly annealed (5 min at 400 °C) to obtain a good 2×1 reconstructed 2D surface that is the Ge(001) starting point for the doped layer. The (Ge,Mn) layer is 80 nm-thick and grown at different temperatures (T_g) ranging from 80 °C to 200 °C. In fact, below 80 °C samples are completely amorphous and above 200 °C precipitates are systematically produced. It should be noted that a precise absolute substrate temperature determination during the growth is not straightforward for this system since is not possible to use optical pyrometers as in the case of GaAs [309]. The Mn concentration can vary from 0.1% in the most diluted case (used as reference compound) up to $>$ 20 %; the majority of studied samples is grown at nominal 6% Mn. The growth rate is kept constant at $\approx$ 1 nm/min. The layer by layer growth mode is constantly observed by RHEED in order to monitor the growth quality.

In addition, a Ge_3Mn_5 monocrystalline thin film is also produced in order to use it as a model compound for the analysis. Ge_3Mn_5 has an hexagonal structure [310] and for epitaxial growth on the diamond structure is normal practice to use the (111) face. Once obtained a Ge(111) 2D surface reconstructed 8×2 [311], the Ge_3Mn_5 is formed by annealing a deposited Mn layer [312], due to the strong Ge and Mn interdiffusion. In this way a crystalline layer with *c* axis parallel to Ge [111] direction is obtained.

6.3 Structural characterizations

6.3.1 TEM

A detailed (HR)TEM investigation, assisted by chemical mapping (EFTEM and EELS), on the studied samples is given in Ref. [174]. Sample preparation for TEM measurements in cross section geometry (parallel to the film) is conducted by standard mechanical polishing, followed by Ar^+ ion milling at 3 KV and for plane view (perpendicular to the film) by a chemical procedure specific for Ge substrates, that is, using a solution of H_3PO_4 and H_2O_2.

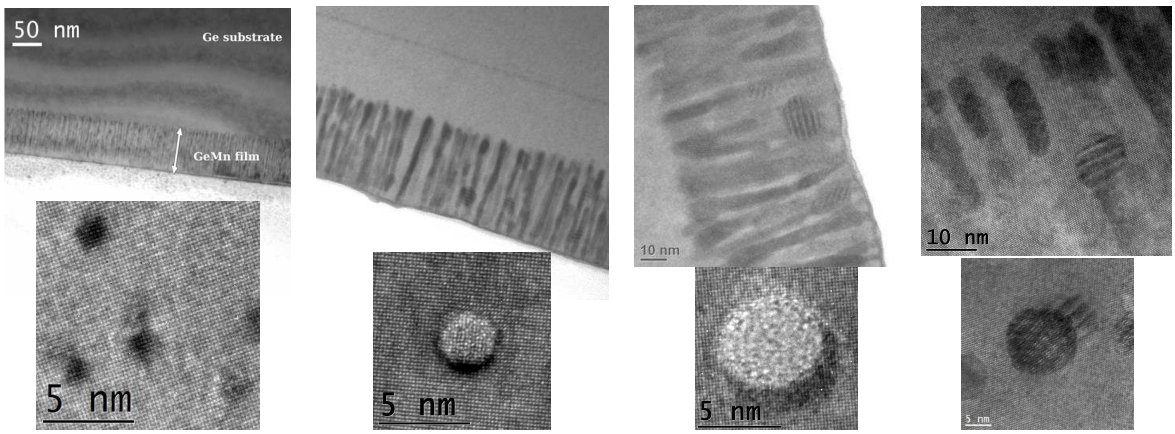

(a) < 120 °C. (b) 120 – 145 °C. (c) 145 – 180 °C. (d) > 180 °C.

Figure 6.1: The GeMn nanocolums phase diagram as function of T_g as seen by (HR)TEM. Cross-sectional images in the upper panels and the plane view in the lower panels. Images adapted from [174].

The main results are summarized in Fig. 6.1, giving the GeMn nanocolums phase diagram as a function of T_g. In fact, it is observed that this parameter is crucial for the formation and the evolution of the NCs. On the other hand, the Mn concentration mostly produces an increase in the NCs density and size. For $T_g < 120$ °C (Fig. 6.1(a)) low-T_C NCs are present, with narrow size distribution. Increasing T_g up to 145 °C (Fig. 6.1(b)) results in a wider size distribution and a diameter increase of the NCs and start the formation of Ge_3Mn_5 clusters. In particular, in a small window around 130 °C, high-T_C ferromagnetic NCs are present. With T_g going up to 180 °C (Fig. 6.1(c)), the columns become large and amorphous and the Ge_3Mn_5 precipitates mainly contribute to the magnetic properties. Finally, for $T_g > 180$ °C (Fig. 6.1(d)) the NCs are replaced by Ge_3Mn_5 clusters and the Moiré fringes relative to this phase are clearly visible.

6.3.2 Synchrotron GIXRD

In addition to the conventional laboratory XRD characterization, synchrotron XRD in grazing incidence geometry (GIXRD) is conducted on these samples in collaboration with the *Université Joseph Fourier* and *CEA-Grenoble*. The experiments are conducted at the ESRF on the beamlines ID01 and BM32. Although have been conducted additional measurements of reflectivity, grazing incidence small-angle x-ray scattering and anomalous diffraction at the Mn K-edge, only GIXRD is briefly reported here due to the fact that a conclusive analysis of the collected information is still lacking.

GIXRD measurements are conducted at an incident energy of 11 KeV and at grazing angle of 0.24°, that is slightly above the critical angle giving information only from the GeMn thin

film. In order to determine the crystal structure of the GeMn columns, maps of the $\{hk0\}$ planes around Ge (400) and (220) peaks are collected as shown in Fig. 6.2. For samples grown at low temperature (130 °C) that present ferromagnetic nanocolumns as observed by TEM, several diffuse streaks are visible with peaks around (310), (2.65 0.5 0) and (1.4 1.4 0) as shown in Fig. 6.2(a). On the other hand, for deposition temperatures greater than 180 °C additional peaks in the reciprocal space appear and their position can be indexed with the Ge_3Mn_5 peaks and the 2×1 surface reconstruction as seen by RHEED (Fig. 6.2(b)).

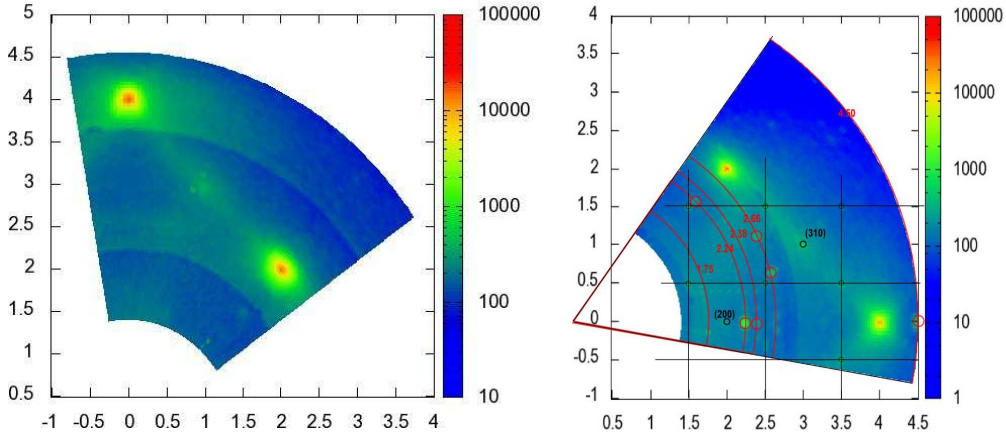

(a) No secondary phases are visible below 150 °C.

(b) Additional diffraction peaks appear above 180 °C due to Ge_3Mn_5 precipitates and sample surface reconstruction (highlighted).

Figure 6.2: GIXRD maps of $\{hk0\}$ planes for two $Ge_{0.94}Mn_{0.06}$ samples. Reproduced from [174].

6.4 Magnetic characterization

The study of the magnetic properties for GeMn system is not an easy task due to the fact that the principal magnetic characterization tool, the SQUID magnetometer, is sensitive to a global magnetic signal coming from the whole sample and the separation of the magnetic components due to the presence of different nano-objects is done during the data analysis using a modelization process based on data coming from model compounds, as the Ge_3Mn_5 thin film, the samples at low Mn content and complementary experimental and theoretical investigations. Following the detailed analysis given in Refs. [290, 291, 174] it is possible to summarize the magnetic properties to the following classes.

Diluted Mn The signal coming from Mn atoms isolated in the Ge matrix is always present and it consists in a paramagnetic contribution that is enhanced and dominates at low temperature (< 30 K). The magnetic moment follow a Brillouin law and, supposing the Mn in the matrix occupying specific sites (e.g. for substitutional Mn in Ge the theoretical m_0 is 3 μ_B [287, 313, 314]), it is possible to determine the diluted Mn concentration.

Ge_3Mn_5 precipitates These precipitates represent the main signal for $T_g > 180$ °C and coexist with nanocolumns for 130 °C $< T_g <$ 180 °C. They are identified comparing experimental data with the Ge_3Mn_5/Ge(111) thin film. This last one has a T_C of 295 K and a magnetization of

2.4 μ_B/Mn, in line with literature results reported for the bulk phase [315]. In addition, using the *zero field cooled - field cooled* (ZFC-FC) measurements it is possible to detect that Ge_3Mn_5 precipitates present superparamagnetism [316, 317] due to their nanometric size. Finally, a perpendicular anisotropy induced by the hexagonal crystal structure of Ge_3Mn_5 clusters is found, confirming that the *c* axis is parallel to Ge(001).

Low T_C nanocolumns These nanocolumns are ferromagnetic with $T_C < 200$ K and, due to their small size, superparamagnetic. Using a Langevin function it is possible to fit their magnetic moment [318] and find that from a magnetic point of view they correspond to a smaller size than that observed by TEM. On the other hand, this model suppose a weak magnetic interaction between the nanostructures but in the present case an antiferromagnetic coupling between nanocolumns is found [174], so it is difficult to establish the magnetic moment in this case. In addition, there is no evidence of magnetic anisotropy, explained as a compensation between shape anisotropy and magneto-elastic anisotropy.

High T_C nanocolumns This is the most interesting GeMn phase for spintronics applications. For a given precise $T_g = 130$ °C and Mn concentration of 6 %, ferromagnetic nanocolums are observed; they present a Curie temperature $T_C > 400$ K [290] and high magnetic moment of 4.9 μ_B/Mn. Although they present a columnar structure and small size, no superparamagnetic behavior is found in the studied temperature range. The magnetic anisotropy is slightly in-plane (competition between magneto-elastic, and shape anisotropy).

6.5 Local structure

The investigation of the local structure in this system is quite difficult due to the fact that from the XAFS local point of view, it appears as a highly disordered compound, like an amorphous material with the presence in the Fourier transform (FT) of a main broad peak and additional peaks of low intensity. This dramatically reduces the information content in the EXAFS spectra and the whole data analysis is conducted constantly comparing the proposed theoretical models with the experimental information coming from a detailed study of the reference compounds: Mn at very low concentration in Ge and Ge_3Mn_5/Ge(111) thin film.

In addition, *ab initio* calculations in the framework of DFT (LSDA approximation) on the Mn defects in Ge are conducted in collaboration with the L_{Sim} laboratory of CEA-Grenoble and are tested on the experimental data. Unfortunately, at the current status, the distances found in relaxed structures are not compatible with the experiment, meaning that the underlying approximations systematically affect the calculations. For this reason, it is chosen to build the fits models for the XAFS analysis on the crystallographic structures and adjusting the models in a self-consistent way in order to reach a description of the local structure independent of the DFT calculations, leaving the theoretical justification for further investigations.

Thus, working on the whole series of the EXAFS collected data, it is possible to compensate the lack of information on the single spectrum. In fact, it is found that the fits with a single coordination shell can be significantly improved adding other coordination shells inside the main FT peak and fitting some of the small additional FT peaks permits to partially reproduce the higher frequencies in the EXAFS spectrum that are responsible of the main differences between spectra of the studied series. For this reason the following models are built going beyond the first coordination shell considering these small contributions to the spectra as the key points in the evolution of the observed local structure as a function of the deposition

parameters. In particular, the present study is an extension of the previous results reported in Ref. [319] and is conducted with the leading idea of finding a model that could link elementary defects in Ge with the spinodal decomposition of Mn-rich nano-columns and the nucleation of Ge_3Mn_5.

All the XAFS measurements at the Mn-K edge (6539 eV) are carried out at the "GILDA" beamline in fluorescence detection at standard geometry (45° incidence angle) and liquid nitrogen temperature, using the monochromator equipped with double Si[111] crystals. The common details about the data collection and the analysis are, respectively, detailed in Sec. 2.3.1 and Sec. 2.4 and only specific information for this system are reported in the following.

6.5.1 Ge_3Mn_5 thin film

An important reference sample is the monocrystalline Ge_3Mn_5 thin film grown on Ge(111). The film has a thickness of ≈ 10 nm and is grown by MBE at 350 °C. Seen that Ge_3Mn_5 has hexagonal structure, XAFS spectra are collected at different incidence angles in order to exploit the dichroic effect due to the linear polarization of the beam (Fig. 6.3). In particular, for the EXAFS the main effect is a global reduction of the amplitude term while for XANES the effect is more important. In addition, due to the reduced thickness of the layer, the effects due to self-absorption can be ruled out; this is tested using the Booth's algorithm [320] for self-absorption correction of the EXAFS spectra.

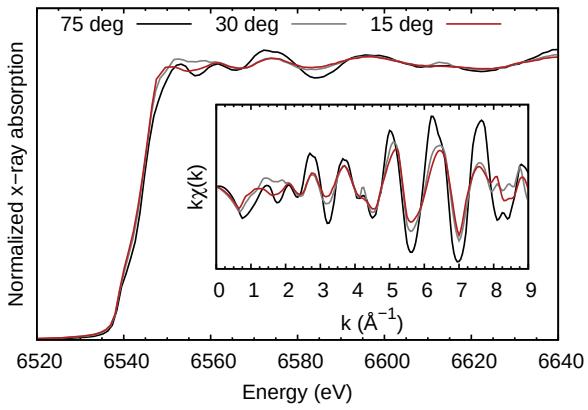

Figure 6.3: XANES and EXAFS spectra changing the incident angle between sample surface and the polarized beam.

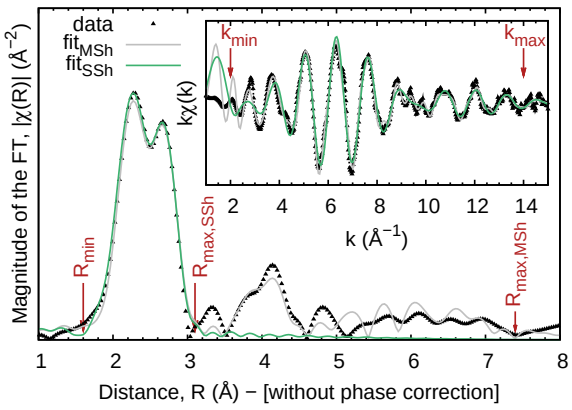

Figure 6.4: EXAFS fits for the Ge_3Mn_5 thin film in R and k spaces using two models: the multi-shell (MSh) and single shell (SSh) fit. Data collected at 45 °.

Keeping in mind the polarization effect, the EXAFS analysis is conducted on the measurement at 45°, due to the fact that all samples are probed in this geometry and the polarization in the calculation of theoretical paths used in the analysis is neglected, even if this is not its magic angle [321]. The crystallographic structure of Ge_3Mn_5 is the space group $P6_3/mcm$ (n. 193), a = b = 7.184(6) c = 5.053(4) [289]. In this structure Mn occupies two non equivalent sites, in the Wyckoff positions 4*d* (Mn_1) and 6*g* (Mn_2); a graphical representation of the unit cell and the two configurations are shown in Fig. 6.5 with the highlighted distances up to 3.1 Å reported in Tab. 6.1. Considering a configuration average of both sites and including all single scattering and multiple scattering paths up to $R_{max,MSh}$ = 7.4 Å a multi-shell model (MSh) is built for the analysis. The results are shown in Fig. 6.4. The fit uses only few variables and is kept

Table 6.1: Atomic environment around Mn_1 (40 % of the sites) and Mn_2 (60 % of the sites) up to 3.1 Å using crystallographic distances [289] grouped following the model SSh. In addition, it is worth noting that for this structure additional distances in the range [3.1–4.1] Å are not present.

	Mn_1		Mn_2		Average	
	coordination	distance (Å)	coordination	distance (Å)	coordination	distance (Å)
d_2	2 Mn_1	2.526	2 Ge	2.488	4.4 Ge&Mn	2.507
	6 Ge	2.538				
d_3			1 Ge	2.610	1.8 Ge	2.715
			2 Ge	2.768		
d_4	6 Mn_2	3.065	2 Mn_2	2.983	8.4 Mn	3.053
			4 Mn_2	3.058		
			4 Mn_1	3.065		

simple in order to obtain accurate results on long-distance structure; the global parameters used for all scattering paths are: a scaling factor, ΔR, for the distances, resulting in a 2.0(1) % contraction, the S_0^2 amplitude reduction term, resulting of 0.57(2) due to polarization effects, the edge shift ΔE_0 = 7(1) eV (considering that E_0 is chosen at the first derivative peak present at 6539.0(5) eV) and the DWFs following a correlated Debye model [243], where the experimental liquid nitrogen temperature and the value of 396 K for the Debye temperature [322] are setted.

On the other hand, a second theoretical model (SSh) for this compound is necessary in order to study the local structure at shorter distance ($R_{max,SSh}$ = 3.1 Å) and apply these results in the study of GeMn nanocolums. This model is built on single scattering paths grouped in three characteristic distances, d_2, d_3 and d_4 as shown in Tab. 6.1 and independently fitted with their coordination number after fixing the common S_0^2 factor. The results of this fit are also plotted in Fig. 6.4 and quantitatively reported in Tab. 6.3 in order to compare with the following models; the distances do not differ from the previous model in the limit of the error bars, while the model is an useful simplification for the Ge_3Mn_5 alloy in order to study the case where the disorder limits the information content in the spectra.

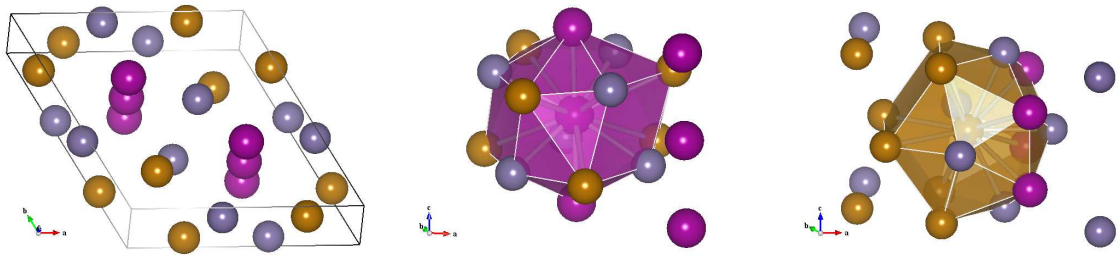

(a) Unit cell. (b) Mn_1 at the center. (c) Mn_2 at the center.

Figure 6.5: Crystallographic structure of Ge_3Mn_5: ball-and-stick model where Ge, Mn_1 and Mn_2 atoms are reported, respectively, in dark blue, violet and brown. The polyhedra contains the bonds to Mn central atom up to 3.1 Å.

6.5.2 Mn "diluted" in Ge

In order to have a reference sample for Mn at low concentration in Ge, a sample with 0.1 % Mn content - GeMn(0.1%) in the following - the minimum concentration reachable in the present

Table 6.2: Ge distances and coordination numbers from the Mn absorbing atom (up to 5 Å) in different sites, considering the crystallographic structure given in Ref. [242]. The distances are grouped following the experimental results given in Tab. 6.3.

Site	Distance (Å) / Coordination											
	d_1		d_2		d_3		d_5		d_6		d_7	
Mn_S	–	–	2.45	4	–	–	–	–	4.00	12	4.69	12
Mn_T	–	–	2.45	4	2.83	6	–	–	–	–	4.69	12
Mn_H	2.35	6	–	–	–	–	3.67	8	–	–	4.64	6

growth conditions, is grown at relatively low temperature (125 °C) in order to avoid additional phases. In fact, even at this low concentration, a sample grown at high temperature (350 °C) presents a full Ge_3Mn_5 signal. Established that the low temperature is the required condition, the first observation coming from the EXAFS data is that, already at this concentration level, no signal is visible from the second and third coordination shells of the tetrahedral structure as instead present in (Ga,Mn)As (e.g. [230] or Chap. 4). This is a typical effect of local structural disorder as encountered in amorphous Ge [323] and has been observed also for Mn implanted in Si [324] and Ge [306, 308].

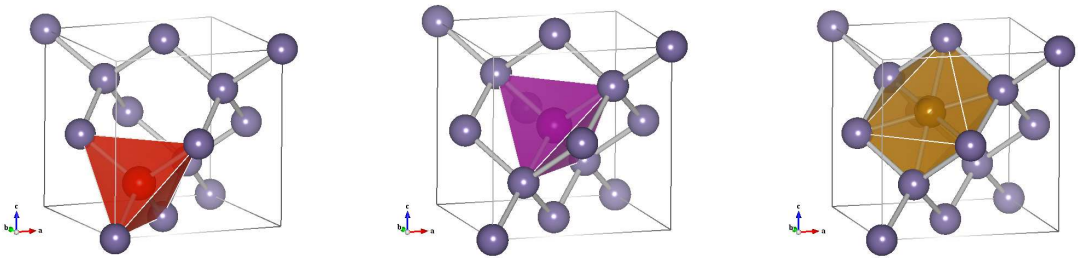

(a) Substitutional, Mn_S. (b) Tetrahedral interstitial, Mn_T. (c) Hexagonal interstitial, Mn_H.

Figure 6.6: Ball-and-stick model for the native defects in diamond Ge (dark blue) occupied by Mn, with the polyhedra containing the nearest neighbors distances.

The theoretical model used for the fit is built considering the native defects in diamond Ge (Fig. 6.6): substitutional (Mn_S), tetrahedral interstitial (Mn_T) and hexagonal interstitial (Mn_H). Taking the diamond space group, $Fd\bar{3}m$ (n. 227), and, putting Ge in the site 8*a* (0,0,0), the positions are, respectively, at site 8*a* (0, 0, 0), 8*b* (1/2, 1/2, 1/2) and 16*d* (5/8, 5/8, 5/8), where, for each structure, one Mn is inserted in the host lattice and considered as the absorbing atom for the theoretical paths generation. The resulting environments using a lattice parameter a = 5.65675(1) [242] are reported in Tab. 6.2, where distance labels are given in order to follow the experimental findings reported in the following.

From the fit (Fig. 6.7) it is found that the main distance is d_2 = 2.47(1) Å coming from Mn_S with a coordination of 4.2(5). This distance results expanded respect to the crystallographic Ge–Ge distance of 2.45 Å, a typical effect already seen for Mn_{Ga} in Chap. 4. It is interesting to note that DFT calculations on Mn_S find an even shorter distance of 2.39 Å, meaning that in this case the LSDA approximation fails to follow the expansion trend found experimentally. The local disorder is visible also from the resulting fitted Debye-Waller factor (DWF) giving a value σ_1^2 = 0.010(3) Å^2. In addition, it is found that the fit is statistically improved adding the d_5 contribution from the Mn_H structure. This permits to properly fit the second lower FT peak visible in Fig. 6.7, while additional distances from Mn_S or Mn_T models do not fit with the data.

The quantitative result (Tab. 6.3) for d_5 is 3.57(2) Å with a coordination of 1.2(4); this strongly differs from the crystallographic hexagonal interstitial and, considering also the fact that d_1 is lacking, could be the result of a local distortion due to the Mn insertion. Unfortunately, at the moment, a theoretical model explaining the observed distance is missing.

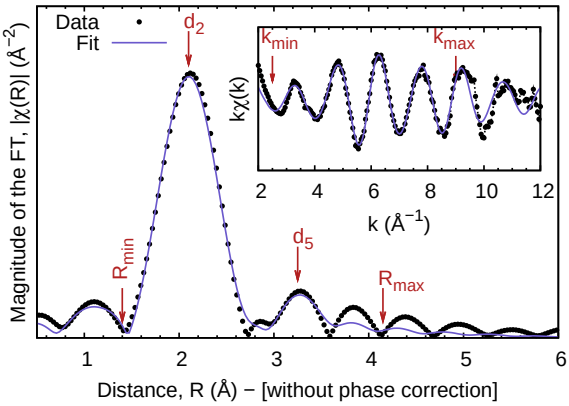

Figure 6.7: Fit results for GeMn(0.1%) using a Mn_S + Mn_H model. The main plot shows the Fourier-transformed spectrum of the $k\chi(k)$ EXAFS (inset) in [k_{min}–k_{max}] with the relative fit between [R_{min}–R_{max}]. d_2 and d_5 distances used in the fit are also indicated.

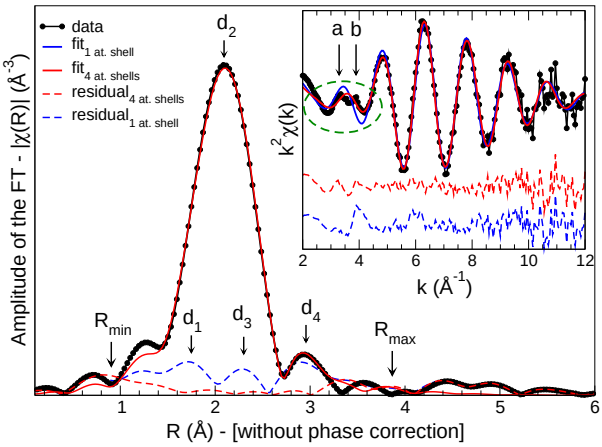

Figure 6.8: Fit results for the GeMn(130°C) sample in the Fourier-transformed R-space (main plot) and k-space (inset). Two models are reported: 1 atomic shell (blue) and 4 atomic shells (red) with relative residuals (dashed lines). The fitted distances $d_\#$ are indicated and the low-k region where main differences in the fit of peaks a and b is highlighted.

6.5.3 GeMn nanocolumns

Going further in the analysis, the local structure of a sample grown at T_g = 130 °C, showing high-T_C ferromagnetic nanocolumns, GeMn(130°C) in the following, is studied in detail. Also in this case a single substitutional defect at a distance d_2 could not account for the EXAFS oscillations in the low-k range. In fact, as visible in Fig. 6.8, the fit with one atomic shell present a clear residual in the highlighted k-region. For this reason including additional distances d_3 and d_4, as in the case of Ge_3Mn_5, results in an improvement of the fit in the high R part of the main peak in the Fourier transform. It is important to note that, for these bonds, it is difficult to make a difference between Ge and Mn backscatterers. The EXAFS oscillations for distances d_3 and d_4 are in antiphase with the oscillations of distance d_2 leading to the appearance of both peaks a and b (Fig. 6.8) in the low-k region. Finally, the addition of a fourth shorter scattering path at a Mn-Mn distance d_1 permits to improve the fit. This last distance, found at 2.11(2) Å, is too short to be considered as part of the Mn_H model while could account for Mn-Mn dimers as have been already observed in experimental EXAFS studies of Mn in InAs [325] and Ge [306] and is consistent with *ab-initio* calculations [326, 327]. Noteworthy, other possibilities, namely an oxide contribution, are also explored and result not to improve the agreement with the experiment. In addition, each time an additional scattering path is added in the fit, its effectiveness is verified by a χ^2-test (Sec. 2.4). Since the four atomic shells model presents an increased number of variables, to reduce correlations, the DWFs factors for distances d_1, d_3 and d_4 are set equal to the value found for distance d_2, σ_1 = 0.012(1) Å^2. The quantitative results

of the final fit are reported in Tab. 6.3, in addition with previous results and the following temperature and concentration series.

6.5.4 Temperature and concentration dependence

The previous fitting models are also validated in the analysis of the whole studied samples series. In fact, looking at the EXAFS spectra reported in Fig. 6.9, an evolution in the experimental signal is visible as a function of T_g and Mn content. Starting from the lowest concentration spectrum (0.1 %) and going up to high concentration (20 %) at fixed T_g = 125 °C, the main effects are visible in the low-k region where the peak a reduces while b increases (Fig. 6.9). On the other hand, fixing the concentration to the common value of 6 %, and increasing T_g in an interesting relatively small temperature window, the evolution is even more accentuated toward the Ge_3Mn_5 signal reported for comparison. Not only the peaks a and b present an opposite trend but also c and d (Fig. 6.9), bringing to the rearrangement of the local structure. This evolution is the fingerprint of the GeMn nanocolums.

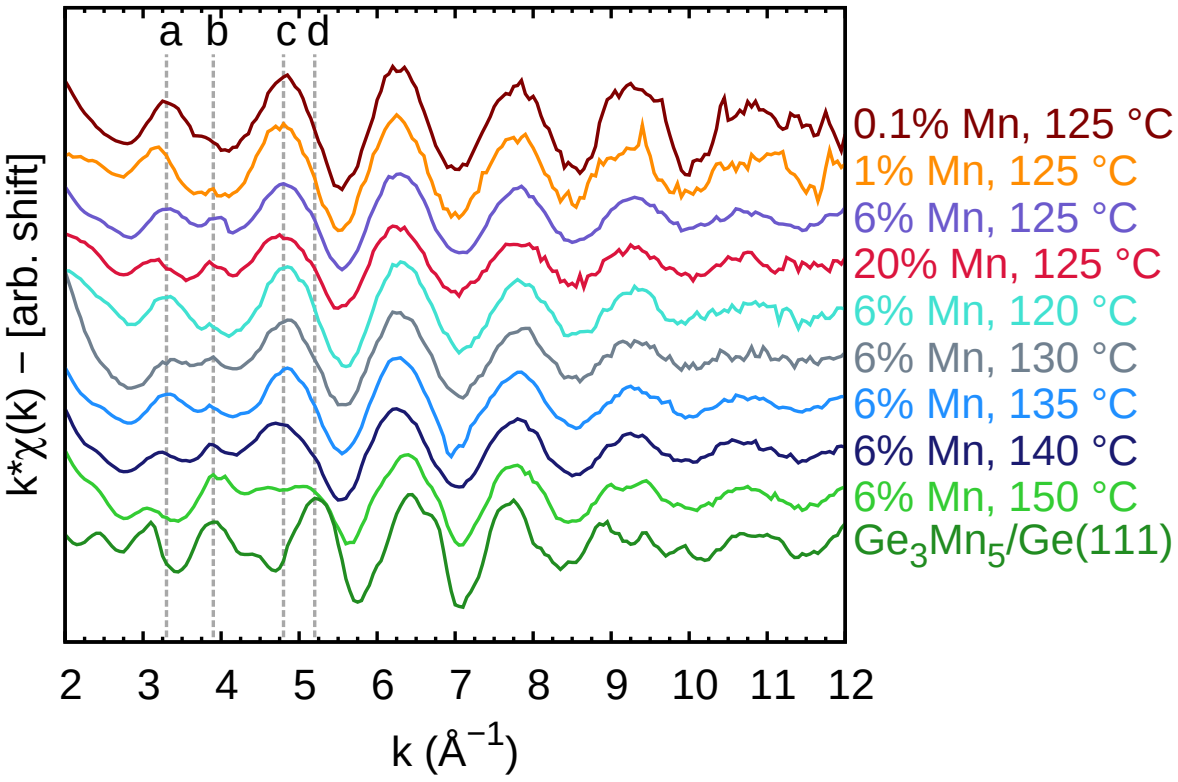

Figure 6.9: Evolution of the EXAFS signal with growth temperature and concentration. Spectrum of the Ge_3Mn_5 on Ge(111) thin film (multiplied by 0.5 in the plot) is added for comparison. The qualitative evolution of the spectra in the low k region is highlighted by vertical dashed lines and labelled a–d, while the quantitative results of the fits are reported in Tab. 6.3.

The quantitative results of the analysis, using the theoretical models previously detailed, are given in Tab. 6.3 where some common features can be extracted on the basis of the distances and coordination numbers found. The fingerprint of the Ge_3Mn_5 precipitation resides in the elongation of the distance d_2 and the high coordination number of d_4. In particular, this last

Table 6.3: Results of the EXAFS analysis: interatomic distances, coordination numbers and corresponding backscatterers are reported. Error bars on the last digit are given in brackets. For sample GeMn(130°C) a significant Mn-Mn bond is also found with a short distance, d_1, at 2.11(1) Å with a coordination of 0.2(1).

Sample	Distance (Å) / Coordination							
	d_2		d_3		d_4		d_5	
T_G = 125 °C:								
GeMn(0.1%)	2.47(1)	4.2(5)[a]	–	–	–	–	3.57(2)	1.2(4)[a]
GeMn(1%)	2.48(1)	4.0(5)[a]	–	–	–	–	3.60(4)	0.8(5)[a]
GeMn(6%)	2.49(1)	4.0(5)[a]	2.82(4)	0.8(4)[c]	3.09(4)	0.8(4)[c]	–	–
GeMn(20%)	2.49(1)	4.0(5)[a]	2.82(2)	1.6(2)[b]	3.10(2)	1.4(3)[b]	–	–
Mn 6 %:								
GeMn(120°C)	2.48(1)	4.2(5)[a]	–	–	–	–	3.57(4)	0.7(3)[a]
GeMn(130°C)	2.49(1)	4.0(5)[a]	2.86(5)	1.2(4)[c]	3.10(5)	1.3(4)[c]	–	–
GeMn(135°C)	2.49(1)	4.0(5)[a]	2.80(2)	1.0(2)[c]	3.07(2)	1.2(2)[b]	–	–
GeMn(140°C)	2.49(1)	4.0(5)[a]	2.80(2)	1.4(2)[c]	3.06(2)	1.1(3)[b]	–	–
GeMn(150°C)	2.49(1)	4.0(5)[a]	2.81(2)	3.7(7)[b]	3.01(2)	2.2(4)[b]	–	–
Reference sample on Ge(111):								
Ge_3Mn_5	2.52(1)	5.0(5)[d]	2.70(5)	1.2(4)[a]	3.04(5)	8.4(5)[b]	–	–

Backscatterer: [a] Ge; [b] Mn; [c] Ge or Mn; [d] Ge and Mn.

Mn-Mn coordination increases with the concentration and T_g. On the other hand, the distance d_3 is longer than its average counterpart in Ge_3Mn_5 and tend to be Mn-Mn coordinated at higher coordination. This can be the signature of the NCs and a possible model is presented in the next section. In addition, the d_5 distance is more puzzling since it is found only in samples with low concentration as well as for the lowest temperature. This could be a contracted ($\approx$ 3 %) Mn_H partially present in the samples (due to the small coordination number) when the growth conditions do not permit the aggregation.

6.5.5 GeMn building block

In order to explain the previous experimental results, a model for the NCs decomposition and the evolution toward Ge_3Mn_5 is proposed here. Despite the complex hexagonal structure of Ge_3Mn_5, Mn-Mn and Mn-Ge distances in this compound are comparable within error bars to the three experimental lengths d_2, d_3 and d_4 respectively. The main difference arises from the coordination number of distance d_4 which is much higher in the case of Ge_3Mn_5. This difference can be assigned to the presence of two sites for Mn atoms in the Ge_3Mn_5 structure (see Fig. 6.10). The Ge_3Mn_5 structure can be described using two kind of Ge-3Mn tetrahedra. However, only the tetrahedron that just contains Mn atoms in site 6*g* (Mn_2), the orange tetrahedron in Fig. 6.10, fits with the local structure parameters experimentally found in the Mn-rich NCs samples. Therefore it is possible to assume that Mn-rich NCs are mostly made of these Ge-3Mn tetrahedra that contains only Mn_2 atoms. Indeed, in GeMn(130°C) the d_2 distance involves a Ge backscatterer at 2.49(1) Å that is larger than the d_2 distance in GeMn(0.1%), 2.47(1) Å, and approaches the Ge-Mn_2 distance d_2 in the orange tetrahedron (Fig. 6.10) of hexagonal Ge_3Mn_5 (2.4876 Å).

Structural similarities between Mn-rich nanostructures embedded in a germanium matrix and Ge_3Mn_5 have already been proposed [306, 328, 308, 292]. The agreement arises from the

common Ge-3Mn tetrahedron found in both structures. These tetrahedra are indeed building blocks of Ge_3Mn_5 as well as NCs. Nevertheless, the formation of these Ge_3Mn_5 building blocks can be induced by the low temperature used during the MBE growth. Moreover it is possible to suggest that the high-T_C ferromagnetism properties of Mn-rich NCs might be connected to the long Mn-Mn distance within this tetrahedron (d_2 and d_3) as proposed by Forsyth and Brown to explain the magnetic structure of Ge_3Mn_5 [289]. The absence of the d_2 Mn-Mn distance (only present between Mn_1-type atoms) could explain the high magnetization found in the Mn-rich NCs sample [290]. However this interpretation has to be investigated in more detail in the future. Indeed, using different growth conditions (Mn concentration and growth temperature) is possible to evidence Mn-rich NCs exhibiting different magnetic properties while keeping their diamond-like crystalline structure [291]. This demonstrates that the Mn concentration and position in the NCs is highly sensitive to growth conditions on Ge(001) and fully determines the magnetic properties.

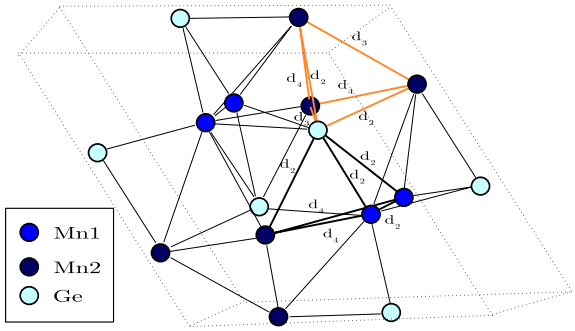

Figure 6.10: Perspective view of the Ge_3Mn_5 unit cell showing the proposed building block for the NCs. Coloured spheres denote Ge (cyan) and the two types of Mn atoms, Mn_1 (blue) and Mn_2 (dark blue). The black Ge-3Mn tetrahedron, that contains both Mn_1 and Mn_2 atoms, exhibits d_2 and d_4 distances including Mn and Ge backscatterers for the d_2 distance. The orange Ge-3Mn tetrahedron, that contains only Mn_2 atoms, exhibits d_2, d_3 and d_4 distances and only Mn-Ge bonds at d_2.

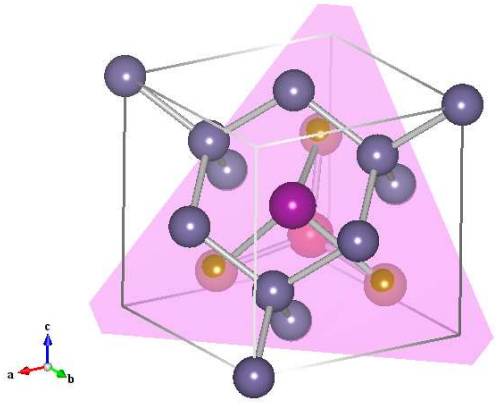

Figure 6.11: The linker block as proposed in Ref. [292] in terms of Ge native defects occupied by Mn atoms that permit to link the Ge_3Mn_5 cell to the Ge(111) planes. Three Mn_H (brown) on the (111) plane (pink) corresponding to Mn_2 are linked to one Mn_T (violet) on the front side and one Mn_S (red) on the back side, corresponding both to Mn_1. The average distances (configuration averaged coordination) based on the Ge crystallographic data are: $d_2 = 2.37$ Å (5.4), $d_3 = 2.83$ Å (0.6), $d_4 = 3.08$ Å (1.2).

Finally, to link the Ge_3Mn_5 cell to the diamond structure, a possible linker block has been recently proposed in terms of native defects [292]. In fact, using the Ge(111) plane (the easy way to epitaxy Ge_3Mn_5) the linker block is built as shown in Fig. 6.11. Three Mn_2 atoms go on the (111) plane in Mn_H sites, while two Mn_1 atoms go perpendicular, respectively, in Mn_T and Mn_S. This permits to create a seeding nucleus that can be responsible for both Ge_3Mn_5 clusterization and NCs. In fact, it is compatible with the d_3 and d_4 distances found in the present study while it does not agree with d_2. This last point is due to the inclusion in the average of the d_1 distance for Mn_H equivalent to the crystallographic one. On the other hand, it is not possible to compare experimental results to this last structure since it is a pure ball-and-stick model and, for a more realistic picture, a relaxed structure should be considered.

6.6 Summary

To summarize, EXAFS measurements are used to investigate the local structure of Mn-rich nanocolumns grown by low temperature MBE. The EXAFS analysis has shown that Mn-rich NCs present complex local structure that cannot be described only with a simple substitutional model. Additional interatomic distances have to be considered in the EXAFS analysis which are in good qualitative and quantitative agreement with the structure of one of the Ge-3Mn building block tetrahedron found in Ge_3Mn_5 crystal. The formation of such tetrahedra in Mn-rich NCs should be allowed due to the low temperature MBE growth. Finally it is suggested that the high-T_C ferromagnetism properties of the MBE films may originate from this local order found in both GeMn NCs and Ge_3Mn_5.

Mn dans le nano-fils de type III-V

Résumé du Chapitre 7

La dernière partie de ce travail de thèse est consacrée à l'environnement locale du Mn dans les nano-fils (NWs) de GaAs et InAs. Ceci constitue un sujet de recherche très intéressant car la bonne réussite d'un dopage par ions magnetiques de NWs semiconducteurs permettrait d'aller vers des DMS mono-dimensionnels. Normalement les NWs sont produits par MBE (ou autres techniques de déposition) en suivant le modèle VLS (vapeur-liquide-solide), qui consiste à utiliser un catalyseur de métal qui forme des nano-gouttes d'eutectique sous les quelles se fait la croissance du fil. Le catalyseur les plus utilisé est l'Au mais il a été montré que c'est aussi possible d'utiliser le Mn pour les NWs de GaAs [329]. Ici on montre que le Mn peut aussi induire la croissance de NWs de InAs, mais surtout on fait une investigation systématique de la structure locale soit quand la croissance se fait avec le Mn, soit quand se fait avec l'Au et le Mn est introduit comme dopant. Ceci permet d'obtenir des informations détaillées sur le comportement du Mn pendant la croissance ; informations qui ne peuvent pas être obtenues par la microscopie, surtout dans les parties amorphes présent à la pointe du NW (comme il est visible en Fig. 7.1).

Le caractère peu ordonné se retrouve à l'échelle locale dans les NWs de GaAs catalysés par le Mn. En effet, depuis les spectre EXAFS de la Fig. 7.3(a) on retrouve une seule fréquence principale qui se traduit dans un pic en FT (Fig. 7.3(b)) et quantitativement on obtient une distance Mn-As autour de 2.58 Å, avec un nombre de coordination réduit (Tab. 7.2) ; ce qui laisse penser à la formation de clusters de MnAs hexagonale. En plus, pour les échantillons fabriqués à plus basse temperature on trouve un épaulement à bas R (pic *a* en Fig. 7.3(b)) qui est identifié comme des dimères de Mn-Mn.[1] D'autre part, pour les NWs de InAs un caractère locale plus ordonné est observé, avec la présence de couches de coordination à plus longue distance (pic *b* en Fig. 7.3(b)) ; ceci se traduit quantitativement dans la formation de MnAs massif (Tab. 7.3). Un bon ordre locale se trouve aussi pour les NWs de GaAs catalysés par l'Au où, en plus du MnAs déjà trouvé dans les autres cas, il y a formation de l'alliage Mn-Au ; ceci est visible en Fig. 7.4(b) où on retrouve deux pics en FT bien distingués et se traduisent quantitativement dans les contribution Mn-As et Mn-Au (Tab. 7.4).

En conclusion ce chapitre montre que on est bien loin de l'incorporation de Mn substitutionel

[1] Il faut noter que avec une phase d'oxyde on n'obtient pas le même accord avec les données expérimentales et aussi on peut exclure cette hypothèse car avant chaque mesure les échantillons subissent un attaque chimique pour enlever justement la partie d'oxyde.

dans les NWs de GaAs ou InAs et beaucoup de travail reste à faire, car, si d'un coté la formation de précipités et alliages est liée à la haute temperature de croissance, de l'autre on ne peut pas travailler à basse temperature pour la croissance des NWs. D'autres paramètres restent donc à investiguer pour ce sujet stimulant.

7 Mn in III-V nanowires

In this chapter the EXAFS study of the Mn atomic environment in GaAs and InAs nanowires is presented. The work is conducted in collaboration with the TASC laboratory *in Trieste (Italy).*

7.1 Introduction

The trend towards increasing density and miniaturization of semiconductor devices has encouraged researchers to explore novel methods to obtain nano-scale structures. The conventional scaling methods based on lithography techniques face increasing challenges and limitations in obtaining sufficient uniformity in feature size below the sub 100 nm level; size fluctuations inevitably lead to a detrimental spread in device properties. As one of the most promising and fascinating advances, the so-called bottom-up approach has emerged; in this case, self-assembly at the atomic level and out-of-equilibrium growth regimes are exploited to produce nanometer-size objects with a high yield. Examples of the bottom-up approach to the fabrication of nanostructures include semiconductor quantum dots, carbon nanotubes and semiconductor nanowires (NWs). Several devices based on NWs, such as biochemical sensors [330], light-emitting diodes [331], single-electron transistors [332] or solar cells [333] have been demonstrated.

The fabrication of NWs generally occurs via the use of a metal nanoparticle (NP) catalyst, typically Au, which induces and dictates the growth. The vapor-liquid-solid (VLS) model, initially proposed in the 1960s to produce μm-sized Si "whiskers" [334] and later justified thermodynamically and kinetically [335], is generally used to rationalize the growth mechanism. In this model, the metal nanoparticle is heated above the eutectic temperature for the metal - semiconductor alloy system and is exposed to a flux of the semiconductor in the vapor phase, producing a liquid nanoparticle droplet. When the concentration of semiconductor atoms increases above a critical level, the semiconductor precipitates and a solid semiconductor NW nucleates at the liquid-solid interface. Depending on the used substrate the NWs can be grown with a well defined orientation and a with a diameter determined by the size of the catalyst nanoparticle.

The combination of the NWs research field with that of DMS (or magnetic semiconductors in general) opens the possibility to envisage 1D spintronics devices. Attempts to dope semiconductor nanowires with Mn have been reported for ZnO [336, 337], and GaN [338, 339, 340]; more recently, a number of II–VI and III–V materials have been doped with Mn in a chemical vapour deposition reactor [341]. In all these reports, Mn doping of the semiconductor

Table 7.1: Details of the sample preparation. The equivalent thickness of the catalyst (Mn or Au) is in all cases $\approx$ 1 nm.

Sample	Wire material	Catalyst Metal	Growth temperature (°C)	Growth time (min)
E650	GaAs	Mn	540	30
E651	GaAs	Mn	580	30
E672	GaAs	Mn	610	30
E652	GaAs	Mn	620	30
E656	GaAs	Au	540	30
E697	GaAs	Au	580	30
E683	InAs	Mn	390	60

material is provided by supplying Mn precursors during the growth or by post-growth ion implantation.

Recently, an alternative method was reported to deposit GaAs NWs [329]; it consists in employing Mn as a growth catalyst in MBE growth. It was found that the wires have a wurtzite (WZ) lattice and both EXAFS and transport measurements suggested that Mn atoms actually diffuse into the NWs where they act as dopants. Subsequently, two other groups have reported the growth of GaMnAs NWs exploiting the formation of 3D precursor structures during the growth of alloys layers on GaAs substrates [342, 343], the actual incorporation of Mn in the GaAs lattice was not studied by these groups.

It is clear that a characterization and a physical understanding of the local structure of Mn in III–V NWs is of great importance. In the wire growth induced by Mn NPs, two main questions arise: the degree of substitutional incorporation of Mn in the NW lattice and/or whether Mn - defective structures are formed.

7.2 Growth

GaAs NWs are grown by MBE on SiO_2 substrates. Before the NW growth, a thin film of Mn or Au is deposited on the substrates at room temperature in a metallization chamber, connected in ultra-high vacuum with the growth chamber. For all GaAs NWs samples, an equivalent two-dimensional growth rate of 1 μm/h is used with a V/III beam-equivalent-pressure ratio (BEPR) of 15. Sample growth is terminated by keeping As overpressure on the samples during their cool down. Three types of NWs are studied as a function of growth temperature, nature of the catalyst nanoparticle and doping. Samples E650, E651, E672 and E652 are grown using 5 monolayers (ML) of Mn ($\approx$ 1 nm) at growth temperatures 540 °C, 580 °C, 610 °C and 620 °C, respectively, and the growth is carried out for 30 minutes. Samples E656 and E697 are grown at 540 °C and 580 °C, respectively, using 5ML ($\approx$ 1 nm) of Au as catalyst and are doped during the growth with Mn, using an effusion cell for the dopant. The Mn deposition rates are 4×10^{12} at/cm^2/s in case of sample E656 and roughly one order of magnitude lower in case of sample E697.

Finally, the sample E683 consists in InAs NWs, grown for 1h at 390 °C, with equivalent two-dimensional growth rate of 0.26 ML/s and BEPR = 25 after having deposited 5 ML of Mn to induce the growth. The Mn-grown InAs NWs on SiO_2 are obtained in the 370–410 °C temperature range. This temperature range is the same found for the growth of Au-catalyzed InAs NWs [344]. The details of the preparation of the various samples are summarized in Tab. 7.1.

7.3 Electron microscopy

The morphological features and the structural properties of the NWs are studied, respectively, by scanning electron microscopy (SEM) and by scanning transmission electron microscopy (STEM). To perform STEM experiments, the NWs are mechanically transferred on a carbon coated copper grid. A JEOL TEM/STEM JEM 2010F UHR microscope is used, with accelerating voltage of 200kV and spherical aberration coefficient of 0.47 ± 0.01 mm equipped with a field emission gun; spatial resolution in phase contrast imaging, at Sherzer defocus, is 0.19 nm.

The SEM images of representative samples are reported Fig. 7.1. A detailed description of SEM and TEM investigations of the Mn-grown GaAs NWs was reported in a previous study [329]: it was found that the NWs have a WZ lattice and that α-Mn particles are found at the free end of the wires. In this study the microscopic analysis is mainly conducted on the InAs NWs. The SEM images of InAs NWs as in Fig. 7.1(c) show two distinct families of objects: most of the structures are mainly one dimensional, as typical for nanowires, while an appreciable number of two-dimensional structures (nano-leaves) are also visible. This latter type of structures was also observed for GaAs nanostructures grown on GaAs substrates.

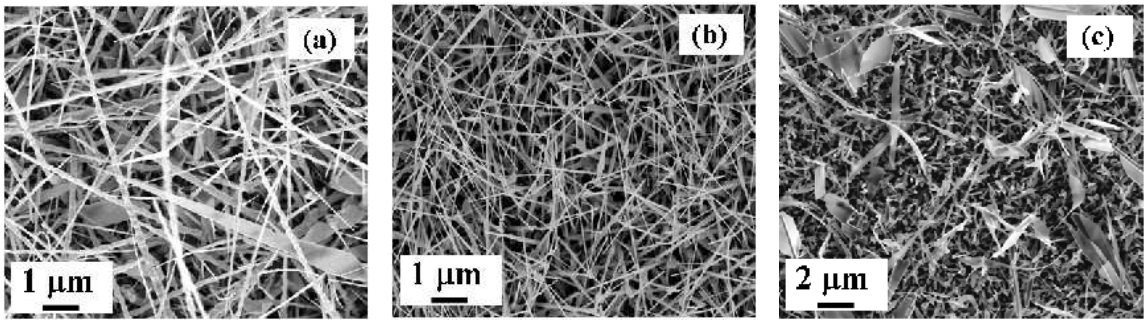

(a) Mn-grown GaAs NWs. (b) Au-catalyzed and Mn-doped GaAs NWs. (c) Mn-grown InAs NWs.

Figure 7.1: SEM images of representative samples.

A significant number of InAs NWs is studied by high-resolution TEM (HRTEM). Fig. 7.2(a) shows a HRTEM image of a representative nanowire in the region close to the tip. A catalyst nanoparticle is clearly visible in the lower part of the image and has a spherical shape with a diameter of 19 nm, while the wire body in its proximity has a diameter of 12 nm. The InAs nanowires are several μm long and generally have a tapered shape: moving away from the end tip, the wire diameter increases. All the investigated wires have a NP at their free end. The tips generally have the shape of a spherical section, with diameter varying between 10 and 22 nm, a few nm larger than the wire diameter measured at the NP/wire interface. Close to the tip, wire diameters vary between 7 and 18 nm. Another general feature, visible in Fig.7.2(a), is the presence of a thin amorphous layer, 2 or 3 nm thick, surrounding the wire body. This amorphous region, also present in GaAs NWs [329], is probably a thin oxide layer formed after the exposure of the samples to air. Moreover, the intensity along the section diameter of the wire body varies very smoothly, indicating a compositional homogeneity and the absence of facets. Fast Fourier Transform (FFT) is applied to HRTEM image reported in Fig.7.2(a) to analyze the body of the wire and reported in the inset of the same figure. The diffractogram is consistent with an InAs wurtzite structure with lattice spacings a = 0.427 nm, c = 0.702nm, as reported in the literature [345]. The wire is oriented along $[2\bar{1}\bar{1}1]$ zone axis and its growth direction is close to the $[\bar{2}111]$ direction. The hexagonal phase is the most common one found in

the InAs NWs (as also found in GaAs), however nanowires with zincblende (ZB) structure are also observed. It is worth pointing out that in WZ NWs large defect-free regions are generally observed, while ZB NWs regions are characterized by a large number of extended defects, stacking faults or twins.

The analysis on other wires unveils the presence of a small crystalline region embedded in an amorphous matrix. This case is reported in Fig. 7.2(b) where the lattice fringes are clearly visible at the center of the tip nanoparticle. The FFT performed in the dotted box is consistent with cubic α-Mn phase oriented along the [011] zone axis. This assignment is in agreement with the previous results on Mn catalyzed GaAs NWs.

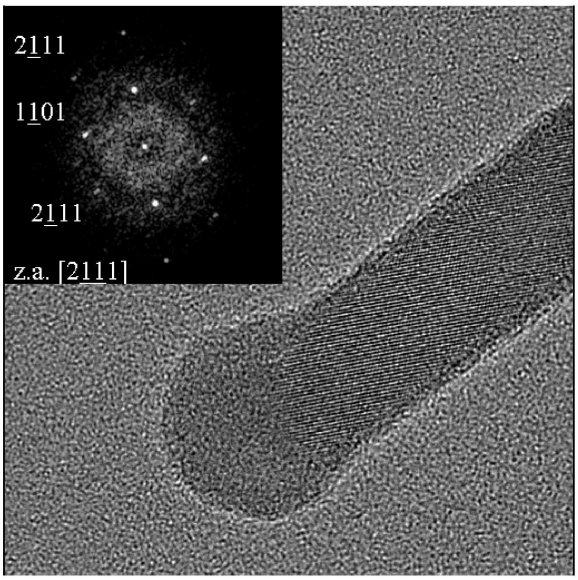

(a) HRTEM image of a representative NW (Fourier filtered). The wire shows a hexagonal structure, as indicated by the diffractogram reported in the inset.

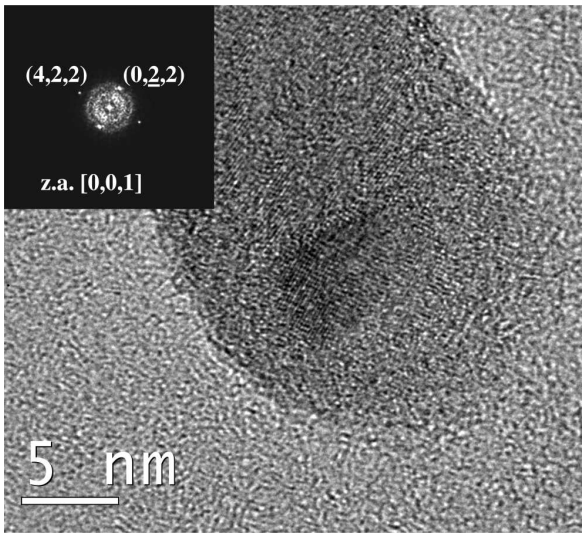

(b) HRTEM image of the tip of another NW. In this case a crystalline region inside the tip nanoparticle is observed.

Figure 7.2: Images from InAs NWs.

7.4 Local structure

EXAFS data at the Mn-K edge are collected at the GILDA beamline in standard fluorescence conditions as already reported in Sec. 2.3.1. The specific settings for these experiments are: the monochromator equipped with a pair of Si(111) crystals and the measurements carried out at T = 10 K using the liquid He cryostat in order to minimize the damping of the EXAFS signal originated from thermal atomic vibrations. Two to four spectra per sample are collected in order to improve the signal-to-noise ratio. Prior to each EXAFS measurement, the samples are chemically etched in HF for 3 seconds to remove the oxide layer, formed because of the exposure to air after the growth, and then immediately loaded into the vacuum chamber.

The data analysis is conducted using the standard procedures described in Sec. 2.4 with particular attention to the statistical analysis in order to discriminate between different models which reproduce the data in a similar fashion.

7.4.1 Analysis

Mn-grown GaAs and InAs NWs

The background subtracted EXAFS data of GaAs and InAs NWs are presented in Fig. 7.3(a) whereas the related Fourier transforms (FT) is shown in Fig. 7.3(b). In the EXAFS spectra of the GaAs samples only a single-frequency oscillation is visible and in the related FT there is only a dominating structured peak. This means that only coordination with a first neighbor can be detected and a considerable structural disorder prevents the detection of higher coordination shells. In all cases the FT exhibit a main peak above 2 Å with some GaAs samples presenting a shoulder at lower R values (peak a in Fig. 7.3(b)).

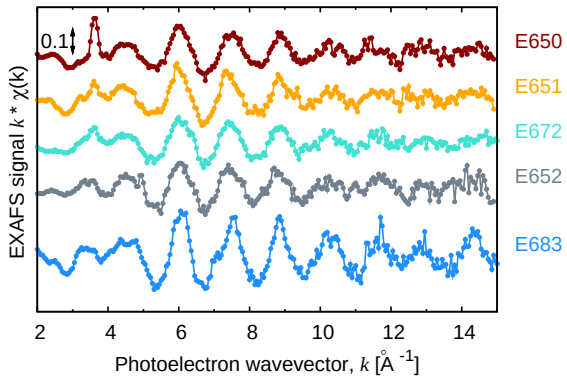

(a) EXAFS data.

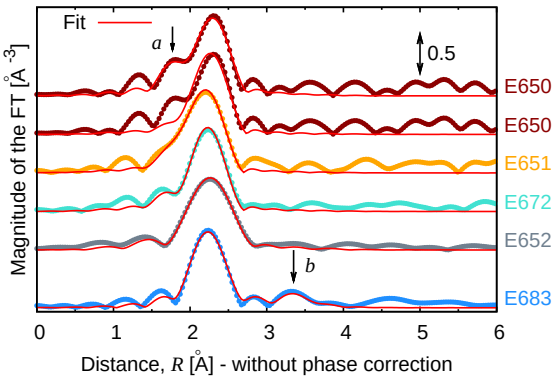

(b) Fourier transforms and best fit curves. The arrow labeled by "a" marks the short Mn-Mn bond whereas the arrow labelled by "b" marks second shell Mn-Mn bonds in the MnAs structure. In the case of sample E650 two fits are shown for comparison: with (upper curve) and without (lower curve) the inclusion of the contribution from Mn-Mn bond.

Figure 7.3: Samples of Mn-grown GaAs (E650, E651, E672, and E652) and InAs (E683) NWs.

For this class of samples three theoretical models are considered: pure Mn substituting Ga in a GaAs matrix (Mn_{Ga} site to account for Mn-As bonds, model 1) and two combinations of this site with another contribution to reproduce the shoulder at low R values. In particular is chosen a local coordination of Mn with oxygen (Mn_{Ox}, model 2) to account for possible Mn-O bonds as already found in [329] where no etching of the samples was carried out. The final model takes into account short Mn-Mn pairs (Mn_{Mn}, model 3) that are well distinguishable from Mn-As bonds because they exhibit considerably a reduced bond length, as reported in Mn-implanted Ge [306]. Contributions from Mn_{Ox} phases are expected to be reduced by the etching process carried out right before the measurements. All three physical models are tested and the determination of the one which best reproduces the data is established by a χ^2 analysis of the fits. Sample E652 is well reproduced by model 1 whereas sample E650 is reproduced by model 3. Considering different FT regions and windows does not affect this finding. The improvement of the fit by addition of this contribution is also evident in the FT as shown in Fig. 7.3(b) by comparing the two fits for sample E650 with (lower curve) and without (upper curve) the Mn-Mn bond. The principal quantitative results of all the fits are summarized in Tab. 7.2.

A different situation is present in the InAs wires: in this case the FT exhibits peaks beyond

Table 7.2: Results of the quantitative EXAFS analysis on the Mn-grown GaAs wires. Data are transformed in the interval k = [3.2–12.9] Å with a k^2 weight and fitted in R space in the interval 1.5–3.0 Å. For the Mn-Mn bond a length of about 2.18(3) Å is found with a coordination number decreasing from 0.3(1) to 0.0(1) for increasing growth temperature.

Sample	N_{As}	R_{As}	σ^2_{As}
		Å	10^{-3}Å^2
E650	1.6(3)	2.59(1)	4(1)
E651	2.8(3)	2.56(1)	7(1)
E672	2.4(3)	2.56(1)	6(1
E652	3.4(3)	2.59(1)	9(1)

Table 7.3: Quantitative results of the analysis of the Mn-grown InAs wires. Data are transformed in the interval k = [3.7–12.6] Å with a k^2 weight and fitted in R space in the interval [1.7–4.1] Å.

Sample	R_{As}	σ^2_{As}	R_{Mn}	σ^2_{Mn}	R_{Mn}	σ^2_{Mn}
	Å	10^{-3}Å^2	Å	10^{-3}Å^2	Å	10^{-3}Å^2
MnAs [346]	2.58	-	2.85	-	3.72	-
E683A	2.57(1)	4(1)	2.84(1)	10(1)	3.71(1)	12(1)

the first (peak *b* in Fig. 7.3(b)) that denotes the presence of a well ordered environment around Mn. A first fit with a model consisting in Mn substitutional in a wz-InAs environment (space group $P6_3mc$ - n. 186, lattice parameters a = 4.2840 Å, c = 6.9960 Å, u = 3/8, Ref. [345]) does not match the part at high R of the FT spectrum. Indeed, according to this structure, the peak due to the 2nd coordination shell should appear in the FT at an apparent distance [1] of ≈ 4.0 Å that is not present in the experimental spectrum. Conversely, an excellent fit is obtained with the structure of hexagonal MnAs, space group $P6_3/mmc$ (n. 194), lattice parameters a = 3.7253 Å, c = 5.7037 Å [346] where the peaks at high R values are due to Mn-Mn distances at 2.85 Å and 3.72 Å in that structure as resumed in Tab. 7.3.

Au-catalyzed and Mn-doped GaAs NWs

The EXAFS signals of the samples belonging to this class are shown in Fig. 7.4(a) whereas the related FT are presented in Fig. 7.4(b). An oscillating signal, still present at high k values (above k = 10 Å^{-1}), is particularly well evident in sample E656 revealing the presence of a heavy backscatterer around Mn. In the FT a double peak is present in both samples in the region 2–3 Å and an additional broad peak is present at about 5 Å in the E656 sample. In this case, two models are tested, consisting in Mn substitutional in GaAs plus a Mn in a tetrahedral interstitial site (Mn_{Ga} + Mn_I, model *a*) or a cubic MnAu (space group $Pm\bar{3}m$, n. 221, lattice parameter a = 3.2220 [347]) phase (model *b*). The choice of model *a* is suggested by the fact that the interstitial site in the GaAs structure could in principle give rise to a double peak in the first shell, as previously evidenced in Chap. 4. In the quantitative analysis the model *b* best fits the data from a statistical point of view. In fact, it is worth noting that the broad peak in the region around 5 Å is well reproduced by the collinear Mn-Au-Mn paths present in the high R part of the cubic structure, whereas it remains completely unexplained by model *a*. In sample E697 the peak at 5 Å is not present, while the other features are very similar to those exhibited

[1] It is important to recall here that the R value shown in the FT of the EXAFS data does not correspond to the real distance. This is due to the linearly decreasing dependence of the phase term $\psi(k)$ in the EXAFS formula. A negative shift of ≈ 0.3–0.4 Å is observed in the present case.

Table 7.4: Results of the quantitative EXAFS analysis on the Au-catalysed GaAs wires doped with Mn. Data are transformed in the interval k = [3.0–14.4] Å with a k^2 weight and fitted in R space in the interval [1.2–5.5] Å.

Sample	N_{As}	R_{As} Å	σ^2_{As} 10^{-3}Å^2	N_{Au}	R_{Au} Å	σ^2_{Au} 10^{-3}Å^2
E656	3.5(8)	2.56(1)	8(2)	0.8(6)	2.75(1)	0.5
E697	2.2(7)	2.58(1)	9(2)	3.1(5)	2.82(1)	5
MnAu [347]	-	-	-	8	2.79	-

by sample E656. It is reasonable that the local environment in these samples is similar, with a greater disorder in sample E697. The quantitative results for the fits with model *b* are reported in Tab. 7.4 for both samples.

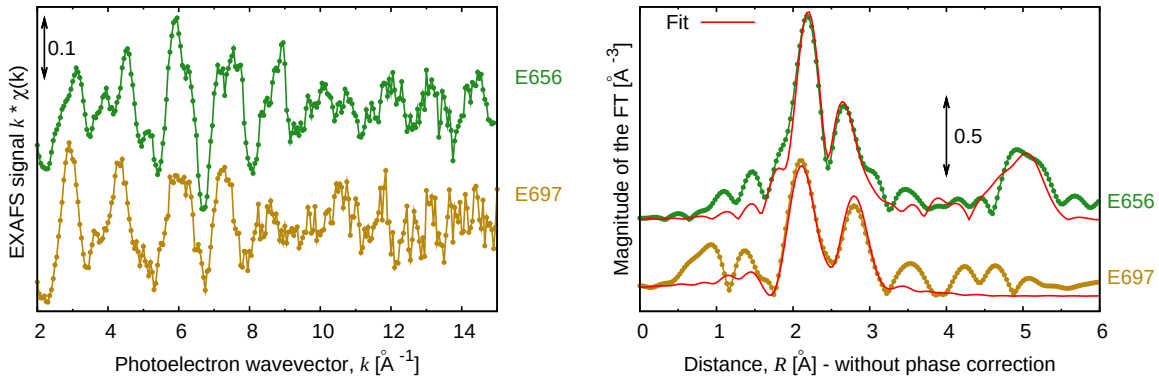

(a) EXAFS data.

(b) Fourier transforms and best fit curves.

Figure 7.4: Au-catalyzed and Mn-doped GaAs nanowires.

7.4.2 Discussion

From the EXAFS quantitative analysis it is clear that Mn in GaAs wires does not occupy a pure substitutional site. This appears to be true independently of the growth process, using Mn as the growth catalyst or doping the wires with Mn during the growth of Au catalyzed NWs. First of all, the first shell bond length is R_{Mn-As} = 2.59(1) Å, appreciably longer than that observed for Mn in a substitutional site in epitaxial GaAs, R_{Mn-As} = 2.50(1) Å. The WZ crystal structure of the NWs cannot explain that value. Indeed, in the commonly encountered ZB structure, the elongation of the Mn-As bond, respect to the Ga-As bond, is only about 2 %. In the WZ structure a similar effect is expected as the chemical interaction between Mn and As is the same in the two cases. This bond in WZ GaAs, using the lattice parameters a = 3.912 Å, c = 6.441 Å, u = 0.374 [348], is R_{Ga-As} = 2.399 Å and supposing the same ratio for the R_{Mn-As}/R_{Ga-As} distances as in ZB, in WZ should be R_{Mn-As} = 2.45 Å, a value well below the observed data. On the other hand, the actual fitted value is very close to the first shell distance in hexagonal MnAs (see Tab.7.3). A similar value, associated to a coordination number Mn-As of about 2.5, was observed in Mn/GaAs digital alloys annealed at 550 °C [349] and interpreted as due to the formation of a precursor phase for MnAs particles. Similar results on the Mn-As bond length are reported on (Ga,Mn)As alloys annealed at 600 °C [232]. It can be derived that the

growth temperature used in the preparation of the present samples could be responsible for the formation of the MnAs-like phase. The low value of the coordination number (about 3 instead of 6) suggests that, rather than creating extended crystals of the hexagonal phase, Mn forms small precursors of this structure.

Another finding from the presented analysis is the presence of Mn-Mn bonds at a distance of $\approx$ 2.18 Å that disappear for samples grown at higher temperatures (see Fig.7.3(b)). This separation between the Mn atoms is considerably shorter than that theoretically calculated for free Mn dimers (R_{Mn-Mn} = 2.89 Å [350], R_{Mn-Mn} = 2.60 Å [351]) and for the Mn-Mn separation in α-Mn (R_{Mn-Mn} = 2.58–2.77 Å, [352]). However, it matches previous experimental findings namely in Mn-doped InAs (R_{Mn-Mn} = 2.19 Å [325]) and Mn-doped Ge (R_{Mn-Mn} = 2.04 Å [306]) that were derived with completely different analysis codes and methods. It should be noted that Mn atoms in ZB-GaAs have been found to have a strong tendency to cluster [78, 353], namely in complexes involving two substitutional sites neighboring an interstitial site (Mn_{Ga}-Mn_I-Mn_{Ga}, [354]). The present study points out the presence of Mn aggregates also in the WZ structure. A complete understanding of this observation will need further studies, namely based on *ab initio* DFT calculations.

A different situation is found investigating the Mn-site in InAs wires. Here the environment is more ordered and a clearer evidence of formation of extended hexagonal MnAs islands is inferred by the higher quality of the EXAFS oscillations and by the fit that is able to explain the first three shells. There are two main differences between the GaAs and the InAs NWs. The first one is simply related to the lattice parameter that is larger in the second material by about 7%, the second one is the much lower growth temperature needed to obtain the InAs NWs.

Finally, interesting and unexpected results are found for Au-catalyzed and Mn-doped samples. As in previous cases, the Mn-As bond length is longer than expected for a substitutional impurity, however, a Mn-Au bond is also found. This indicates the formation of an intermetallic compound with evidence of chemical ordering. The degree of ordering of the alloy depends on the growth temperature; for samples grown at 580 °C there is evidence of even chemical ordering as proven by the presence of the chains Mn-Au-Mn found in the EXAFS spectrum. This observation suggests that Mn somehow participates to the growth process of the NWs playing a role similar to that of Ga, creating a supersaturated alloy with Au in the NP that successively separates creating the NW. A similar effect was reported in the preparation of ternary $In_xGa_{1-x}As$ NWs [355]. This might indicate a more general behavior, the participation of impurity atoms to the growth process of the nanowires.

7.5 Summary

The analysis of the atomic environment of Mn impurities incorporated in III-V semiconductor nanowires has revealed that Mn forms chemical bonds with As with a bond distance of 2.56–2.58 Å, longer than the expected value for a substitutional site and probably due to the occupation of defect sites. These sites are supposed to be the seeds for the formation of hexagonal MnAs precipitates. This behavior is observed, at different degrees of evolution, in both GaAs and InAs nanowires. Moreover, in the case of GaAs, similar findings are found both when Mn is incorporated because of catalyst diffusion into the wires and when Mn is supplied during the growth of Au-catalyzed nanowires. In this last case the penetration of Mn into the Au nanoparticle is revealed by the finding of a Mn-Au intermetallic bond.

Conclusions générales et perspectives

Dans cette thèse l'ordre locale autour d'impuretés magnétiques (Mn et Fe) dans des semiconducteurs pour les applications dans l'électronique de spin est étudié en détail par le biais de la spectroscopie d'absorption de rayons-X. Le choix des matériaux est basé sur les systèmes les plus prometteurs et a été possible grâce à la fructueuse collaboration avec des groupes parmi les plus actifs dans ce domaine. Ainsi, afin de couvrir une large gamme de matériaux, sont pris en compte le Mn dans le GaAs, le Fe dans le GaN, le Mn dans le Ge et Mn dans les nano-fils III-V ; ce qui permet également de découvrir les potentialités et les limites de la technique XAFS comme une sonde chimiquement sensibles à la caractérisation des nano-objets. D'autres systèmes, notamment le Mn dans les II-VI ont été étudiés dans les premiers temps de ce travail mais ne sont pas présentés ici car l'intérêt pour ces matériaux c'est orienté vers les boîtes quantiques dopés [356] ; les oxydes semiconducteurs, comme les DMS à base de ZnO, sont délibérément tenus à l'écart car l'origine du ferromagnétisme observé est controversée et le sujet nécessiterait un travail à part entière.

Le travail de thèse est effectué sur une ligne de lumière (GILDA) installée sur la source Européenne de rayonnement synchrotron (ESRF). Donc, en plus de la caractérisation des cas d'étude, il s'insère dans le programme de développement du laboratoire afin de fournir des appareils et des outils de pointe dans l'étude des couches minces dopés. En fait, il a été mis en œuvre un nouveau porte-échantillon pour les mesures en incidence rasante qui accroît le rapport signal-bruit pour ce type de systèmes. Deuxièmement il a été mis au point une nouvelle méthode d'analyse de données pour les mesures ReflEXAFS qui permet d'étudier quantitativement les surfaces et interfaces avec résolution en profondeur.

La première partie de l'étude est consacré au contexte scientifique et à la technique XAFS. En outre, avec une introduction générale sur l'emploi des outils complémentaires, cela permet d'encadrer la présente enquête dans les derniers développements de l'électronique de spin avec le semiconducteurs. En fait, la croissance rapide de ce domaine de recherche a vu de nouveaux résultats au cours des trois dernières années qui se sont orientés vers la recherche de nano-objets magnétiques auto-organisés dans les semiconducteurs et le contrôle du niveau de Femi pendant la croissance. Ces deux questions sont examinées ici à partir d'un point de vue structurel. Pour chaque système étudié, après avoir donné les détails de la croissance, sont présentés les caractérisations structurales (p.ex., XRD, TEM) et les caractérisations magnétiques (p.ex. SQUID) dans le but de fixer le cadre de l'investigation de la structure locale détaillée en fonction des paramètres de dépôt et, éventuellement, les traitements après croissance.

Le point de départ est le bien connu (Ga,Mn)As où le travail originale apporté ici est l'é-

tude de la structure locale autour du Mn résolue en profondeur. En fait, pour ce système, il est important de comprendre les mécanismes physiques impliqués dans les traitements après croissance comme les procédures de recuit et attaque chimique plus recuit. On a donc confirmé que le LT-MBE permet la fabrication d'un bon système DMS avec incorporation du Mn en substitutionel dans un environnement cristallin même pour une concentration relativement élevée. Cette étude a aussi permis de constater un enrichissement de Mn interstitiel à la surface, confirmant la collection de donnés en incidence rasante comme une puissante sonde locale de surface. Les effets du recuit sur la migration en surface du Mn interstitiel ont été aussi étudiés mais il n'est pas possible de lier le fait d'observer l'efficacité de cette méthode à l'interaction avec l'oxyde de surface, car, d'un point de vue XAFS, la présence de l'oxyde réduit la sensibilité à ces défauts, même avec l'utilisation d'une couche de plafonnement de GaAs de différentes épaisseurs. D'autre part, il est constaté que l'etch-annealing est efficace dans l'élimination des interstitiel ; ceci constituant la première preuve directe du processus de neutralisation induit par cette méthode.

Un pas en avant est fait par la caractérisation d'un nouveau matériau : le GaN dopé Fe. Ce système, en utilisant des outils de caractérisation avancée, s'est révélé un bon materiel de test pour les récentes théories sur l'ingénierie du niveau de Fermi et le contrôle de la nano-agrégation. On s'est donc intéressé à la structure locale et l'état de charge du Fe autour de la limite de solubilité. Cela a permis de montrer comment l'incorporation du Fe est efficacement contrôlée par son débit, la vitesse de croissance, et le co-dopage avec le Si. En particulier, l'agrégation des cations de Fe peut être minimisée en augmentant la vitesse de croissance et par la co-dopage avec Si ; ceci déplace la limite de solubilité à plus forte teneur en Fe. La structure atomique est également modélisée par des calculs *ab initio* avec la méthode DFT et un bon accord est trouvé avec les résultats expérimentaux. En outre, dans certains cas, les régions de décomposition spinodale sont observés par HRTEM et confirmés par une augmentation de la réponse ferromagnétique. D'autre part, la quantité de Fe dans ces régions est encore minoritaire par rapport à l'occupation substitutionelle. Donc elle reste en dessous de la limite de sensibilité XAFS et, pour le moment, n'est pas possible de donner une description détaillée de la structure locale dans ces régions décomposés.

Au contraire, cette question est traitée dans le Ge:Mn où la décomposition spinodale est dominante sous la forme de nano-colonnes riches en Mn. L'analyse EXAFS a montré qu'elles présentent une structure locale complexe qui est en bon accord qualitatif et quantitatif avec la structure de l'un des tétraèdres Ge-3Mn de base de la structure du Ge_3Mn_5 cristallin. La formation de ces tétraèdres dans les nano-colonnes devraient être autorisées en raison de la croissance à basse temperature et il est suggéré que le ferromagnétisme à haut T_C observé, soit du à cet ordre local qui se trouve dans les nano-colonnes de GeMn et aussi dans Ge_3Mn_5.

Enfin, sur la route pour la réalisation de dispositifs 1D, le rôle du Mn est étudié dans les nano-fils de GaAs et InAs, où le Mn est fourni soit par le dopage de fils catalysé par Au, soit en utilisant Mn à la place de l'Au dans la croissance de type VLS. Pour ces matériaux, l'analyse de l'environnement locale a révélé que le Mn formes des liaisons chimiques avec l'As à une distance plus longue que la valeur d'un site substitutionel et probablement en raison de l'occupation de sites censés être les germes de la formation de précipités de MnAs hexagonal. Ce comportement est observé, à des degrés différents d'évolution, à la fois dans des nano-fils de GaAs et de InAs. En outre, dans le cas de GaAs, les conclusions sont similaires soit quand le Mn remplace l'Au catalyseur dans la croissance des fils, soit quand il est fourni comme dopant. Dans ce dernier cas, le Mn entre dans la sphère d'Au à la tête des fils car est il révélé la formation d'un intermetallique Mn-Au.

En conclusion, à travers l'étude de différents systèmes prometteurs pour les applications en spintronique, il est démontré que la technique XAFS, combinée avec d'autres outils de caractérisation avancée, donne une description détaillée de la structure locale autour des impuretés magnétiques et aide dans le réglage des paramètres de croissance et le traitements après croissance. En outre, grâce à la caractérisation fine à l'échelle nanométrique, il est possible de tester les prédictions théoriques et de comprendre les mécanismes physiques sous-jacents responsables des propriétés macroscopiques des systèmes étudiés.

Perspectives

Inspiré par les résultats sur certains systèmes, l'extension naturelle de la présente étude serait de vérifier ces résultats sur d'autres systèmes. Tout d'abord, le réglage de l'incorporation en manipulant le niveau de Fermi, expérimentalement démontré ici pour GaFeN, devraient être testé sur GaMnAs et GeMn. Pour le GaMnAs le dopage de type n (en utilisant, par exemple, du Si) devrait être une stratégie pour accroître la T_C par l'augmentation de l'incorporation du Mn substitutionel en raison du fait qu'une fois le niveau de Fermi est atteint, en fournissant un donneur au cours de la croissance permets à la concentration total de trous de ne pas dépasser la valeur maximale autorisée [208]. Les premiers résultats sur GaMnAs :Si ont étés reporté dans la Réf. [218], mais la caractérisation structurale n'est toujours pas portée et pourrait fournir une preuve directe de cette stratégie. Aussi pour le GeMn dopage n (en utilisant, par exemple, As) a récemment été prévu comme un moyen efficace d'augmenter la limite de solubilité [357].

En outre, sur la base des résultats des nano-colonnes de GeMn et le rôle crucial joué par la température dans l'auto-organisation de ces nano-objets, également sur le système GaFeN, qui montre une tendance à la décomposition spinodale et l'allongement des nano-cristaux de ϵ-Fe_3N le long de la direction de croissance, il devrait être possible d'affiner le paramètre de la température afin d'obtenir des nano-colonnes riches en Fe dans le GaN.

Enfin, le dopage avec des accepteurs (par exemple, le Be en GaMnAs) devrait donner des résultats intéressants comme il a été récemment proposé en Réf. [358, 43] : en travaillant avec une densité de trous suffisamment élevée pour atteindre la transition métal-isolant (MIT), la présence du métal de transition crée un potentiel profond qui lie les trous et donc déplace la MIT vers des valeurs plus élevées. Dans ce cas, même si la région où les trous font pas la médiation de l'interaction spin-spin est plus large, des valeurs plus élevées de T_C sont prévus dans les VCA et MFA. En raison d'une forte énergie de liaison, un bon candidat pour tester cette théorie serait (Ga,Mn)N, mais en principe, ceci pourrait être obtenu dans d'autres DMS de type p.

8

General conclusions and outlook

In this thesis the local order around magnetic impurities (Mn and Fe) in selected semiconductors for spintronic applications is investigated into details by means of the x-ray absorption spectroscopy, using state-of-the-art data collection and analysis. The choice of the characterized materials is conducted on the basis of the most promising systems found nowdays in the research community. This has been possible through the fruitful collaboration with some of the most active groups in this field. Thus, to cover a wide spectrum of materials, Mn in GaAs, Fe in GaN, Mn in Ge and Mn in III-V NWs are taken into consideration; this also permits to find out the potentialities and limits of the XAFS technique as a chemically sensitive nano-characterization tool. Other important systems as the Mn-doped II-VI class were investigated at the early times of this work and are not reported here since the interest in these materials moved to doped quantum dots [356]; the oxides semiconductors, like ZnO-based DMS, are also deliberately kept apart since there is controversy on the origin of the observed ferromagnetism and the subject would require a dedicated work.

The thesis work is conducted on a synchrotron radiation facility beamline (GILDA at ESRF) and, in addition to the characterization of the case studies, it is inserted in the laboratory's development program in order to provide state-of-the-art apparata and tools in the study of thin films on a substrate. In fact, this has permitted the implementation of a new sample holder for measurements in grazing-incidence geometry that enhances the signal-to-noise ratio for doped epilayers and a new data analysis method for ReflEXAFS measurements that permits to properly quantitatively study surfaces and interfaces with depth resolution.

The first part of the study is focused on the scientific context and the XAFS technique. In addition with a general introduction on the employed complementary tools, this permits to locate the present investigation in the updated framework of the semiconductor spintronics. In fact, this fast-growing research field has seen important new findings in the last three years that have oriented the scientific community in the search for self-organized magnetic nano-objects in semiconductors and the control of the Femi level while the material is being grown. Both issues are investigated here from a structural point of view. For each studied system, after giving the growth details, a status of the structural (e.g. XRD, TEM) and magnetic characterizations (e.g. SQUID) is presented in order to set the framework of the local structure investigation given into details as a function of the deposition parameters and, eventually, post-growth treatments.

The starting point is the well-known (Ga,Mn)As where the additional original contribution is a depth-resolved investigation of the Mn local structure. In fact, for this system it is important to understand the physical mechanisms involved in the post growth treatments as the annealing and etch-annealing procedures. The XAFS investigation has confirmed that LT-MBE

permits the fabrication of a good DMS system with Mn substitutional incorporation in a crystalline environment even for relatively high concentration. It has also permitted to observe an enrichment of interstitial Mn at the surface, confirming the grazing-incidence collection mode as a powerful surface local probe. The effects of post-growth annealing on interstitials surface migration are investigated but it is not possible to link the observed efficacy of this method to the interaction with the surface oxide since, from a XAFS point of view, the presence of the oxide phase reduces the sensitivity to these defects, even with the use of a GaAs capping layer of different thickness. On the other hand, it is observed that the etch-annealing process is fruitful in removing interstitials. This is the first direct evidence of the neutralization process induced by this method.

A step forward is done by the characterization of a new promising material: Fe-doped GaN. This system, combining advanced characterization tools, has revealed as a workbench for recent theories on the Fermi level engineering and the control of nano-aggregation. Using XAFS, the local structure and charge state of Fe is investigated around the solubility limit. This has permitted to show how the Fe incorporation can be efficiently controlled by Fe flow, growth rate, and co-doping with Si. In particular, the aggregation of Fe cations can be minimized by increasing the growth rate and by co-doping with Si, shifting the solubility limit towards higher Fe content at given growth conditions. The atomic structure is also modelized by *ab initio* DFT calculations and good agreement is found with the experimental results. In addition, in selected cases, spinodally decomposed regions are observed by HRTEM and confirmed by an increased ferromagnetic response. On the other hand, the Fe amount present in these regions is still minority to respect the substitutional occupation, resulting below the sensitivity limit of the XAFS and without the possivility, at the moment, to give a detailed description of the local structure.

To the contrary, this issue is addressed in Ge:Mn where spinodally decomposed phase is dominant in the form of ferromagnetic Mn-rich nanocolumns. The EXAFS analysis has shown that they present a complex local structure that is in good qualitative and quantitative agreement with the structure of one of the Ge-3Mn building block tetrahedron found in Ge_3Mn_5 crystal. The formation of such tetrahedra in Mn-rich nanocolumns should be allowed due to the LT-MBE growth and it is suggested that the high-T_C ferromagnetism properties may originate from this local order found in both GeMn nanocolumns and Ge_3Mn_5.

Finally, on the road to ID spintronic devices, the role of Mn in GaAs and InAs NWs is investigated, where Mn is provided by doping Au-catalyzed wires during the growth or even by using Mn instead of Au for the VLS growth. For these materials, the analysis of the atomic environment has revealed that Mn forms chemical bonds with As with a bond distance longer than the expected value for a substitutional site and probably due to the occupation of defect sites supposed to be the seeds for the formation of hexagonal MnAs precipitates. This behavior is observed, at different degrees of evolution, in both GaAs and InAs nanowires. Moreover, in the case of GaAs, similar findings are found both when Mn is incorporated because of catalyst diffusion into the wires and when Mn is supplied during the growth of Au-catalyzed nanowires. In this last case the penetration of Mn into the Au nanoparticle is revealed by the finding of a Mn-Au intermetallic bond.

In conclusion, through the study of different promising systems for spintronic applications, it is demonstrated in this study that XAFS combined with complementary advanced characterization tools gives a detailed description of the local structure around the magnetic impurities and helps in the fine tuning of the deposition parameters and post-growth treatments. In addition, through the fine characterization at the nanoscale, it is possible to test theoretical

predictions and understand the physical underlying mechanisms responsible for the macroscopic properties of the studied species.

Outlook

Inspired by the peculiar results on some systems, the natural expansion of the present study would be to check them on other systems. First of all, the Fermi level engineering experimentally demonstrated here for GaFeN, should be tried on GaMnAs and GeMn. For GaMnAs the *n*-type counter-doping (using, e.g., Si) should be a strategy for increasing T_C as increasing substitutional Mn incorporation due to the fact that once the maximum Fermi level is reached, providing a donor during the growth will let the total hole concentration does not exceed the allowed maximum value [208]. First results on GaMnAs:Si are reported in Ref. [218] but the local structural characterization is still missing and could provide a direct evidence of this strategy. Also for GeMn the *n*-doping (using, e.g., As) has been recently predicted as an effective way to increase the solubility limit [357].

In addition, based on the results for GeMn nanocolumns and the crucial role played by the temperature in the self-organization of these nano-objects, also on the GaFeN system that shows tendency to spinodal decomposition and elongation of the found ϵ-Fe_3N nanocrystals along the growth direction, should be possible to fine tune the temperature parameter in order to get Fe-rich nanocolumns in GaN.

Finally, doping with shallow acceptors (e.g., Be in GaMnAs) interesting results should be found as recently proposed in Ref. [358, 43]: working with a hole density sufficiently high to reach the metal-insulator transition (MIT) the presence of the TM creates a deep potential that binds the holes and consequently shifts the MIT transition to higher values. In this case, even if the region where the holes do not mediate the spin-spin interaction is wider, higher values of T_C are predicted within the virtual crystal and mean field approximations. Due to a stronger binding energy, the a good candidate to test this theory would be (Ga,Mn)N but in principle this could be obtained in other *p*-type DMS.

Part III

Additional work

A

Apparatus for optimized x-ray absorption experiments on epilayers

A state-of-the-art experimental apparatus and a proper setup to perform XAFS experiments in grazing incidence mode is presented here. This geometry is appropriate for doped thin films or interfaces buried at moderate depth in a thick matrix, whenever the scattering and/or fluorescence from the matrix has to be strongly attenuated. Both a calculation and the experimental data demonstrate that the specific setup that consists in a grazing incidence and grazing collection geometry is extremely advantageous. In fact, with respect to the standard geometry used to perform XAS experiments in fluorescence mode, the present setup allows an enhancement of the interesting fluorescence signal from the surface layer without a corresponding increase of the elastic scattering contribution from the matrix. The sample holder especially designed for this kind of experiments can work in vacuum and at low temperature. An easy and quick automatic sample alignment procedure is also detailed. The present work is developed "on site" by the GILDA group and the described apparatus is currently operative on the beamline.

A.1 Introduction

A large part of the samples encountered in this field of research consists in thin films deposited on surfaces or buried at a moderate depth (10^{-2}–10^{0} μm); most of the times, the thin films cannot be taken out from their substrate without breaking. In this case it is convenient to confine as much as possible the incoming x-ray beam close to the sample surface in order to i) maximize the beam intensity in the thin film, ii) limit the beam penetration into the substrate to reduce the spurious signals originated from scattering and/or fluorescence from other components. To this respect, XAS experiments in total reflection condition or very close to it either for the incoming x-ray [116, 133, 119, 121] or for the outgoing fluorescence [359, 360] have been demonstrated to be very helpful; nevertheless, they require stringent conditions on the surface flatness and roughness and on the sample size, that cannot always be fulfilled. In these cases it is better to work at low incidence angle but well above the critical value for total reflection condition (Grazing Incidence X-ray Absorption Spectroscopy, GIXAS). In fact, if the x-ray extinction length is much longer than the film thickness, the intensity of the fluorescence signal from the dopant in the film is proportional to the beam footprint area, i.e. to the inverse of $\sin(\phi)$, where ϕ is the incidence angle. So, it is sufficient to use an incidence angle of 1 deg to obtain a net gain of a factor 40 in the fluorescence yield with respect to the standard XAS geometry in fluorescence mode (ϕ = 45 deg) [140]. On the other hand, at low incidence angle the scattering volume in the sample is closer to the sample surface, so that one should be aware

that the radiation scattered from the substrate is much less attenuated by the substrate itself: this means that, together with the increase of the fluorescence intensity, the scattering signal from the sample increases as well. Depending on the matrix and on the x-ray energy, in many practical cases the elastic scattering can be very intense and much higher than the fluorescence signal. This high scattered intensity can easily pile-up the energy-resolving detector, obliging to reduce the solid angle of collection to work in linear condition, with the net result to loose at least partially the advantage of working in grazing incidence geometry.

In the following is presented an experimental apparatus and a proper setup to perform GIXAS experiments. It is shown that with a proper collection geometry, the elastic signal impinging onto the detector can be considerably reduced; the real equipment, operative on GILDA beamline (Sec. 2.3.1), has the possibility to cool down the sample to limit the thermal vibrations; it does not need a complex goniometric stage, so that can be easily assembled and the samples can be easily aligned with the described automatic alignment procedure. Finally, according to the simulations presented in the first part, it is shown that for a real case of the measure of the fluorescence signal from a thin diluted layer on a thick substrate the fluorescence/scattering signal can be greatly enhanced: this is realized by (i) increasing the fluorescence signal itself (working at a low incidence angle) and (ii) reducing the scattering from the matrix (collecting the radiation coming out from the sample at a low angle).

A.2 Geometrical considerations

Focus on the setup to perform a XAS experiment in grazing incidence geometry using a detector (typically a high-purity Ge) to collect the fluorescence signal coming from the dopant species embedded into a thin layer deposited onto a substrate. Here and in the following, the angles of the incoming and outgoing x-ray beams are well above the critical angle, so that the refraction corrections are negligible and are not taken into account. As a case study, it is considered a sample where the atomic species whose x-ray absorption spectrum has to be measured is confined (possibly as dopant) in a thin layer deposited on a thick substrate (i.e. the film thickness is much lower than the x-ray penetration length). Due to sample dilution, the x-ray absorption spectrum has to be recorded by measuring the fluorescence signal from the dopant. To minimize the elastic scattering contribution, the fluorescence detector has to be placed to collect the radiation in a solid angle centered around the direction of the incoming x-ray polarization vector: for a synchrotron radiation emitted from a bending magnet this means that the detector has to be placed in the horizontal plane, "looking at" the sample in the direction almost perpendicular to the direction of the incoming x-ray beam. Then, the point to be addressed is how to realize the grazing incidence geometry for the sample. The two easiest practical setups are depicted in Fig. A.1 and consist in tilting the sample surface either around the vertical z axis (this geometry from now on will be referred to as "vertical geometry", Fig. A.1(a,c)) or around the horizontal y axis ("horizontal geometry", Fig. A.1(b,d)). Is is shown in the following that, for the same case study and the same incidence angle ϕ, the two setups lead to dramatically different fluorescence versus scattering yield ratios.

A.2.1 Vertical geometry

Considering an incoming x-ray beam of size D_y (D_z) along the y (z) axis, with $D_z \ll D_0$ (this will not affect the considerations done in the following) and using the parameters defined in Fig. A.1(c), the fluorescence intensity I_{fluo} and the scattered intensity I_{el} at a given angle ψ are

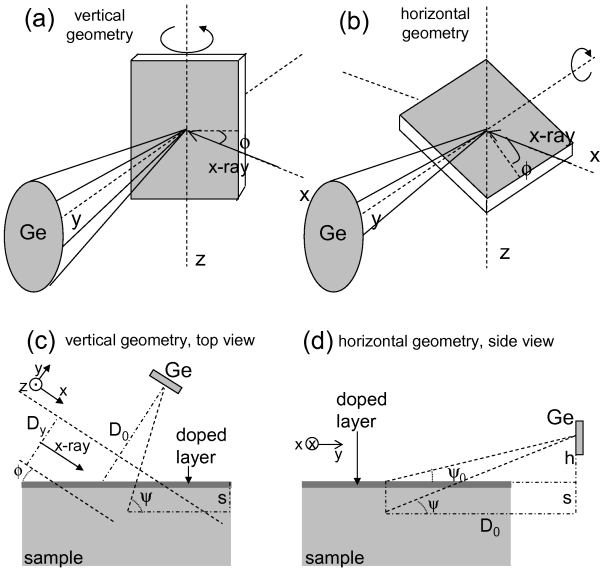

Figure A.1: The two different setups for GIXAS experiments described in the text: the incoming x-ray beam is parallel to the x-axis and the energy-resolving detector "Ge" is perpendicular to the incoming beam to minimize the elastic scattering from the sample. (a) Vertical geometry: the sample rotation is around the z axis, (b) Horizontal geometry: the sample rotation is around the x axis. (c) Vertical geometry, top view. (d) Horizontal geometry, side view.

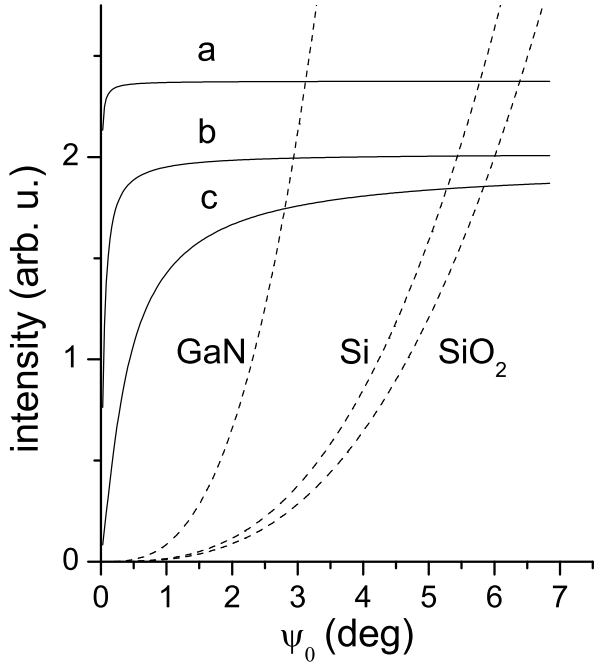

Figure A.2: Results on the horizontal geometry in the case of 6×10^{14} cm^{-2} Er atoms embedded in different matrices (SiO_2, Si or GaN); the intensity of the Er L_α fluorescence line (solid lines) is calculated for a doped surface layer of 10 nm (a), 100 nm (b) and 1000 nm (c), and shown as a function of the detection angle ψ_0 (see Fig. A.1(b,d)); correspondingly, the elastic scattered radiation from the different matrices (dashed lines) is also shown.

$$I_{fluo}(\psi) = I_0\, \sigma_{fluo} \int_0^{+\infty} f(s)\, ds \int_{\psi_1(s)}^{\psi_2(s)} e^{-(\mu_e/\sin\phi + \mu_f/\sin\psi)s}\, d\psi \tag{A.1}$$

$$I_{el}(\psi) = I_0\, n\, \sigma_{el} \int_0^{+\infty} ds \int_{\psi_1(s)}^{\psi_2(s)} e^{-(1/\sin\phi + 1/\sin\psi)\mu_e s}\, \sin^2(\alpha)\, d\psi \tag{A.2}$$

Here I_0 is the intensity of the incident beam, σ_{fluo} (σ_{el}) is the cross section for the fluorescence emission (elastic scattering), μ_e (μ_f) is the absorption coefficient for the elastic scattered (fluorescence) radiation, $f(s)$ is the concentration depth profile of the absorber atoms and n is the atomic density of the matrix. The angular dependence of the elastic scattering on the polarization is accounted for with the term $\sin^2(\alpha)$, where $\alpha = \psi - \phi$ is the angle between the scattered beam and the electric field of the incoming x-ray beam. The limits of the angular integral $\psi_{1,2}(s)$ depend on the parameters D_y, D_0, ϕ indicated in Fig. A.1(c)[1]. From the Eq. A.1 for the elastic scattered intensity one can define an effective extinction length $\lambda_{eff,el}$, so that $\lambda_{eff,el}^{-1} = \mu_e(1/\sin\phi + 1/\sin\psi)$. This parameter essentially determines the effective thickness for the elastic scattering radiation to be collected by the energy-resolving detector, so that for the scattered intensity, the integral in the s variable (depth) can be restricted with a good ap-

[1]Where $tg(\psi_{1,2}(s)) = \frac{D_0 cos\phi + s}{D_0 \sin\phi - \frac{s}{tg\phi} \pm \frac{D_y}{2\sin\phi}}$

proximation to the range [0; $\approx 3\lambda_{eff,el}$]. In the actual hypothesis of dealing with a thin doped layer, the effective thickness from which the fluorescence intensity can be collected is the whole layer thickness. In this geometry the scattering angle ψ varies around 90 deg, typically within few degrees (for $D_0 \approx 10$ cm, $\phi \gtrsim 1$ deg), so that the attenuation of the scattered intensity is just $\approx e^{-\mu_e s}$; moreover, due to the grazing incidence the scattering volume (that is roughly $D_y / \sin(\phi) \times D_z \times \lambda_{eff,el}$) is closer to the sample surface with respect to the standard condition (ϕ = 45 deg), so that the scattering signal increases significantly. At the same time, the fluorescence intensity increases as well with the same trend: lower is the incidence angle ϕ, higher are both the elastic scattering and the fluorescence contribution from the surface layer. So, in case of a diluted thin layer, this geometry is really useful only if the scattering signal from the substrate (both elastic and Compton) is not the dominant part of the overall signal that impinges onto the detector. Only when the refraction correction are not negligible (i.e. incidence angle close to the critical one), the refracted beam can be confined in a thin layer below the surface and a strong enhancement of the fluorescence signal with respect to the scattering one is produced.

A.2.2 Horizontal geometry

In the case of horizontal geometry (see Fig. A.1(a,d)), the same Eqs. A.1 and A.2 are valid, just with different angular limits (consider here $D_y \ll D_0$)[2]. Also in this case the scattering volume is closer to the sample surface, but with the important difference that here the scattering angle ψ of the recorded radiation is pretty low (grazing incidence and collection geometry) and of about the same order as ψ_0. The attenuation of the scattered signal is much higher than for the vertical geometry (for $\psi \approx 1$ deg, $e^{-\mu_e s / \sin\psi} \approx e^{-57\mu_e s}$): this stronger attenuation is significant only for the scattered intensity from the matrix but not for the fluorescence signal, since this last comes only from a thin surface layer. The result is that the fluorescence signal from the surface layer is greatly enhanced (due to the low incidence angle), without a corresponding increase of the scattering signal (due to the low collection angle).

To better clarify this point, consider a numerical example where the Eqs. A.1 and A.2 are applied to the case study of an Er-doped layer in a SiO_2, Si or GaN matrix, for an x-ray incident radiation of 8.4 keV (just above the Er L_{III} photoelectric absorption edge) and for an incidence angle ϕ = 20 deg. The Fig. A.2 shows the elastic signal and Er fluorescence intensity (the energy of the Er L_α line is 6.7 keV) as a function of the collecting angle ψ_0, for different layer thickness, from 10 to 1000 nm. It is seen that for a low collecting angle ψ_0 the scattered intensity can be much lower than the fluorescence signal. Moreover, the lower is the molecular weight of the matrix, the higher is the collection angle below which the fluorescence contribution is dominant. To this respect, as detailed in the Section A.5, it is worth to consider that in the standard geometry (vertical geometry and ϕ=45 deg) the scattered intensity signal is about one order of magnitude higher than the fluorescence one. The results shown in the Fig. A.2 for a case study are significant for a general class of materials composed of a diluted surface layer deposited onto a substrate, providing that the layer thickness is much lower than the x-ray extinction length: they indicate that in case of grazing collection angle (and grazing incidence angle) the elastic scattering contribution can be significantly reduced, obtaining at the same

[2]The angular integration range has to be split into two intervals, one from $\psi_1(s)$ to ψ_{max} and the other from ψ_{max} to $\psi_2(s)$, where: $tg(\psi_{1,2}(s)) = \frac{s + D_0 tg\psi_0}{\sqrt{(\frac{s}{tg\phi} \mp \frac{D_z}{2\sin\phi})^2 + D_0^2}}$ and $tg(\psi_{max}(s)) = \frac{s + D_0 tg\psi_0}{D_0}$. The polarization factor is $\sin^2\alpha = 1 - \frac{D_0^2}{(h+s)^2(1+\frac{1}{tg^2\psi})}$

time an increase of the fluorescence intensity from the doped layer. This makes this geometry particularly useful for this class of samples.

A.3 The experimental apparatus

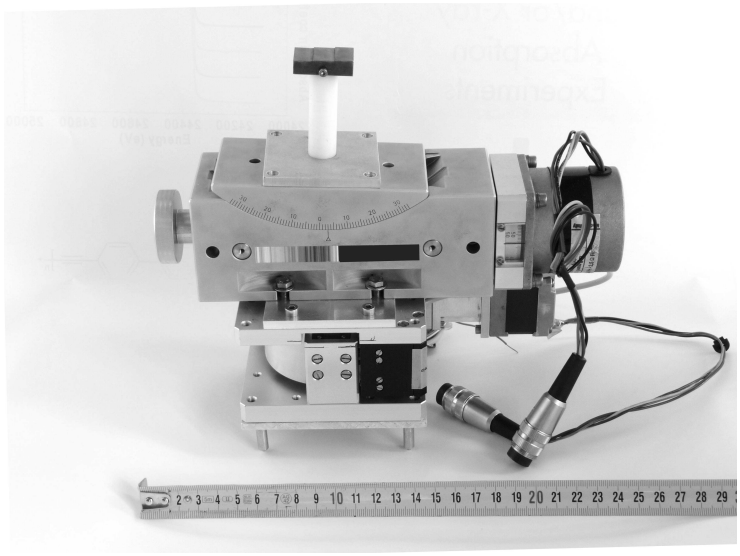

Figure A.3: Picture of the experimental apparatus, equipped with the copper sample holder, placed on top of the white insulating cylinder (to be better visible the sample holder has been 90 deg-rotated along the vertical axis with respect to the standard operation geometry).

The apparatus presented here is currently operative at GILDA. The actual device consists in a translation stage coupled to a Euler cradle for the rotation and is shown in Fig. A.3. The movements are operated by stepper motors working in half-step mode (400 steps/revolution) with one revolution corresponding to 10 μm for the vertical translation and to 1 deg for the rotation. The whole system can be mounted inside a vacuum chamber in order to avoid air absorption and scattering, that is mandatory to analyze light elements or very diluted samples and to work at low temperature. Up to three samples can be mounted on a copper support (see Fig. A.3) that can be cooled down to 110 K by a cold finger linked to the plate via a copper cable. The three surfaces that allocate the samples are parallel one to each other and located at three different quotas (h_0, h_0+0.5 mm and h_0-0.5 mm, where the lower quota is pertinent to the surface closer to the fluorescence detector). In this way even the fluorescence coming from the sample mounted in the furthest position from the detector can be properly collected without being shadowed by the other samples that are closer to it. The sample holder is hold on the motion stage by a thermally and electrically insulating cylinder. The intensity of the beam impinging of the sample is measured by a ionization chamber; another ionization chamber I_1 measures the intensity of the direct beam used by the alignment routine.

A.4 Automatic alignment routine

In order to permit to the user an easy operation of the GIXAS apparatus, an automatic alignment procedure is implemented. It is optimized to be used in conjunction with a large area detector as usually encountered on conventional XAS stations so it does not need a complex

goniometric stage as for some apparata for total reflection measurements (Sec. 2.3.1). The automatic alignment routine is written in Labview language.[3]

A layout of the system is shown in Fig. A.4 where also the key geometrical parameters are indicated. The scope of the procedure is to set the sample surface parallel to the beam and in the middle of the beam itself. For this purpose the sample height z and the tilt angle ϕ have to be optimized by acting on the positioning stage supporting the sample. The procedure is carried out by realizing scans of the sample angle and vertical position while reading the direct beam with the I_1 ion chamber. The analysis of the curves obtained permits to determine the correct position of the sample. The whole process consists in the following steps:

1. Positioning the B_R slit to block the possible reflected beam.
2. Coarse positioning of the sample (z and ϕ coordinates).
3. Fine positioning of the sample (z and ϕ coordinates): this step is crucial only to work at very low incidence angle.
4. Rotation of the sample to the final position.

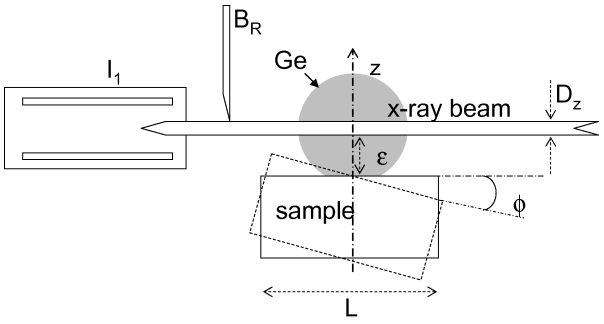

Figure A.4: Layout of the experimental apparatus. The polarization vector of the incoming x-ray beam and the sample rotation axis x are perpendicular to the page; "Ge" indicates the fluorescence detector; the B_R slits used to cut the reflected beam and the ionization chamber I_1 are shown.

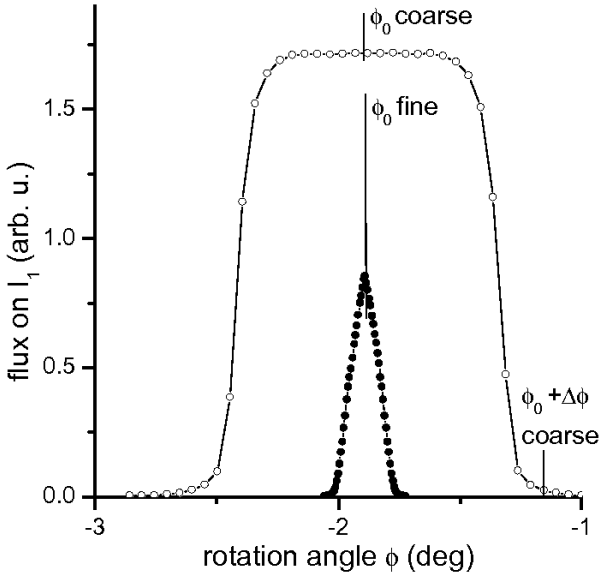

Figure A.5: Beam intensity measured by the ion chamber I_1, as a function of the rotation angle ϕ, during the coarse (open circles) and fine (full circles) alignments.

It is assumed that the beam size D_z and the sample length L are known and that the rotation axis is on the sample surface. Moreover, the procedure is also based on the rough estimation of the initial parameter z_0 and ϕ_0 that correspond to the position in which the sample surface is parallel to the beam and on the beam axis: these starting values are typically those obtained from the first (manual) alignment of one sample at the beginning of the experiment. The procedure starts driving the sample out of the beam and scanning the B_R blade through the beam. The scope of this step is to position the blade at the upper edge of the direct beam as

[3] See `http://www.ni.com/labview/`

shown in Fig. A.4. In this way, the beam reflected by the sample is blocked and only the direct beam intensity is recorded by the ion chamber I_1. As second step, the sample height z is set slightly below the initial z_0 value, $z = z_0 - \epsilon$ ($\epsilon \approx 0.2$ mm is fine for a beam of size $D_z \approx 100\mu$m). At this point a first estimate of the angle at which the sample is parallel to the beam (ϕ_0) has to be done. For this purpose an angular scan is performed in a suitable range, knowing that the sample surface is below the beam. For a definite value of z_0 there are two values of ϕ for which the sample cuts half of the beam, that differ by $\Delta\phi_{coarse}$, given by (see Fig. A.4):

$$\Delta\phi_{coarse} = 2\arcsin(\frac{2\epsilon + D_z}{L}) \tag{A.3}$$

So, the first step is to perform an angular scan centered about the previously determined ϕ_0 and with an angular range of about twice $\Delta\phi_{coarse}$. This results in a plot as shown in Fig. A.5 (open circles). By taking the average between the inflection points of the raising and falling edges (i.e. the maxima of the derivative of $I_1(\phi)$ in Fig. A.5), a first determination of ϕ_0 is obtained. The actual distance ϵ between the sample surface and the beam can be as well estimated from $\Delta\phi_{coarse}$ using:

$$\epsilon = \frac{L}{2}\sin(\frac{\Delta\phi_{coarse}}{2}) - \frac{D_z}{2} \tag{A.4}$$

Then, with the sample positioned at $\phi = \phi_0$ a scan of the sample height z is carried out: at this step the z scan spans a few times the beam size D_z below and above the z_0 value. The z value where the readout of I_1 is halved is then the refined height position of the sample, z_0.
Now, a new angular scan is carried out to refine the ϕ_0 value. The angle between the maximum (i.e. sample parallel to the beam) and zero intensity is determined as follows:

$$\Delta\phi_{fine} = \arcsin(\frac{D_z}{L}); \tag{A.5}$$

it is then sufficient to make an angular scan in a range of about 3 times $\Delta\phi_{fine}$. The result is shown in Fig. A.5 (full circles). The final ϕ_0 angle can now be determined with high accuracy as it corresponds to the sharp maximum of the curve. Then, with the sample in the position $\phi = \phi_0$, a further z scan is carried out to refine the position of the sample that cut by half the beam intensity. Typically the final estimations of the z_0 and ϕ_0 values are within ≈ 5 μm and ≈ 0.02 deg. It has to be noticed that this procedure allows a precise alignment, so that it can also be used in total reflection XAS experiments, where the sample alignment is much more critical; if the incidence angle to be used is of 1-2 deg, the refinement of the sample height and tilt angle (step 3) can be omitted.

Finally, the sample is tilted with respect to the ϕ_0 position by a suitable value in order to have a low incidence angle and a sufficiently short beam footprint on the sample (i.e. the beam footprint should entirely be onto the sample surface). With a beam of 100 μm and an angle of $\phi = 1$ deg the footprint on the sample is 5.5 mm thus matching the size of commonly encountered samples. The whole procedure can be carried out automatically, and it usually takes few minutes to be completed.

A.5 Example of data collection

The sample considered here as a case study is a 1 mm-thick silica slide (sample surface = 1.5 cm $\times$ 1.5 cm) doped by ion implantation with Er and Au and heated at T = 400 °C in reducing

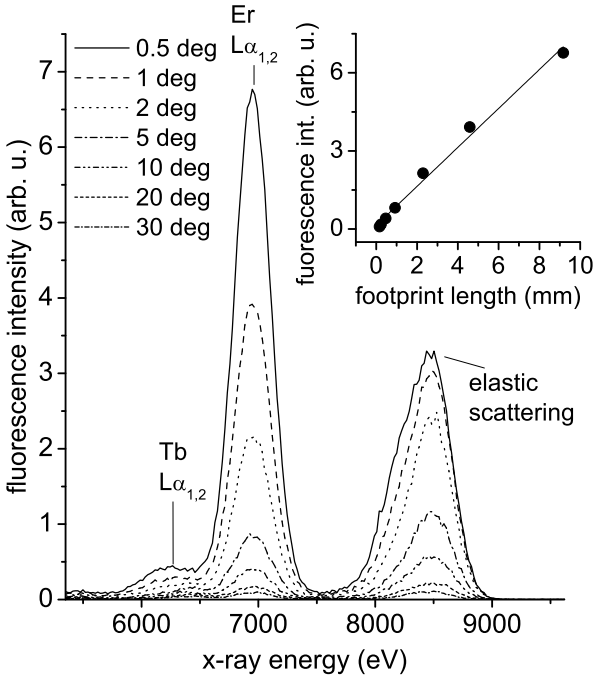

Figure A.6: X-ray spectra recorded from the central element of a Ge detector in horizontal geometry from an Er-doped layer in a SiO_2 matrix, obtained upon excitation at E = 8400 eV for different incidence angles. Inset: fluorescence intensity (full circles) as a function of the beam footprint length on the sample surface, and corresponding linear fit (solid line).

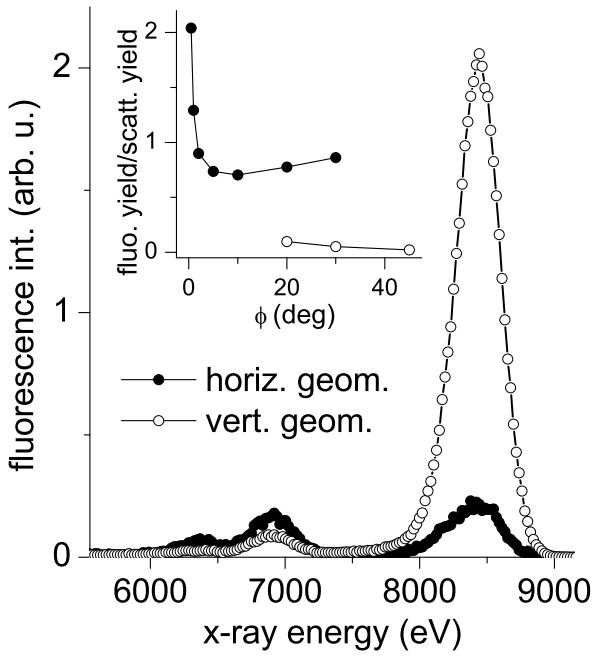

Figure A.7: X-ray spectra recorded for the Er-doped SiO_2 by the Ge central diode for an incidence angle of 20 deg in horizontal (full circles) and vertical (open circles) geometries. In the inset, with the same meaning of the symbols, the ratio of Er fluorescence yield over scattering yield is reported as a function of the incidence angle for the two geometries.

atmosphere.[4] The thickness of the Er-doped region is $\lesssim$ 100 nm and the Er fluence is about 7×10^{14} Er^+/cm^2; other details on the sample preparation can be found in Ref. [361]. A focus on the measure of the x-ray absorption spectrum at the Er L_{III}-edge (E = 8358 eV) is given.

In Fig. A.6 the x-ray spectra collected by the central Ge element upon excitation at E=8400 eV are shown for different values of the incidence angle ϕ. Three different peaks are visible and labelled: the elastic scattering (the inelastic scattering contribution is also visible as a shoulder of the elastic peak at low energy), the fluorescence from Er ($L_{\alpha,1}$ and $L_{\alpha,2}$) and the fluorescence of Tb ($L_{\alpha,1}$ and $L_{\alpha,2}$), present as contaminant of Er. It is clear that the Er fluorescence intensity increases as the incidence angle decreases (the Er fluorescence signal becomes higher than the elastic one for $\phi < 2$ deg) because of the increase of the beam footprint on the sample surface (as discussed in the Section A.2); in the inset of Fig. A.6 the linear relation between the fluorescence intensity and the beam footprint is evidenced. So, as expected, it is interesting to work at low incidence angle to have an high fluorescence yield: the angle should be kept as low as possible, providing to keep the beam footprint entirely onto the sample surface. In Fig. A.7, the two x-ray spectra collected for an incidence angle of 20 deg in the vertical and horizontal geometries are compared. In the inset, the ratio of Er fluorescence intensity over scattering intensity is also plotted as a function of the incidence angle for the two geometries. Note that in both cases the detector remain at the same position, with the sensitive surface

[4]Kindly provided by G. Mattei and G. Perotto.

normal to the horizontal y axis (see Fig. A.1). According to the discussion made in Section A.2, it is evident that in the horizontal geometry the fluorescence versus scattering ratio measured by the detector is significantly higher, so leading to an intrinsically higher signal/noise ratio in the x-ray absorption spectrum. As discussed, this result is valid whenever the element whose fluorescence has to be studied (Er in this case) is confined into a thin surface layer. This setup is extremely interesting for the realization of XAS experiments on this class of samples. In fact, to increase the quality of the x-ray absorption spectrum, one should work with (i) the highest possible fluorescence signal and (ii) with the lowest possible background. Since in most part of the cases the background in the energy range of the interesting fluorescence signal is essentially the low energy tail of the elastic peak (and possibly the Compton scattering) from the matrix, the proposed setup allows a significant step forward on both the point (i) and (ii). The final consideration is that the energy-resolving detector has to be carefully placed to avoid a shadowing effect of the fluorescence signal from the sample itself.

A.6 Conclusion

The presented experimental apparatus and the proper setup to perform GIXAS experiments show that, when the dopant whose XAS spectrum has to be measured is confined into a thin layer deposited onto a substrate or buried at moderate depth in a thick matrix, this geometry is extremely advantageous. In fact, with respect to the standard geometry used to perform XAS experiments in fluorescence mode, it allows an enhancement of the interesting fluorescence signal from the surface layer (because of to the low incidence angle) without a corresponding increase of the elastic scattering contribution from the matrix (because to the low collection angle). In this way the signal to background ratio is considerably enhanced.

B

Code for the Analysis of Reflexafs Data

A novel code for the analysis of EXAFS data collected in total reflection mode (ReflEXAFS) is presented here as a complementary part of the current work. This study is conducted in collaboration with the Department of Physics of the University of Rome "Tor Vergata" (Italy). The procedure calculates the theoretical fine structure signals appearing in the reflectivity spectrum starting from the ab initio *EXAFS calculations. These signals are then used in complex structural refinement (also including multiple scattering paths) with usual fitting programs of EXAFS data. A test case consisting in the analysis of a gold film collected at different incidence angle is presented in detail. The code is called CARD (**C**ode for the **A**nalysis of **R**eflexafs **D**ata), it is implemented in Python programming language and it is distributed to the scientific community under the open source GNU General Public License.*[1]

B.1 Principles of operation

On the basis of the reflEXAFS theory described in Sec. 2.2.3, the proposed method consists in 3 basic steps:

1. determination of sample specific parameters (namely density and roughness) permitting to reproduce the sample reflectivity. At this purpose the formulas from Eqs. 2.11, 2.14 and 2.15 are used to fit the smooth part of the measured reflectivity, $\Re$, both at fixed angle - variable energy, $\Re^{exp}(E)$, and *vice versa*, $\Re^{exp}(\phi)$.

2. generation of EXAFS theoretical scattering paths with an ab-initio code (FEFF, in this particular case).

3. generation of modified *Refl-EXAFS* theoretical scattering paths based on the reflectivity of the sample.

The newly calculated theoretical paths can later be used for the fitting of the oscillating part of the reflectivity, defined as $\chi_{\Re} = \Re^{exp}(E) - \Re_{background}$ with the standard fitting routines (IFEFFIT [148] in the present case). The flow diagram of the whole procedure, with the various steps evidenced, is shown in Fig. B.1.

The theoretical reflectivity $\Re$ is obtained via the Fresnel Theory [115], accounting for the surface roughness with the Névot-Croce formalism (see Eq. 2.15, [128]). This last approximation

[1] GNU General Public License as published by the Free Software Foundation, either version 3 of the License, or any later version. See `http://www.gnu.org/licenses/`

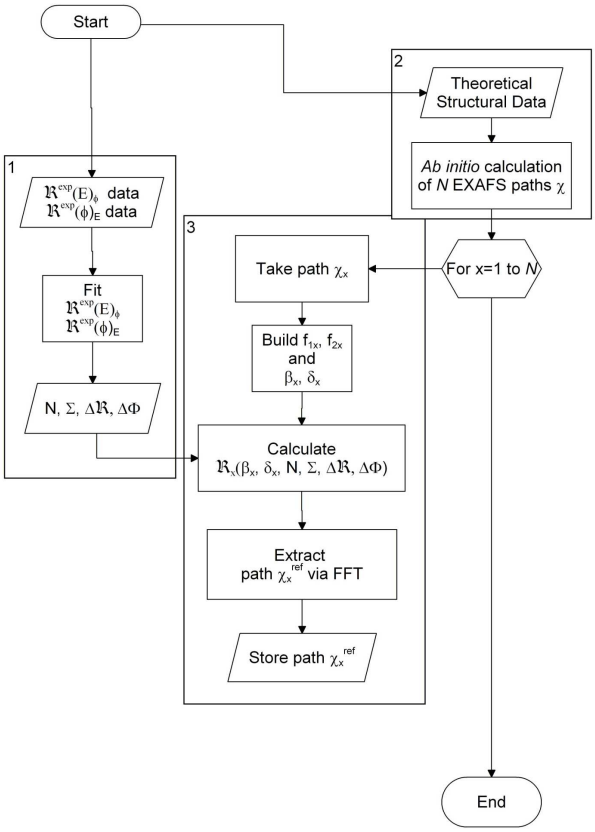

Figure B.1: Basic flowchart for the software algorithm.

was recently reviewed and shown to be fully valid in the description of EXAFS spectra collected in specular reflection geometry [362]. In the simple case of a thick homogeneous film presented here, the sample is described by only two variables: the material density N and the surface roughness Σ but the method can in principle deal also with more complex systems. The atomic scattering factors f_1 and f_2 necessary for the calculation are taken from the Cromer-Liebermann tables [363]. The experimental reflectivity spectrum at variable angle ϕ and fixed energy E, $\Re^{exp}(\phi)$, is then fitted to a model where N and Σ are refined together with experiment-peculiar variables as a constant level on the reflectivity $\Delta\Re$ and a small correction on the absolute value of the incidence angle $\Delta\phi$. The function $\sqrt{(\Re^{exp}(\phi))^2 - (\Re(\phi+\Delta\phi)+\Delta\Re)^2}$ is minimized at this purpose: note that the dependence on N is hidden in the expressions for δ and β contained in $\Re$. Taking the results of this first refinement, the fit is repeated on the reflectivity spectrum at variable energy $\Re^{exp}(E)$ neglecting the oscillating part of $\Re^{exp}$ and with the aim of reproducing correctly the shape of $\Re^{exp}$ far from the edge. At this stage the correction to the nominal incidence angle $\Delta\phi$ is refined again to account for the unavoidable positioning errors.

The parameters found in the previous step will be used to generate the modified scattering paths. First of all a new form for the f_2 function will be created that includes the oscillating part coming from a general x-th scattering path χ_x. This is done by summing this path to the tabulated values of f_2: note that the χ_x function generated by FEFF is a correction to the absorption coefficient μ and is normalized to an unitary edge step. In order to correctly carry out the sum, the χ_x signal has to be converted in f_2 units scaling it to the edge step of the absolute μ and inverting the right-side formula in Eq.2.11. In this way, a new oscillating function f_{2x} is thus obtained. Then, the associated f_{1x} function is calculated via a Kramers-

Kronig (KK) transformation using the DIFFKK algorithm included in IFEFFIT. Successively, a new pair of functions β_x, δ_x is calculated using Eq. 2.11 and the refined value of N. Finally, the $\Re_x(E)$ function is generated with using Eqq. 2.14 and 2.15 with the refined values for Σ at the angle ϕ with its correction $\Delta\phi$ and the constant level $\Delta\Re$. The newly calculated $\Re_x$ will contain an oscillatory part due to the x-th theoretical path χ_x that is extracted after the removal of the background and the separation in amplitude and phase terms (this, through a back-and-forth Fourier Transform) and finally saved as a new theoretical signal χ_x^{ref}. The operation is repeated for all the x scattering paths present in the FEFF calculation taken in consideration. Note that all these operations exploit dedicated functions of the IFEFFIT code. The generalization of the procedure to more complex systems like multilayers or buried layers can be carried out by suitably adapting the part of the code that calculates the reflectivity $\Re$, namely using the recursive formulation of the reflectivity given in Ref. [115]).

These new signals χ_x^{ref} possess the same structure as the standard files generated by FEFF so they can be used in conventional fitting routines based on IFEFFIT to extract quantitative structural parameters from the $\chi_\Re$ function. They are specific of the sample under investigation via the dependance on N and Σ and must be recalculated for different data collection angles ϕ. In this way, the method permits to take into account all paths generated by FEFF so it makes possible the fit of the experimental data also for multiple shells and including Multiple Scattering paths.

B.2 Application to a test case

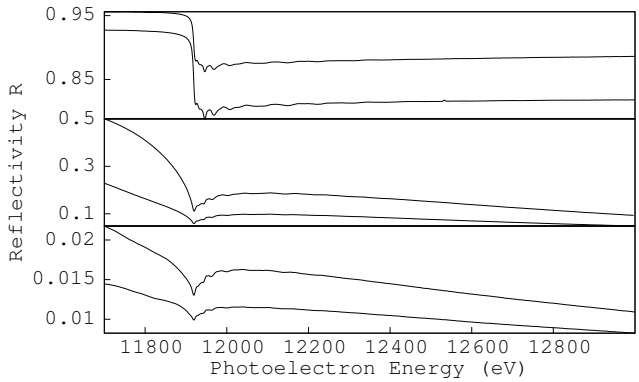

Figure B.2: Experimental ReflEXAFS data collected at different angles; top: total reflection regime (0.145 and 0.195 deg); center: around critical angle (0.345 and 0.365 deg); bottom: high angle (0.425 and 0.455 deg).

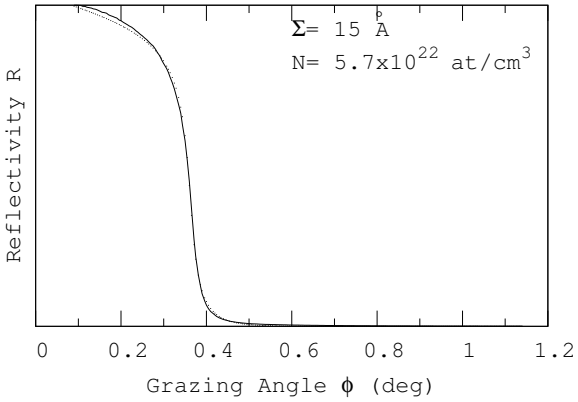

Figure B.3: Fit of the experimental $\Re^{exp}(\phi)$ spectrum collected at a fixed energy E=11700 eV. The dotted line represents the fit and the refined values of the volume atomic density N and the roughness Σ are shown in the inset. The value for $N = 5.7 \times 10^{22}$ at/cm^3 is smaller than the theoretical value of 5.9×10^{22} at/cm^3.

The measurements for the validation of the method are carried out at the gold L_{III} edge (11919 eV) on a gold film deposited on Silicon in the experimental ReflEXAFS chamber at the GILDA beamline (details in Sec. 2.3.1). The sample analyzed consisted in a nominally 2000 Å Au film deposited on a Si (111) substrate by evaporation[2]. Reflectivity at fixed energy (11700

[2]Kindly provided by C. Battocchio and G. Polzonetti from the *Roma Tre* University.

eV) is collected in a range from 0 to 1.14 deg, with a step of 0.005 deg. The experimental value for the critical angle is found to be ϕ_c = 0.36 deg in good agreement with the theoretical value (ϕ_c^{th} = 0.37 deg). Successively, a set of reflEXAFS spectra are collected at room temperature and fixed angle ranging from 0.145 to 0.455 deg in the energy range 11700 ÷ 12300 eV and some of them are shown in Fig. B.2. In order to obtain real reflectivity values from the raw data a blank spectrum - without the sample - is collected to calibrate the detectors response as a function of the energy. The spectrum of an Au foil in transmission mode, collected at the end of the experimental session, is used as reference compound.

As described in the previous section, the first operation of the procedure is the fitting of the $\Re^{exp}(\phi)$ spectrum as shown in Fig. B.3. Successively, for each spectrum of the data-set a fit of the $\Re^{exp}(E)$ data is carried out and the results are shown in Fig. B.4 for the spectra at two distinct collection angles. The refined values of the collection angles ϕ at this stage are presented in the first column of Tab. B.1.

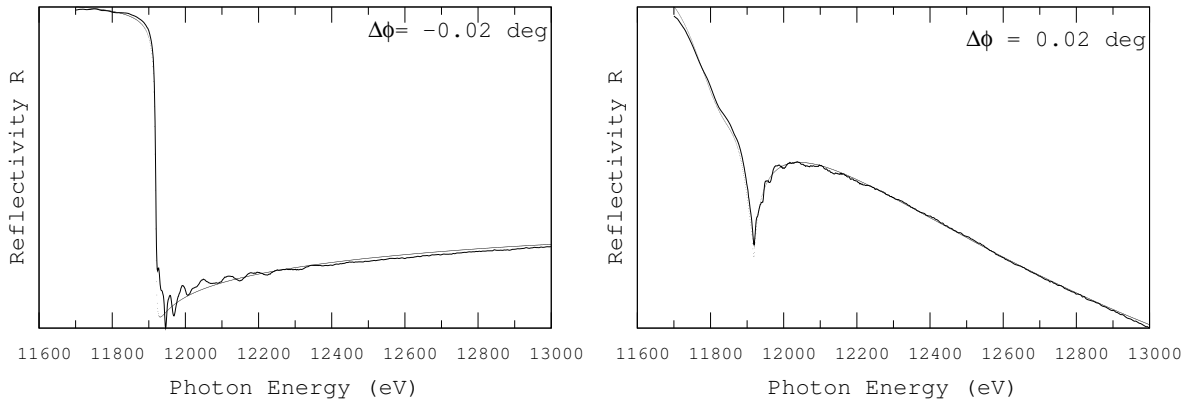

Figure B.4: Fits of $\Re^{exp}(E)$ at two angles: the first in total reflection (nominal ϕ=0.125 deg) and the second an high angle (0.474 deg). In both cases the dotted line represents the fit and the result of the angle refinement ($\Delta\phi$) is shown in the inset.

The oscillating part of the $\Re^{exp}(E)$ spectra, $\chi_{\Re}$, is extracted with the AUTOBK routine contained in IFEFFIT. Note that $\chi_{\Re}$ is defined as the the bare difference between $\Re^{exp}(E)$ and the approximating spline ($\Re_{background}$). This subtraction method produces $\chi_{\Re}$ functions that appear to be reversed in sign if compared with χ functions from conventional EXAFS data. Eventually, the value of E_0 is determined on the spectrum collected at the lowest angle and then transferred to all other spectra. The theoretical model for the analysis is built using the known gold structure (space group Fm$\bar{3}$m, lattice parameter, a = 4.080 Å taken from Ref. [364]. The fit of the data is carried out including all principal single and multiple scattering paths up to the 4^{th} shell. This model reveals to be sufficiently accurate to reproduce correctly the spectrum of a bulk Au foil.

Subsequently, the code is used to generate the modified scattering paths at different grazing angles. Finally, the structural refinements of the data at all collection angles are carried out following the standard procedure. The fits are carried out in R-space weighting data with k^2, and using Hanning windows for both k and R spaces (apodization parameters dk=1 Å^{-1} and dR = 0.5 Å). The k window is variable for the different measurements because of the considerable noise at high k due to the small EXAFS signal in spectra collected above the critical angle. The R window is kept constant (1.7–5.7 Å to take into account the first four shell peaks. The fitting parameters are defined as follows: for the first shell the shell radius R_1

Table B.1: Results of the quantitative analysis for the experimental ReflEXAFS data collected at different grazing angles (first column). The errors on the refined parameters are indicated in brackets; for the first column the value in square brackets indicates the nominal value of the collection angle.

$\phi(deg)$	S_0^2	R_1 Å	$delR$	$\sigma^2 \times 10^{-4}$Å^2	dTemp (K)	$\Delta E_0(eV)$
0.125[0.145]	0.78(5)	2.855(3)	-0.002(2)	86(5)	171(7)	5.2(3)
0.181[0.195]	0.79(4)	2.858(3)	-0.001(1)	87(4)	167(5)	5.4(4)
0.248[0.245]	0.78(4)	2.857(3)	-0.002(1)	85(4)	165(5)	5.3(3)
0.283[0.275]	0.78(4)	2.858(3)	-0.002(1)	86(4)	167(6)	5.4(3)
0.326[0.315]	0.86(5)	2.863(3)	0.001(1)	91(5)	167(6)	5.9(4)
0.353[0.345]	0.78(5)	2.867(4)	-0.001(2)	88(5)	167(6)	5.5(4)
0.371[0.365]	0.73(6)	2.858(4)	-0.001(2)	91(7)	170(8)	5.1(4)
0.398[0.385]	0.77(6)	2.868(4)	0.002(2)	81(7)	170(8)	5.6(5)
0.430[0.405]	0.85(7)	2.865(4)	0.0(2)	83(8)	167(8)	5.1(5)
0.452[0.425]	0.84(8)	2.865(5)	0.002(2)	85(9)	167(10)	5.3(5)
0.474[0.455]	0.8(1)	2.858(8)	-0.002(3)	8(1)	169(17)	4.8(7)
Au bulk foil	0.83(4)	2.858(2)	-0.002(1)	78(3)	173(5)	5.3(3)

and the related Debye-Waller factor (DWf) σ_1^2 are refined. For all the further shells is used a common scaling factor $delR$ for the the path length and the correlated Debye model [106, 243], with the Debye temperature ($dTemp$) as the fit parameter, for the DWf. $dTemp$ is not intended to be a determination of the physical Debye temperature but it represents a way to refine, using a single free parameter, the σ^2 values of a great number of paths including MS [243]. Further fit parameters are the many-body amplitude reduction factor S_0^2 and the correction of the edge position ΔE_0 and are common to all paths. The results of the quantitative analysis are shown in Tab. B.1.

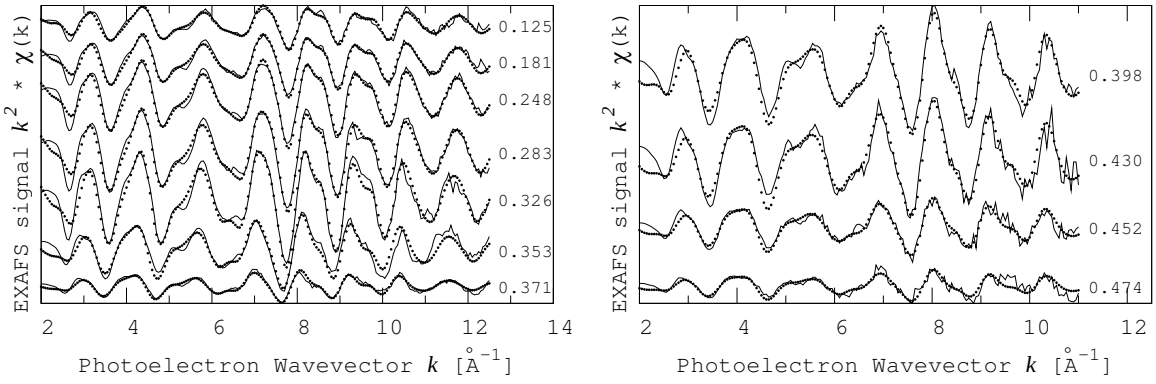

Figure B.5: Fit of the ReflEXAFS functions $\chi_{\Re}(k)$ of data collected at different grazing angles. The refined values of the grazing angles are displayed on the right side (in deg.). The continuous lines represents the experimental data, the dotted lines are the fit.

In Figs. B.5 and B.6 are represented respectively the fit results in k and R space. In all cases the fits are of good quality, reproducing all the main features of the $\chi_{\Re}$ function, and the results are constant, within the error bars, at all collection angles. It is worth to note a considerable stability of the fitting parameters denoting a correct determination of the signal phase and amplitude. For the the S_0^2 parameter however appreciable variations are visible on the spectra collected around the critical angle. In this region even small errors in the determination of the

angle have a considerable effect on the reflectivity so making very critical a precise amplitude analysis. The value of first shell σ^2 for the thin films is in general slightly greater than the value found for the bulk sample as already found in [365] and the overall values are in good agreement with recent data on Au clusters presented by [366].

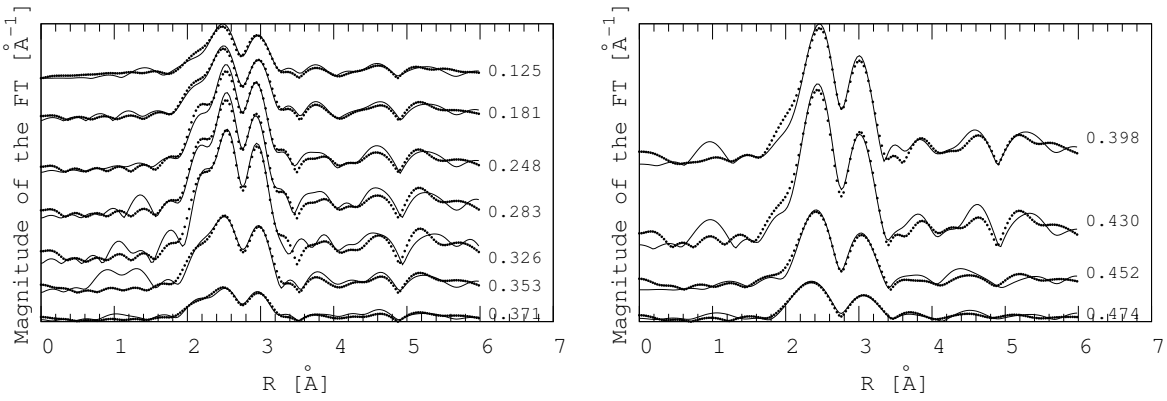

Figure B.6: Moduli of the Fourier Transforms of the $\chi_{\Re}(k)$ at different grazing angles (continuous line) with the corresponding best fit curves (dots). The refined values of the grazing angles are displayed on the right side (in deg.).

B.3 Conclusion

A new procedure permitting the structural refinement of the ReflEXAFS data at any collection angle is presented. The program permits the realization of complex structural refinements, also including MS paths. The results are accurate and do not depend on the grazing angle in the case of homogeneous samples. A good agreement is found with previously published data on Au films and nanoparticles.

In addition, the software is still under development in collaboration with the Scientific Software group of the ESRF, in order to provide a graphical user interface (GUI) and to permit the users to build specific theoretical models going beyond the simple case of a thin layer presented here. This will be implemented using the Pythonic Programming for Multilayers package.[3]

[3]See `http://www.esrf.eu/UsersAndScience/Experiments/TBS/SciSoft/OurSoftware/PPM`

Bibliography

[1] Samarth, N. An introduction to semiconductor spintronics. In Ehrenreich, H. & Spaepen, F. (eds.) *Solid State Physics*, vol. 58 of *Advances in Research and Applications*, chap. An introduction to semiconductor spintronics, 1–72 (Academic Press, 2004). 3, 5

[2] Zutic, I., Fabian, J. & Das Sarma, S. Spintronics: Fundamentals and applications. *Rev. Mod. Phys.* **76**, 323 (2004). 3, 5

[3] Datta, S. & Das, B. Electronic analog of the electro-optic modulator. *Appl. Phys. Lett.* **56**, 665–667 (1990). 3, 5

[4] Schmidt, G., Ferrand, D., Molenkamp, L. W., Filip, A. T. & van Wees, B. J. Fundamental obstacle for electrical spin injection from a ferromagnetic metal into a diffusive semiconductor. *Phys. Rev. B* **62**, R4790 (2000). 3, 5, 6

[5] Chiba, D. *et al.* Magnetization vector manipulation by electric fields. *Nature* **455**, 515 (2008). 3, 6

[6] Dietl, T., Ohno, H., Matsukura, F., Cibert, J. & Ferrand, D. Zener model description of ferromagnetism in zinc-blende magnetic semiconductors. *Science* **287**, 1019 (2000). 3, 8, 9

[7] Wolf, S. A. *et al.* Spintronics: A spin-based electronics vision for the future. *Science* **294**, 1488 (2001). 5

[8] Awschalom, D. D. & Flatte, M. E. Challenges for semiconductor spintronics. *Nat. Phys.* **3**, 153–159 (2007). 5

[9] Fabian, J., Matos-Abiague, A., Ertler, C., Stano, P. & Zutic, I. Semiconductor spintronics. *Acta Physica Slovaca* **57**, 565 (2007). 5

[10] Felser, C., Fecher, G. H. & Balke, B. Spintronics: A challenge for materials science and solid-state chemistry. *Angew. Chem. Int. Ed.* **46**, 668 (2007). 5

[11] Fert, A. Nobel lecture: Origin, development, and future of spintronics. *Rev. Mod. Phys.* **80**, 1517 (2008). 5

[12] Grünberg, P. A. Nobel lecture: From spin waves to giant magnetoresistance and beyond. *Rev. Mod. Phys.* **80**, 1531 (2008). 5

[13] Prinz, G. A. Magnetoelectronics applications. *J. Magn. Magn. Mater.* **200**, 57–68 (1999). 5

[14] Parkin, S. S. P. *et al.* Exchange-biased magnetic tunnel junctions and application to nonvolatile magnetic random access memory (invited). *J. Appl. Phys.* **85**, 5828–5833 (1999). 5

[15] Grünberg, P. Layered magnetic structures: History, highlights, applications. *Phys. Today* **54**, 31–37 (2001). 5

[16] Baibich, M. N. *et al.* Giant magnetoresistance of (001)fe/(001)cr magnetic superlattices. *Phys. Rev. Lett.* **61**, 2472 (1988). 5

[17] Binasch, G., Grünberg, P., Saurenbach, F. & Zinn, W. Enhanced magnetoresistance in layered magnetic structures with antiferromagnetic interlayer exchange. *Phys. Rev. B* **39**, 4828 (1989). 5

[18] Moodera, J. S., Kinder, L. R., Wong, T. M. & Meservey, R. Large magnetoresistance at room temperature in ferromagnetic thin film tunnel junctions. *Phys. Rev. Lett.* **74**, 3273– (1995). 5

[19] Ney, A., Pampuch, C., Koch, R. & Ploog, K. H. Programmable computing with a single magnetoresistive element. *Nature* **425**, 485–487 (2003). 5

[20] Zutic, I., Fabian, J. & Erwin, S. C. Bipolar spintronics: from spin injection to spin-controlled logic. *J. Phys.: Condens. Matter* **19**, 165219 (23pp) (2007). 5

[21] Gurzhi, R. N., Kalinenko, A. N., Kopeliovich, A. I. & Yanovsky, A. V. Spin field-effect transistor with electric control. *J. Appl. Phys.* **105**, 103713 (2009). 5

[22] Ramsteiner, M. *et al.* Electrical spin injection from ferromagnetic mnas metal layers into gaas. *Phys. Rev. B* **66**, 081304 (2002). 5

[23] Khaetskii, A. *et al.* Spin injection across magnetic/nonmagnetic interfaces with finite magnetic layers. *Phys. Rev. B* **71**, 235327– (2005). 5

[24] Furdyna, J. K. Diluted magnetic semiconductors. *Journal Applied Physics* **64**, R29–R64 (1988). 5, 6

[25] Kossut, J. & Dobrowolski, W. Diluted magnetic semiconductors. In Buschow, K. H. J. (ed.) *Handbook of Magnetic Materials*, vol. 7, chap. 4 (Elsevier, 1993). 5, 6

[26] Dietl, T. Dilute magnetic semiconductors: Functional ferromagnets. *Nat. Mater.* **2**, 646 (2003). 5

[27] Camarero, J. & Coronado, E. Molecular vs. inorganic spintronics: the role of molecular materials and single molecules. *J. Mater. Chem.* **19**, 1678 (2009). 5

[28] Matsukura, F., Chiba, D. & Ohno, H. Spintronic properties of ferromagnetic semiconductors. In Weber, E. (ed.) *Spintronics*, vol. 82 of *Semiconductors and Semimetals*, chap. 5, 207 – 240 (Elsevier, 2008). 5

[29] Fert, A. & Jaffrès, H. Conditions for efficient spin injection from a ferromagnetic metal into a semiconductor. *Phys. Rev. B* **64**, 184420 (2001). 6

[30] Rashba, E. I. Theory of electrical spin injection: Tunnel contacts as a solution of the conductivity mismatch problem. *Phys. Rev. B* **62**, R16267 (2000). 6

[31] Fiederling, R. *et al.* Injection and detection of a spin-polarized current in a light-emitting diode. *Nature* **402**, 787 (1999). 6

[32] Ohno, Y. *et al.* Electrical spin injection in a ferromagnetic semiconductor heterostructure. *Nature* **402**, 790 (1999). 6

[33] Gałązka, R. R. Semimagnetic semiconductors based on mercury manganese telluride (hgmnte) and cadmium manganese telluride (cdmnte). *Inst. Phys. Conf. Series* **43**, 133 (1979). 6

[34] Dobrowolski, W., Kossut, J. & Story, T. Ii–vi and iv–vi diluted magnetic semiconductors – new bulk materials and low-dimensional quantum structures. In Buschow, K. H. J. (ed.) *Handbook of Magnetic Materials*, vol. 15, chap. 3, 289 (Elsevier, 2003). 6

[35] Matsukura, F. & Ohno, H. Ferromagnetic semiconductors. In *Handbook of Magnetism and Advanced Magnetic Materials* (John Wiley & Sons, 2007). 6

[36] Bonanni, A. Ferromagnetic nitride-based semiconductors doped with transition metals and rare earths. *Semicond. Sci. Technol.* **22**, R41–R56 (2007). 6, 10

[37] Ludwig, G. W. & Woodbury, H. H. In Ehrenreich, H., Seitz, F. & Turnbull, D. (eds.) *Solid State Physics: Advances in Research and Applications*, vol. 13, 263 (Academic, New York, 1962). 6

[38] Anderson, P. W. Model for the electronic structure of amorphous semiconductors. *Phys. Rev. Lett.* **34**, 953– (1975). 6

[39] Haldane, F. D. M. & Anderson, P. W. Simple model of multiple charge states of transition-metal impurities in semiconductors. *Phys. Rev. B* **13**, 2553 (1976). 6

[40] Singh, V. A. & Vengurlekar, A. S. Transition-metal impurities in semiconductors and the haldane-anderson model. *Phys. Rev. B* **30**, 3527 (1984). 6

[41] Dietl, T. Lecture notes on semiconductor spintronics (2007). ArXiv:0801.0145v1. 7

[42] Dietl, T. Semiconductor spintronics. In *Modern Aspects of Spin Physics*, Lecture Notes in Physics, 1–46 (Springer Berlin / Heidelberg, 2007). 6, 9

[43] Dietl, T. Exchange interactions and nanoscale phase separations in magnetically doped semiconductors. In Weber, E. (ed.) *Spintronics*, vol. 82 of *Semiconductors and Semimetals*, chap. 9, 371 – 432 (Elsevier, 2008). 6, 8, 9, 99, 103

[44] Wolos, A. & Kaminska, M. Magnetic impurities in wide band[hyphen (true graphic)]gap iii-v semiconductors. In Weber, E. (ed.) *Spintronics*, vol. 82 of *Semiconductors and Semimetals*, chap. 8, 325 – 369 (Elsevier, 2008). 6

[45] Kaminska, M., Twardowski, A. & Wasik, D. Mn and other magnetic impurities in gan and other iii–v semiconductors – perspective for spintronic applications. *J. Mater. Sci.: Mater. Electron.* **19**, 828 (2008). 6

[46] Malguth, E., Hoffmann, A. & Phillips, M. R. Fe in iii-v and ii-vi semiconductors. *Phys. Status Solidi B* **245**, 455–480 (2008). 6, 67

[47] Dietl, T. Ferromagnetic semiconductors. *Semicond. Sci. Technol.* **17**, 377–392 (2002). 7

[48] Jungwirth, T., Sinova, J., Masek, J., Kucera, J. & MacDonald, A. H. Theory of ferromagnetic (iii,mn)v semiconductors. *Rev. Mod. Phys.* **78**, 809 (2006). 7, 8, 44

[49] Ashcroft, N. W. & Mermin, N. D. *Solid state Physics* (Saunders College / Harcourt Brace College, 1976). 7, 33

[50] Smirnov, S., Bercioux, D., Grifoni, M. & Richter, K. Quantum dissipative rashba spin ratchets. *Phys. Rev. Lett.* **100**, 230601 (2008). 7

[51] Flatte, M. E. Spin ratchets: A one-way street for spin current. *Nat. Phys.* **4**, 587–588 (2008). 7

[52] Saarikoski, H. & Bauer, G. E. W. Spin accumulation with spin-orbit interaction. *Phys. Rev. Lett.* **102**, 097204 (2009). 7

[53] Duan, F. & Guojun, J. *Introduction to Condensed Matter Physics* (World Scientific, 2005). 7, 8

[54] Marder, M. P. *Condensed Matter Physics* (Wiley, New York, 1999). 7

[55] Sanvito, S., Theurich, G. & Hill, N. A. Density functional calculations for iii–v diluted ferromagnetic semiconductors: A review. *J. Supercond.* **15**, 85–104 (2002). 7

[56] Sato, K. & Katayama-Yoshida, H. First principles materials design for semiconductor spintronics. *Semicond. Sci. Technol.* **17**, 367 (2002). 7

[57] Liu, C., Yun, F. & Morkoç, H. Ferromagnetism of zno and gan: A review. *J. Mater. Sci.: Mater. Electron.* **16**, 555–597 (2005). 7, 8, 55

[58] Anderson, P. W. Antiferromagnetism. theory of superexchange interaction. *Phys. Rev.* **79**, 350 (1950). 7

[59] Zener, C. Interaction between the d-shells in the transition metals .2. ferromagnetic compounds of manganese with perovskite structure. *Phys. Rev.* **82**, 403 (1951). 8

[60] Zener, C. Interaction between the d-shells in the transition metals. *Phys. Rev.* **81**, 440 (1951). 8

[61] Van Vleck, J. H. Note on the interactions between the spins of magnetic ions or nuclei in metals. *Rev. Mod. Phys.* **34**, 681– (1962). 8

[62] Ziener, C. H., Glutsch, S. & Bechstedt, F. Rkky interaction in semiconductors: Effects of magnetic field and screening. *Phys. Rev. B* **70**, 075205– (2004). 8

[63] Kacman, P. Spin interactions in diluted magnetic semiconductors and magnetic semiconductor structures. *Semicond. Sci. Technol.* **16**, R25–R39 (2001). 8

[64] Cibert, J. & Scalbert, D. Diluted magnetic semiconductors: Basic physics and optical properties. In *Spin Physics in Semiconductors*, 389–431 (Springer Berlin Heidelberg, 2008). 8

[65] Dietl, T., Ohno, H. & Matsukura, F. Hole-mediated ferromagnetism in tetrahedrally coordinated semiconductors. *Phys. Rev. B* **63**, 195205 (2001). 8

[66] Dietl, T. Origin and control of ferromagnetism in dilute magnetic semiconductors and oxides (invited). *J. Appl. Phys.* **103**, 07D111 (2008). Proceedings of the 52nd Annual Conference on Magnetism and Magnetic Materials. 8

[67] Dietl, T. Origin of ferromagnetic response in diluted magnetic semiconductors and oxides. *J. Phys.: Condens. Matter* **19**, 165204 (15pp) (2007). 10

[68] Martinez-Criado, G. *et al.* Mn-rich clusters in gan: Hexagonal or cubic symmetry? *Appl. Phys. Lett.* **86**, 131927 (2005). 10

[69] Gu, L. *et al.* Characterization of al(cr)n and ga(cr)n dilute magnetic semiconductors. *J. Magn. Magn. Mater.* **290-291**, 1395 (2005). Proceedings of the Joint European Magnetic Symposia (JEMS' 04). 10

[70] Samarth, N. Ferromagnetic semiconductors: Ruled by a magnetic-rich minority. *Nat. Mater.* **6**, 403 (2007). 10

[71] Kuroda, S. *et al.* Origin and control of high-temperature ferromagnetism in semiconductors. *Nat. Mater.* **6**, 440–446 (2007). 10, 74

[72] Cahn, J. W. & Hilliard, J. E. Free energy of a nonuniform system. i. interfacial free energy. *J. Chem. Phys.* **28**, 258–267 (1958). 10

[73] Cahn, J. W. Free energy of a nonuniform system. ii. thermodynamic basis. *J. Chem. Phys.* **30**, 1121–1124 (1959). 10

[74] Cahn, J. W. & Hilliard, J. E. Free energy of a nonuniform system. iii. nucleation in a two-component incompressible fluid. *J. Chem. Phys.* **31**, 688–699 (1959). 10

[75] Cahn, J. W. On spinodal decomposition. *Acta Metallurgica* **9**, 795 – 801 (1961). 10

[76] Cahn, J. W. Coherent fluctuations and nucleation in isotropic solids. *Acta Metallurgica* **10**, 907 – 913 (1962). 10

[77] Cahn, J. W. Phase separation by spinodal decomposition in isotropic systems. *J. Chem. Phys.* **42**, 93–99 (1965). 10

[78] Schilfgaarde, M. v. & Mryasov, O. N. Anomalous exchange interactions in iii-v dilute magnetic semiconductors. *Phys. Rev. B* **63**, 233205 (2001). 10, 96

[79] Ferhat, M. & Bechstedt, F. First-principles calculations of gap bowing in inxga1-xn and inxal1-xn alloys: Relation to structural and thermodynamic properties. *Phys. Rev. B* **65**, 075213 (2002). 10

[80] Katayama-Yoshida, H. *et al.* Theory of ferromagnetic semiconductors. *Phys. Status Solidi A* **204**, 15–32 (2007). 10

[81] Dederichs, P. H., Sato, K. & Katayama-yoshida, H. Dilute magnetic semiconductors. *Phase Transitions* **78**, 851 (2005). 10

[82] Atzmon, M. Monte-carlo simulations of spinodal ordering and decomposition in compositionally modulated alloys. *J. Mater. Res.* **5**, 92 (1990). 11

[83] Sato, K., Katayama-Yoshida, H. & Dederichs, P. H. High curie temperature and nano-scale spinodal decomposition phase in dilute magnetic semiconductors. *Jpn. J. Appl. Phys.* **44**, L948–L951 (2005). 11, 57

[84] Fukushima, T., Sato, K., Katayama-Yoshida, H. & Dederichs, P. H. Spinodal decomposition under layer by layer growth condition and high curie temperature quasi-one-dimensional nano-structure in dilute magnetic semiconductors. *Jpn. J. Appl. Phys.* **45**, L416 (2006). 11, 74

[85] Mermin, N. D. & Wagner, H. Absence of ferromagnetism or antiferromagnetism in one- or two-dimensional isotropic heisenberg models. *Phys. Rev. Lett.* **17**, 1133 (1966). 11

[86] Sayers, D. E., Stern, E. A. & Lytle, F. W. New technique for investigating noncrystalline structures: Fourier analysis of the extended x-ray absorption fine structure. *Phys. Rev. Lett.* **27**, 1204–1207 (1971). 13, 15

[87] Lee, P. A. & Pendry, J. B. Theory of the extended x-ray absorption fine structure. *Phys. Rev. B* **11**, 2795– (1975). 13, 18

[88] Natoli, C. R. & Benfatto, M. A unifying scheme of interpretation of x-ray absorption spectra based on the multiple scattering theory. *J. Phys. Colloques* **47**, C8–11 (1986). 13, 19, 20

[89] Rehr, J. J. & Albers, R. C. Theoretical approaches to x-ray absorption fine structure. *Rev. Mod. Phys.* **72**, 621– (2000). 13, 15, 19

[90] Raoux, D. *et al.* Effet mossbauer et techniques complémentaires : Iii. l'exafs appliqué aux déterminations structurales de milieux désordonnés. *Revue de Physique Appliquée* **15**, 1079–1094 (1980). 15

[91] Lee, P. A., Citrin, P. H., Eisenberger, P. & Kincaid, B. M. Extended x-ray absorption fine structure: its strengths and limitations as a structural tool. *Rev. Mod. Phys.* **53**, 769– (1981). 15, 20

[92] Hayes, T. M. & Boyce, J. B. Extended x-ray absorption fine-structure spectroscopy. *Solid State Physics - Advances In Research And Applications* **37**, 173–351 (1982). 15

[93] Stumm von Bordwehr, R. A history of x-ray absorption fine structure. *Annales de Physique* **14**, 377–465 (1989). 15

[94] Filipponi, A., Di Cicco, A. & Natoli, C. R. X-ray-absorption spectroscopy and n-body distribution functions in condensed matter. i. theory. *Phys. Rev. B* **52**, 15122 (1995). 15, 19

[95] Crozier, E. D. A review of the current status of xafs spectroscopy. *Nuclear Instruments and Methods B* **133**, 134–144 (1997). 15

[96] Filipponi, A. Exafs for liquids. *J. Phys.: Condens. Matter* **13**, R23–R60 (2001). 15

[97] Natoli, C. R., Benfatto, M., Longa, S. D. & Hatada, K. X-ray absorption spectroscopy: state-of-the-art analysis. *J. Synchrotron Rad.* **10**, 26–42 (2003). 15

[98] Teo, B. K. (ed.) *EXAFS spectroscopy : basics principles and data analysis* (Springer-Verlag, New York, 1986). 15

[99] Koningsberger, D. & Prins, R. (eds.) *X-ray Absorption: Principles, Applications, Techniques of EXAFS, SEXAFS and XANES* (John Wiley & Sons Inc, 1988). 15

[100] Boscherini, F. X-ray absorption fine structure in the study of semiconductor heterostructures and nanostructures. In Lamberti, C. (ed.) *Characterization of Semiconductor Heterostructures and Nanostructures*, chap. 9, 289–330 (Elsevier, 2008). 15

[101] Kronig, R. d. L. Zur theorie der feinstruktur in den röntgenabsorptionsspektren. *Zeitschrift Physik* **70**, 317–323 (1931). 15

[102] Stern, E. A. Musings about the development of xafs. *J. Synchrotron Rad.* **8**, 49–54 (2001). 15

[103] Brandsen, B. & Joachain, C. *Physics of Atoms and Molecules* (Prentice Hall, 2003). 17

[104] Parratt, L. G. Electronic band structure of solids by x-ray spectroscopy. *Rev. Mod. Phys.* **31**, 616 (1959). 17

[105] Beni, G. & Platzman, P. M. Temperature and polarization dependence of extended x-ray absorption fine-structure spectra. *Phys. Rev. B* **14**, 1514– (1976). 19

[106] Zabinsky, S. I., Rehr, J. J., Ankudinov, A., Albers, R. C. & Eller, M. J. Multiple-scattering calculations of x-ray-absorption spectra. *Phys. Rev. B* **52**, 2995 (1995). 19, 121

[107] Bianconi, A. *et al.* Multiple-scattering effects in the k-edge x-ray-absorption near-edge structure of crystalline and amorphous silicon. *Phys. Rev. B* **36**, 6426– (1987). 20

[108] Joly, Y. X-ray absorption near-edge structure calculations beyond the muffin-tin approximation. *Phys. Rev. B* **63**, 125120– (2001). 20

[109] Stöhr, J. *NEXAFS Spectroscopy*, vol. 25 of *Springer Series in Surface Sciences* (Springer-Verlag, 1992), 1 edn. 20

[110] Longa, S. D., Arcovito, A., Girasole, M., Hazemann, J. L. & Benfatto, M. Quantitative analysis of x-ray absorption near edge structure data by a full multiple scattering procedure: The fe-co geometry in photolyzed carbonmonoxy-myoglobin single crystal. *Phys. Rev. Lett.* **87**, 155501– (2001). 20

[111] Benfatto, M. & Della Longa, S. Geometrical fitting of experimental xanes spectra by a full multiple-scattering procedure. *J. Synchrotron Rad.* **8**, 1087–1094 (2001). 20

[112] Benfatto, M., Della Longa, S. & Natoli, C. R. The *mxan* procedure: a new method for analysing the xanes spectra of metalloproteins to obtain structural quantitative information. *J. Synchrotron Rad.* **10**, 51–57 (2003). 20

[113] Wilke, M., Farges, F., Petit, P.-E., Brown, J., Gordon E. & Martin, F. Oxidation state and coordination of fe in minerals: An fe k-xanes spectroscopic study. *Am. Mineral.* **86**, 714–730 (2001). 20

[114] Barchewitz, R., Cremonese-Visicato, M. & Onori, G. X-ray photoabsorption of solids by specular reflection. *J. Phys. C* **11**, 4439–4445 (1978). 20

[115] Parratt, L. G. Surface studies of solids by total reflection of x-rays. *Phys. Rev.* **95**, 359 (1954). 21, 117, 119

[116] Heald, S. M., Chen, H. & Tranquada, J. M. Glancing-angle extended x-ray-absorption fine structure and reflectivity studies of interfacial regions. *Phys. Rev. B* **38**, 1016 (1988). 21, 22, 107

[117] D'Acapito, F., Ghigna, P., Alessandri, I., Cardelli, A. & Davoli, I. Probing the initial stages of solid-state reactions by total reflection exafs (reflexafs). *Nucl. Instr. Meth. B* **200**, 421 (2003). 21

[118] Hecht, D., Borthen, P. & Strehblow, H. H. An x-ray absorption fine structure study of the initial stages of the anodic oxidation of silver. *Surf. Sci.* **365**, 263 – 277 (1996). 21

[119] Lützenkirchen-Hecht, D. & Frahm, R. Reflection mode x-ray absorption spectroscopy: new applications in surface science research. *Physica B* **357**, 213 (2005). 21, 107

[120] Jiang, D. T., Crozier, E. D. & Heinrich, B. Structure determination of metastable epitaxial cu layers on ag(001) by glancing-incidence x-ray-absorption fine structure. *Phys. Rev. B* **44**, 6401 (1991). 21

[121] D'Acapito, F., Milita, S., Satta, A. & Colombo, L. Depth resolved study of impurity sites in low energy ion implanted as in si. *J. Appl. Phys.* **102**, 043524 (2007). 21, 107

[122] Jiang, D. T., Alberding, N., Seary, A. J. & Crozier, E. D. Angular scanning stage for glancing-incidence surface exafs. *Rev. Sci. Instrum.* **59**, 60–63 (1988). 21

[123] Pizzini, S. *et al.* Instrumentation for glancing angle x-ray absorption spectroscopy on the synchrotron radiation source. *Rev. Sci. Instrum.* **60**, 2525 (1989). INTERNATIONAL CONFERENCE ON SYNCHROTRON RADIATION INSTRUMENTATION. 21

[124] Oyanagi, H. *et al.* A new apparatus for surface x-ray absorption and diffraction studies using synchrotron radiation. *Rev. Sci. Instrum.* **66**, 5477–5485 (1995). 21

[125] Hecht, D., Frahm, R. & Strehblow, H.-H. Quick-scanning exafs in the reflection mode as a probe for structural information of electrode surfaces with time resolution: an in situ study of anodic silver oxide formation. *J. Phys. Chem.* **100**, 10831–10833 (1996). 21

[126] D'Acapito, F., Davoli, I., Ghigna, P. & Mobilio, S. The reflexafs station at the gilda beamline (bm08) of esrf. *J. Synchrotron Rad.* **10**, 260 (2003). 21, 23

[127] Lopez-Flores, V. *et al.* Optimized end station and operating protocols for reflection extended x-ray absorption fine structure (reflexafs) investigations of surface structure at the european synchrotron radiation facility beamline bm29. *Rev. Sci. Instrum.* **78**, 013109 (2007). 21

[128] Névot, L. & Croce, P. Caractérisation des surfaces par réflexion rasante de rayons x. application à l'étude du polissage de quelques verres silicates. *Rev. Phys. Appl.* **15**, 761 (1980). 21, 117

[129] Martens, G. & Rabe, P. Exafs studies on superficial regions by means of total reflection. *Phys. Status Solidi A* **58**, 415–424 (1980). 21

[130] Borthen, P. & Strehblow, H.-H. X-ray-reflectivity fine structure and exafs. *Phys. Rev. B* **52**, 3017 (1995). 21, 22

[131] Poumellec, B., Cortes, R., Lagnel, F. & Tourillon, G. A new method to extract the x-ray absorption fine structures from the reflectivity spectra : application to the study of (ti, nb) o2 amorphous solid solutions. *Physica B* **158**, 282 – 283 (1989). 21

[132] Benzi, F., Davoli, I., Rovezzi, M. & d'Acapito, F. A new procedure for the quantitative analysis of extended x-ray absorption fine structure data in total reflection geometry. *Rev. Sci. Instrum.* **79**, 103902 (2008). 22

[133] Jiang, D. T. & Crozier, E. D. Glancing angle exafs of ultra thin films: Negligible anomalous dispersion effects. *J. Phys. IV* **C2**, 247–248 (1997). 22, 107

[134] D'Acapito, F. *et al.* Gilda (italian beamline) on bm08. *ESRF Newsletter* **30**, 42 (1998). 22

[135] Pascarelli, S. *et al.* X-ray optics of a dynamical sagittai-focusing monochromator on the gilda beamline at the esrf. *J. Synchrotron Rad.* **3**, 147 (1996). 22, 59

[136] Ice, G. E. & Sparks, C. J. Conical geometry for sagittal focusing as applied to x rays from synchrotrons. *J. Opt. Soc. Am. A* **11**, 1265 (1994). 22

[137] Hazemann, J., Nayouf, K. & de Bergevin, F. Modelisation by finite elements of sagittal focusing. *Nucl. Instr. Meth. B* **97**, 547 (1995). Synchrotron Radiation in Materials Science. 22

[138] Batterman, B. W. & Bilderback, D. H. X-ray monochromators and mirrors. In *Handbook on Synchrotron Radiation*, chap. 4 (Amsterdam: North-Holland, 1991). 23

[139] Mills, D. & Pollock, V. Stabilizing feedback system for synchrotron radiation monochromators. *Rev. Sci. Instrum.* **51**, 1664–1668 (1980). 23

[140] Jaklevic, J. *et al.* Fluorescence detection of exafs: Sensitivity enhancement for dilute species and thin films. *Solid State Commun.* **23**, 679 – 682 (1977). 23, 107

[141] Gudat, W. & Kunz, C. Close similarity between photoelectric yield and photoabsorption spectra in the soft-x-ray range. *Phys. Rev. Lett.* **29**, 169 (1972). 23

[142] Janousch, M. *et al.* Lucia — a new 1–7 kev mu-xas beamline. *AIP Conf. Proc.* **705**, 312–315 (2004). 24

[143] Flank, A.-M. *et al.* Lucia, a microfocus soft xas beamline. *Nucl. Instr. and Meth. in Phys. Res. B* **246**, 269 – 274 (2006). Synchrotron Radiation and Materials Science - Proceedings of the E-MRS 2005 Symposium O on Synchrotron Radiation and Materials Science. 24

[144] Lagarde, P., Flank, A.-M., Vantelon, D. & Janousch, M. Micro-soft x-ray spectroscopy with the lucia beamline. *AIP Conf. Proc.* **882**, 852–857 (2007). 24

[145] Klementev, K. V. Extraction of the fine structure from x-ray absorption spectra. *J. Phys. D: Appl. Phys.* **34**, 209–217 (2001). 26

[146] Newville, M., Līviņš, P., Yacoby, Y., Rehr, J. J. & Stern, E. A. Near-edge x-ray-absorption fine structure of pb: A comparison of theory and experiment. *Phys. Rev. B* **47**, 14126 (1993). 26

[147] Ravel, B. & Newville, M. *ATHENA*, *ARTEMIS*, *HEPHAESTUS*: data analysis for X-ray absorption spectroscopy using *IFEFFIT*. *J. Synchrotron Rad.* **12**, 537–541 (2005). 26, 27

[148] Newville, M. *IFEFFIT*: interactive XAFS analysis and *FEFF* fitting. *J. Synchrotron Rad.* **8**, 322–324 (2001). 27, 117

[149] Ankudinov, A. L., Ravel, B., Rehr, J. J. & Conradson, S. D. Real-space multiple-scattering calculation and interpretation of x-ray-absorption near-edge structure. *Phys. Rev. B* **58**, 7565– (1998). 27

[150] Taylor, J. R. *An Introduction to Error Analysis: The Study of Uncertainties in Physical Measurements* (University Science Books; 2nd edition, 1997). 27

[151] NIST/SEMATECH. *Engineering Statistics Handbook* (2006). See http://www.itl.nist.gov/div898/handbook. 27

[152] Filipponi, A. Statistical errors in x-ray absorption fine-structure data analysis. *J. Phys.: Condens. Matter* **7**, 9343 (1995). 27

[153] Michalowicz, A., Provost, K., Laruelle, S., Mimouni, A. & Vlaic, G. F-test in exafs fitting of structural models. *J. Synchrotron Rad.* **6**, 233 (1999). 27

[154] Venables, J. A., Spiller, G. D. T. & Hanbucken, M. Nucleation and growth of thin films. *Rep. Prog. Phys.* **47**, 399–459 (1984). 31

[155] Nishinaga, T. Atomistic aspects of molecular beam epitaxy. *Prog. Cryst. Growth Charact. Mater.* **48-49**, 104 – 122 (2004). Vapour Growth of Bulk Crystals and Epitaxy: Part II. 31

[156] Frank, F. C. & van der Merwe, J. H. One-dimensional dislocations. i. static theory. *Proc. R. Soc. Lond. A* **198**, 205–216 (1949). 31

[157] Frank, F. C. & van der Merwe, J. H. One-dimensional dislocations. ii. misfitting monolayers and oriented overgrowth. *Proc. R. Soc. Lond. A* **198**, 216–225 (1949). 31

[158] Volmer, M. & Weber, A. Keimbildung in übersättingten gebilden (nucleus formation in supersaturated systems). *Z. Phys. Chem.* **119**, 277 (1926). 31

[159] Stranski, I. N. & Krastanov, L. Sitzungbericht der akademie der wissn-scaften wien. *Math.-Naturwiss. Klasse IIb* **146**, 797 (1937). 31

[160] O'Connell, S., Hoevel, R., Deschler, M. & Juergensen, H. Movpe for production scale manufacturing. *III-Vs Review* **10**, 14 – 17 (1997). 32

[161] DenBaars, S. P. & Keller, S. Metalorganic chemical vapor deposition (mocvd) of group iii nitrides. In *Semicondutors and semimetals*, vol. 50, 11–37 (Academic Press Inc, 1998). 32

[162] Fujiwara, H. Introduction to spectroscopic ellipsometry. In *Spectroscopic Ellipsometry*, 1–11 (John Wiley & Sons Inc, 2007). 32

[163] Aspnes, D. E., Quinn, W. E. & Gregory, S. Application of ellipsometry to crystal growth by organometallic molecular beam epitaxy. *Appl. Phys. Lett.* **56**, 2569 (1990). 32

[164] Bonanni, A. *et al.* In situ spectroscopic ellipsometry of mocvd-grown gan compounds for on-line composition determination and growth control. *J. Cryst. Growth* **248**, 211–215 (2003). 32, 53, 55

[165] Ramil, A. M. *et al.* In-situ growth monitoring by spectroscopy ellipsometry of mocvd cubic-gan(001). *Thin Solid Films* **455-456**, 684 – 687 (2004). The 3rd International Conference on Spectroscopic Ellipsometry. 32

[166] Tompkins, H. G. *A User's Guide to Ellipsometry* (Dover Publications, 2006). 32

[167] Aspnes, D. E. Minimal-data approaches for determining outer-layer dielectric responses of films from kinetic reflectometric and ellipsometric measurements. *J. Opt. Soc. Am. A* **10**, 974–983 (1993). 32

[168] Friedrich, W., Knipping, P. & Laue, M. Interferenz-erscheinungen bei rontgenstrahlen. *Proc. Bavarian Acad. Sci.* 303 (1912). 33

[169] Bragg, W. H. & Bragg., W. L. *Proc. Royal Soc. A* **88**, 428 (1913). 33

[170] Warren, B. E. *X-ray Diffraction* (Dover Publication, New York, 1990). 33

[171] Bowen, D. K. & Tanner, B. K. *HIgh Resolution X-ray Diffractometry and Topography* (Taylor & Francis Ltd., 1998). 33

[172] Williamson, G. & Hall, W. X-ray line broadening from filed aluminium and wolfram. *Acta Metallurgica* **1**, 22 – 31 (1953). 34

[173] Rietveld, H. M. A profile refinement method for nuclear and magnetic structures. *J. Appl. Crystallogr.* **2**, 65–71 (1969). 34

[174] Devillers, T. *Ferromagnetic phases of Ge(1-x)Mn(x) for spintronics applications*. Ph.D. thesis, Université Joseph Fourier, Grenoble (2008). N.: tel-00367396. 34, 71, 73, 74, 75, 76, 77

[175] Golovin, A. L., Imamov, R. M. & Stepanov, S. A. Experimental study of x-ray diffraction under specular reflection conditions. *Acta Cryst. A* **40**, 225–228 (1984). 34

[176] Dosch, H., Batterman, B. W. & Wack, D. C. Depth-controlled grazing-incidence diffraction of synchrotron x radiation. *Phys. Rev. Lett.* **56**, 1144– (1986). 34

[177] Jach, T., Cowan, P. L., Shen, Q. & Bedzyk, M. J. Dynamical diffraction of x rays at grazing angle. *Phys. Rev. B* **39**, 5739– (1989). 34

[178] Hirsch, P., Howie, A., Nicholson, R., Pashley, D. W. & Whelan, M. J. *Electron Microscopy of Thin Crystals* (R. E. Krieger Publishing Co., 1977). 35

[179] Ruska, E. Über fortschritte im bau und in der leistung des magnetischen elektronenmikroskops (on the progress in the construction and performance of the magnetic electron microscope). *Z. Phys.* **87**, 580–602 (1934). 35

[180] Ruska, E. The development of the electron microscope and of electron microscopy. *Rev. Mod. Phys.* **59**, 627– (1987). 35

[181] Rose, H. H. Optics of high-performance electron microscopes. *Sci. Technol. Adv. Mater.* **9**, 014107 (2008). 35

[182] Bendersky, L. A. & Gayle, F. W. Electron diffraction using transmission electron microscopy. *J. Res. Natl. Inst. Stand. Technol.* **106**, 997 (2001). 35

[183] O'Keefe, M. A., Buseck, P. R. & Iijima, S. Computed crystal structure images for high resolution electron microscopy. *Nature* **274**, 322–324 (1978). 35

[184] Hillier, J. & Baker, R. F. Microanalysis by means of electrons. *J. Appl. Phys.* **15**, 663–675 (1944). 35

[185] Egerton, R. F. Electron energy-loss spectroscopy in the tem. *Rep. Prog. Phys.* **72**, 016502 (25pp) (2009). 35

[186] Sarikaya, M., Qian, M. & Stern, E. A. Exelfs revisited. *Micron* **27**, 449 – 466 (1996). 35

[187] Crescenzi, M. D. *et al.* Extended els fine structures above the m2,3 edges of cu and ni. *Solid State Commun.* **40**, 613 – 617 (1981). 35

[188] Crescenzi, M. D. Extended energy loss fine structures (eelfs): A new structural probe for surfaces and interfaces. *Surf. Sci.* **162**, 838 – 846 (1985). 35

[189] Moreno, M., Jorissen, K. & Rehr, J. Practical aspects of electron energy-loss spectroscopy (eels) calculations using feff8. *Micron* **38**, 1 – 11 (2007). 35

[190] Braginski, A. & Clarke, J. Fundamentals and technology of squids and squid systems. In *The SQUID Handbook*, vol. 1, 1–28 (Wiley-VCH, 2004). 36

[191] Erné, S. N., Hahlbohm, H.-D. & Lubbig, H. Theory of rf-biased superconducting quantum interference device for nonhysteretic regime. *J. Appl. Phys.* **47**, 5440–5442 (1976). 36

[192] Jaklevic, R. C., Lambe, J., Silver, A. H. & Mercereau, J. E. Quantum interference effects in josephson tunneling. *Phys. Rev. Lett.* **12**, 159– (1964). 36

[193] Josephson, B. D. The discovery of tunnelling supercurrents. *Rev. Mod. Phys.* **46**, 251– (1974). 36

[194] Kohn, W. Nobel lecture: Electronic structure of matter – wave functions and density functionals. *Rev. Mod. Phys.* **71**, 1253– (1999). 36

[195] Capelle, K. A bird's-eye view of density-functional theory. *Braz. J. Phys.* **36**, 1318 (2006). 36

[196] Burke, K. The abc of dft (2007). See `http://chem.ps.uci.edu/~kieron/dft/`. 36

[197] Giannozzi, P. *et al.* Quantum espresso: a modular and open-source software project for quantum simulations of materials (2009). ArXiv:0906.2569v1. 36, 60

[198] Perdew, J. P., Burke, K. & Ernzerhof, M. Generalized gradient approximation made simple. *Phys. Rev. Lett.* **77**, 3865– (1996). 36

[199] Anisimov, V. I., Aryasetiawan, F. & Lichtenstein, A. I. First-principles calculations of the electronic structure and spectra of strongly correlated systems: the lda+ u method. *J. Phys.: Condens. Matter* **9**, 767–808 (1997). 36

[200] Cococcioni, M. & de Gironcoli, S. Linear response approach to the calculation of the effective interaction parameters in the lda + u method. *Phys. Rev. B* **71**, 035105 (2005). 36

[201] Kulik, H. J., Cococcioni, M., Scherlis, D. A. & Marzari, N. Density functional theory in transition-metal chemistry: A self-consistent hubbard u approach. *Phys. Rev. Lett.* **97**, 103001 (2006). 36

[202] Vanderbilt, D. Soft self-consistent pseudopotentials in a generalized eigenvalue formalism. *Phys. Rev. B* **41**, 7892– (1990). 36

[203] Monkhorst, H. J. & Pack, J. D. Special points for brillouin-zone integrations. *Phys. Rev. B* **13**, 5188– (1976). 36

[204] Berne, B. J., Ciccotti, G. & Coker, D. F. (eds.) *Classical and Quantum Dynamics in Condensed Phase Simulations* (World Scientific, 1998). 36

[205] Jungwirth, T. *et al.* Prospects for high temperature ferromagnetism in (ga,mn)as semiconductors. *Phys. Rev. B* **72**, 165204 (2005). 41, 44

[206] Olejnik, K. *et al.* Enhanced annealing, high curie temperature, and low-voltage gating in (ga,mn)as: A surface oxide control study. *Phys. Rev. B* **78**, 054403 (2008). 42, 43, 44, 51

[207] Ohno, H. *et al.* (ga,mn)as: A new diluted magnetic semiconductor based on gaas. *Appl. Phys. Lett.* **69**, 363–365 (1996). 43

[208] Yu, K., Wojtowicz, T., Walukiewicz, W., Liu, X. & Furdyna, J. Fermi level effects on mn incorporation in iii[hyphen (true graphic)]mn[hyphen (true graphic)]v ferromagnetic semiconductors. In Weber, E. (ed.) *Spintronics*, vol. 82 of *Semiconductors and Semimetals*, chap. 3, 89 – 133 (Elsevier, 2008). 43, 99, 103

[209] Yu, K. M. *et al.* Effect of the location of mn sites in ferromagnetic $ga_{1-x}mn_x$as on its curie temperature. *Phys. Rev. B* **65**, 201303 (2002). 43, 44

[210] Edmonds, K. W. *et al.* High-curie-temperature ga[sub 1 - x]mn[sub x]as obtained by resistance-monitored annealing. *Appl. Phys. Lett.* **81**, 4991–4993 (2002). 43

[211] Chiba, D., Takamura, K., Matsukura, F. & Ohno, H. Effect of low-temperature annealing on (ga,mn)as trilayer structures. *Appl. Phys. Lett.* **82**, 3020–3022 (2003). 43

[212] Stone, M. B. *et al.* Capping-induced suppression of annealing effects on ga[sub 1 - x]mn[sub x]as epilayers. *Appl. Phys. Lett.* **83**, 4568–4570 (2003). 43

[213] Bliss, D. E. *et al.* Annealing studies of low-temperature-grown gaas:be. *J. Appl. Phys.* **71**, 1699–1707 (1992). 43

[214] Ohya, S., Ohno, K. & Tanaka, M. Magneto-optical and magnetotransport properties of heavily mn-doped gamnas. *Appl. Phys. Lett.* **90**, 112503 (2007). 44

[215] Chiba, D., Nishitani, Y., Matsukura, F. & Ohno, H. Properties of ga[sub 1 - x]mn[sub x]as with high mn composition (x > 0.1). *Appl. Phys. Lett.* **90**, 122503 (2007). 44

[216] Mack, S., Myers, R. C., Heron, J. T., Gossard, A. C. & Awschalom, D. D. Stoichiometric growth of high curie temperature heavily alloyed gamnas. *Appl. Phys. Lett.* **92**, 192502 (2008). 44

[217] Cho, Y. J., Liu, X. & Furdyna, J. K. Collapse of ferromagnetism in (ga, mn)as at high hole concentrations. *Semicond. Sci. Technol.* **23**, 125010 (2008). 44

[218] Cho, Y. J., Yu, K. M., Liu, X., Walukiewicz, W. & Furdyna, J. K. Effects of donor doping on ga[sub 1 - x]mn[sub x]as. *Appl. Phys. Lett.* **93**, 262505 (2008). 44, 99, 103

[219] Burch, K. S. *et al.* Impurity band conduction in a high temperature ferromagnetic semiconductor. *Phys. Rev. Lett.* **97**, 087208 (2006). 44

[220] Jungwirth, T. *et al.* Character of states near the fermi level in (ga,mn)as: Impurity to valence band crossover. *Phys. Rev. B* **76**, 125206 (2007). 44

[221] Edmonds, K. W. *et al.* Mn interstitial diffusion in (ga,mn)as. *Phys. Rev. Lett.* **92**, 037201 (2004). 44

[222] Kirby, B. J. *et al.* Effects of capping on the ga[sub 1 - x]mn[sub x]as magnetic depth profile. *Applied Physics Letters* **86**, 072506 (2005). 44

[223] Kirby, B. J. *et al.* Magnetic and chemical nonuniformity in ga[sub 1 - x]mn[sub x]as films as probed by polarized neutron and x-ray reflectometry. *Phys. Rev. B* **74**, 245304 (2006). 44

[224] Schmid, B. *et al.* Surface segregation of interstitial manganese in ga[sub 1 - x]mn[sub x]as studied by hard x-ray photoemission spectroscopy. *Phys. Rev. B* **78**, 075319 (2008). 44

[225] Wang, M. *et al.* Achieving high curie temperature in (ga,mn)as. *Appl. Phys. Lett.* **93**, 132103 (2008). 44

[226] Holy, V. *et al.* Mn incorporation in as-grown and annealed (ga,mn)as layers studied by x-ray diffraction and standing-wave fluorescence. *Phys. Rev. B* **74**, 245205 (2006). 44

[227] Storchak, V. G. *et al.* Spatially resolved inhomogeneous ferromagnetism in (ga,mn)as diluted magnetic semiconductors: A microscopic study by muon spin relaxation. *Phys. Rev. Lett.* **101**, 027202 (2008). 44

[228] Shioda, R., Ando, K., Hayashi, T. & Tanaka, M. Local structures of iii-v diluted magnetic semiconductors ga1-xmnxas studied using extended x-ray-absorption fine structure. *Phys. Rev. B* **58**, 1100 (1998). 44, 47

[229] Soo, Y. L. *et al.* Local environment surrounding ferromagnetically ordered mn in mn/gaas digital alloys and (mn, ga)as random alloys. *Phys. Rev. B* **67**, 214401 (2003). 44, 47

[230] D'Acapito, F. *et al.* Site of mn in mn delta-doped gaas: X-ray absorption spectroscopy. *Phys. Rev. B* **73**, 035314 (2006). 44, 47, 80

[231] Bacewicz, R. *et al.* Local structure of mn in (ga,mn)as probed by x-ray absorption spectroscopy. *J. Phys. Chem. Solids* **66**, 2004 (2005). 44

[232] Demchenko, I. N. *et al.* Modification of the local atomic structure around mn atoms in (ga,mn)as layers by high temperature annealing. *J. Phys.: Condens. Matter* **19**, 496205 (2007). 44, 95

[233] Wolska, A. *et al.* Xanes studies of mn k and l-3,l-2 edges in the (ga,mn) as layers modified by high temperature annealing. *Acta Physica Polonica A* **114**, 357–366 (2008). 44

[234] Bihler, C. *et al.* Local structure of mn in hydrogenated ga[sub 1 - x]mn[sub x]as. *Phys. Rev. B* **78**, 235208 (2008). 44

[235] Goncharuk, N. A. *et al.* Study of mn k-edge xanes in (ga,mn)as diluted magnetic semiconductors (2008). ArXiv:0805.0957v1. 44

[236] Liu, X. *Thin semiconductor alloy films: fabrication and physical properties*. Ph.D. thesis, University of Notre Dame (USA) (2002). 44

[237] Furdyna, J. K. *et al.* Ferromagnetic iii-mn-v semiconductors: Manipulation of magnetic properties by annealing, extrinsic doping, and multilayer design. *J. Korean Phys. Soc.* **42**, 579 (2003). 44

[238] Potashnik, S. J. *et al.* Effects of annealing time on defect-controlled ferromagnetism in ga[sub 1 - x]mn[sub x]as. *Appl. Phys. Lett.* **79**, 1495–1497 (2001). 44

[239] Gennes, P. G. D. & Friedel, J. Anomalies de résistivité dans certains métaux magnéques. *J. Phys. Chem. Solids* **4**, 71 – 77 (1958). 44

[240] Fisher, M. E. & Langer, J. S. Resistive anomalies at magnetic critical points. *Phys. Rev. Lett.* **20**, 665 (1968). 44

[241] Novak, V. *et al.* Curie point singularity in the temperature derivative of resistivity in (ga,mn)as. *Phys. Rev. Lett.* **101**, 077201 (2008). 44

[242] Cooper, A. S. Precise lattice constants of germanium, aluminum, gallium arsenide, uranium, sulphur, quartz and sapphire. *Acta Cryst.* **15**, 578–582 (1962). 46, 80

[243] Poiarkova, A. V. & Rehr, J. J. Multiple-scattering x-ray-absorption fine-structure debye-waller factor calculations. *Phys. Rev. B* **59**, 948 (1999). 47, 79, 121

[244] Guo, X. G. *et al.* Local structural distortions and mn random distributions in (ga,mn)as: A first-principles study. *Phys. Rev. B* **69**, 085206 (2004). 47

[245] Schott, G. M., Faschinger, W. & Molenkamp, L. W. Lattice constant variation and complex formation in zincblende gallium manganese arsenide. *Appl. Phys. Lett.* **79**, 1807–1809 (2001). 47

[246] Kuriyama, M. & Hosoya, S. X-ray measurement of scattering factors of manganese and oxygen atoms in manganous oxide. *J. Phys. Soc. Jpn.* **17**, 1022 (1962). 47

[247] Fert, A. Structure de quelques oxydes de terres rares. *Bull. Soc. Francaise Mineral. Cristallogr.* **85**, 267 (1962). 47

[248] Boucher, B., Buhl, R. & Perrin, M. Proprietes et structure magnetique de mn3o4. *J. Phys. Chem. Solids* **32**, 2429 (1971). 47

[249] Bonanni, A. *et al.* Doping of gan with fe and mg for spintronics applications. *Phys. Status Solidi B* **243**, 1701–1705 (2006). 53, 55, 56

[250] Bonanni, A. *et al.* Paramagnetic gan:fe and ferromagnetic (ga,fe)n: The relationship between structural, electronic, and magnetic properties. *Phys. Rev. B* **75**, 125210 (2007). 53, 55, 56, 57, 58, 64, 67

[251] Navarro-Quezada, A. *et al.* Fe onto gan(0001) grown in a full movpe process. *J. Cryst. Growth* **310**, 1772 – 1776 (2008). The Proceedings of the 15th International Conference on Crystal Growth (ICCG-15) in conjunction with the International Conference on Vapor Growth and Epitaxy and the US Biennial Workshop on Organometallic Vapor Phase Epitaxy. 53, 55, 65

[252] Navarro-Quezada, A. *Control of TM ion aggregation in (Ga,Fe)N*. Ph.D. thesis, Johannes Kepler Universität, Linz (2009). 53, 55, 56, 57, 58, 66

[253] Jacobs, H., Rechenbach, D. & Zachwieja, U. Structure determination of [gamma]'-fe4n and [epsilon]-fe3n. *J. Alloys Compd.* **227**, 10 – 17 (1995). 53, 61, 62, 63

[254] Basinski, Z. S., Hume-Rothery, W. & Sutton, A. L. The lattice expansion of iron. *Proc. Royal Soc. London, A: Math. Phys. Sci.* **229**, 459 (1955). 54, 62, 63, 66

[255] Heikman, S., Keller, S., DenBaars, S. P. & Mishra, U. K. Growth of fe doped semi-insulating gan by metalorganic chemical vapor deposition. *Appl. Phys. Lett.* **81**, 439–441 (2002). 55, 56

[256] Heikman, S., Keller, S., Mates, T., DenBaars, S. P. & Mishra, U. K. Growth and characteristics of fe-doped gan. *J. Cryst. Growth* **248**, 513–517 (2003). 55

[257] Malguth, E. *et al.* Structural and electronic properties of fe[sup 3+] and fe[sup 2+] centers in gan from optical and epr experiments. *Phys. Rev. B* **74**, 165202 (2006). 55

[258] Kane, M. H. *et al.* Comparative study of mn and fe incorporation into gan by metalorganic chemical vapor deposition. *Phys. Status Solidi A* **204**, 61–71 (2007). 55

[259] Theodoropoulou, N. *et al.* Use of ion implantation to facilitate the discovery and characterization of ferromagnetic semiconductors. *J. Appl. Phys.* **91**, 7499–7501 (2002). 55

[260] Shon, Y. *et al.* Ferromagnetic behavior of p-type gan epilayer implanted with fe[sup +] ions. *J. Appl. Phys.* **95**, 761–763 (2004). 55

[261] Bonanni, A. *et al.* Controlled aggregation of magnetic ions in a semiconductor: An experimental demonstration. *Phys. Rev. Lett.* **101**, 135502 (2008). 55, 74

[262] Sonoda, S., Shimizu, S., Sasaki, T., Yamamoto, Y. & Hori, H. Molecular beam epitaxy of wurtzite (ga,mn)n films on sapphire(0001) showing the ferromagnetic behaviour at room temperature. *J. Cryst. Growth* **237-239**, 1358 – 1362 (2002). 55

[263] Zheng, R. *et al.* On the understanding of the microscopic origin of the properties of diluted magnetic semiconductors by atom probe tomography. *J. Magn. Magn. Mater.* **321**, 935 (2009). 55

[264] Nakarmi, M. L., Kim, K. H., Li, J., Lin, J. Y. & Jiang, H. X. Enhanced p-type conduction in gan and algan by mg-delta-doping. *Appl. Phys. Lett.* **82**, 3041–3043 (2003). 56

[265] Simbrunner, C. *et al.* On the effect of periodic mg distribution in gan:delta-mg. *Appl. Phys. Lett.* **90**, 142108 (2007). 56

[266] Kharchenko, A. *et al.* In situ and real-time characterization of metal-organic chemical vapor deposition growth by high resolution x-ray diffraction. *Rev. Sci. Instrum.* **76**, 033101 (2005). 56

[267] Simbrunner, C. *et al.* In situ monitoring of periodic structures during movpe of iii-nitrides. *J. Cryst. Growth* **310**, 1607 – 1613 (2008). The Proceedings of the 15th International Conference on Crystal Growth (ICCG-15) in conjunction with the International Conference on Vapor Growth and Epitaxy and the US Biennial Workshop on Organometallic Vapor Phase Epitaxy. 56

[268] Li, T. *et al.* Phase-dependent distribution of fe-rich nanocrystals in movpe-grown (ga,fe)n. *J. Cryst. Growth* **310**, 3294 – 3298 (2008). 57, 62, 64

[269] Tullio, V. *et al.* Porta campione oscillante. Internal note, LNF-INFN (2001). 59

[270] Bearden, J. A. & Burr, A. F. Reevaluation of x-ray atomic energy levels. *Rev. Mod. Phys.* **39**, 125 (1967). 60

[271] Bogusławski, P., Briggs, E. L. & Bernholc, J. Native defects in gallium nitride. *Phys. Rev. B* **51**, 17255– (1995). 60

[272] Bonapasta, A. A., Filippone, F. & Giannozzi, P. Nitrogen passivation by atomic hydrogen in gaasyn1-y and inxga1-xasyn1-y alloys. *Phys. Rev. B* **68**, 115202– (2003). 60

[273] de Walle, C. G. V. & Neugebauer, J. First-principles calculations for defects and impurities: Applications to iii-nitrides. *J. Appl. Phys.* **95**, 3851–3879 (2004). 60

[274] Amore Bonapasta, A., Filippone, F. & Giannozzi, P. Structure, electronic properties, and formation mechanisms of hydrogen-nitrogen complexes in gapyn1-y alloys. *Phys. Rev. B* **69**, 115207– (2004). 60

[275] Nishidate, K. *et al.* Density-functional electronic structure calculations for native defects and cu impurities in cds. *Phys. Rev. B* **74**, 035210 (2006). 61

[276] Wyckoff, R. *Crystal Structures* (John Wiley & Sons, 1964). 61

[277] Jack, K. H. The iron–nitrogen system: the crystal structures of ϵ-phase iron nitrides. *Acta Crystallographica* **5**, 404–411 (1952). 61, 62

[278] Leineweber, A. *et al.* [var epsilon]-fe3n: magnetic structure, magnetization and temperature dependent disorder of nitrogen. *J. Alloys Compd.* **288**, 79 – 87 (1999). 61

[279] Swanson, H. & Tatge, E. Standard x-ray diffraction powder patterns. *National Bureau of Standards* **539**, 1–75 (1955). 62, 63, 64, 66

[280] Dasarathy, C. & Hume-Rothery, W. The system iron-gallium. *Proc. Royal Soc. London, A: Math. Phys. Sci.* **286**, 141 (1965). 62

[281] Sawada, H., Nogami, A., Matsumiya, T. & Oguchi, T. Structural, electronic, and magnetic properties of fe16n2. *Phys. Rev. B* **50**, 10004– (1994). 62

[282] Schulz, H. & Thiemann, K. H. Crystal structure refinement of aln and gan. *Solid State Commun.* **23**, 815 – 819 (1977). 63

[283] Kumagai, Y. *et al.* Fe-doped semi-insulating gan substrates prepared by hydride vapor-phase epitaxy using gaas starting substrates. *J. Cryst. Growth* **296**, 11 – 14 (2006). 62

[284] Galoisy, L., Calas, G. & Arrio, M. A. High-resolution xanes spectra of iron in minerals and glasses: structural information from the pre-edge region. *Chem. Geol.* **174**, 307–319 (2001). 66

[285] Westre, T. E. *et al.* A multiplet analysis of fe k-edge 1s → 3d pre-edge features of iron complexes. *J. Am. Chem. Soc.* **119**, 6297–6314 (1997). 66, 67

[286] Giuli, G., Pratesi, G., Cipriani, C. & Paris, E. Iron local structure in tektites and impact glasses by extended x-ray absorption fine structure and high-resolution x-ray absorption near-edge structure spectroscopy. *Geochim. Cosmochim. Acta* **66**, 4347–4353 (2002). 67

[287] Park, Y. D. *et al.* A group-iv ferromagnetic semiconductor: Mnxge1-x. *Science* **295**, 651–654 (2002). 71, 73, 76

[288] Woodbury, H. H. & Tyler, W. W. Properties of germanium doped with manganese. *Phys. Rev.* **100**, 659– (1955). 71, 73

[289] Forsyth, J. B. & Brown, P. J. The spatial distribution of magnetisation density in mn5ge3. *J. Phys.: Condens. Matter* **2**, 2713–2720 (1990). 71, 78, 79, 84

[290] Jamet, M. *et al.* High-curie-temperature ferromagnetism in self-organized ge1-xmnx nanocolumns. *Nat. Mater.* **5**, 653–659 (2006). 71, 73, 76, 77, 84

[291] Devillers, T. *et al.* Structure and magnetism of self-organized ge[sub 1 - x]mn[sub x] nanocolumns on ge(001). *Phys. Rev. B* **76**, 205306 (2007). 71, 73, 76, 84

[292] Ahlers, S. *Magnetic and electrical properties of epitaxial GeMn*. Ph.D. thesis, Technische Universität München (2009). ISBN: 978-3-932749-96-0. 72, 73, 83, 84

[293] Zwicker, U., Jehn, E. & Schubert, E. *Z. Metallkd.* **40**, 433 (1949). 73

[294] Predel, B. *Landolt-Börnstein - Group IV Physical Chemistry*, chap. Ge-Mn (Germanium-Manganese), 1–5 (Springer-Verlag, 1996). 73

[295] Devillers, T. *et al.* Structural and magnetic properties of gemn layers; high curie temperature ferromagnetism induced by self organized gemn nano-columns. *Phys. Status Solidi A* **204**, 130–135 (2007). 73

[296] Ahlers, S. *et al.* Ferromagnetic ge(mn) nanostructures. *Physica E* **32**, 422 – 425 (2006). Proceedings of the 12th International Conference on Modulated Semiconductor Structures. 73

[297] Bougeard, D., Ahlers, S., Trampert, A., Sircar, N. & Abstreiter, G. Clustering in a precipitate-free gemn magnetic semiconductor. *Phys. Rev. Lett.* **97**, 237202 (2006). 73

[298] Ahlers, S. *et al.* Magnetic and structural properties of ge[sub x]mn[sub 1 - x] films: Precipitation of intermetallic nanomagnets. *Phys. Rev. B* **74**, 214411 (2006). 73

[299] Holy, V. *et al.* Diffuse x-ray scattering from inclusions in ferromagnetic ge[sub 1 - x]mn[sub x] layers. *Phys. Rev. B* **78**, 144401 (2008). 73, 74

[300] Li, A. P., Shen, J., Thompson, J. R. & Weitering, H. H. Ferromagnetic percolation in mn[sub x]ge[sub 1 - x] dilute magnetic semiconductor. *Applied Physics Letters* **86**, 152507 (2005). 73

[301] Li, A. P. *et al.* Magnetism in mnx ge1-x semiconductors mediated by impurity band carriers. *Phys. Rev. B* **72**, 195205– (2005). 73

[302] Li, A. P. *et al.* Dopant segregation and giant magnetoresistance in manganese-doped germanium. *Phys. Rev. B* **75**, 201201 (2007). 73

[303] Zeng, C., Zhang, Z., van Benthem, K., Chisholm, M. F. & Weitering, H. H. Optimal doping control of magnetic semiconductors via subsurfactant epitaxy. *Phys. Rev. Lett.* **100**, 066101 (2008). 73, 74

[304] Park, Y. D. *et al.* Magnetoresistance of mn:ge ferromagnetic nanoclusters in a diluted magnetic semiconductor matrix. *Appl. Phys. Lett.* **78**, 2739–2741 (2001). 74

[305] Moreno, M., Trampert, A., Jenichen, B., Daweritz, L. & Ploog, K. H. Correlation of structure and magnetism in gaas with embedded mn(ga)as magnetic nanoclusters. *J. Appl. Phys.* **92**, 4672–4677 (2002). 74

[306] Ottaviano, L. *et al.* Direct structural evidences of mn dilution in ge. *J. Appl. Phys.* **100**, 063528 (2006). 74, 80, 81, 83, 93, 96

[307] Ottaviano, L., Passacantando, M., Verna, A., D'Amico, F. & Gunnella, R. Mn l[sub 2,3] x-ray absorption spectra of a diluted mn–ge alloy. *Appl. Phys. Lett.* **90**, 242105 (2007). 74

[308] Gunnella, R., Pinto, N., Morresi, L., Abbas, M. & Cicco, A. D. Mbe grown mnge alloys: An xas study. *J. Non-Cryst. Solids* **354**, 4193 – 4197 (2008). Functional and Nanostructured Materials, 4th Conference on Functional and Nanostructured Materials. 74, 80, 83

[309] Aleksandrov, S. *et al.* Pyrometer unit for gaas substrate temperature control in an mbe system. *Tech. Phys.* **49**, 123–127 (2004). 74

[310] Castelliz, L. Kristallstruktur vom mn5 ge3 und einiger ternaerer phasen mit zwei uebergansmetallen. *Monatshefte fuer Chemie* **84**, 765 (1953). 74

[311] Srivastava, G. P. Theory of semiconductor surface reconstruction. *Rep. Prog. Phys.* **60**, 561–613 (1997). 74

[312] Zeng, C. *et al.* Epitaxial ferromagnetic mn[sub 5]ge[sub 3] on ge(111). *Appl. Phys. Lett.* **83**, 5002–5004 (2003). 74

[313] Stroppa, A., Picozzi, S., Continenza, A. & Freeman, A. J. Electronic structure and ferromagnetism of mn-doped group-iv semiconductors. *Phys. Rev. B* **68**, 155203– (2003). 76

[314] Zhao, Y.-J., Shishidou, T. & Freeman, A. J. Ruderman-kittel-kasuya-yosida–like ferromagnetism in mnxge1-x. *Phys. Rev. Lett.* **90**, 047204– (2003). 76

[315] Tawara, Y. & Sato, K. On the magnetic anisotropy of single crystal of mn_5ge_3. *J. Phys. Soc. Jpn.* **18**, 773–777 (1963). 77

[316] Kittel, C. Theory of the structure of ferromagnetic domains in films and small particles. *Phys. Rev.* **70**, 965 (1946). 77

[317] Néel, L. Théorie du traînage magnétique des ferromagnétiques en grains fins avec application aux terres cuites. *Ann. Géophys.* **5**, 99 (1949). 77

[318] Gittleman, J. I., Abeles, B. & Bozowski, S. Superparamagnetism and relaxation effects in granular ni-sio2 and ni-al2o3 films. *Phys. Rev. B* **9**, 3891 (1974). 77

[319] Rovezzi, M. *et al.* Atomic structure of mn-rich nanocolumns probed by x-ray absorption spectroscopy. *Appl. Phys. Lett.* **92**, 242510 (2008). 78

[320] Booth, C. H. & Bridges, F. Improved self-absorption correction for fluorescence measurements of extended x-ray absorption fine-structure. *Phys. Scr.* **T115**, 202–204 (2005). 78

[321] Katsikini, M., Paloura, E. C. & Moustakas, T. D. Experimental determination of the n-p-partial density of states in the conduction band of gan: Determination of the polytype fractions in mixed phase samples. *J. Appl. Phys.* **83**, 1437–1445 (1998). 78

[322] Pāssler, R. Basic moments of phonon density of states spectra and characteristic phonon temperatures of group iv, iii–v, and ii–vi materials. *J. Appl. Phys.* **101**, 093513 (2007). 79

[323] Evangelisti, F. *et al.* Exafs investigation of amorphous-to-crystal transition in ge. *Solid State Commun.* **37**, 413–416 (1981). 80

[324] Wolska, A., Lawniczak-Jablonska, K., Klepka, M., Walczak, M. S. & Misiuk, A. Local structure around mn atoms in si crystals implanted with mn[sup +] studied using x-ray absorption spectroscopy techniques. *Phys. Rev. B* **75**, 113201 (2007). 80

[325] Soo, Y. L. *et al.* Local structure around mn atoms in room-temperature ferromagnetic (in,mn)as thin films probed by extended x-ray absorption fine structure. *Appl. Phys. Lett.* **84**, 481–483 (2004). 81, 96

[326] da Silva, A. J. R., Fazzio, A. & Antonelli, A. Stabilization of substitutional mn in silicon-based semiconductors. *Phys. Rev. B* **70**, 193205 (2004). 81

[327] Continenza, A., Profeta, G. & Picozzi, S. Transition metal impurities in ge: Chemical trends and codoping studied by electronic structure calculations. *Phys. Rev. B* **73**, 035212 (2006). 81

[328] Kim, S.-K. *et al.* High-temperature ferromagnetism in amorphous semiconductor ge[sub 3]mn thin films. *Appl. Phys. Lett.* **90**, 192505 (2007). 83

[329] Martelli, F. *et al.* Manganese-induced growth of gaas nanowires. *Nano Lett.* **6**, 2130–2134 (2006). 87, 90, 91, 93

[330] Cui, Y., Wei, Q., Park, H. & Lieber, C. M. Nanowire nanosensors for highly sensitive and selective detection of biological and chemical species. *Science* **293**, 1289 (2001). 89

[331] Duan, X., Huang, Y., Cui, Y., Wang, J. & Lieber, C. M. Indium phosphide nanowires as building blocks for nanoscale electronic and optoelectronic devices. *Nature* **409**, 66–69 (2001). 89

[332] Thelander, C. *et al.* Single-electron transistors in heterostructure nanowires. *Appl. Phys. Lett.* **83**, 2052–2054 (2003). 89

[333] Baxter, J. B. & Aydil, E. S. Nanowire-based dye-sensitized solar cells. *Appl. Phys. Lett.* **86**, 053114 (2005). 89

[334] Wagner, R. S. & Ellis, W. C. Vapor-liquid-solid mechanism of single crystal growth. *Appl. Phys. Lett.* **4**, 89–90 (1964). 89

[335] Givargizov, E. Fundamental aspects of vls growth. *J. Cryst. Growth* **31**, 20 (1975). 89

[336] Ronning, C., Gao, P. X., Ding, Y., Wang, Z. L. & Schwen, D. Manganese-doped zno nanobelts for spintronics. *Appl. Phys. Lett.* **84**, 783 (2004). 89

[337] Chang, Y. Q. *et al.* Synthesis, optical, and magnetic properties of diluted magnetic semiconductor zn[sub 1 - x]mn[sub x]o nanowires via vapor phase growth. *Appl. Phys. Lett.* **83**, 4020 (2003). 89

[338] Deepak, F. L., Vanitha, P. V., Govindaraj, A. & Rao, C. N. R. Photoluminescence spectra and ferromagnetic properties of gamnn nanowires. *Chem. Phys. Lett.* **374**, 314 (2003). 89

[339] Han, D. S., Park, J., Rhie, K. W., Kim, S. & Chang, J. Ferromagnetic mn-doped gan nanowires. *Appl. Phys. Lett.* **86**, 032506 (2005). 89

[340] Baik, J. M., Shon, Y., Kang, T. W. & Lee, J.-L. Fabrication of (ga,mn)n nanowires with room temperature ferromagnetism using nitrogen plasma. *Appl. Phys. Lett.* **87**, 042105 (2005). 89

[341] Radovanovic, P. V., Barrelet, C. J., Gradečak, S., Qian, F. & Lieber, C. M. General synthesis of manganese-doped ii–vi and iii–v semiconductor nanowires. *Nano Lett.* **5**, 1407–1411 (2005). 89

[342] Jeon, H. C. *et al.* Magnetic and optical properties of (ga[sub 1 - x]mn[sub x])as diluted magnetic semiconductor quantum wires with above room ferromagnetic transition temperature. *J. Appl. Phys.* **101**, 023508 (2007). 90

[343] Sadowski, J. *et al.* Gaas:mn nanowires grown by molecular beam epitaxy of (ga,mn)as at mnas segregation conditions. *Nano Lett.* **7**, 2724–2728 (2007). 90

[344] Jabeen, F., Rubini, S. & Martelli, F. Growth of iii-v semiconductor nanowires by molecular beam epitaxy. *Microelectronics Journal* **40**, 442 – 445 (2009). Workshop of Recent Advances on Low Dimensional Structures and Devices (WRA-LDSD). 90

[345] Larsson, M. W. *et al.* Strain mapping in free-standing heterostructured wurtzite inas/inp nanowires. *Nanotechnology* **18**, 015504 (2007). 91, 94

[346] Willis, B. T. M. & Rooksby, H. P. Magnetic transitions and structural changes in hexagonal manganese compounds. *P. Phys. Soc. Lond. B* **67**, 290 (1954). 94

[347] Morris, D. & Preston, R. P. Structural transition and anti-ferromagnetism in the alloy au mn. *P. Phys. Soc. Lond.* **69**, 849 (1956). 94, 95

[348] Yeh, C.-Y., Lu, Z. W., Froyen, S. & Zunger, A. Zinc-blende–wurtzite polytypism in semiconductors. *Phys. Rev. B* **46**, 10086 (1992). 95

[349] Soo, Y. L. *et al.* Variations of long- and short-range-order structural and magnetic properties of thermally annealed mn/gaas digital alloys. *Appl. Phys. Lett.* **83**, 2354–2356 (2003). 95

[350] Mejía-Lòpez, J., Romero, A. H., Garcia, M. E. & Morán-López, J. L. Noncollinear magnetism, spin frustration, and magnetic nanodomains in small mn[sub n] clusters. *Phys. Rev. B* **74**, 140405 (2006). 96

[351] Sekine, R., Kondo, R., Yamamoto, T. & Onoe, J. Geometric and electronic structures of tc and mn clusters by density functional calculations. *Radiochemistry* **45**, 233–236 (2003). 96

[352] Oberteuffer, J. A. & Ibers, J. A. A refinement of the atomic and thermal parameters of α-manganese from a single crystal. *Acta Cryst. B* **26**, 1499 (1970). 96

[353] Mahadevan, P., Osorio-Guillén, J. M. & Zunger, A. Origin of transition metal clustering tendencies in gaas based dilute magnetic semiconductors. *Appl. Phys. Lett.* **86**, 172504 (2005). 96

[354] Mahadevan, P. & Zunger, A. Ferromagnetism in mn-doped gaas due to substitutional-interstitial complexes. *Phys. Rev. B* **68**, 075202 (2003). 96

[355] Jabeen, F., Rubini, S., Grillo, V., Felisari, L. & Martelli, F. Room temperature luminescent ingaas/gaas core-shell nanowires. *Applied Physics Letters* **93**, 083117 (2008). 96

[356] Maingault, L. *Insertion d'ions magnétiques dans les boîtes quantiques de semiconducteurs II-VI*. Ph.D. thesis, Université Joseph Fourier - Grenoble I (2006). N.: tel-00186925. 97, 101

[357] Chen, H., Zhu, W., Kaxiras, E. & Zhang, Z. Optimization of mn doping in group-iv-based dilute magnetic semiconductors by electronic codopants. *Phys. Rev. B* **79**, 235202 (2009). 99, 103

[358] Dietl, T. Hole states in wide band-gap diluted magnetic semiconductors and oxides. *Phys. Rev. B* **77**, 085208 (2008). 99, 103

[359] Noma, T. & Iida, A. Surface analysis of layered thin films using a synchrotron x-ray microbeam combined with a grazing-exit condition. *Rev. Sci. Instrum.* **65**, 837 (1994). 107

[360] Meirer, F., Pepponi, G., Streli, C., Wobrauschek, P. & Zoeger, N. Grazing exit versus grazing incidence geometry for x-ray absorption near edge structure analysis of arsenic traces. *J. Appl. Phys.* **105**, 074906 (2009). 107

[361] Trave, E. *et al.* Sub-nanometric metallic au clusters as efficient er[sup 3+] sensitizers in silica. *Appl. Phys. Lett.* **89**, 151121 (2006). 114

[362] Keil, P., Lutzenkirchen-Hecht, D. & Frahm, R. Calculation of grazing incidence exafs: Fresnel theory versus dwba. *Phys. Scr.* **T115**, 246–248 (2005). 118

[363] Cromer, D. T. & Liberman, D. Relativistic calculation of anomalous scattering factors for x rays. *J. Chem. Phys.* **53**, 1891 (1970). 118

[364] Kittel, C. *Introduction to Solid State Physics* (Wiley, 1976), fifth edn. 120

[365] Balerna, A. *et al.* Extended x-ray-absorption fine-structure and near-edge-structure studies on evaporated small clusters of au. *Phys. Rev. B* **31**, 5058 (1985). 122

[366] Comaschi, T., Balerna, A. & Mobilio, S. Temperature dependence of the structural parameters of gold nanoparticles investigated with exafs. *Phys. Rev. B* **77**, 075432 (2008). 122

List of Acronyms

AD as deposited

AN annealed

CL capping layer(s)

DFT density functional theory

DMS diluted magnetic semiconductor(s)

EDS energy dispersive x-ray spectroscopy

EELS electron energy loss spectroscopy

ESRF european synchrotron radiation facility

EXAFS extended x-ray absorption fine structure

FMS full multiple scattering

GI grazing incidence

GILDA general purpose italian beamline for diffraction and absorption

HI high incidence

HRTEM high resolution transmission electron microscopy

IXRD *in situ* x-ray diffraction

LUCIA line for ultimate characterisation by imaging and absorption

LSDA local spin density approximation

LT low temperature

MBE molecular beam epitaxy

MFA mean field approximation

MOVPE metalorganic vapor phase epitaxy

MS multiple scattering

NC nano-column(s)

NW nano-wire(s)

sccm standard cubic centimeters per minute

SS single scattering

ReflEXAFS total reflection mode EXAFS

RHEED reflection high-energy electron diffraction

RT room temperature

SE spectroscopic ellipsometry

SD standard geometry

SQUID superconducting quantum interference device

SS single scattering

TEM transmission electron microscopy

TR total reflection

VCA virtual crystal approximation

VLS vapor liquid solid

XAFS x-ray absorption fine structure

XANES x-ray absorption near-edge structure

XAS x-ray absorption spectroscopy

XRD x-ray diffraction

List of publications

Part of the work presented in this thesis is published in the following peer-reviewed papers:

❶ *Atomic structure of Mn-rich nanocolumns probed by x-ray absorption spectroscopy*
M. Rovezzi, T. Devillers, E. Arras, F. d'Acapito, A. Barski, M. Jamet, P. Pochet
Appl. Phys. Lett. **92**, 242510 (2008)

❷ *Controlled Aggregation of Magnetic Ions in a Semiconductor: An Experimental Demonstration*
A. Bonanni, A. Navarro-Quezada, T. Li, M. Wegscheider, Z. Matěj, V. Holý, R. T. Lechner, G. Bauer, M. Rovezzi, F. d'Acapito, M. Kiecana, M. Sawicki, T. Dietl
Phys. Rev. Lett. **101**, 135502 (2008)

❸ *A new procedure for the quantitative analysis of extended x-ray absorption fine structure data in total reflection geometry*
F. Benzi, I. Davoli, M. Rovezzi, F. d'Acapito
Rev. Sci. Instrum. **79**, 103902 (2008)

❹ *Local structure of (Ga,Fe)N, (Ga,Fe)N:Si investigated by x-ray absorption fine structure spectroscopy*
M. Rovezzi, F. d'Acapito, A. Navarro-Quezada, B. Faina, T. Li, A. Bonanni, F. Filippone, A. Amore Bonapasta, T. Dietl
Phys. Rev. B **79**, 195209 (2009)

❺ *Setup for optimized grazing incidence x-ray absorption experiments on thin films on substrates*
C. Maurizio, M. Rovezzi, F. Bardelli, H. G. Pais, F. d'Acapito
Rev. Sci. Instrum. **80**, 063904 (2009)

Résumé

Les semiconducteurs dopés avec des ions magnétiques (DMS) sont des matériaux prometteurs pour des applications dans le domaine émergent de la spintronique. Pour relever ce défi, une grande quantité d'impuretés magnétiques devraient entrer dans le cristal de la structure d'accueil sans séparation de phase, donc une caractérisation détaillée à l'échelle nanométrique est obligatoire. La spectroscopie d'absorption des rayons X est une technique bien adaptée pour sonder l'ordre locale, de manière à comprendre les mécanismes responsables de la spécificité des propriétés physiques de ces matériaux. Le point de départ de cette étude est le bien connu GaAs dopés avec Mn où la présence de défauts de Mn interstitiel réduit la température de transition ferromagnétique (T_C) et des traitements après croissance sont nécessaires en tant que remède. Un nouveau matériau prometteur c'est le GaN dopé Fe, présentant des propriétés magnétiques intéressantes quand dopé autour de la limite de solubilité du Fe. Dans ce cas, la question clé est la transition du Fe substitutionel à la précipitation en nano-cristaux riches en Fe, en passant par des conditions de décomposition spinodale. En effet, on observe que la T_C est augmentée considérablement par l'exploitation de la décomposition spinodale comme le montre le cas du Mn dans le Ge où il y a la création de nano-colonnes ferromagnétiques riches en Mn présentant un caractère de structure locale désordonnée dans un hôte cristallin. Enfin, les premières données de l'incorporation du Mn dans les nano-fils de GaAs et InAs sont enregistrées. Ces systèmes sont appelés à jouer un rôle clé dans la fabrication de dispositifs DMS à une dimension.

Mots-clés : Semiconducteurs magnétiques, Spintronique, GaMnAs GaFeN GeMn nano-fils, EXAFS XANES

Abstract

The semiconductors doped with magnetic ions (DMS) are promising materials for applications in the emerging field of spintronics. To address this challenge, a relatively high amount of magnetic impurities should enter the host crystal structure without phase separation, thus a detailed characterization at the nano-scale is mandatory. X-ray absorption fine structure spectroscopy is a technique well suited for probing the short-range order, so as to understand the underlying mechanisms responsible for the special physical properties of these materials. The starting point of this study is the well known GaAs doped with Mn where the creation of Mn interstitial defects reduce the ferromagnetic transition temperature (T_C) and post-growth treatments are necessary as a remedy. A new promising material is Fe-doped GaN showing interesting magnetic properties when doped around the solubility limit of Fe. In this case the key issue is the transition from Fe substitutional to the precipitation of Fe-rich nano-crystals at the conditions of spinodal decomposition. In fact, it is observed that T_C is considerably increased exploiting the spinodal decomposition as in the case of Mn in Ge, where Mn-rich ferromagnetic nanocolumns are formed in the crystalline host with a disordered local structure. Finally, first data are reported on the Mn incorporation in GaAs and InAs nanowires that are expected to play a key role in fabricating one dimensional DMS devices.

Keywords: Magnetic semiconductors, Spintronics, GaMnAs GaFeN GeMn nano-fils, EXAFS XANES